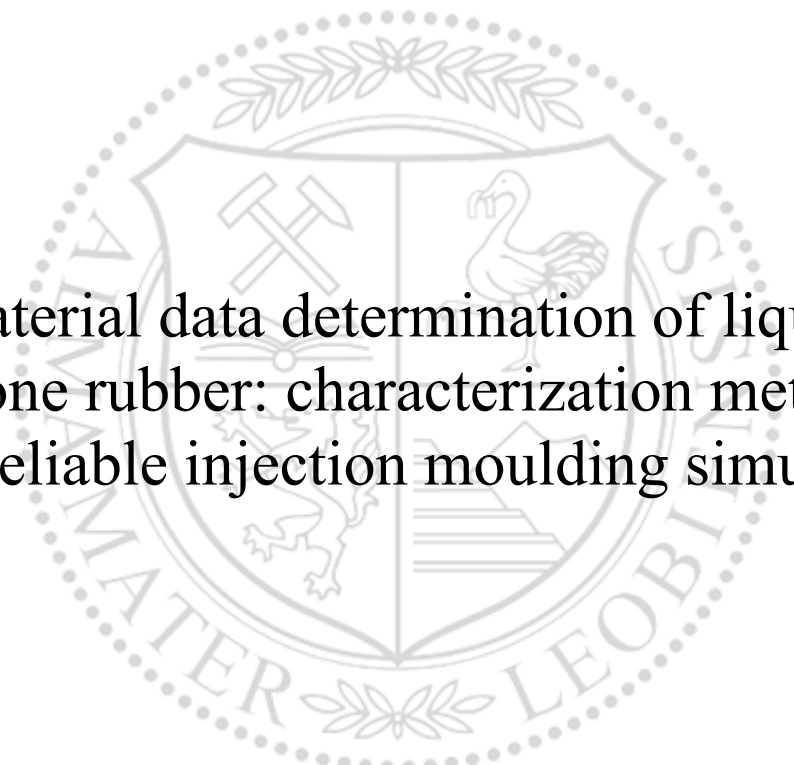




Chair of Polymer Processing

Doctoral Thesis



Material data determination of liquid
silicone rubber: characterization methods
for a reliable injection moulding simulation

Mauricio Azevedo de Freitas

September 2024



AFFIDAVIT

I declare on oath that I wrote this thesis independently, did not use any sources and aids other than those specified, have fully and truthfully reported the use of generative methods and models of artificial intelligence, and did not otherwise use any other unauthorized aids.

I declare that I have read, understood and complied with the "Preamble on Integrity in Academic Study, Teaching, and Research Operations" of the Montanuniversität Leoben.

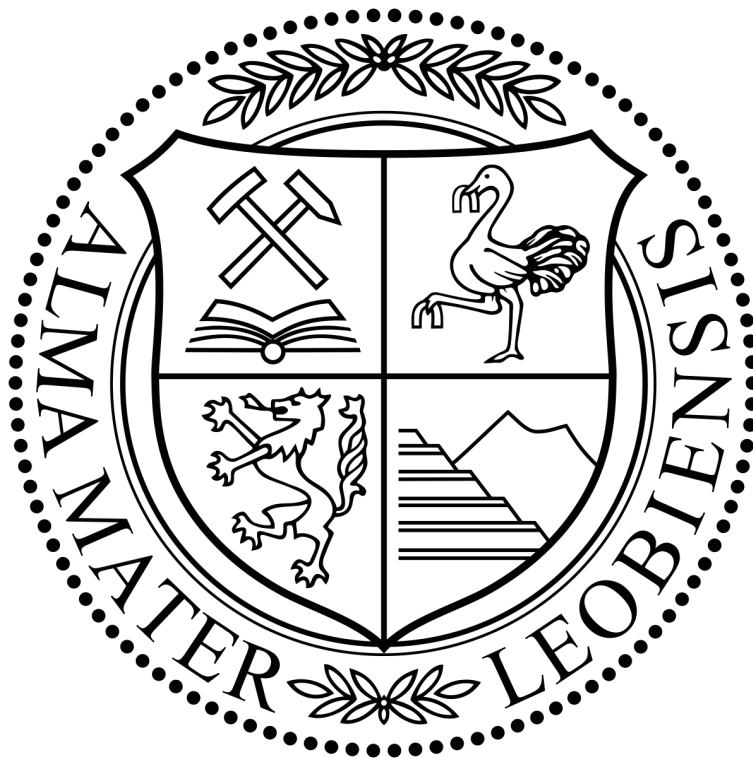
Furthermore, I declare that the electronic and printed versions of the submitted thesis are identical in form and content.

Date

(The original signature is kept at the university)

MATERIAL DATA DETERMINATION OF LIQUID SILICONE
RUBBER: CHARACTERIZATION METHODS FOR A RELIABLE
INJECTION MOULDING SIMULATION

MAURÍCIO AZEVEDO, M.ENG.



Thesis submitted in partial fulfillment of the requirements for the degree Doctor of
Philosophy (Dr.mont.)

Department of Polymer Engineering and Science
Chair of Polymer Processing
Montanuniversität Leoben

March 2022 - September 2024

Maurício Azevedo, M.Eng.: *Material data determination of liquid silicone rubber: characterization methods for a reliable injection moulding simulation*
© September, 2024

SUPERVISOR:

Univ.-Prof. Dipl.-Ing. Dr.mont. Clemens Holzer

MENTOR:

Univ.-Prof. Dipl.-Ing. Dr.mont. Gerald Pinter

LOCATION:

Leoben, Austria

TIME FRAME:

March 2022 - September 2024

To my family.
To the whole scientific and civil communities.

ABSTRACT

Silicones, or poly(siloxanes), are distinguished by their thermal stability, flexibility, and resistance to environmental degradation; qualities that render them ideal for numerous engineering applications, particularly in scenarios demanding robust performance materials. The simulation of liquid silicone rubber (LSR) injection moulding (IM) is complex due to the material's unique properties and behavior under processing conditions. This thesis systematically explores the critical properties of LSR relevant to improving the accuracy of IM simulations: flow behaviour (viscosity), thermal characteristics (specific heat capacity, thermal conductivity, and specific volume), and curing kinetics. Distinct experimental methodologies to characterize these properties are critically and systematically compared, aiming to achieve important insights about material data characterization for IM simulation. Concerning the flow behaviour of liquid silicone rubber, the focus was on detailing how viscosity responds to temperature and shear rate changes, employing different methodologies. It was discovered that steady shear-based techniques are adept at capturing the microstructural transformations of LSR, crucial to account for the presence of structuring fillers in the silicone matrix. Next, the study delves into thermal properties variations with temperature and curing state. The results underscore that specific heat capacity is mainly influenced by temperature rather than curing state, also being dominated by the presence of fillers, facilitating more precise energy conservation modeling in simulations. Besides, different methodologies were able to reach similar results for the thermal properties. The curing kinetics investigation compares different methodologies for determining LSR's crosslinking behaviour. The findings reveal that calorimetry and rheology provide different insights, with calorimetry supporting an autocatalytic model and rheology indicating an n^{th} -order model. Finally, the simulation trials integrate these insights into injection moulding simulations, assessing the impact of varying material datasets on simulation outcomes. The simulations highlighted that oscillatory measurements of viscosity under large amplitude oscillation can be compared to high pressure capillary rheometer data, but with important differences concerning the injection phase in terms of pressure. Furthermore, distinct specific heat capacity data affected mostly the curing phase, with differences concerning curing onset. Finally, via applying distinct curing kinetics parameters, the compared simulations reached different curing behaviours, but the curing time at a practical ejection point was not significantly changed.

ZUSAMMENFASSUNG

Silikone oder Poly(siloxane) zeichnen sich durch ihre thermische Stabilität, ihre Flexibilität und ihre Widerstandsfähigkeit gegenüber Umwelteinflüssen aus. Diese Eigenschaften qualifizieren sie für zahlreiche technische Anwendungen, insbesondere dort, wo zuverlässige und leistungsfähige Werkstoffe erforderlich sind. Demzufolge ist die Simulation des Spritzgießens von Flüssigsilikonkautschuk (LSR), aufgrund der einzigartigen Eigenschaften des Materials und dessen Materialverhalten unter den jeweiligen Verarbeitungsbedingungen, sehr komplex. In der vorliegenden Arbeit werden systematisch die einzigartigen Eigenschaften von LSR mit Hilfe von unterschiedlichen Methoden untersucht, die für die Verbesserung der Genauigkeit von Spritzgießsimulationen relevant sind: Fließverhalten (Viskosität), thermische Eigenschaften (spezifische Wärmekapazität, Wärmeleitfähigkeit und spezifisches Volumen) und Vernetzungskinetik. Beim Fließverhalten von Flüssigsilikonkautschuk lag der Schwerpunkt auf der Untersuchung der Reaktion der Viskosität auf Temperatur- und Schergeschwindigkeitsänderungen, wobei verschiedene Methoden zum Einsatz kamen. Es wurde festgestellt, dass Techniken, die auf gleichmäßiger Scherung basieren, die mikrostrukturellen Veränderungen von LSR gut erfassen können, was für die Berücksichtigung des Vorhandenseins von strukturgebenden Füllstoffen in der Silikonmatrix entscheidend ist. Als Nächstes befasst sich die vorliegende Arbeit mit den Veränderungen der thermischen Eigenschaften in Abhängigkeit von der Temperatur und dem Vernetzungszustand. Die Ergebnisse unterstreichen, dass die spezifische Wärmekapazität hauptsächlich von der Temperatur und nicht vom Vernetzungszustand beeinflusst wird, wobei auch das Vorhandensein von Füllstoffen eine Rolle spielt, wodurch eine genauere Modellierung der Energieerhaltung in Simulationen möglich ist. Außerdem konnten mit verschiedenen Methoden ähnliche Ergebnisse für die thermischen Eigenschaften erzielt werden. Die Untersuchung der Vernetzungskinetik vergleicht verschiedene Methoden zur Bestimmung des Vernetzungsverhaltens von LSR. Die Ergebnisse zeigen, dass Kalorimetrie und Rheologie unterschiedliche Erkenntnisse liefern, wobei die Kalorimetrie ein autokatalytisches Modell unterstützt und die Rheologie auf ein Modell n-ter Ordnung hinweist. In den Simulationsversuchen wurden diese Erkenntnisse schließlich in Spritzgussimulationen integriert und die Auswirkungen unterschiedlicher Materialdatensätze auf die Simulationsergebnisse bewertet. Diese haben gezeigt, dass oszillatorische Messungen der Viskosität unter großen Amplitudenschwingungen mit Hochdruck-Kapillarrheometerdaten verglichen werden können, allerdings mit wichtigen Unterschieden hinsichtlich der Einspritzphase in Bezug

auf den Druck. Außerdem wirkten sich die unterschiedlichen Daten zur spezifischen Wärmekapazität hauptsächlich auf die Vernetzungsphase aus, mit Unterschieden hinsichtlich des Vernetzungsbegins. Schließlich erreichten die vergleichenden Simulationen durch die Anwendung unterschiedlicher Vernetzungskinetik-Parameter ein anderes Vernetzungsverhalten, aber die gesamte Vernetzungszeit wurde nicht wesentlich verändert.

PUBLICATIONS

Some concepts, ideas, and figures of this Thesis have appeared previously in the following publications:

1. **M. Azevedo**, A.-M. Monks, R.C. Kerschbaumer, and C. Holzer. "Crosslinking of high consistency silicone with dicumylperoxide: predicting curing behaviour using a rubber process analyser". In book: *Constitutive Models for Rubber XII* (2022). DOI: <http://dx.doi.org/10.1201/9781003310266-37> .
2. A.-M. Monks, **M. Azevedo**, R.C. Kerschbaumer, and C. Holzer. "Crosslinking of silicone rubber with dicumylperoxide: an assessment employing the rubber process analyser". Poster contribution in: *30th Leoben Conference on Polymer Engineering and Science* (2022). DOI: <http://dx.doi.org/10.13140/RG.2.2.10117.63205> .
3. **M. Azevedo**, A.-M. Monks, R.C. Kerschbaumer, S. Schlögl, and C. Holzer. "Peroxide-Based Crosslinking of Solid Silicone Rubber, Part I: Insights into the Influence of Dicumylperoxide Concentration on the Curing Kinetics and Thermodynamics Determined by a Rheological Approach". In: *Polymers* 14(20) (2022), pp. 4404. DOI: <http://dx.doi.org/10.3390/polym14204404> .
4. **M. Azevedo**. "Crosslinking of high consistency silicone with dicumylperoxide: characterization of physical, thermal, and mechanical properties". In the proceedings of: *2022 International Rubber Conference* (2022). DOI: <http://dx.doi.org/10.13140/RG.2.2.32185.03680>.
5. **M. Azevedo**, A.-M. Monks, R.C. Kerschbaumer, S. Schlögl, K. Saalwächter, M. Walluch, G. Consolati, and C. Holzer. "Peroxide-based crosslinking of solid silicone rubber, part II: The counter-intuitive influence of dicumylperoxide concentration on crosslink effectiveness and related network structure". In: *J. App. Polym. Sci* 140(31) (2023), pp. e54111. DOI: <https://doi.org/10.1002/app.54111>.
6. **M. Azevedo**, R.C. Kerschbaumer, and C. Holzer. "Process simulation and the environment: what reliable material properties have to do with saving energy and CO₂". Poster contribution in: *31st Leoben Conference on Polymer Engineering and Science* (2023).
7. **M. Azevedo**, R.C. Kerschbaumer, and C. Holzer. "Mastering the flow: Navigating the challenges of measuring liquid silicone

rubber's viscosity for injection moulding simulation". Poster contribution in: *International Conference on Rheology* (2023). DOI: <http://dx.doi.org/10.13140/RG.2.2.15263.12961>.

8. **M. Azevedo**, R.C. Kerschbaumer, and C. Holter. "Liquid silicone rubber injection moulding simulation: the challenges for a reliable material data set". In the proceedings of: *3rd International Conference on Polymer Process Innovation* (2023).
9. **M. Azevedo**, R.C. Kerschbaumer, F. Gerstbauer, M. Sommer, K. Lamnawar, A. Maazouz, and C. Holzer. "Large amplitude oscillatory shear rheology of liquid silicone rubber: insights into filler structure and viscoelasticity". In the proceedings of: *2024 International Rubber Conference* (2024).
10. **M. Azevedo**, R.C. Kerschbaumer, F. Gerstbauer, M. Sommer, K. Lamnawar, A. Maazouz, and C. Holzer. "Thixotropy in injection moulding liquid silicone rubber: filler structure as a key feature for processing-related viscosity determination". Poster contribution in: *2024 International Rubber Conference* (2024).

Additional publications belonging to the framework of this Thesis are also listed as follows:

11. **M. Azevedo**, A.-M. Monks, R.C. Kerschbaumer, and G. Pilz. "Temperature scanning stress relaxation (TSSR): a characterization opportunity for elastomeric crosslinked networks". Poster contribution in: *30th Leoben Conference on Polymer Engineering and Science* (2022).
12. J. Schieppati, T. Gehling, **M. Azevedo**, R.C. Kerschbaumer, P. Christöfl, G. Oreski, M.A. Fasching, T. Schwarz, and G. Pinter. "Investigation into the state of cure of elastomers through nanoindentation". In: *Polym. Test.* 133 (2024), pp. 108417. DOI: <https://doi.org/10.1016/j.polymertesting.2024.108417>.
13. M. Traintinger, **M. Azevedo**, R.C. Kerschbaumer, B. Lechner, T. Lucyshyn. "Optimization Strategy for Process Design in Rubber Injection Molding: A Simulation-Based Approach Allowing for the Prediction of Mechanical Properties of Vulcanizates". In: *Polymers* 16(14) (2024), pp. 2033. DOI: <https://doi.org/10.3390/polym16142033>.
14. R.C. Kerschbaumer, G. Weinhold, F. Leins, M. Traintinger, M. Horbachner, **M. Azevedo**, and T. Lucyshyn. "Shifting Focus to Quality: An Innovative Modeling Approach Includes Processing History for Rubber Part Quality Simulation". Submitted to *J. App. Polym. Sci.*

*I am among those who think that science has great beauty.
A scientist in his laboratory is not only a technician:
he is also a child placed before natural phenomena
which impress him like a fairy tale.*

— *Maria Salomea Skłodowska-Curie*

ACKNOWLEDGMENTS

First and foremost, I am profoundly grateful to my parents, brothers, and sister for their unwavering support since my childhood, nurturing my natural curiosity for discovery and innovation. Their encouragement throughout my professional journey has been invaluable, empowering me to pursue my dreams and seek what I believe will bring me the greatest happiness.

I owe a deep debt of gratitude to my supervisor, Univ.-Prof. Dipl.-Ing. Dr.mont. Clemens Holzer, for his steadfast support, openness to discussing ideas, and encouraging words. His guidance and the freedom he afforded me to conduct this research have been crucial to its success.

Special thanks go to my colleague and mentor, Dipl.-Ing. Dr.mont. Roman Kerschbaumer, for his essential support throughout the development of this work and for the valuable suggestions during the writing of this Thesis. His patience, trust, and belief in my ideas were pivotal in shaping this research, and I am grateful for the wealth of theoretical and practical knowledge he generously shared.

I am also thankful to the Institut National des Sciences Appliquées de Lyon (INSA Lyon, France), under the guidance of Prof. Abderrahim Maazouz, for providing the necessary support for the rheological studies of this Thesis. Additionally, I extend my sincere appreciation to Starlim Spritzguss GmbH (Austria), particularly Dipl.-Ing. Ferdinand Gerstbauer and Dipl.-Ing. Maximilian Sommer, for their continuous support concerning liquid silicone rubber.

My heartfelt thanks go to all the colleagues who dedicated their time to assist me with experimental support and discussion of ideas: Bernhard Lechner, Anna-Maria Monks, Dipl.-Ing. Dr.mont. Martin Traintinger, Dipl.-Ing. Dr.mont. Ivica Duretek, Caroline Parajua-Sejil, and Dr. Felipe Teles Barbosa.

Finally, I wish to express my deep gratitude to all my friends, human and spiritual, especially those from across the ocean, who supported me through this significant journey. Your encouragement has meant the world to me.

CONTENTS

I Introduction and motivation

1	Introduction to liquid silicone rubber injection moulding	3
1.1	Molecular structure	4
1.2	Main properties	5
1.2.1	Synthesis and molecular weight distribution	5
1.2.2	Glass transition and crystallinity	7
1.2.3	Thermal stability	8
1.2.4	Silica as filler for LSR	9
1.3	Injection moulding of LSR	10
1.4	Injection moulding simulation	13
2	Motivation and objectives	15

II Rheology of liquid silicone rubber

3	Theory of rheology	21
3.1	Injection moulding, shear, and viscoelasticity	21
3.2	Methods for shear viscosity determination	23
3.2.1	Rotational rheology - oscillatory shear	23
3.2.2	Rotational rheology - steady shear	26
3.3	The Cox-Merz proposition	27
3.4	Capillary rheology - high pressure capillary rheometer	28
4	Experimental description: rheology	29
4.1	Materials	29
4.2	Rotational rheology	29
4.2.1	Oscillatory experiments	29
4.2.2	Steady flow experiments	30
4.3	Capillary rheology	31
5	Results and conclusions	33
5.1	Aspects on the linearity of viscoelastic properties	33
5.2	Determination of complex viscosity $\eta^*(\omega)$	40
5.3	Determination of the steady shear viscosity	43
5.4	Determination of viscosity via HPCR	44
5.4.1	Comparison among viscosities and the Cox-Merz proposition	46
5.4.2	Filler network recovery after shear	49
5.5	Conclusions of the chapter	53

III Thermal properties

6	Theoretical background	57
6.1	Heat transfer during injection moulding	57
6.2	Internal energy and mechanism of phonon conductivity in polymers	58
6.3	Compressibility of polymers	62

7	Experimental description	65
7.1	Determination of the specific heat capacity under constant pressure	65
7.1.1	Materials	65
7.1.2	The sapphire method - ASTM E1296-11	65
7.1.3	The modulated temperature calorimetry approach	67
7.2	Measurement of the thermal conductivity	68
7.2.1	Materials	68
7.2.2	Transient line-source technique	69
7.2.3	Guarded heat flow meter method	70
7.3	Determination of the specific volume	70
7.3.1	Materials	70
7.3.2	Piston-based isobaric method	71
8	Results and conclusions	73
8.1	Specific heat capacity c_p	73
8.2	Thermal conductivity λ	79
8.3	Specific volume or pvT behaviour	82
8.4	Conclusions of the chapter	83
iv Crosslinking kinetics		
9	Theoretical background	87
9.1	Crosslinking reaction in injection moulding	87
9.2	Curing mechanisms of poly(siloxane)s	89
9.2.1	Peroxide-based crosslinking	89
9.2.2	Platinum-catalysed curing	91
9.3	Curing kinetics determination	93
10	Experimental description	97
10.1	Preliminary investigations with high consistency silicone	97
10.1.1	Materials	97
10.1.2	Isothermal rotational rheometry	98
10.1.3	Determination of the activation energy	99
10.1.4	Fitting of curing rates $d\alpha/dt$	101
10.2	Liquid silicone rubber investigation	101
10.2.1	Materials	102
10.2.2	Non-isothermal rotational rheometry	102
10.2.3	Dynamic scanning calorimetry	102
11	Results and conclusions	105
11.1	Curing kinetics of high consistency silicone	105
11.1.1	Curing characteristics	105
11.1.2	Peroxide-based crosslinking kinetics	110
11.2	Curing kinetics of liquid silicone rubber	115
11.2.1	Curing kinetics via DSC	116
11.2.2	Curing kinetics via RPA	118
11.2.3	Fitting and comparison between DSC and RPA	123
11.3	Conclusion of the chapter	127

v Injection moulding simulation

12	Simulation trials	131
12.1	The governing constitutive equations	131
12.2	Boundary conditions and meshing	132
12.3	Available commercial software	134
12.4	Comparison routines - simulation setup	135
12.4.1	Part geometry and simulation settings	136
12.4.2	Viscosity data: oscillatory LAOS and HPCR	138
12.4.3	Specific heat capacity: standard and modulated DSC	138
12.4.4	Curing kinetics: calorimetry and rheology approaches	139
12.5	Comparison results	139
12.5.1	Viscosity datasets A and B	139
12.5.2	Specific heat capacity datasets B and C	144
12.5.3	Specific heat capacity datasets B and D	146
12.5.4	Curing kinetics datasets B and E	151
12.6	Conclusions of the chapter	155

vi Conclusions and final remarks

13	Final remarks	159
13.1	Philosophical objectives	159
13.2	Scientific goals	160
13.3	Limitations of the study	163
13.4	Future research directions	163

vii Appendix

A	Appendix	167
A.1	Molecular weight distribution	167
A.1.1	High consistency silicone	167
A.1.2	Liquid silicone rubber	168
A.2	Chemical characterization	168
A.2.1	High consistency silicone	168
A.2.2	Liquid silicone rubber	170
A.3	Filler content determination	171
A.3.1	High consistency silicone	171
A.3.2	Liquid silicone rubber	172
A.4	Rheology - reproducibility study	173
A.5	Hysteresis curves for 2070 B	174
A.6	Strain and stress sinusoidal signals	175
A.7	Intensity of Chebyshev coefficients at 90°C	175
A.8	Edge instability during steady shear experiments	175
A.9	Python scripts	179
A.10	Use of AI-based tools	184
A.11	Residual analysis of the Kamal model fitting	185
A.12	Viscosity data fitting	185

Bibliography 201

Part I

INTRODUCTION AND MOTIVATION

INTRODUCTION TO LIQUID SILICONE RUBBER INJECTION MOULDING

Silicones, or poly(siloxane)s, have emerged as indispensable materials with diverse applications, owing to their exceptional properties and versatility. From the first commercial development in 1944 [1], silicones gained prominence due to their remarkable heat resistance, flexibility, and biocompatibility. Notably, in 1969, Neil Armstrong made history by using boots with silicone soles, leaving the first human footprint on the moon's surface, showcasing silicone's durability and reliability even in the harshest environments. Its versatility finds application across various sectors, including automotive, electronics, healthcare, and consumer goods. From automotive gaskets and seals to medical implants and consumer electronics cases, silicone's mouldability and resilience have revolutionized product design and manufacturing processes, contributing significantly to technological advancements and everyday living comforts.

Commercially available silicones encompass a spectrum of formulations, each tailored to specific applications and processing requirements. High consistency silicone rubber (HCR) and liquid silicone rubber (LSR) represent two distinct categories within this spectrum, but that share a common feature: they are crosslinked in order to be employed as final products. HCR, also known as solid silicone rubber, is characterized by its high viscosity (soft solid) and mouldability, derived from its high molecular weight (above $100000 \text{ g}\cdot\text{mol}^{-1}$, or 100 kDa). It typically comes in the form of solid compounds that require further processing, such as compression molding, to achieve the desired shape via curing. On the other hand, LSR is a two-part liquid compound that cures into a flexible, durable rubber upon mixing and crosslinking. LSR offers advantages in injection molding processes due to its low viscosity (it is composed of poly(siloxane) oligomers) and fast curing time. While HCR is preferred for applications requiring intricate details or thicker parts, LSR excels in producing thin-walled or complex geometries with high precision and consistency. Additionally, LSR's biocompatibility and sterilizability make it ideal for medical and food-grade applications, whereas HCR is often used in industrial seals, gaskets, and automotive components. Within the spectrum of poly(siloxane)s lie also silicone fluids and greases, which possess even lower molecular weight (around $50000 \text{ g}\cdot\text{mol}^{-1}$, or 50 kDa [2]) when compared to LSR and are not crosslinked. These silicone compounds will not be addressed in this work.

The unique set of applications described before arise from the particular chemical structure of poly(siloxane)s, which is distinct from hydrocarbon polymers, such as the commodities poly(ethylene) and poly(propylene). The molecular structure, result from a particular synthetic route, and the derived properties are described next. Furthermore, the main aspects of liquid silicone rubber injection moulding are introduced, bringing in the most widely employed polymer processing technique for LSR.

1.1 MOLECULAR STRUCTURE

The base of all silicones is composed of macromolecules with successive silicon–oxygen bonds as backbone and the Si atom having two monovalent organic side groups, normally referred to as R_1 and R_2 , as shown in Figure 1.1. From the Figure, one can realize the first and most significant difference between silicones and hydrocarbon polymers: the chemical nature of the backbone. While hydrocarbon polymers, such as poly(butadiene) and poly(vinyl chloride), possess an organic backbone, silicones have an inorganic base structure. This alternating inorganic backbone of Si and O atoms provides strong and long chain bonds: $106 \text{ kJ}\cdot\text{mol}^{-1}$ bond energy and 1.64 \AA bond length, compared to $85 \text{ kJ}\cdot\text{mol}^{-1}$ and 1.53 \AA for C–C bond. The stronger bond between Si and O, and the wide O–Si–O angle, can be explained in terms of the theory of molecular orbital and the electronegativity difference between the atoms.

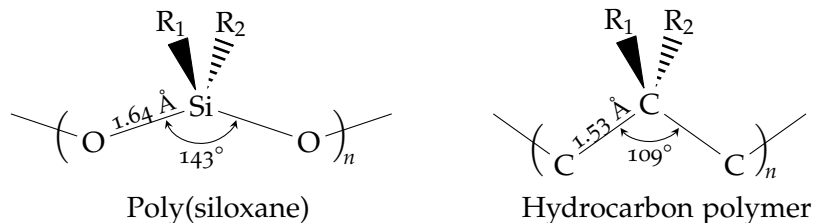


Figure 1.1: Molecular structure of a general poly(siloxane) and a hypothetical hydrocarbon polymer, where, for instance, for poly(siloxane)s, $R_1 = R_2 = \text{CH}_3$ for poly(dimethylsiloxane) (PDMS). For the hydrocarbon polymer, $R_1 = R_2 = \text{H}$ for poly(ethylene), and $R_1 = \text{H}$ and $R_2 = \text{CH}_3$ for poly(propylene), for example.

As explained by Dankert and von Hähnisch [3], the high Si–O bond energy is associated to three aspects. The first two concern hyperconjugation interactions between silicon and oxygen atoms based on the fact that Si has $3d$ orbitals available to be occupied by electron density (carbon atoms have only s and p orbitals). These interactions are the predominant negative hyperconjugation of the type $p(\text{O}) \rightarrow \sigma^*(\text{Si} - \text{C})$, i.e., backbonding into the antibonding molecular orbital (located away from the bonding axis) of the Si–C bond; and the less extensive $p(\text{O}) \rightarrow d(\text{Si})$, i.e., electron density occupation

of silicon's d orbital from oxygen's p orbital. Besides these covalent aspects, the Si–O bond also has an ionic character absent in C–C, since there is a significant difference between silicon's and oxygen's electronegativities: according to the electronegativity scale of Allred and Rochow [4], Si/O have an electronegativity difference of 1.76, while C/O, for instance, differ only by 1 unit. This electronegativity difference polarizes the Si–O bond with a high electron density at the oxygen atom, which enhances even more the hyperconjugation phenomena explained before. Polarization not only strengthens the bond and brings the Si and O atoms close together (the sum of the covalent radii for Si–O is 1.77 Å, higher than the actual 1.65 Å bond length which considers ionic contributions), but also widens the O–Si–O angle, since adjacent oxygen atoms are equally negatively charged. Besides bond strength, length, and angle, the flexibility of O–Si–O also has to be highlighted here. The bonding of oxygen and silicon atoms in the main poly(siloxane) chain and of silicon and (normally) carbon atoms in the radical positions R_1 and R_2 reassembles the one in hydrocarbons, i.e., in a tetrahedron fashion. Thus, the sp^3 hybridization of silicon is responsible for the chain segment's ease of rotation, as happens with poly(ethylene), for example, but with easier rotation barrier [5] in the case of Si–O bonds. All aforementioned *intramolecular* aspects help to define the macro-properties of liquid silicone rubber, along with considerations concerning *intermolecular* features, such as dispersion forces and entanglements, which will be covered in the next sections.

1.2 MAIN PROPERTIES

The following section will describe the properties of poly(siloxane)s that are most relevant to injection moulding, starting from how the polymer is synthesized. Special focus will be given to temperature-related properties, since these are directly connected to processing. Particular properties, such as flow behaviour, specific heat capacity, thermal conductivity, specific volume, and reactivity will be discussed in dedicated Chapters in the respective Parts of this Thesis.

1.2.1 *Synthesis and molecular weight distribution*

The production of poly(siloxane)s comprises three main synthesis steps: i) production of organochlorosilanes by the Müller-Rochow process; ii) hydrolysis or methanolysis of organochlorosilanes into linear and cyclic oligomeric siloxanes; and finally iii) polymerization mainly via polycondensation or ring-opening polymerization. [6–8]

The Müller-Rochow [9, 10] process has been used since its development to synthesize organochlorosilanes from elementary silicon. This synthetic route engages the reaction of silicon with chloroalkanes

in the presence of a catalyst in fluidized bed reactors, leading to a mixture of silanes containing, among others, dimethyldichlorosilanes and hydride-containing silanes, such as $(\text{CH}_3)_2\text{SiHCl}_2$. The latter silane is the crucial reactant to further synthesize the poly(siloxane) to be used in liquid silicone rubber, since it contains the hydride moiety necessary for the crosslinking reaction via hydrosilylation. The fact that organochlorosilanes are highly sensitive to protic substances, such as water and alcohols, is explored as strategy to synthesize polymeric silicones via hydrolysis or methanolysis, as the next synthesis step.

Hydrolysis of organochlorosilanes leads to a mixture of linear or cyclic oligomeric siloxanes and hydrochloric acid, while methanolysis produces the same oligomers, but chloromethane is generated instead. These two by-products are recovered in the process to be used in the Müller-Rochow step. The siloxane oligomers, either linear via polycondensation, or cyclic via ring-opening polymerization, are then polymerized to produce poly(siloxane)s.

For polymerization of oligomeric siloxanes, two routes are possible: polycondensation and ring-opening polymerization. For the industry scenario, polycondensation is preferred due to the higher cost associated to ring-opening strategies. [8] Both polymerization routes are usually catalyzed by acid or base compounds; however, the main difference between these approaches is the molecular weight and polydispersity control of the produced poly(siloxane)s. As a step polymerization, polycondensation normally results in polymers with broad molecular weight distribution [11] (up to 2.0). On the other hand, ring-opening polymerization is able to produce poly(siloxane)s with defined molecular weight distribution, mainly aiming to be employed in special applications. [8] Within the silicone world, controlling the conversion of such polymerizations will result in a variety of materials, from oils (low molecular around $1 \text{ kg}\cdot\text{mol}^{-1}$) to high viscosity polymers, such as liquid silicone rubber and high consistency silicone, or solid silicone.

Concerning liquid silicone rubber, it is widely employed as a two-component system comprising part A and part B. Both parts contain poly(siloxane) as base with molecular weight around $100 \text{ kg}\cdot\text{mol}^{-1}$ [12], but incorporate distinct additives. To part A, an organometallic catalyst is added, aiming to trigger the crosslinking reaction. To part B, a crosslinker compound, also made of poly(siloxane) but with lower molecular weight (below $10 \text{ kg}\cdot\text{mol}^{-1}$ [12]) than the base polymer, is added, being the responsible to connect two silicone macromolecules via the hydrosilylation reaction. More details about the crosslinking reaction will be given in Chapter 9. High consistency silicone, however, presents a substantially higher molecular weight (400 to $600 \text{ kg}\cdot\text{mol}^{-1}$ [13]) when compared to liquid silicone rubber.

The fact that both liquid silicone rubber and high consistency silicone present moderate-to-high molecular weight imposes to them

important macromolecular features. One of these is the presence of entanglements. As the siloxane oligomers turn into poly(siloxane) polymers with the polymerization development, the macromolecules depart from only a coiled state (as accurately described by the beads-and-springs Rouse model) to an entangled conformation more precisely represented by the reptation model. [14, 15] The alternating silicon-oxygen backbone grows and starts to entangle with itself and other adjacent macromolecules when the molecular weight reaches around $34 \text{ kg}\cdot\text{mol}^{-1}$ [16–18]. For comparison, poly(ethylene oxide) (T_g around -60°C) presents a critical molecular weight for entanglements of $6 \text{ kg}\cdot\text{mol}^{-1}$ [19], while for poly(styrene) (T_g around 100°C), it lies between 30 and $34 \text{ kg}\cdot\text{mol}^{-1}$ [20]. The existence of entanglements influences mainly the viscoelastic behaviour of poly(siloxane)s. The other macromolecular features, such as glass transition and the possibility of crystallization, will be presented in the next section.

1.2.2 Glass transition and crystallinity

Poly(siloxane)s with molecular weight characteristic of liquid silicone rubber and high consistency silicone present three typical thermal transitions: α relaxation (segmental relaxation, or glass transition), melt/cold crystallization, and melting. The glass transition temperature (T_g) of silicone is around -120°C , as widely reported for multiple poly(siloxane)s in the literature [21–24], including by our group [25], mainly for poly(dimethyl siloxane). It is important to notice that depending on R_1 and R_2 (see Figure 1.1), the glass transition temperature reaches -28°C for poly(methylphenyl siloxane) and $+40^\circ\text{C}$ for poly(diphenyl siloxane) [24, 26]. The change in the monovalent ligands of the silicon atom alters the macromolecule's ability to undergo thermal relaxation via spacial hindering, increasing the glass transition temperature for bulky groups, such as phenyl. The very low glass transition temperature of silicones when compared to hydrocarbon polymers is the macroscopic result of the molecular structure as described previously in this Chapter: the high chain flexibility coupled with the weak inter- and intramolecular interactions lead to a large free volume, which results in a low glass transition temperature. Indeed, the large free volume is the responsible for the high gas permeability associated to silicones. [27]

The next important thermal transitions are crystallization and melting. Silicone crystallization occurs due to the high flexibility and regularity of the poly(siloxane) macromolecules, which are able to organize into lamellae structures. These structures grow from small nuclei, which are formed in the bulk of the polymer network. For silicones, both cold (during heating) and melt (during cooling) crystallization occur and they were reported to occur at around -90°C [21–23, 28]. During heating, the cold crystallization of silicone appears in dy-

dynamic scanning calorimetry (DSC) experiments as an exothermic peak. On the other hand, melting demands energy to occur, since the organized lamellae structure is only destroyed when the macromolecules have enough thermal energy to move and assume a higher entropic state, characterizing an endothermic event at the DSC. Melting of poly(siloxane) crystalline phase occurs at around -40°C . [21–23, 25, 28]

1.2.3 Thermal stability

As explained in Section 1.1, poly(siloxane)s are composed of macromolecules with stronger atomic bonds than hydrocarbon polymers. The fact that both covalent (backbonding) and ionic (electronegativity difference) features additionally strengthen the Si–O bond turns silicones into high thermally stable polymers. In fact, silicones undergo significant mass loss (higher than 10%) only above 400°C [29–33], varying according to the molecular weight, the end-group chemistry, and the presence of impurities [34]. The main thermal degradation mechanism is the molecular back-biting depolymerization, as pictured in Figure 1.2. Interesting to note is that scission occurs at the stronger Si–O bond and not at the weaker Si–C due to the formation of a cyclic transition state [29]. Again, it is highlighted the importance of the *d* orbitals in the formation of such cyclic transition state, which is favoured by chain flexibility that allows back-biting. For telechelic poly(siloxane)s, the presence of end groups may lead to back-biting mechanisms from the chain ends. The literature reports [29] a second thermal degradation mechanism based on the homolytic bond scission of the Si–CH₃ bond, leading to CH₄.

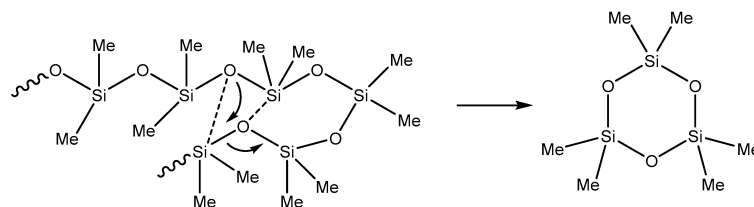


Figure 1.2: Main thermal degradation mechanism of poly(dimethyl siloxane) based on intramolecular back-biting and formation of a cyclic oligomer ([35], adapted from [29]).

Specifically for liquid silicone rubber, under inert atmosphere, the thermogravimetric analysis of pure poly(dimethylsiloxane) (no catalyst) leads to no residue at 800°C [36], while for filled PDMS, the residue is proportional to the amount of incorporated filler. Indeed, fillers such as silicon dioxide (SiO₂) are often added to liquid silicone rubber in order to provide mechanical characteristics, such as strength, hardness, or to control rheological properties.

1.2.4 Silica as filler for LSR

Due to the poor mechanical properties of pure liquid silicone rubber, fillers are normally introduced in the silicone formulation for reinforcement in practical applications. Amongst the large variety of fillers that can be incorporated to elastomers, reinforcing silica is one of the most employed filler due to its easy accessibility, low cost, environmental acceptance, and structural and chemical similarity to siloxane-based elastomers. [37] The incorporation of rigid particles in the viscoelastic poly(siloxane) network leads to several structural changes, which are tightly connected to both the interaction between silica particles (filler-filler interaction) and the interaction between the silica particles and the polymer macromolecules (polymer-filler interaction).

Silica when dispersed in a polymeric matrix acquires an hierarchical structure as shown in Figure 1.3. The nanometric sphere-like primary particles (level 1) are composed of amorphous silicon dioxide, which interact with other primary particles via strong hydrogen bonding to form aggregates (level 2). Aggregates then further associate to become agglomerates (level 3), being the structural level where physical changes occur, for example due to oscillatory strain. For silicones, fumed and precipitated silica grades are mostly employed, and it is commonly understood that the reinforcing effect of fumed silica is higher than the one provided by precipitated silica. [38] This fact is justified by their distinct aggregate structure: fumed silica has fumed aggregates with dendritic structures and higher surface area, while precipitated silica aggregates into irregular regimental structures with smaller aggregation size, as also shown in Figure 1.4. [38, 39]

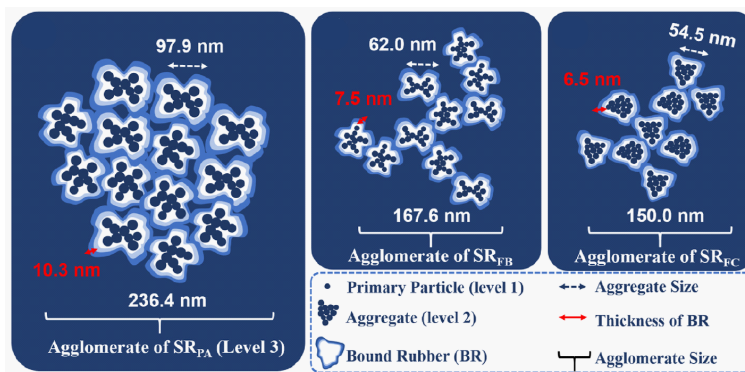


Figure 1.3: Schematics illustration of the hierarchical structure of distinct silicas in silicone rubber: SR_{PA} : precipitated silica; SR_{FB} and SR_{FC} : fumed silica modified by hexamethyldisilazane (from [40])

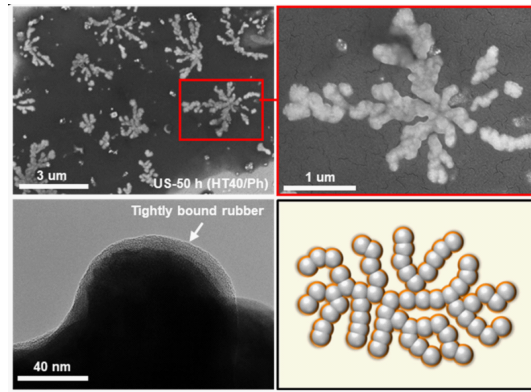
While primary particles interact almost exclusively with themselves due to their high surface energy and therefore strong hydrogen bonding, agglomerates and aggregates possess a larger interface with the polymer matrix, which is where polymer-filler interactions mostly

occur. This stiff interphase where the poly(siloxane) macromolecules interact with the filler particle's surface either via secondary bonds (hydrogen bonding or van der Waals interaction) or covalent bonds (when the filler surface is chemically modified to react with the polymer [39–43]) is commonly referred to as bound rubber. Bound rubber and hydrodynamic effect are thus understood as the dominant microscopic mechanisms typically responsible for the enhanced macroscopic stiffness of filled silicones. [44] Scanning electron microscopy (SEM) and transmission electron microscopy (TEM) images of the tightly bound rubber layer in fumed and precipitated silica, as studied by Huang *et al.* [38], are respectively shown in Figure 1.4. This layer is commonly accepted to be composed of chemically bonded or physically adsorbed macromolecules with progressive increasing hindered movement as they reach closer distances to the filler particle. In this sense, one can assume that in liquid silicone rubber-filled compounds, the poly(siloxane) molecules assume four distinct dynamic states as: i) free rubber, distant from the filler particle and considered as in the bulk; ii) loosely bound rubber, which are polymer chains physically entangled to the tightly bound layer; iii) tightly bound rubber, composed of macromolecules in close contact with the filler surface either via secondary or chemical bonding; and iv) entrapped rubber, consisting of the chains wrapped by the nanofiller network. [45]

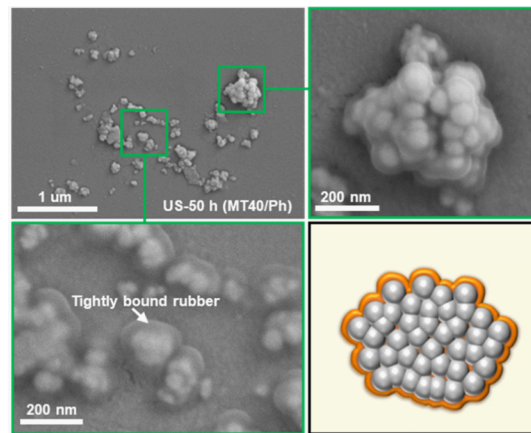
Besides reinforcement, the introduction of silica in liquid silicone rubber leads to non-linear effects, being the most known one the Payne effect. It has been widely accepted that this effect is mainly related to the filler agglomeration in the polymer matrix. At moderate and high strains, these agglomerates are, to a certain degree, destroyed and the rubber trapped within the agglomerates is released lowering the modulus. [46] The decrease of modulus as typical of the Payne effect is also attributed to the damaged filler structure, which is then not able to withstand the same strain as when intact. This effect will be further stressed in Chapter 3.

1.3 INJECTION MOULDING OF LSR

As an important polymer processing technique not only for liquid silicone rubber but for polymers in general, injection moulding (IM) is a versatile method to shape products and, regardless of the material to be injected, it is composed of two major steps: shaping and solidification. For liquid silicone rubber, shaping is preceded by dosing the right amount of components A and B, mixing them usually employing static mixers, and transporting the mixture with a barrel of reciprocating screw injection unit or with a plunger injection unit. The barrel and its screw/plunger are responsible to inject LSR into the mould, where the curing reaction occurs. For this scenario, shaping is



(a)



(b)

Figure 1.4: SEM and TEM images of (a) fumed and (b) precipitated silica. The schematics in the bottom right portion of the figures represent the tightly bound rubber layer in orange, while the silica particle is depicted in gray (adapted from [45])

considered to be the injection of uncured LSR into the mould, while solidification consists of the curing reaction *per se*.

When compared to thermoplastics injection moulding (here called *conventional* injection moulding), liquid silicone rubber (or *reactive* injection moulding) injection moulding presents important distinctions concerning the main phenomena that drive the shaping and solidification steps. For thermoplastics injection moulding (diagram (a) in Figure 1.5), shaping is accomplished via transferring energy as heat to the solid thermoplastic pellets, melting them, and moving the molten polymer following the fluid mechanics laws through the barrel into the mould. For the solidification step, the molten thermoplastic exchanges heat with the cold mould, transferring its total energy to heat the mould and, therefore, transitioning from a molten to a solid state, finally acquiring the mould's cavity shape. For such process, heat transfer and fluid mechanics govern the whole injection moulding cycle and no chemical reaction occurs, i.e., during the whole IM

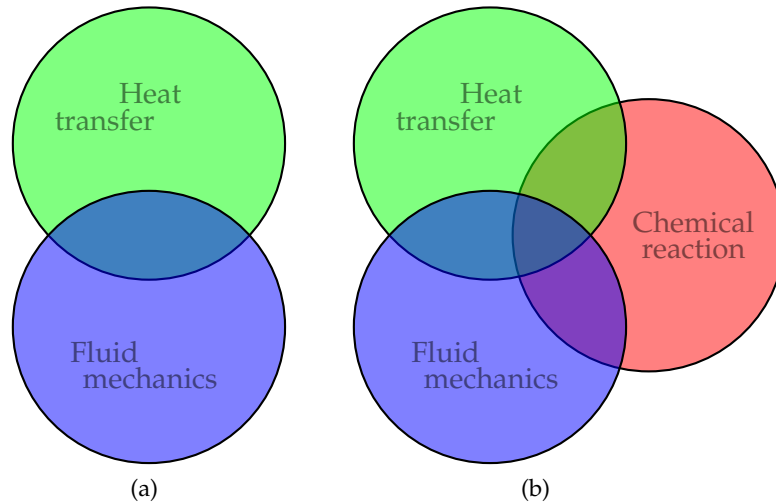


Figure 1.5: For shaping and solidification, the phenomena involved in (a) conventional thermoplastics injection moulding and (b) liquid silicone rubber (reactive) injection moulding (adapted from [47])

process the polymer is chemically the same, varying in physical state (amorphous/semi-crystalline and molten).

For all rubbers, including hydrocarbon rubbers and liquid silicone rubber, and poly(urethane)s, for example, injection moulding is also based on shaping and solidification, however an additional phenomenon controls the process: a chemical reaction. During shaping, the usually 1:1 part A:part B mixture is transferred from the dosing unit to the mould via the injection unit following the fluid mechanics rules mostly without heat transfer. Due to the low viscosity, the mixture is easily transferred without heat input, setting the first major difference when compared to thermoplastics IM: there is no phase-transition (melting) during shaping. After the mixture reaches the hot mould (temperature is set according to the LSR grade to be moulded) and fills it, heat transfer from the mould to the mixture occurs and triggers the curing reaction, starting the solidification step. Fluid mechanics still controls the filling phase and governs the change in flowing behaviour as the mixture starts to polymerize (resistance to movement increases due to molecular weight escalation), along with the chemical reaction rules concerning kinetic and thermodynamic factors. In this sense, solidification involves three realms of phenomena for LSR injection moulding: heat transfer to trigger curing as soon as the mixture reaches the hot mould; fluid mechanics to dictate cavity filling and considering the change in viscosity due to molecular weight increase; and kinetics/thermodynamic aspects of the chemical reaction set the solidification time prior to demoulding. In this sense, LSR undergoes a chemical change during the IM process, passing from a viscous liquid with microstructure dictated mainly by entanglements and polymer-

polymer/polymer-filler interactions to a viscoelastic solid with higher molecular weight and a three-dimensional molecular structure also comprising entanglements and polymer-polymer/polymer-filler interactions, with additional covalent crosslink points.

From the aforementioned aspects, one can realize that thermoplastics and LSR injection moulding are two similar processes, but with important differences. For simulation purposes, most of the already developed strategies to computationally simulate the IM process of thermoplastics can be transferred to the LSR case. However, key aspects concerning heat transfer, fluid mechanics, and chemical reaction have to be addressed and modified to lead to reliable LSR IM simulation routines. Since Bont *et al.* [48] carefully described the peculiarities of LSR injection moulding, including typical processing parameters, in a recent review paper, these aspects will not be covered in this Chapter. Moreover, details concerning fluid mechanics will be given in the Chapter dedicated to rheology (Chapter 3); specifics related to heat transfer will be stressed in Chapter 6 (thermal properties); and finally the chemical reaction will be fully described in Chapter 9 (crosslinking theory).

1.4 INJECTION MOULDING SIMULATION

Process optimization within the injection moulding context is a complex task considering the intrinsically complicated manufacturing process via IM. As described by Mitsoulis [49], the injection moulding process comprises time-dependent, 3D, compressible, and non-isothermal flows, with moving free boundaries, and, in the case of liquid silicone rubber IM, holding a chemical reaction inside the mould. Such optimization involves intense knowledge and experience regarding the process itself, being time and resource consuming. Besides, considering the widespread employment of injection moulding techniques, minimal marketing time also plays an important role when optimization is performed aiming to become more competitive. [50] In this sense, computer-aided engineering (CAE) simulation technologies based on computational fluid dynamics (CFD) are widely employed to optimize the injection moulding process, since they present the following not-exhaustive list of assets [51]:

- It is cheaper and less time consuming, since trial and error analyses based on industrial pilot lines would be unaffordable.
- Numerical tools allow the evaluation of a material response without the physical use of the real material and without compromising mould manufacturing.
- CAE simulation routines provide the possibility to shorten the cycle time and optimize the curing duration to save energy and avoid material waste.

- Simulation is able to avoid re-design of the mould.
- CFD studies are able to predict processing-related defects in the injected part, such as weld lines and air traps.

To achieve the mentioned benefits, the performed simulation must be reliable in a sense that it mimics the real material behaviour and, therefore, the real IM process. The accuracy of such simulation depends on many factors, such as the representation of the mould and cavity geometries, the chosen flow modeling method, the realistic set of runner, sprue, and gating system, and the material data that is provided as input to solve the governing equations of mass, momentum, and energy conservation. [52] If the aim of the simulation is to predict processing parameters, such as pressure and temperature profiles, and cycle time (that includes the curing time for a reactive material injected into the mould's cavity), precise material data must be provided, since these feed the phenomenological models that are able to explain the fluid mechanics, heat transfer, and chemical reaction kinetics/thermodynamics associated to the IM process.

The injection moulding simulation of LSR has been unsatisfactorily published in the available literature. In 2002, Haberstroh *et al.* [53] proposed a material data strategy to simulate the filling and curing phases of LSR. Shortly after, the research advanced and Capellmann *et al.* [54] enhanced a tool for the simulation of the injection moulding process enabling it to take into account undervolumetric filling. However, when determining the viscosity of LSR, the authors could not prove the validity of the employed approach for low shear rates and high temperatures applying plate-plate rheometers. Matysiak *et al.* [50] extended the previous work and included in the simulation data from pressure measurements to gather knowledge on thermal expansion of LSR, but with a simple pressure-temperature model. More recently, Ou *et al.* [55] investigated the simulation of two-component injection moulding of silicone rubber into a thermoplastic polymer. All the cited investigations reached reasonable simulation results when the predicted processing parameters were compared to the measured values. However, the majority of the studies adapted material data characterization techniques from the thermoplastic materials and employed them with some approximations. For example, none of the mentioned authors stressed the strong impact of the presence of fillers in the characterization methods, or discussed what was the best method, from the several available ones, to define the curing behaviour of LSR.

From the literature, precise guidelines about material data characterization of LSR based on a systematic investigation of all available state-of-the-art methods were not found in the context of injection moulding simulation. Thus, this field still has a knowledge gap to be filled, even with positive simulation results for LSR. Thus, the motivation and objectives of the present work will be disclosed next, taking into consideration the introductory background presented here.

MOTIVATION AND OBJECTIVES

Determination of properties that are necessary to implement injection moulding simulation routines already reached technological maturity for thermoplastics in a sense that these simulations are accurate and reliably describe the real injection moulding process. However, for reactive injection moulding, such as for liquid silicone rubber (LSR), the measurement of said properties is still highly adapted from the thermoplastic counterpart. This adaptation is reasonable for some properties, such as LSR's viscosity, which can be compared to a molten thermoplastic; but it fails to consider important morphological aspects when highly filled polymers are under study. Besides, thermoplastic injection moulding does not involve chemical transformations, but rather physical solidification when the molten polymer cools down inside the cold mould. For LSR, the solidification due to a temperature-triggered chemical reaction has to be precisely described in order to be implemented in simulation routines. The fact that a change of chemical state occurs during processing leads to other important considerations that are neglected for thermoplastic characterization; for instance, the difference in properties between the reactants (mixture of component A and B) and the product (crosslinked silicone part). In this sense, a methodological investigation of the characterization procedures aiming to determine liquid silicone rubber's material properties represents an open gap in the current state-of-art.

Thus, the main scientific and technological motivation of the present thesis is to systematically investigate the main properties related to LSR that are necessary to be implemented to injection moulding simulation routines. Throughout this work, relevant material features will be discussed and linked to the injection moulding process with the objective to explain why some characterization methodologies are more suitable than others. Besides, the current available literature lacks an organized *corpus* of knowledge concerning liquid silicone rubber grades developed for injection moulding, mainly when related to material properties determination for processing simulation. It is true, though, that relevant literature shows interesting and necessary material characterization of filled poly(siloxane)s, and this knowledge will serve as a base for the current investigation.

The objectives of this work are divided into scientific goals and philosophical purposes. The scientific goals are technological targets realizable by the scientific method and relevant to this Thesis' scope. The philosophical objectives, on the other hand, are the *prima causae* for this doctoral Thesis, and also reflect the main reasons why this author

conducted the investigation. Being less quantitatively measured when compared to the scientific goals, the philosophical objectives allow a reflection about the true contribution of the present work.

The general scientific objective of the present work is to provide organized and precise guidelines for material data determination that are necessary for LSR injection moulding simulation considering the unique processing conditions and the material's morphology. As specific objectives, these are divided per Part of this Thesis as follows:

PART II - RHEOLOGY To reliably define LSR's viscosity η as a function of the temperature T and of the shear rate $\dot{\gamma}$ taking into consideration its structure in terms of polymer-polymer, filler-filler, and polymer-filler interactions.

PART III - THERMAL PROPERTIES To accurately determine LSR's specific heat capacity c_p and thermal conductivity λ in terms of the temperature and of the samples' chemical state (non-crosslinked or cured). Besides, to compare the individual components' thermal properties with the crosslinked specimen's. It is also an objective of this Chapter to show the pressure-volume-temperature (pVT) behaviour of LSR and the change of specific volume in terms of the sample's chemical state.

PART IV - CROSSLINKING KINETICS To precisely identify LSR's crosslinking kinetics and to compare distinct approaches to determine the curing behaviour, addressing differences, advantages, and intrinsic considerations on each method.

PART V - SIMULATION To compare diverse datasets obtained via different characterization methods as inputs for an injection moulding simulation routine in terms of the output parameters, stressing the main discrepancies concerning processing parameters.

To compose the philosophical objective of this work, four main questions are intended to be answered by the end of the study and will serve as scientific and technological guidance. These are:

1. How has this research contributed to the *generation of knowledge*?
2. How has this investigation contributed to the *development of individuals*?
3. How has this Thesis contributed to the *wider research community*?
4. How has this work contributed to *broader society*?

The objectives outlined in this Thesis align closely with the United Nations Sustainable Development Goals (SDGs) [56], particularly Goals 9, 12, and 13. By systematically investigating the properties essential for LSR injection moulding simulation, this research directly

contributes to Goal 9 by advancing technological innovation and industrial processes, specifically within the realm of sustainable materials science and manufacturing. Furthermore, by optimizing material characterization methodologies for LSR, this work promotes Goal 12 by fostering sustainable consumption and production patterns, critical for reducing waste and enhancing resource efficiency in manufacturing industries. Additionally, by addressing the unique challenges of LSR processing and striving for more environmentally friendly manufacturing practices, this Thesis supports Goal 13's objective of combating climate change. Through these endeavors, this research seeks to play a meaningful role in advancing the broader agenda of sustainable development outlined by the UN SDGs, contributing to a more sustainable and resilient future for all.

Aiming to demonstrate how this thesis is structured, the chart in Figure 2.1 shows the 5 Parts of this document along with their individual chapters and their contents. For each of these Parts, a thorough theoretical explanation is given, followed by an experimental chapter, and finally a chapter dedicated to show and discuss the results. An exception is Part I, which is entirely theoretical and dedicated to introduce the scope of this work, its objectives, and the most relevant state-of-the-art knowledge on silicones and LSR injection moulding.

The research work of this Thesis was performed at the Polymer Competence Center Leoben GmbH (PCCL, Austria) within the framework of the COMET-program of the Federal Ministry of Labour and Economy and the Federal Ministry for Climate Action, Environment, Energy, Mobility, Innovation and Technology and at the Institut National des Sciences Appliquées de Lyon (INSA Lyon, France), with contributions from the Montanuniversitaet Leoben (Department of Polymer Engineering and Science, Polymer Processing), and Starlim Spritzguss GmbH. PCCL is funded by the Austrian Government and the State Governments of Styria, Lower Austria and Upper Austria.

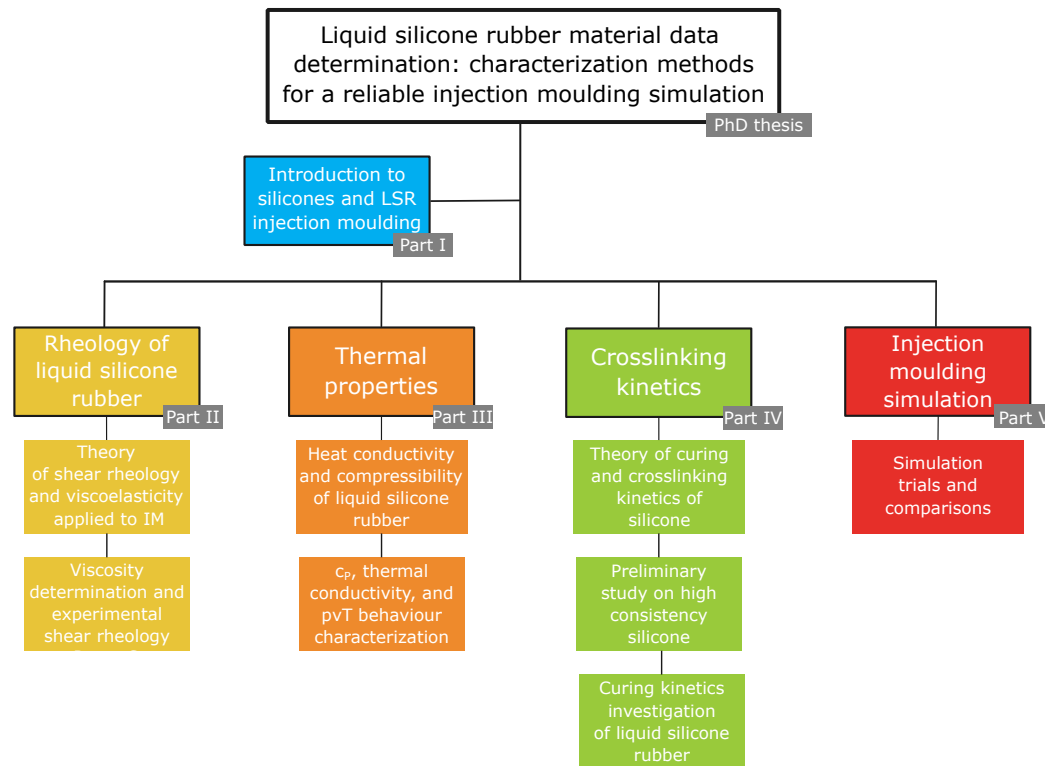


Figure 2.1: Thesis' structure diagram.

Part II

RHEOLOGY OF LIQUID SILICONE RUBBER

The movement of polymer to fill a cavity inside a mould to be further solidified can be described employing the rheology rules of fluid flow. In this sense, this Chapter is dedicated to present the context of rheological studies for the present Thesis, as well as to outline the main definitions and considerations that are used to analyse and interpret rheology measurements. It is not the goal to be exhaustive in terms of rheology principles, but to highlight the most important ones, which are the foundation for the following Chapters.

3.1 INJECTION MOULDING, SHEAR, AND VISCOELASTICITY

Viscoelasticity, the property that encompasses both viscous and elastic characteristics, is a fundamental aspect of liquid silicone rubber (LSR) behaviour during injection moulding. This dual nature allows LSR to flow into intricate mould geometries when in the uncured state, while also recovering its shape upon removal of stress mainly when cured. During the moulding process, LSR's viscoelasticity is critical in managing the material's response to the high shear forces and varying temperatures encountered. The elastic component enables the material to store and release energy, which aids in the smooth filling of the mould and reduces the likelihood of defects such as sink marks or voids. Concurrently, the viscous component ensures that LSR flows adequately under the applied pressure, allowing for complete and uniform filling of the mould cavities.

Shear behaviour is equally important in the injection moulding of LSR. Shear forces are generated as the material is injected through narrow gates and runners, leading to shear thinning, where the viscosity of LSR (and most industrially-employed polymers) decreases with increasing shear rate. This property is advantageous because it reduces the required injection pressure and promotes better flow characteristics, resulting in more precise and detailed replication of the mould features. However, managing shear is crucial to prevent excessive heating and potential degradation of the material, besides allowing the precise processing settings for a specific product manufacturing, enabling energy saving. By understanding and controlling the shear behavior of LSR, manufacturers can optimize the injection moulding process to produce high-quality parts with consistent mechanical properties, minimal internal stresses, and optimized energy consumption.

To effectively control and optimize the injection moulding process, especially via injection moulding simulations, it is essential to accurately characterize the viscosity of liquid silicone rubber under various conditions. Viscosity characterization methods provide crucial insights into how LSR will behave under different shear rates and temperatures, enabling precise adjustments to processing parameters. For simulation, the resistance to flow is present in the constitutional conservation equations as the viscosity terms in the momentum conservation (Equation 3.1) and energy conservation (Equation 3.2) equations, as expressed next:

$$\rho \frac{\partial}{\partial t} \vec{v} = \rho \vec{g} - \nabla p + 2\nabla \cdot \eta \vec{D} - \rho \vec{v} \cdot \nabla \vec{v} \quad (3.1)$$

$$\rho c_p \left(\frac{\partial T}{\partial t} + \vec{v} \cdot \nabla T \right) = \beta T \left(\frac{\partial p}{\partial t} + \vec{v} \cdot \nabla p \right) + \eta \dot{\gamma}^2 + \lambda \nabla^2 T + \dot{Q} \quad (3.2)$$

At this moment, it is important to highlight the influence of viscosity η in the term $2\nabla \cdot \eta \vec{D}$ (Equation 3.1), which is responsible to account for the contact forces that arise from intermolecular forces exerted by the macromolecules outside the control volume where the equations are solved. For the energy conservation equation (Equation 3.2), viscosity η appears to characterize the energy due to viscous dissipation ($\eta \dot{\gamma}^2$, conversion of kinetic energy into thermal energy due to the viscous forces within the fluid).

In this Thesis, the focus will be specifically on shear viscosity, despite the recognition that extensional viscosity also plays a crucial role in certain scenarios of the injection molding process. Notably, in the nozzle and gating sections, where the LSR transitions from a larger to a smaller cross-sectional area, the material undergoes extensional deformation. This shift forces the polymer to stretch or elongate rather than merely shear, making extensional deformation a potentially dominant form of deformation in these critical areas. [57] While the detailed study of extensional viscosity is beyond the scope of this work, its influence is acknowledged, particularly as it can significantly affect the flow dynamics and the overall integrity of the molded parts. Addressing only shear viscosity, this Thesis aims to simplify the complex interactions in LSR flow behavior while ensuring that the primary flow dynamics within the bulk of the mold are comprehensively understood and accurately simulated.

The next Section will delve into viscosity characterization methods, exploring various techniques and their relevance in ensuring reliable and reproducible moulding outcomes. Through a detailed understanding of viscosity characterization, one can better predict and manipulate the flow behaviour of LSR, thereby enhancing the efficiency and quality of the injection molding process and of the associated computer simulation.

3.2 METHODS FOR SHEAR VISCOSITY DETERMINATION

In the sense of viscosity determination, the approaches to determine the variation of viscosity with temperature and shear rate are usually the ones applied to characterize the rheological behaviour of polymers. In the context of polymer structure investigation and of studies concerning effect of molecular or filler modification in the polymer's rheological response, rheological properties are studied via applying shear to polymer melts by two means: either in a Couette flow-like scenario, where the polymer melt is sheared due to the movement of the surfaces where it is confined (such as the plates in rotational rheology), reaching a laminar flow; or in a Poiseuille-like flow, which is pressure-driven and the surfaces that confine the polymer flow are stationary. [58] These two types of flow characterize the two main techniques that are currently employed to study the rheological behaviour of polymers: rotational (Couette-based), and capillary (Poiseuille-based) rheologies. As an intrinsic and intensive property (resistance to flow), viscosity values should agree between these two approaches when the polymer's microstructure is kept the same during measurement.

For LSR, viscosity determination specifically for injection moulding simulation purposes has been performed by various means. In regards to the approaches based on a Couette flow, rotational rheology investigations are widely employed to determine complex viscosity η^* under oscillatory shear or steady-state viscosity η_s under steady shear. In regards to the approaches that employ pressure-driven-based experimental setups to impose a Poiseuille-like flow to study the rheological behaviour of polymers, high pressure capillary rheometers (HPCR) are widely utilized to determine the so called true shear viscosity η . These three approaches are described below.

3.2.1 Rotational rheology - oscillatory shear

Based on a Couette flow, rotational rheology experiments under an oscillatory shear are normally accomplished by shearing the sample between two plates via spinning one of these plates and keeping the other static. The plate's spinning in this case is sinusoidal, i.e., the applied strain (for strain-controlled rheometers) is characterized by a magnitude (or strain amplitude γ_0) and by a frequency (angular frequency ω). In the case of strain-controlled rheometers, a strain $\gamma(\omega t)$ (and a correspondent strain rate $\dot{\gamma}(\omega t)$) are transferred to the sample and can be defined as:

$$\gamma(\omega t) = \gamma_0 \sin(\omega t) \quad (3.3)$$

The applied sinusoidal strain imposes a stress response $\sigma(\omega t)$ that, for viscoelastic materials such as liquid silicone rubber, is out-of-phase by δ from the applied strain:

$$\sigma(\omega t) = \sigma_0 \sin(\omega t + \delta) \quad (3.4)$$

If the sample is in mechanical equilibrium during the sufficiently small oscillations that generate the strain $\gamma(\omega t)$, one considers that this is a linear viscoelastic scenario (viscoelastic parameters are independent of the strain amplitude) and the general term for this kind of experiment is small amplitude oscillatory shear, or SAOS. Within this context, Equation 3.4 can be expressed in terms of the material properties G' (elastic shear modulus) and G'' (viscous shear modulus):

$$\sigma(\omega t) = \gamma_0 [G' \sin(\omega t) + G'' \cos(\omega t)] \quad (3.5)$$

By determining G' and G'' , one can derive the complex viscosity η^* as:

$$\eta^* \equiv \frac{\sqrt{G'^2(\omega) + G''^2(\omega)}}{\omega} \quad (3.6)$$

The determination of complex viscosity is generally performed first checking if viscoelastic conditions are met, and then applying Equation 3.6. Thus, the usual *modus operandi* is as follows: i) determination of the linear viscoelastic range (LVE, i.e., the amplitude range where the elastic shear modulus G' and the viscous shear modulus G'' do not face abrupt change) in terms of oscillating shear amplitude via an amplitude sweep; ii) determination of the complex viscosity in terms of the oscillating angular frequency ω via a frequency sweep, either with increasing or decreasing frequency, employing an amplitude value within LVE. Choosing an amplitude within the LVE, that is, at which G' and G'' are only dependent on the angular frequency (and not on the shear amplitude) guarantees the linearity of viscoelastic properties. This method is widely applied and belongs to the state-of-the-art not only for LSR injection moulding simulation purposes, as described by Ziebell and Bhogesra [59] and by Weißer *et al.* [60], but also to characterize the effect of fillers on poly(siloxane)s' rheological properties [61–63] and to draw aspects on silicone 3D printing [64].

For shear amplitudes (γ_0) or shear rates ($\dot{\gamma}_0$) above the ones within the linear viscoelastic range, i.e., for higher shear rates, the stress response to the imposed sinusoidal strain (for strain-controlled experiments) is distorted and deviates from a sinusoidal output. In this circumstance, the definition as described in Equation 3.6 is not valid, since the stress response (Equation 3.5) $\sigma(\omega t)$ cannot be described in terms of G' and G'' . Otherwise, a more complex expression for $\sigma(\omega t)$

has to be determined. For these cases when the strain amplitudes surpass the linear viscoelastic range, medium and large amplitude oscillatory shear (MAOS and LAOS) experiments are conducted. Within this context, non-linear viscoelastic phenomena are characterized [65]. The first approach to describe $\sigma(\omega t)$ under non-linear viscoelastic conditions was introduced by Wilhelm *et al.* [66] as Fourier-transform rheology. In this sense, the stress signal can be described by a Fourier series [67] in the elastic ($\sigma'(t; \omega; \gamma_0)$) and viscous ($\sigma''(t; \omega; \gamma_0)$) forms:

$$\sigma'(t; \omega; \gamma_0) = \gamma_0 \sum_{n=\text{odd}} G'_n(\omega, \gamma_0) \sin(n\omega t) + G''_n(\omega, \gamma_0) \cos(n\omega t) \quad (3.7)$$

$$\sigma''(t; \omega; \gamma_0) = \dot{\gamma}_0 \sum_{n=\text{odd}} \eta''_n(\omega, \gamma_0) \sin(n\omega t) + \eta'_n(\omega, \gamma_0) \cos(n\omega t) \quad (3.8)$$

Equations 3.7 and 3.8 highlight that under non-linear viscoelastic conditions the fundamental harmonic ($n = 1$) is not enough to describe the stress response due to the imposed sinusoidal strain. Thus, additional harmonics are necessary, which only the odd ones are included because the stress response is independent of the shear direction and due to the fact that the sign of the shear stress changes as the sign of shearing changes [65, 68]. Even harmonics were observed when secondary flows were present [69] or dynamic wall slip occurred [70]. It is worth mentioning that for the fundamental harmonics $n = 1$ and Equation 3.7 returns Equation 3.5 ($G'_1 \equiv G'$ and $G''_1 \equiv G''$).

Even though the differentiation between SAOS and MAOS/LAOS is usually purely qualitative (G' and G'' are constant within the linear viscoelastic range characterized by SAOS and face change when higher amplitudes are reached), the harmonics' intensities are commonly used to quantify the non-linearity. Taking the 1st harmonic as a reference, the other odd harmonics' intensities $I_{(2n+1)/1}$ ($I_{3/1}$, $I_{5/1}$, etc) are calculated [71] as:

$$I_{2n+1/1} = \frac{I_{2n+1}}{I_1} = \frac{\sqrt{I_{2n+1}'^2 + I_{2n+1}''^2}}{\sqrt{I_1'^2 + I_1''^2}} = \frac{\sqrt{(\gamma_0 G'_{2n+1})^2 + (\gamma_0 G''_{2n+1})^2}}{\sqrt{(\gamma_0 G'_1)^2 + (\gamma_0 G''_1)^2}} \quad (3.9)$$

These intensity values, mainly $I_{3/1}$, are parameters constantly used to define the deviation from linearity in terms of viscoelastic behaviour when rheological experiments are performed within a range of shear amplitudes. For instance, $I_{3/1} \approx 0$ indicates SAOS [65], while not negligible $I_{3/1}$ indicates MAOS and LAOS. These definitions are important

in the sense that for the calculation of viscosity according to Equation 3.6, considerations regarding non-linearity have to be addressed, since for LAOS more than one harmonic exist to define the stress response. This fact becomes even more critical when rheological experiments are conducted under shear rates closer to the ones experienced during injection moulding, which are typically associated to high amplitudes (LAOS).

A second approach to account for non-linearities in the stress response was introduced by Ewoldt *et al.* [72] employing Chebyshev polynomials of the first kind. Due to mainly their orthogonality over a finite domain and the odd symmetry about $x = 0$, n^{th} -order Chebyshev polynomials T_n of the first kind define σ' and σ'' as functions of $x = \gamma/\gamma_0$ and $y = \dot{\gamma}/\dot{\gamma}_0$, respectively:

$$\sigma'(x) = \gamma_0 \sum_{n=\text{odd}} e_n(\omega, \gamma_0) T_n(x) \quad (3.10)$$

$$\sigma''(y) = \dot{\gamma}_0 \sum_{n=\text{odd}} v_n(\omega, \gamma_0) T_n(y) \quad (3.11)$$

where $e_n(\omega, \gamma_0)$ and $v_n(\omega, \gamma_0)$ are respectively the n^{th} -harmonic elastic and viscous Chebyshev coefficients.

Similarly to the harmonics' intensity approach defined in Equation 3.9, the scaled third harmonic Chebyshev coefficients e_3/e_1 and v_3/v_1 are also employed to measure a system's non-linearity. These quantities are derived directly from the employed polynomials or can be calculated from the familiar Fourier coefficients (Equations 3.7 and 3.8):

$$\frac{e_3}{e_1} = \frac{-|G_3^*| \cos(\delta_3)}{-|G_1^*| \cos(\delta_1)} \quad (3.12)$$

$$\frac{v_3}{v_1} = \frac{|G_3^*| \sin(\delta_3)}{|G_1^*| \sin(\delta_1)} \quad (3.13)$$

3.2.2 Rotational rheology - steady shear

For rotational experiments under a constant shear rate $\dot{\gamma}$ (imposed by an angular velocity $\dot{\phi}$) employing the cone-and-plate geometry (radius R and truncated angle α), the steady-state viscosity η_s can be determined using the definition in Equation 3.14, considering that the shear stress response σ (or the torque M) to the imposed shear strain is time-independent, or the shear stress growth function σ^+ reached a plateau ($t \rightarrow \infty$), i.e., steady flow conditions exist [73]:

$$\eta_s = \frac{\sigma^+(t = \infty, \dot{\gamma})}{\dot{\gamma}} = \frac{3M \tan \alpha}{2\pi R^3 \dot{\phi}} \quad (3.14)$$

Equation 3.14 calculates the steady shear viscosity in terms of the sample radius R , thus changes in the geometry would imply distinct viscosity values for the same torque M and angular velocity $\dot{\phi}$. Change in the gap geometry often occurs when highly viscoelastic polymeric samples (as liquid silicone rubber) are sheared in a torsional flow device (such as parallel-plate rotational rheometers) [74], which intrinsically place the sample in a fashion that it has a free surface with the outside air. This free surface is highly susceptible to destabilising when the sample is sheared and, above a critical imposed shear rate, the surface deforms into a more complicated edge profile [75] that is not anymore characterized by the radius R . Such edge profile can even form an indentation that invades the fluid bulk, as shown in Figure 3.1, invalidating the viscosity measurement. When the shear rate increases further, part of the sample can be even ejected from the flow cell, leading to completely unreliable data.

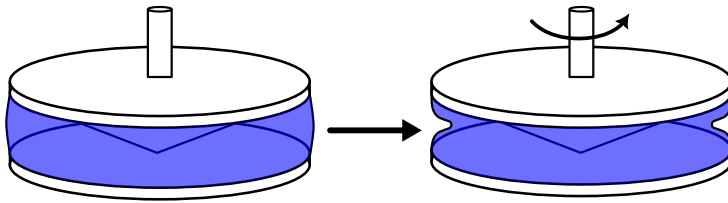


Figure 3.1: Schematic formation of edge fracture during steady-shear viscosity determination via rotational rheology (adapted from [76]).

The origin and the physical description of edge instability are still being debated, but a common understanding is that the phenomenon is widely connected to the second normal stress differences that result from the imposed shear rate. Thus, this issue represents a strong limitation on the characterization of steady shear viscosity employing parallel-plates that should be taken into consideration when planning material data determination. [77]

3.3 THE COX-MERZ PROPOSITION

The correlation between η^* and η_s is well-known as the Cox-Merz proposition [78]. This proposition establishes a reasonable equality between the viscosity measured under linear viscoelastic conditions (oscillatory shear, SAOS) and the resistance to flow under non-linear viscoelastic circumstances (constant steady shear). This relationship can be defined as:

$$\eta_s(\dot{\gamma}) \approx |\eta^*(\omega)|_{\dot{\gamma}=\omega} \quad (3.15)$$

It is important to stress that the relationship $\dot{\gamma} = \omega$ has to be defined as $s^{-1} = rad.s^{-1}$. Besides, it is already established [79, 80] that the Cox-Merz proposition is not valid for all polymer systems, and it usually fails for filled systems. However, this proposition has still been greatly used in academia and industry to easily establish steady shear viscosities out of complex viscosity values under SAOS, even for silica-filled liquid silicone rubber [59].

Very recently, Shim *et al.* [81] reexamined the Cox-Merz proposition employing recovery rheology. The researchers, followed by Burgeson and Rogers [82] proposed a comprehensive understanding of this correlation based on the differentiation between unrecoverable and recoverable strains. In this sense, they concluded that steady shear viscosity and dynamic viscosity only are equal in terms of their unrecoverable components. A similar conclusion will be derived from the studies of the present Thesis.

3.4 CAPILLARY RHEOLOGY - HIGH PRESSURE CAPILLARY RHEOMETER

In regards to the approaches that employ pressure-driven-based experimental setups to impose a Poiseuille-like flow to study the rheological behaviour of polymers, high pressure capillary rheometers (HPCR) are widely utilized. The true shear viscosity η as determined by HPCR can also be considered as derived from non-linear viscoelastic conditions, as η_s , since the polymer is driven out of mechanical equilibrium by the rapid and intense pressure-driven deformation. [71] A thorough explanation of HPCR with the relevant equations are given by Kukla *et al.* [83], and will not be addressed again here.

EXPERIMENTAL DESCRIPTION: RHEOLOGY

The aim of this Chapter is to describe in details the experimental procedure that was employed to study the flow behaviour of liquid silicone rubber. Besides, it will be stated here the materials that were investigated, as well as all necessary mathematical formalism adopted in this Thesis. Since the main goal of this Part is to compare different rheology methodologies, these will be described separately here.

4.1 MATERIALS

Liquid silicone rubber (SiloprenTM LSR 2070, $M_w = 86673 \text{ g}\cdot\text{mol}^{-1}$, $M_w/M_n = 1.6$, hardness after cured = 70 Shore A), containing approximately 32 wt% of an inorganic filler, was supplied as a 2-component (A and B) system by Momentive Performance Materials Inc. (USA). LSR characterization in terms of molecular weight and filler content is described in the Appendix (A.1 and A.3, respectively) of this Thesis. SiloprenTM LSR 2070 is a standard liquid silicone rubber for injection moulding processes and has a mixing ratio of components A:B = 1:1.

4.2 ROTATIONAL RHEOLOGY

All rotational rheology experiments (oscillatory - small and large amplitudes -, and steady shear modes) were performed with a strain-controlled rheometer (ARES-G2, TA Instruments, USA) located in the Institut National des Sciences Appliquées de Lyon (INSA, France). A cone-and-plate geometry (25 mm diameter, 0.1 rad cone) was employed and the sample was placed inside a forced air convection oven for analysis at various temperatures. The parameters derived from the measurements were calculated by the device's internal software TRIOS (TA Instruments) and were exported and interpreted without further processing.

4.2.1 Oscillatory experiments

In order to determine the sample's complex viscosity η^* , a sinusoidal shear was applied with defined angular frequency ω and strain amplitude γ . The linearity of viscoelastic properties G' and G'' was studied via amplitude sweep (increasing strain amplitude γ from 0.01% to 100%) under 0.1 Hz, 1.0 Hz, and 10 Hz ($0.628 \text{ rad}\cdot\text{s}^{-1}$, $6.28 \text{ rad}\cdot\text{s}^{-1}$, and $62.8 \text{ rad}\cdot\text{s}^{-1}$) of angular frequency. Within the studied strain amplitude range, two strain amplitudes were arbitrarily selected to define the fre-

quency sweep investigations: 0.1% (considered for the present work as imposing a small amplitude oscillatory shear, or SAOS) and 10% (here denoted frequently as large amplitude oscillatory shear, or LAOS). The complex viscosity was finally determined during frequency sweep runs carried out between $500 \text{ rad}\cdot\text{s}^{-1}$ and $0.1 \text{ rad}\cdot\text{s}^{-1}$ (79.62 Hz and 0.016 Hz) with decreasing frequency and under 0.1% or 10% strain amplitude.

Aiming to study the filler's network structuring/recovery after intense shear, two experimental setups were conducted. With sample 2070 B, complex viscosity η^* (calculated according to Equation 3.6) was used as the parameter to account for filler structuring. After the amplitude sweeps previously described (now at temperatures ranging from 25°C to 200°C), time sweeps (30 min) under 0.1% strain amplitude (linear viscoelastic condition) and equal frequency as the amplitude sweeps' were conducted. Since the recovery time sweeps were conducted at $\gamma = 0.1\%$, the $\eta^*(\gamma = 0.1\%)$ as determined during amplitude sweep (step before the recovery period) was used as initial viscosity and recovered viscosity ratios were calculated as

$$\text{viscosity ratio} = \frac{\eta^*(\text{recovery}, \omega = 0.1/1.0/10 \text{ Hz}, \gamma = 0.1\%, t = 30 \text{ min})}{\eta^*(\text{amplitude sweep}, \omega = 0.1/1.0/10 \text{ Hz}, \gamma = 0.1\%)} \quad (4.1)$$

With sample 2070 A, the time evolution (15 min, at 50°C , 70°C , and 90°C) of stress/strain amplitude (σ/γ , elastic) and stress/shear rate ($\sigma/\dot{\gamma}$, viscous) hysteresis curves (under linear viscoelastic conditions: $\gamma = 0.1\%$ and $\omega = 1 \text{ Hz}$) was studied after applying the most intense shear condition under investigation ($\omega = 10 \text{ Hz}$ or $62.8 \text{ rad}\cdot\text{s}^{-1}$ under $\gamma = 10\%$). A schematic representation of the applied methods is shown in Figure 4.1. Since it is expected (and further concluded) that both LSR components are rheologically similar, the aforementioned procedure was conducted with the respective parts due to discretionary purposes of the author.

For the oscillatory experiments, a reproducibility study (see in the Appendix A.4) was conducted with sample 2070 B at 50°C to identify the maximum coefficient of variation for this method. As shown in the Appendix, the variation among 3 triplicates was inferior to 5%, and this deviation was assumed for all other samples.

4.2.2 Steady flow experiments

The variation of viscosity η under increasing and sequential shear rates $\dot{\gamma}$ (0.001 s^{-1} to 0.7 s^{-1}) was investigated via shear rate sweep experiments. A constant shear rate was applied for 30 s, which was

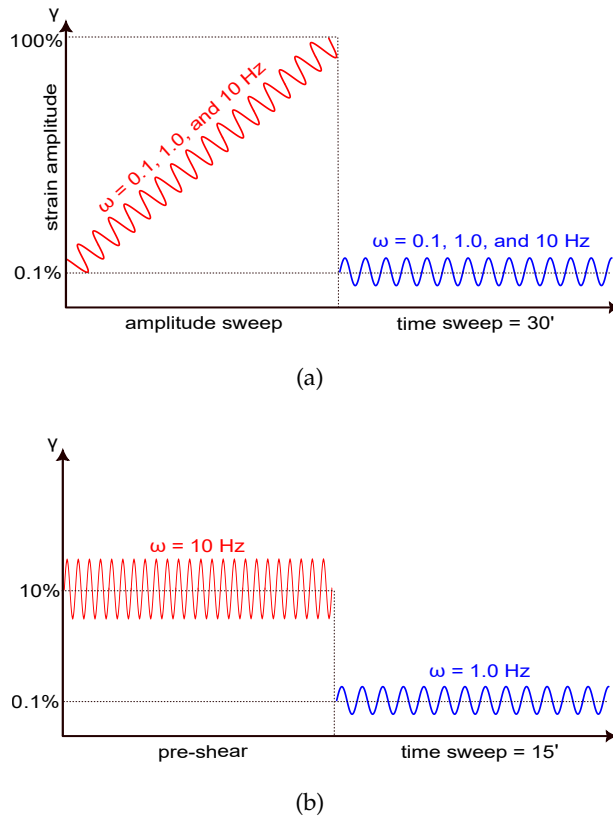


Figure 4.1: Graphic representation of the methods applied to study filler recovery on **(a)** sample 2070 B after amplitude sweep and on **(b)** sample 2070 A after pre-shear.

long enough for a stable torque value to be reached. Under steady shear, edge instabilities were visually inspected at each imposed shear rate.

4.3 CAPILLARY RHEOLOGY

The pressure-driven flow of LSR was investigated employing a high pressure capillary rheometer (HPCR, Rheograph 50, GOETTERT Werkstoff-Pruefmaschinen GmbH, Germany) coupled with a 1 mm slit die (fully described in the work of Kukla *et al.* [83], Figure 3). With the aid of 5 pressure sensors placed along the slit die, the steady-shear viscosity was calculated (average of 3 measurements) as a variation of the shear rate (20 s^{-1} - 1300 s^{-1}) applying the Weissenberg-Rabinowitsch [84] correction. The Bagley correction [85] was not applied since the pressure drop was measured along the slit. Component 2070 A was tested at 50°C , 70°C , and 90°C .

RESULTS AND CONCLUSIONS

This Chapter is dedicated to analyse the viscosity variation with either angular frequency ω or shear rate $\dot{\gamma}$ under the various methodological approaches described in the previous Chapter. In this sense, complex viscosity η^* vs. ω values under SAOS ($\gamma = 0.1\%$) and LAOS ($\gamma = 10\%$), steady viscosity η_s vs. $\dot{\gamma}$ values from shear rate sweeps, and viscosity η vs. $\dot{\gamma}$ values from the HPCR runs are critically compared. Furthermore, in order to explain the critical differences among the methods, LSR's filler structure recovery is explored. Since both components A and B can be considered as rheologically similar (the amount of platinum catalyst in part A is limited to the ppm level [48] and the crosslinker loading in part B is around 7 wt%), in some cases only one component will be presented and discussed. For a similar LSR grade, authors [60] reported differences between component A and B. However, this LSR grade (SILOPREN LSR 2050, 50 shore A hardness after cured) possibly presented a lower filler content (20-30 wt%) than the LSR of the present study, due to the lower hardness (50 against 70 Shore A). Due to the fact that the liquid silicone rubber currently being investigated has a high filler content (present on both parts), it is understood that the components behave similarly in terms of rheological properties.

Note: A great part of this work was carried out by the author at the Institut National des Sciences Appliquées de Lyon (INSA Lyon, France).

5.1 ASPECTS ON THE LINEARITY OF VISCOELASTIC PROPERTIES

As aforementioned, the definition of complex viscosity in terms of Equation 3.6 is solely valid when G' and G'' are functions of only the angular frequency, and not of the strain amplitude. This means that the first harmonic $n = 1$ (see Equations 3.7 and 3.8) itself is enough to define the stress response after an applied sinusoidal strain (strain and stress sinusoidal signals for sample 2070 A under various temperatures and strain amplitudes are shown in the Appendix A.6). Thus, it becomes important to emphasize that the values reported here as G' and G'' are actually G'_1 and G''_1 , which are common output parameters of commercial rheometers. In this sense, G' and G'' for the sample 2070 A were determined for a range of strain amplitudes under various angular frequencies, as shown in Figure 5.1. For all angular frequencies and temperatures, G' presented fairly constant values up to $\gamma = 0.2\%$, while G'' remained constant until $\gamma = 0.6\%$. The range up to 0.2% can be then defined as the linear viscoelastic range for this sample, which is in accordance with the range reported by Weißer *et al.* [60]. Within this range, $G' > G''$, meaning that the sample behaves as an elastic solid gel regardless of the frequency. The solid gel-like

behaviour can be justified by the high content of filler particles (most probably silica) and the molecular weight above the critical molecular weight for entanglements formation ($32 \text{ kg}\cdot\text{mol}^{-1}$ according to [62]). Elasticity in this sense comes from both the interaction between the polymeric macromolecules and the filler particles via hydrogen bonds and molecular entrapment, and from the intermolecular interactions via van der Waals forces, hydrogen bonding, and physical entanglements [60], besides the hydrodynamic effect deriving from the solid filler particles.

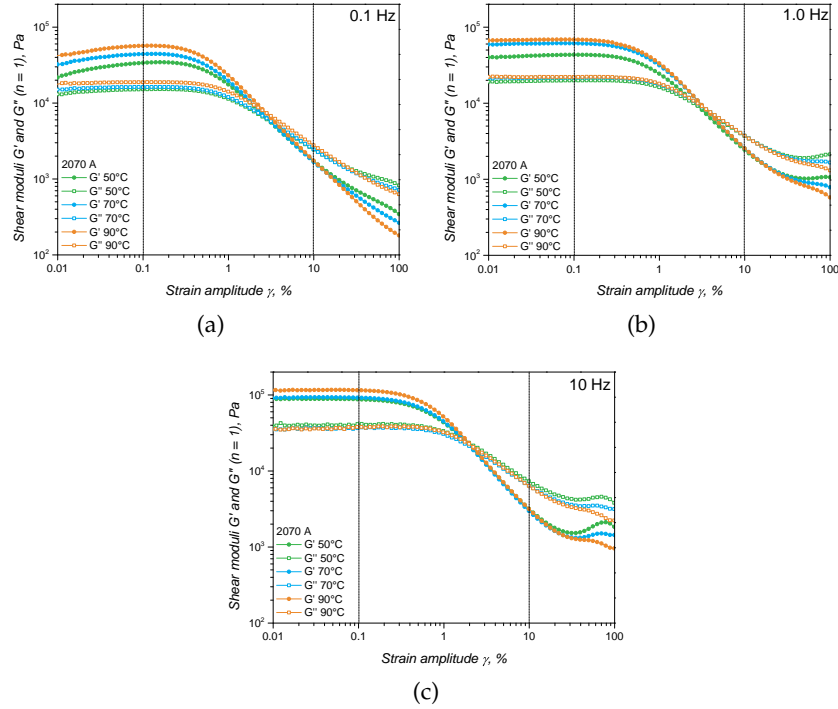


Figure 5.1: Viscoelastic properties G' (full symbol) and G'' (open symbols) of sample 2070 A for a range of strain amplitudes and temperatures under (a) 0.1 Hz, (b) 1.0 Hz, and (c) 10 Hz frequency. For the ease of interpretation, the vertical lines indicate the studied amplitudes $\gamma = 0.1\%$ (SAOS) and $\gamma = 10\%$ (LAOS).

Within the linear viscoelastic range, the shear experienced by the sample is very low when compared to injection moulding's typical shear profiles: up to 10 s^{-1} during dosing, between 10 s^{-1} and 1000 s^{-1} at the injection unit, and higher than 1000 s^{-1} at the runner and inside the cavity during injection. After complete filling of the cavity, the shear imposed to LSR decreases substantially, until it starts crosslinking under quasi static conditions. Besides, for strain amplitudes below 0.2%, LSR's filler structure is understood to be unaffected, i.e., the aggregates and agglomerates are not broken due to the imposed shear. This situation is rarely to occur during typical injection moulding cycles, when LSR is transported under high shear from the dosing unit to the mould's cavity.

As the strain amplitude increases, the sample departs from mechanical equilibrium and a transition zone (MAOS) from constant to decreasing G' and G'' can be observed at all temperatures and frequencies in Figure 5.1. This zone is the onset of strain thinning, where both moduli decrease with the strain amplitude, typical of Type I behaviour as defined by Hyun *et al.* [65]. Shear thinning is the consequence of two phenomena: chain orientation and microstructure alignment along the flow direction, and breakage of the filler structure, also known as Payne effect. This behaviour was also reported under the perspective of SAOS/LAOS by Lim *et al.* [86] when studying poly(caprolactone)/multiwalled carbon nanotubes nanocomposites. The passage from $G' > G''$ to $G' < G''$ represents the transition between the solid gel-like and the liquid-like states of LSR, where it goes from low to high fluidity. This transition occurs at lower amplitudes (evident at Figure 5.2) for higher frequencies due to the also increased imposed shear. Above $\gamma = 10\%$, high amplitude and high frequency effects occur (G' and G'' presented an increase at the end of the experiment) probably due to edge instabilities associated to the cone-and-plate geometry, even in the oscillatory mode [77], so these effects will not be further interpreted here. This strain amplitude zone where G' and G'' are dependant on the amplitude is then considered under non-linear viscoelastic conditions and will be denoted here as LAOS. The associated distorted sine-like stress response under LAOS is shown in the Appendix A.6.

In order to scrutinize the magnitude of viscoelasticity's linearity or non-linearity, it is convenient to qualitatively check the shapes of the Lissajous-Bowditch (LB) curves σ vs. γ (elastic LB curve) and σ vs. $\dot{\gamma}$ (viscous LB curve), which are shown in Figure 5.3. The LB curves at linear viscoelastic conditions ($\gamma = 0.1\%$ or SAOS), presented at the bottom part of the diagram, have the usual elliptical shape associated to viscoelastic materials. It is convenient to remind that pure elastic materials present a straight line in the elastic curve $\sigma(\gamma)$, while pure viscous samples display a circular $\sigma(\dot{\gamma})$ curve. The shape of $\sigma(\dot{\gamma})$ is a line for pure viscous and a circle for pure elastic materials. Increasing frequency causes an increase of the LB curves' areas, which is associated to higher energy dissipation during the analysed shear cycle. However, the shape of the LB curves is not altered neither by angular frequency, nor by temperature. The linear viscoelastic conditions are also confirmed by the sinusoidal signals' shapes related to stress and strain, shown in the Appendix A.6: the stress under SAOS varies in a sinusoidal way with the imposed, also sinusoidal, oscillatory strain, but with a difference in phase.

As the strain amplitude increases to 10%, LAOS conditions are verified by the distorted LB curves (and the distorted stress signals presented in the Appendix A.6), as shown in the top half of Figure 5.3. Non-elliptical shapes observed in the LB curves are evidence of a

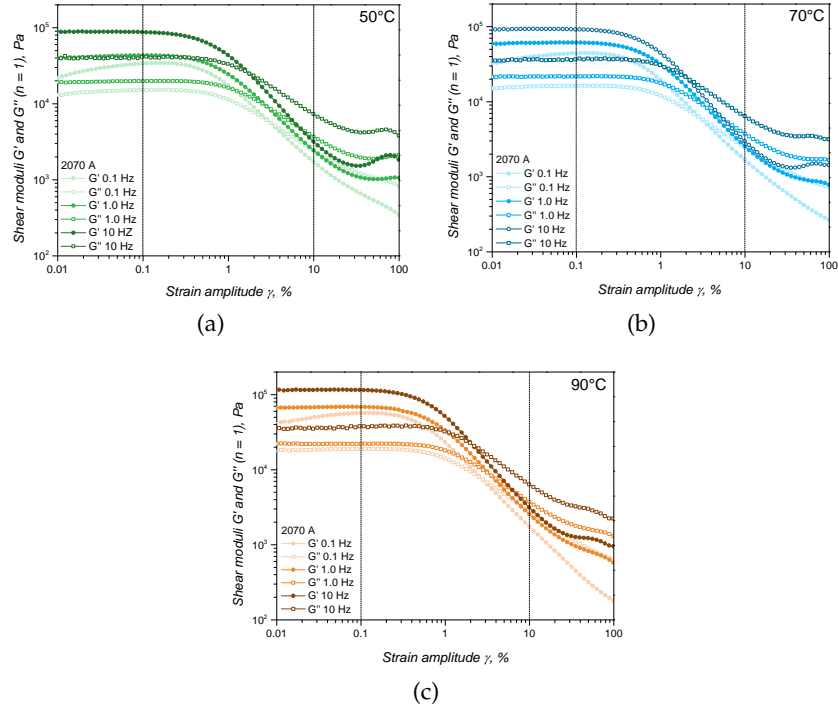


Figure 5.2: Viscoelastic properties G' (full symbol) and G'' (open symbols) of sample 2070 A for a range of strain amplitudes and frequencies at (a) 50°C, (b) 70°C, and (c) 90°C. For the ease of interpretation, the vertical lines indicate the studied amplitudes $\gamma = 0.1\%$ (SAOS) and $\gamma = 10\%$ (LAOS).

non-linear behaviour, as stressed by Kamkar *et al.* [71]. Indeed, at $\gamma = 10\%$, G' and G'' decayed by 1 order of magnitude when compared to $\gamma = 0.1\%$, showing a strong dependence of the viscoelastic properties to the strain amplitude. As explained before, the non-linear viscoelastic response at LAOS can be attributed also to the filler network's destruction. The shape of the LB distorted from the linear elliptic form for both elastic and viscous contributions, however no secondary loops appeared at the non-linear viscoelastic scenario. Self-intersection is a consequence of strong non-linear material behaviour, mainly associated to intense elastic non-linearity derived from stress overshoot during oscillation. [72] In the case of LSR, non-linearity exists, but its extent cannot be directly derived from the LB curves, neither from the shape, nor from the absence of secondary loops. Actually, for these LSR samples under study, stress overshoots are not expected since the time scale of oscillation (less than 10 s for the minimum frequency) is too short for the reform/recovery of the destroyed filler microstructure, as will be clarified in Section 5.4.2. Thus, a quantitative approach is adopted next employing the intensities of both the higher harmonics and the Chebyshev coefficients.

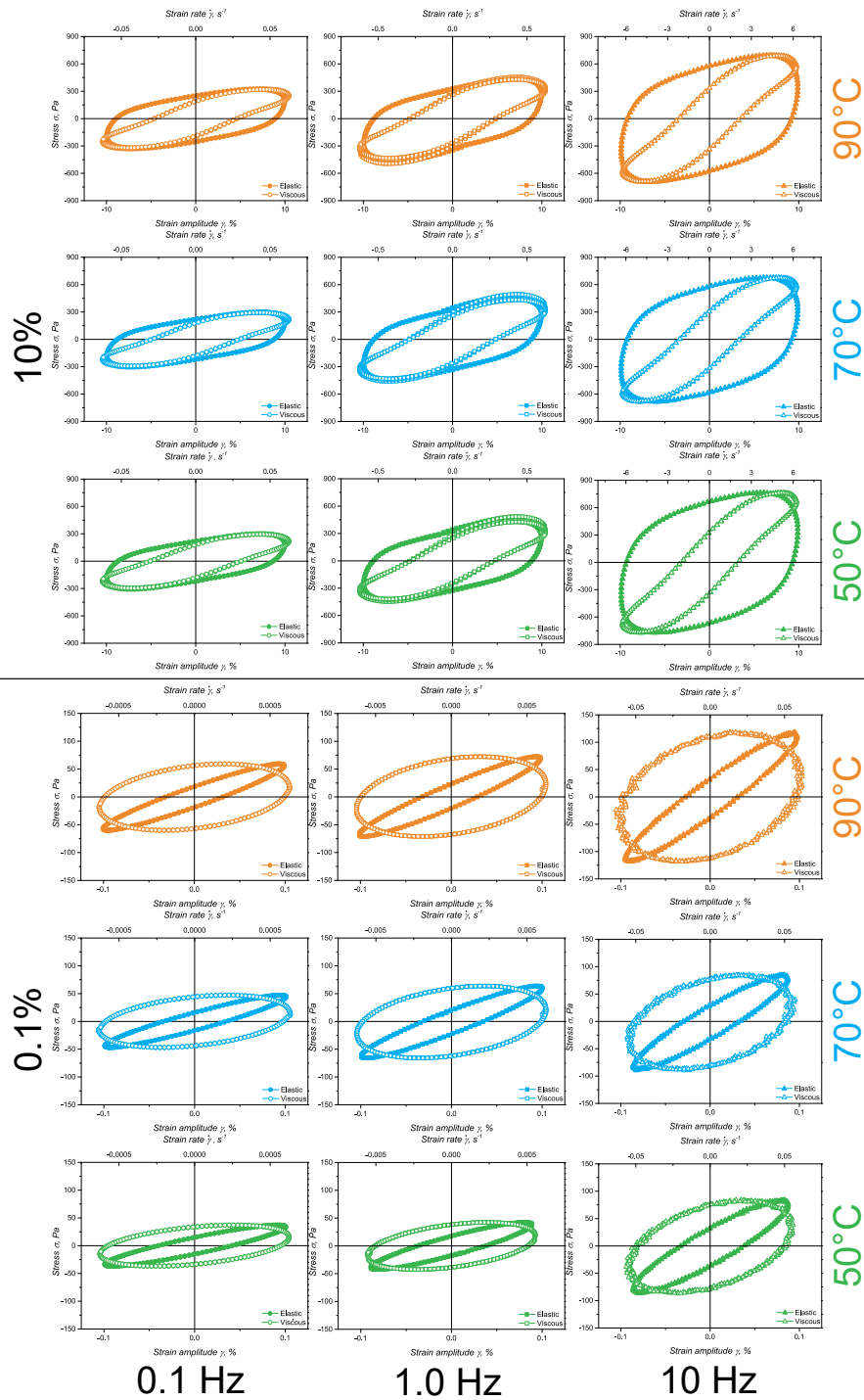


Figure 5.3: Lissajous-Bowditch curves (elastic, filled symbols; and viscous, open symbols) associated to the strain amplitudes $\gamma = 0.1\%$ (bottom, SAOS) and $\gamma = 10\%$ (top, LAOS) at various temperatures and frequencies for sample 2070 A.

As a quantitative parameter to measure the non-linearity of the studied LSR samples, the 3rd harmonic's intensities $I_{3/1}$ in relation to the strain amplitude are shown in Figure 5.4 for all temperatures ((a)-(c)) and angular frequencies. Below $\gamma = 0.1\%$, $I_{3/1}$ varies with the instrument noise and is lower than 0.01, i.e., the 3rd harmonic contribution represents less than 1% of the fundamental harmonic. From 3rd harmonic intensity, it is possible to see that the linear viscoelastic range shortens as the temperature increases, evidenced by the reduced length associated to the instrument noise. This is possibly due to the higher thermal energy that hinders inter- and intramolecular interactions, as well as weakens filler-filler interactions. While the strain amplitude further increases, $I_{3/1}$ increases with γ^2 for sufficiently small amplitudes, as described by Wilhelm [66]. Figure 5.4(d) shows that the $I_{3/1} \propto \gamma^2$ already occurs even when G' and G'' seem to be constant, which means that phenomena ultimately leading to non-linearity already take place. $I_{3/1}$'s slope changes as the strain amplitude further increases, but returns to 2 above 1% and tends to stable $I_{3/1}$ values when approaching $\gamma = 100\%$. This apparent two-step increase of $I_{3/1}$ may be related to the different reasons behind LSR's non-linearity. While interactions among the poly(siloxane) oligomers (entanglements, for example) are changed due to the increasing amplitude, the filler microstructure is also disturbed. These two apparently independent phenomena are probably concomitant, but an independent and distinct rate at which each occurs may exist.

From the $I_{3/1}$ values it is reasonable to state that at $\gamma = 0.1\%$ the contribution of the 3rd harmonic is assuredly negligible and the fundamental harmonic fully describes the stress response due to the applied sinusoidal strain. At $\gamma = 10\%$, $I_{3/1}$ reaches 0.1, which signifies that the 3rd harmonic is 10% of the fundamental harmonic, indicating non-linearity due to the reasons already stressed before. At 10% strain, however, the LSR's microstructure in terms of polymer-polymer, filler-filler, and polymer-filler interactions is closer to the one that is found during the injection moulding cycles. In this sense, when re-visiting the LB curves in Figure 5.3 and the sine signals for stress and strain in the Appendix (A.6), one can argue that: i) an elliptical shape is still present at the 10% LB curves without secondary loops, which suggests that severe non-linearity is not present; and ii) the sine curves for the stress are still smooth S-shaped signals under LAOS conditions. Further study of the Chebyshev coefficients will bring more light to these observations.

Figure 5.5 shows the variation of $e_{3/1}(\gamma)$ and $v_{3/1}(\gamma)$ values for the sample 2070 A at 50°C (the analysis for 90°C is only shown in the Appendix A.9 due to similarity with the 50°C one). For all temperatures and angular frequencies, $e_{3/1} \ll 1$ and $v_{3/1} \ll 1$ at $\gamma = 0.1\%$, which recovers the linear viscoelasticity condition at Equation 3.10 and 3.11, i.e., $e_1 \rightarrow G'$ and $v_1 \rightarrow \eta' = G''/\omega$. [72] However, as the

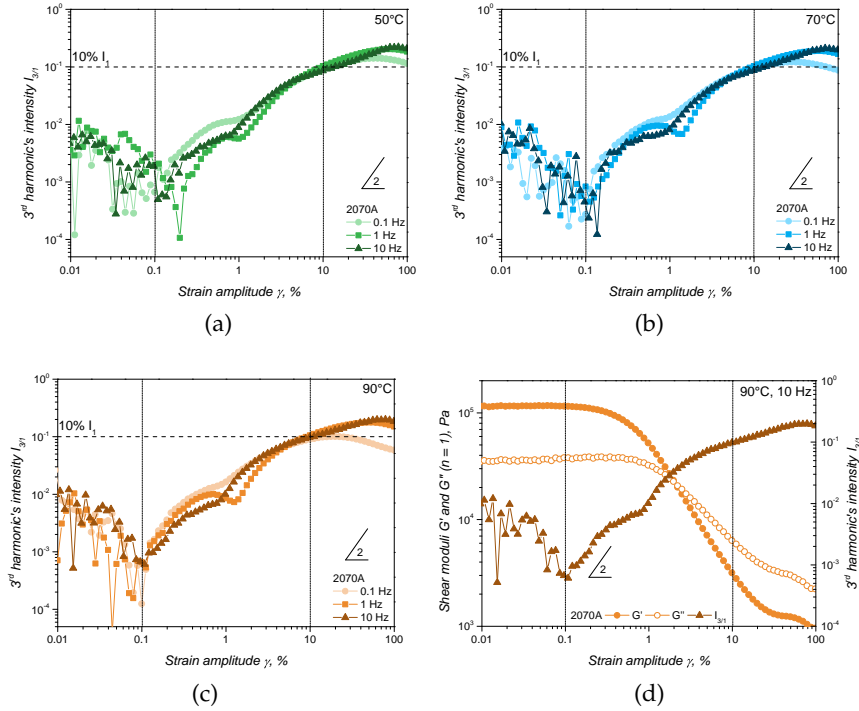


Figure 5.4: Variation of the third harmonic intensity $I_{3/1}$ for the three studied temperatures ((a)-(c)) with the strain amplitude under various frequencies for sample 2070 A. A comparison with G' and G'' is shown in (d) for 90°C and 10 Hz. For the ease of interpretation, the vertical lines indicate the studied amplitudes $\gamma = 0.1\%$ (SAOS) and $\gamma = 10\%$ (LAOS), and the horizontal line represents the level where the 3rd is 10% of the fundamental harmonic.

strain amplitude increases, the moduli of $e_{3/1}$ and $v_{3/1}$ increase and at $\gamma = 10\%$ both $e_{3/1}$ and $v_{3/1}$ assume absolute values of around 0.1. Interestingly, $v_{3/1}$ is zero in the LAOS region at the same strain amplitude as $G' = G''$. The interpretation of the third harmonic Chebyshev coefficients is normally based on their signs and considerations regarding intracycle stiffening/softening and thickening/thinning can be made. [72] However, for this study, these considerations will not be made and only the absolute value of $e_{3/1}$ and $v_{3/1}$ are relevant. In this sense and in agreement with the (Fourier analysis-based) 3rd harmonic intensities, the third harmonic Chebyshev coefficients also represent around 10% of the first harmonic. Most importantly, as $v_1 \rightarrow \eta' = G''/\omega$ under SAOS, an approximation of the complex viscosity η^* (as calculated employing Equation 3.6) under non-linear viscoelastic conditions does not become a bad estimation for the energy dissipation behaviour of LSR when the filler microstructure is disturbed as during injection moulding. Indeed, Heymann *et al.* [87] pointed out that G_1' and G_1'' (parameters calculated by the device and employing the definitions $G'(\omega) = (\sigma_0/\gamma_0(\omega))\cos \delta(\omega)$ and $G''(\omega) = (\sigma_0/\gamma_0(\omega))\sin \delta(\omega)$) are acceptable quantities to characterize the viscoelastic response

when the deviation of the response signal (stress sine curves) from a pure harmonic wave in terms of the portion of higher harmonics (3^{rd} , 5^{th} , etc) does not exceed 0.15 or 15%. In the present case, the intensity of the 5^{th} at $\gamma = 10\%$ is around 0.01 or 1% of the fundamental harmonic (data not shown), regardless of the temperature or the angular frequency.

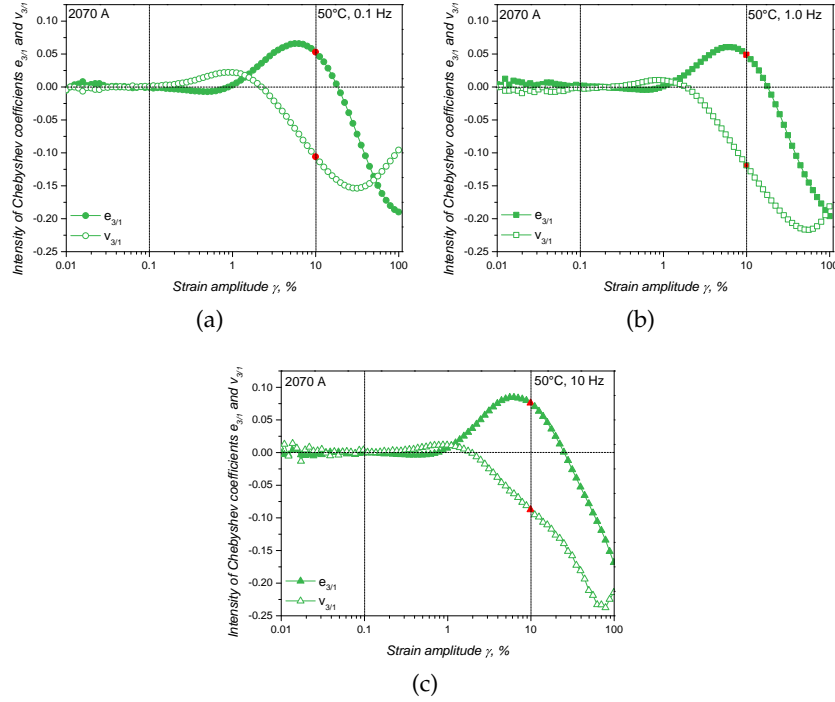


Figure 5.5: Intensity of the Chebyshev coefficients $e_{3/1}$ and $v_{3/1}$ as a variation of the strain amplitude for 3 imposed angular frequencies (a) 0.1 Hz; (b) 1.0 Hz; and (c) 10 Hz and at 50°C. For the ease of interpretation, the vertical lines indicate the studied amplitudes $\gamma = 0.1\%$ (SAOS) and $\gamma = 10\%$ (LAOS), and the horizontal line shows where the coefficients are zero.

In light of the considerations drawn before, the complex viscosity $\eta^*(\omega)$ will be analysed next. Two strain amplitudes were applied for the frequency sweeps: one relevant to the linear viscoelastic region, and another covering the amplitude range where non-linearity arises.

5.2 DETERMINATION OF COMPLEX VISCOSITY $\eta^*(\omega)$

Calculation of the complex viscosity in terms of the Equation 3.6 requires the determination of G' and G'' . These viscoelastic properties for sample 2070 A are shown in Figure 5.6. Under linear viscoelastic conditions ($\gamma = 0.1\%$), G' and G'' vary with the angular frequency as shown in Figure 5.6(a). For the whole range of ω , $G' > G''$, as already observed in Figures 5.1 and 5.2 at the linear viscoelastic range. As the frequency increases, G' and G'' increase due to the response

of the polymer chains to the rapid applied strain associated to high frequencies. Thus, not only the resistance to deformation is increased as the frequency rises (time scale for deformation decreases), but also energy dissipation escalates.

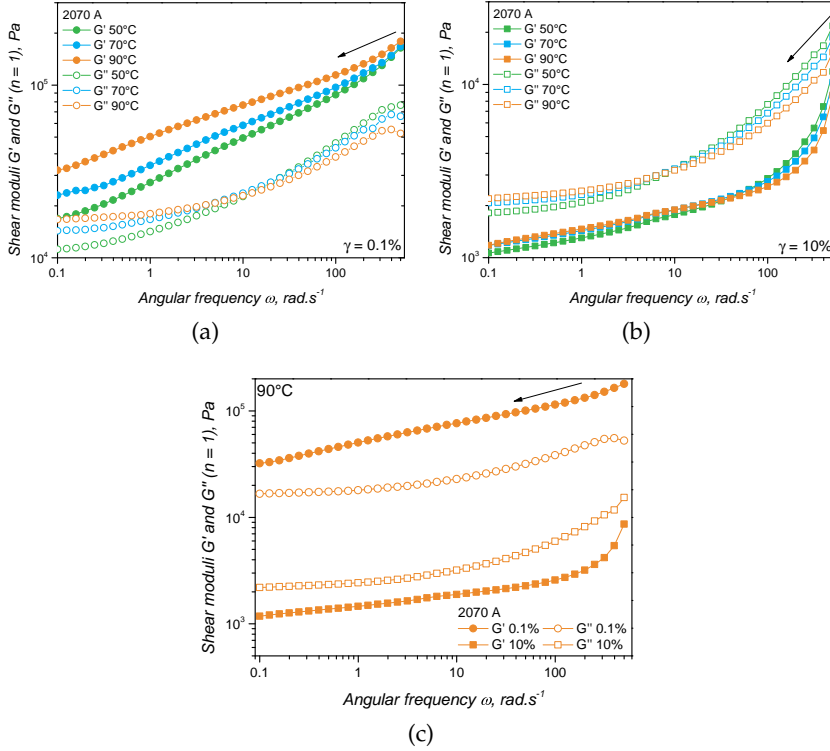


Figure 5.6: Viscoelastic properties G' (full symbol) and G'' (open symbols) of sample 2070 A for a range of angular frequencies and under 0.1% ((a), SAOS, circles) or 10% ((b), LAOS, squares) amplitudes, for three temperatures (50°C, 70°C, and 90°C). $G'(\omega, \gamma)$ and $G''(\omega, \gamma)$ at 90°C are also plotted in (c) for comparison purposes. The arrow indicates that frequency sweeps were conducted with decreasing frequency.

At $\gamma = 10\%$ (Figure 5.6(b)), on the other hand, $G' < G''$, as similarly shown by Figures 5.1 and 5.2. Frequency sweep experiments under 10% amplitude are conducted with a damaged filler-structure sample (result of high shear). The lack of a filler structure leads to $G' < G''$, as also reported by Geng *et al.* [63] for LSR/silica composites. Increase in the strain amplitude not only caused G' and G'' to decrease (shown in Figure 5.6(c)) and inverted the relationship G'/G'' , but also modified the variation of $G'(\omega)$ with temperature. $G'(\omega)$ at 0.1% amplitude increases with increasing temperature for the whole range of frequencies, while $G'(\omega)$ at 10% amplitude increases with temperature until around 10 rad.s^{-1} , when a turn point occurs and $G'(\omega, \gamma = 10\%)$ decreases with temperature. The behaviour of $G''(\omega)$ with temperature remains the same at both strain amplitudes.

The fact that $G'(\omega)$ at 0.1% amplitude increases with increasing temperature is not common, since generally the increase in temperature causes increased mobility to the polymer chains and reduced resistance to shear flow. One possible explanation for $G'(\omega)$'s increase with temperature may rest on the way the frequency sweeps were conducted. The frequency sweep proceeded with logarithmically decreasing angular frequency, in a fashion that from 500 rad.s^{-1} to 10 rad.s^{-1} it took 2 minutes, while from 10 rad.s^{-1} to 0.1 rad.s^{-1} additional 10 minutes were necessary. During this time, thermally-facilitated filler flocculation may occur, as argued by Filipone and de Luna [88] in the case of organo-modified clay and multiwalled carbon nanotubes-filled atactic poly(styrene); and by Wang *et al.* [89] when studying nanocomposites composed of poly(ethylene-co- α -butene) and fumed silica. The mentioned studies propose that annealing of initially solid-like nanocomposites may induce the formation of larger agglomerates. Worth noting is that these researches were based on polymer/filler pairs without polarity match, thus filler agglomeration is further favoured due to lack of interaction with polymer molecules. In the present case, silica (silicon dioxide) and poly(siloxane) are naturally compatible and would interact, even in a small extent in the case of surface-modified (such as incorporation of vinyl) silicas. Recovery studies covered in section 5.4.2 will bring additional arguments to this hypothesis. Another argument that could explain the increase of G' with temperature in the low frequency range is a temperature-induced reaction of the platinum catalyst with the filler surface. This coupling reaction occurs when the filler surface is functionalized to increase polymer-filler interactions, as shown by Delebecq *et al.* [36], which ultimately leads to an increase of G' (the capability of load transfer between silicone macromolecules and the filler is enhanced). However, this hypothesis was not further explored. In terms of the distinction between frequency sweeps carried out under SAOS or LAOS, the main difference in terms of the sample's morphology is the lack of a structured filler network at high strain amplitude. Such structured filler network (32 wt% of filler) is the main responsible for the highly elastic behaviour of the studied LSR samples.

Since G' and G'' experienced a decrease with increasing strain amplitude, the determined complex viscosity also declined, as shown in Figure 5.7. As also observed for G' , the viscosity determined under SAOS conditions showed a non-trivial relationship with temperature: it increased with increasing temperature, mainly for low frequencies. This specific significant influence of G' related to the low-frequency regime was also observed by Li *et al.* [90] for fumed silica-filled poly(lactic acid) and was connected to polymer nanocomposites by different reasons. While under SAOS conditions an inverse relationship of the complex viscosity with temperature occurred within the whole

frequency range, under LAOS conditions and in the high-frequency range the expected $\eta^*(T)$ behaviour appears.

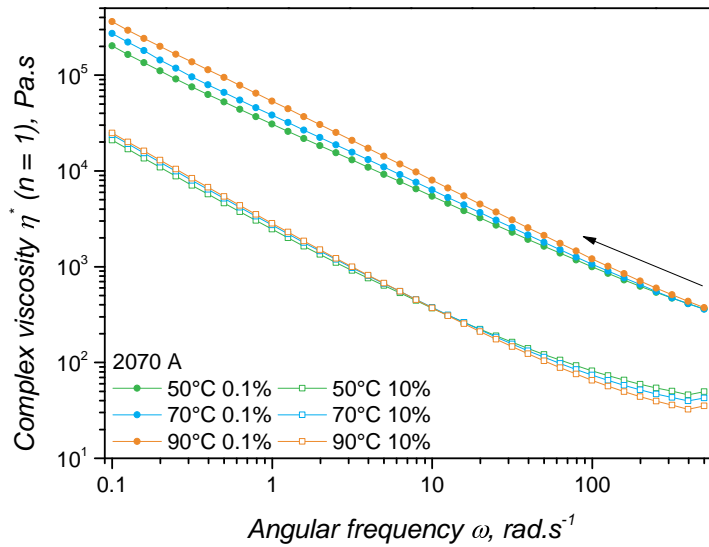


Figure 5.7: 2070 A's complex viscosity variation with angular frequency for all temperatures and strain amplitudes. The arrow indicates that frequency sweeps were conducted with decreasing frequency.

5.3 DETERMINATION OF THE STEADY SHEAR VISCOSITY

Resistance to an increasing imposed shear strain was analysed for sample 2070 A under steady shear conditions for a range of shear rates as shown in Figure 5.8. As it was observed for the complex viscosity under increasing frequency, the sample experienced shear thinning with increasing shear rate. Shear thinning under steady shear is mainly caused by stretching and orientation of the macromolecules in the direction of the shear. The stretching also causes disentanglement, which favours the flow. The variation of η_s with temperature followed the expected trend from 0.01 s⁻¹ up until the end of the experiment. However, at low shear rates, the same behaviour as it was observed during low frequencies at oscillatory measurements occurred: higher temperature caused higher viscosity. In the sense of steady shear, the lower the applied shear rate, the longer it takes for the stabilization of the torque that leads to steady shear conditions.

At high shear rates, issues with reaching steady shear conditions are surpassed, however concerns regarding the cone-and-plate intrinsic measurement geometry arise. As the shear rate increases, inertia effects cause the LSR sample to flow out of the geometry gap due to centrifugal forces emerging from the plate rotation. Furthermore, edge instabilities (change in the geometry at the gap's edge, deviating from a spherical surface) are also present at high shear rates, ultimately causing melt fracture, as critically observed at $\dot{\gamma} = 0.7 \text{ s}^{-1}$, but already

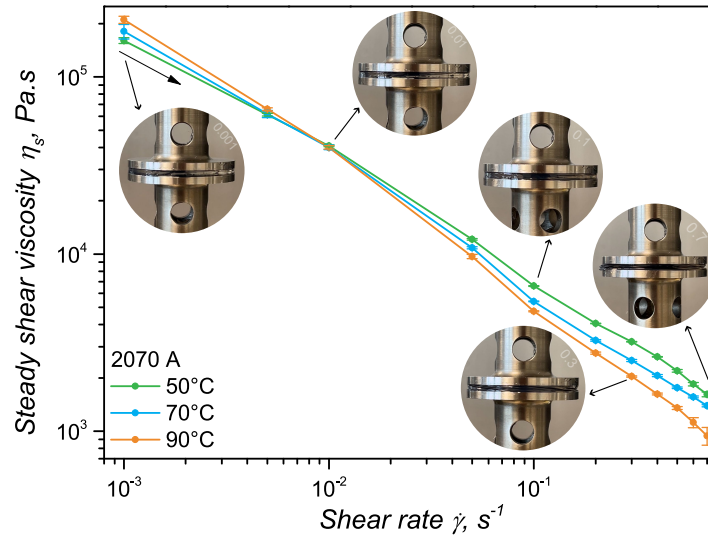


Figure 5.8: Steady shear viscosity variation for sample 2070 A under steady shear for various temperatures. The snapshots taken at 50°C at certain shear rates highlight the sample's conditions inside the gap until edge instabilities occur at high shear rates. The arrow indicates that shear rate sweeps were conducted with increasing shear rate.

present at 0.3 s^{-1} (see sample's concave shape in the right side of the edge). All these artifacts compromise the measurement and insert experimental errors associated to the recorded viscosity values. The snapshots shown in Figure 5.8 are also reported in the Appendix A.8 at larger sizes to aid visualization of the edge instability.

Under the injection moulding perspective, steady shear measurements are closer to reality than oscillatory experiments, since the shear profile during processing is obviously not oscillatory, but continuous. In this sense, it is important to highlight that, for pure material characterization, oscillatory experiments have advantages regarding sample control inside the gap, for example. However, when the goal is to mimic processing conditions inside a laboratory environment to gather material data, rotational steady shear procedures are more adequate, since they are more similar to what occurs to LSR during injection. Decisive in this case is to point out the approach's limitations and sources of uncertainty, such as the edge instabilities and the steady condition (constant torque with time during shear rate) prerequisite. The direct comparison among oscillatory and steady properties will be further explored in section 5.4.1, when the Cox-Merz rule is stressed out.

5.4 DETERMINATION OF VISCOSITY VIA HPCR

Under a pressure-driven Poiseuille flow, 2070 A's resistance to shear flow was determined for several temperatures within 10 and 1400 s^{-1} ,

as presented in Figure 5.9. LSR under a pressure-driven flow also experiences shear thinning due to the same reasons as under a Couette flow (rotational experiments shown before): molecular and filler's microstructure alignment occur in the flow direction, aided by the destruction of any existence filler network that is present while LSR is under mechanic equilibrium. Specifically for HPCR, viscous heating may happen (increase of the sample's temperature and consequent viscosity decrease), but this effect was not taken into consideration here, even though authors (for example [91], [92], and [93]) propose corrective factors for this phenomenon. For all temperatures, strong shear thinning occurs and the viscosity follows a clear trend with temperature. As it is the case with steady shear rotational measurements, the HPCR approach also demands steady conditions regarding the determined pressure inside the slit die.

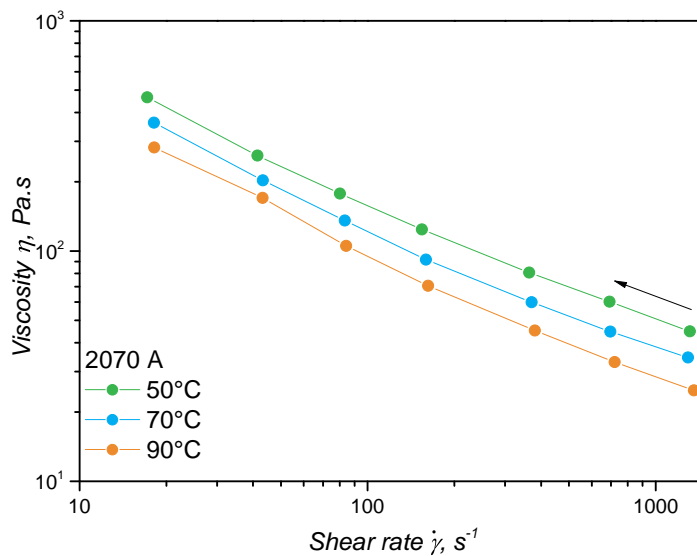


Figure 5.9: Viscosity as determined (average out of 3 replicates, coefficient of variation is less than 5%) by the high pressure capillary rheometer as a function of the imposed shear rate for sample 2070 A under various temperatures. The arrow indicates that the measurement was conducted with decreasing shear rates.

In what concerns the filler structure, the shear experienced by the LSR sample during HPCR experiments is supposed to be sufficient to disturb it. Under oscillatory non-linear viscoelastic conditions (LAOS), a maximum shear rate of $6 s^{-1}$ was experienced by the sample at $\gamma = 10\%$ and $\omega = 10$ Hz (see respective LB curves in Figure 5.3), which corresponded to LB shape distortion, i.e., non-linearity due to filler microstructure change. On this base, one can understand that during shear inside the HPCR's slit die, non-linear viscoelastic conditions would exist and therefore the sample is in a mechanical condition that is not only close to the injection moulding reality, but also in

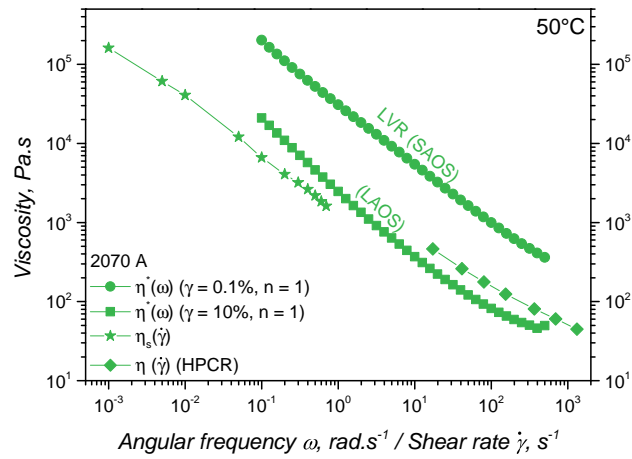
conformity with the LAOS and the steady shear measurements, as it will be shown in the next section.

5.4.1 Comparison among viscosities and the Cox-Merz proposition

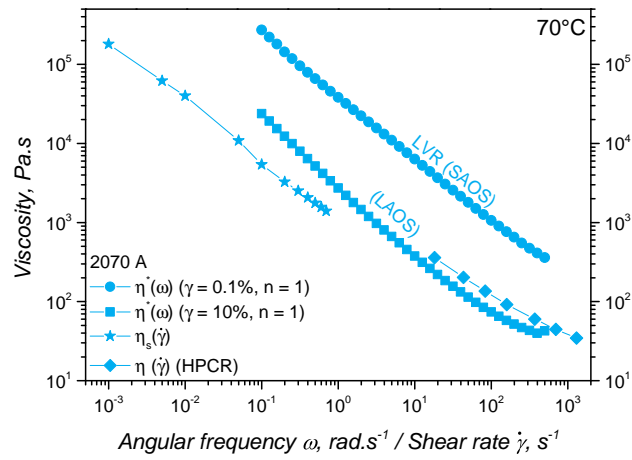
Connecting distinct shear viscosities determined via different methods is not straightforward. Actually, performing several experimental rheological approaches (and leading to the same parameter, i.e., viscosity) is not usual, since normally rheology studies are employed to deliver material-related insights, such as the ones associated to polymer modification, filler influence, etc. For material data determination applied to processing simulation, there are still open gaps in terms of what is the most suitable rheological method to be employed in order to model the viscosity change with shear intensity and temperature (pressure influence is still and widely neglected). Suitability in this sense is mostly regarding proximity to the injection moulding reality, but also considers practicality in terms of level of complexity and time. It is overall agreed that high pressure capillary rheometer-based experiments are time- and resource-consuming, so rheological investigations are often carried out in rotational rheometers. The last are faster and demand less sample volume, even when comparing to the current small HPCRs available in the market. Thus, it becomes valuable to compare the outputs of these approaches and highlight their differences and similarities. Figure 5.10 shows, for each investigated temperature, a diagram containing all viscosity values obtained in the present study. While the y-axis shows simply "shear viscosity" as the resistance to shear flow in Pa.s, the x-axis contains information regarding the flow condition: either under an imposed angular frequency (in rad.s^{-1}) for oscillatory experiments or an imposed shear rate (Couette and Poiseuille flows, in s^{-1}). It is clear that two groups of data exist in the diagrams: one isolated set from the oscillatory measurements under SAOS conditions, and the group with the other data sets, which is shifted to lower viscosities down to 1 order of magnitude. Based on this finding, it is possible to state that the Cox-Merz proposition as displayed in Equation 3.15 is not satisfied, i.e., the shear viscosity information under steady shear conditions is not equivalent to the shear viscosity behaviour under linear viscoelastic oscillatory shear. By considering the findings of Shim *et al.* [81], one can correlate the microstructure changes as reported in this Thesis with the recoverable components of the strain under the perspective of recovery rheology. While the steady shear viscosity comes from purely unrecoverable acquisition of strain, the complex viscosity is defined in terms of both recoverable and unrecoverable contributions. Thus, after the filler perturbation due to shear (LAOS), the unrecoverable component of the complex viscosity surpasses the recoverable one and the Cox-Merz rule is approximately satisfied, i.e., both steady shear and

complex viscosities are defined by their unrecoverable strain components. The reasoning concerning filler disturbance under the scenario of the present study are based on the change of microstructure during the experiment as explained next.

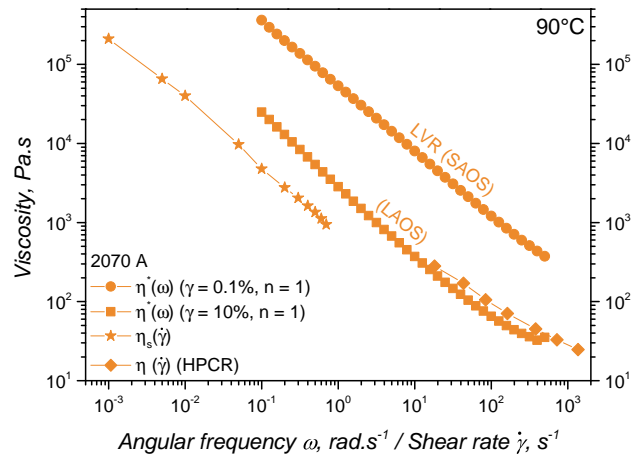
Within the data group containing $\eta^*(\omega)$ (LAOS), $\eta_s(\dot{\gamma})$, and $\eta(\dot{\gamma})$ (HPCR), one can realize that both steady shear-based approaches (rotational steady shear and HPCR) lay on a trend, and the oscillatory method fits in between the first ones. As stressed before, the sample condition in terms of filler structure is the same among these approaches, that is, the silica network is disturbed due to shear. $\eta^*(\omega)$ (SAOS) in this case is derived from a sample with intact filler structure, where agglomerates exist and the polymer-filler and filler-filler interactions are preserved. Grouping of these data sets also shows that the Cox-Merz proposition would be partially satisfied when the oscillatory approach departs from viscoelastic linearity to non-linearity in order to account for the shear-driven microstructure change. The proposition that strong non-linearity derives from filler microstructure change was also pointed out by Sohn and Rajagopalan [94] and by Caratenuito *et al.* [95] when studying model dispersions of hard particles in low viscosity fluids; and by Li *et al.* [90] for poly(lactic acid)-based nanocomposites with fumed silica. All these studies are in agreement to the fact that thixotropic structural transformation, as the one LSR undergoes when shear is applied or when annealed during decreasing frequency sweeps, has a strong role in LSR's non-linear viscoelastic behaviour, which greatly influences rheological measurements concerning viscosity determination. Employing the findings of [82] and [81] on recovery rheology, one can understand that the steady-shear viscosity is mostly dominated by the unrecoverable component for all shear rates, while the complex viscosity is composed of both contributions, recoverable and unrecoverable. For the liquid silicone rubber under study, it seems that the filler structural change at LAOS leads to a dominant effect of the unrecoverable viscosity component for the complex viscosity, approximating it to the values of steady-shear viscosity. Indeed, [81] investigated a similar system composed of a graphene oxide suspension that showed $\eta^*(\omega) > \eta_s(\dot{\gamma})$ for standard rheology measurements, but recovery rheology experiments showed consistency of the Cox-Merz proposition when only the unrecoverable component was considered. Aiming to set solid grounds for these thixotropic structural transformations, the filler structure recovery after intense shear was studied and will be discussed as follows.



(a)



(b)



(c)

Figure 5.10: Comparison among the several experimental approaches covered in this work for the three studied temperatures: **(a)** 50°C, **(b)** 70°C, and **(c)** 90°C. LVR is the linear viscoelastic range, where small amplitude oscillatory shear (SAOS) experiments are held. On the other hand, large amplitude oscillatory shear (LAOS) experiments are conducted in non-linear viscoelastic conditions. $\eta^*(\omega)$ is the complex viscosity determined either via SAOS or LAOS, while $\eta_s(\dot{\gamma})$ is the steady shear viscosity.

5.4.2 Filler network recovery after shear

Since the main microstructure feature responsible for the similarities and discrepancies among the various studied experimental approaches for viscosity determination is the filler structure incorporated into the LSR matrix, this network was further investigated, first concerning sample 2070 B. As this sample contains no catalyst, and thus no reaction takes place between the poly(siloxane) oligomers, the crosslinker, and the chemically modified filler surface, amplitude sweeps were carried out at higher temperatures than for sample 2070 A. After amplitude sweeps at 0.1 Hz, 1.0 Hz, and 10 Hz of angular frequency, it is understood that the filler structure is disturbed and as strain is subsequently substantially decreased and the sample returns to its linear viscoelastic condition, filler network rebuilding and other polymer-related phenomena take place. Figure 5.11(a) shows the evolution of the complex viscosity with time after amplitude sweeps carried out at 0.1 Hz and 10 Hz. It was shown before that the higher frequency imposed a more severe shear condition, which led to stronger non-linearities presented at the LB curves in Figure 5.3. A higher frequency also caused lower complex viscosity values, as equally shown in Figure 5.7 and in Figure 5.11(a), even after the 30 minutes-long recovery step. Note, however, that depending on the frequency, the effect of temperature on viscosity recovery is different. For amplitude sweeps conducted at lower frequencies, the temperature favoured the probable filler network rebuilding, since higher temperatures caused a higher increase of the recovery complex viscosity. On the other hand, for high frequency amplitude sweeps, the shear was so intense that the temperature increase hindered the formation of another structured filler network.

In quantitative terms, Figure 5.11(b) shows the recovered viscosity ratios in terms of the frequency (shear intensity that causes filler structure disturbance) and of the temperature. It becomes clear that for sufficiently low frequencies, as 0.1 Hz, the viscosity values are recovered and even surpassed when compared to the complex viscosity determined during amplitude sweep for the same frequency (0.1 Hz), strain amplitude (0.1%), and equal temperature. Furthermore, the temperature increase supported thixotropy. Temperature also favoured thixotropy for 1.0 Hz, however the viscosity did not recover to the initial value. For the highest frequency, the temperature effect was detrimental to the viscosity recovery, i.e., it hindered the formation of a microstructure that would lead to a solid-like network (physical gel), such as a structured filler system. Worth mentioning is the fact that all recovery steps were conducted under linear viscoelastic conditions, that is, no further breakage or modification of LSR's microstructure occurred. The filler network rebuilding for LSR was similarly reported by Weißer *et al.* [60], but with a focus on the G'/G'' crossover and

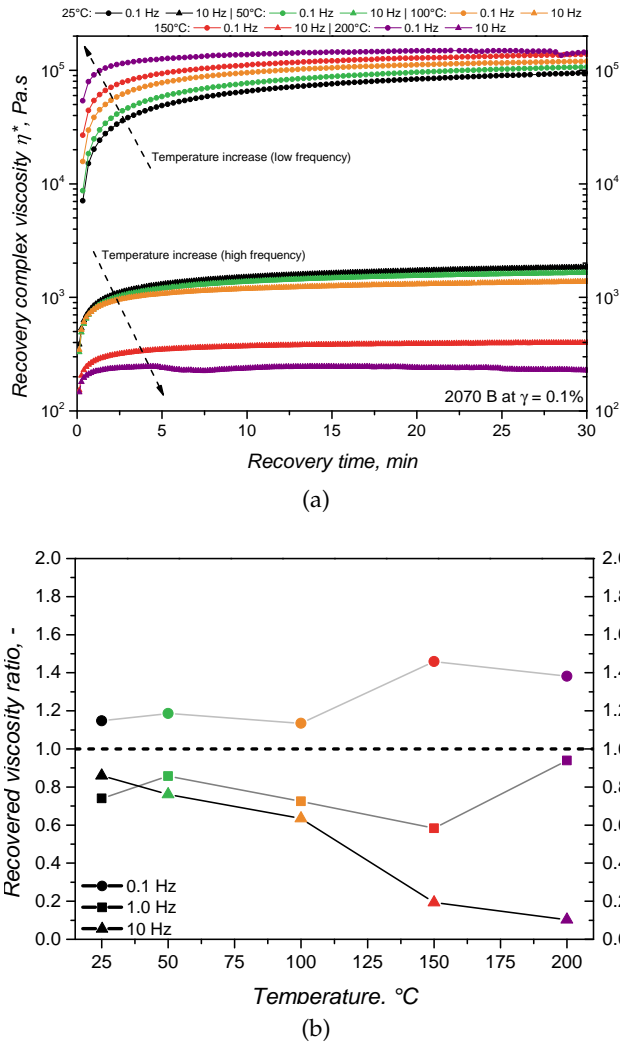


Figure 5.11: **(a)** Complex viscosity (measured under SAOS conditions) increase with time after amplitude sweep (0.01 - 100%, at either low (0.1 and 1.0 Hz) or high frequency (10 Hz)) for various temperatures and **(b)** viscosity ratio as the amount of viscosity recovery after shear.

the time necessary to reach a physical gel state ($G' = G''$). For the present investigation, the same findings were observed: the higher the temperature, the lower the time necessary to reach $G' = G''$ (or $\tan \delta = 1$) at 0.1 Hz, corroborating with Weißer *et al.*'s report. Likewise, Beyer and Wolf [96] also investigated the filler rebuilding of LSR and proposed different LSR grades that minimize this effect.

When subjected to a pre-shear of 10 Hz angular frequency and 10% strain amplitude, 2070 A's viscoelastic properties G' and G'' drop as expected during the 2 minute step, as pictured in Figure 5.12(a). G'' is higher than G' as previously demonstrated in Figure 5.6(b) for $\omega = 10$ Hz and $\gamma = 10\%$. Similarly to 2070 B, G' and G'' increased during the recovery time ($\omega = 0.1$ Hz and $\gamma = 0.1\%$), with temperature favouring

the increment. At 90°C, it is possible that some coupling reaction takes place between the functionalized filler and the poly(siloxane) oligomers aided by the presence of the platinum-catalyst. In this case, an additional boost in the escalation of G' exists. As expected, G' overcomes G'' and the sample returns to a solid-like state. At each oscillation cycle correspondent to a certain recovery time t , the stress was recorded in order to analyse the sample's mechanical hysteresis.

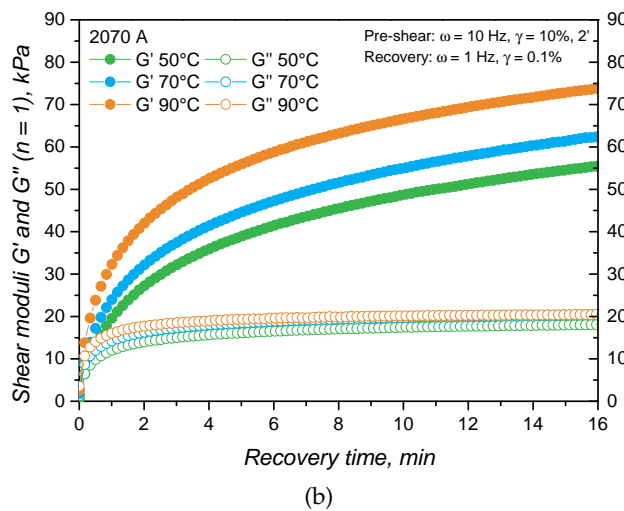
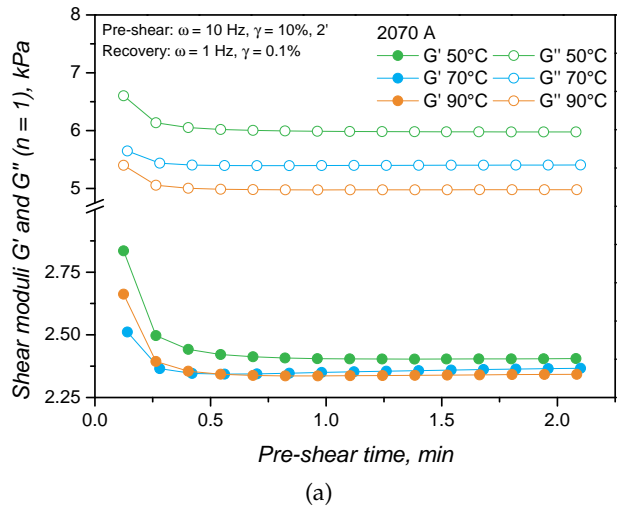


Figure 5.12: Viscoelastic parameters G' and G'' during the intense pre-shear under LAOS conditions (a) and during recovery under SAOS conditions (b).

The curves $\sigma(\gamma)$ (elastic) and $\sigma(\dot{\gamma})$ (viscous) for sample 2070 A during several recovery times are shown in Figure 5.13. Note that both the elastic and the viscous curves are smooth and elliptical, without secondary loops, which indicate that the samples are under linear viscoelastic conditions (G' and G'' theoretically only vary with the strain amplitude). As time evolves, the elastic curves turn counterclockwise, which is derived from the higher stress response for the same imposed

strain, i.e., increase of G' . Energy dissipation also increases with time, since the area of the viscous curves increases, that is, G'' increases. This temporal change in the (linear) viscoelastic properties of LSR demonstrates the thixotropy that arises from the filler structure. Besides, notice that as the temperature increases, the $\sigma(\gamma)$ curves become steeper and the $\sigma(\dot{\gamma})$ loops become wider. These are additional features that corroborate to the formation of a solid gel as time evolves after intense shear, in accordance with the previously reported findings. The $\sigma(\gamma)$ (elastic) and $\sigma(\dot{\gamma})$ (viscous) curves for the sample 2070 B at 50°C are shown in the Appendix A.5 for comparison.

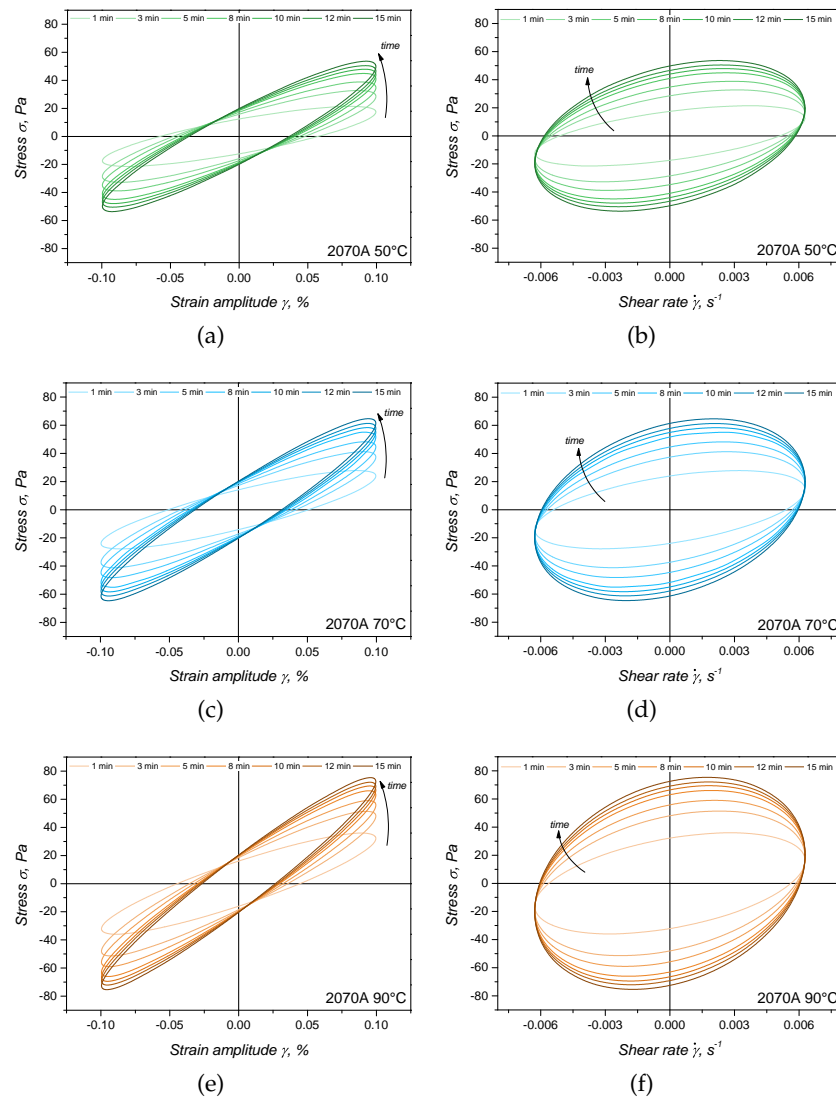


Figure 5.13: Elastic $\sigma(\gamma)$ ((a), (c), and (e)) and viscous $\sigma(\dot{\gamma})$ ((b), (d), and (f)) LB curves for sample 2070 A at various temperatures recorded during recovery period after intense shear.

Acknowledging, identifying, and understanding such time-dependent behaviour is important during the viscosity determination of liquid

silicone rubber in order to avoid misleading results and experimental artifacts. Moreover, modelling of such phenomenon and implementing in injection moulding simulation routines would represent a development of such procedure. Due to the fact that LSR experiences shear gradients during and in-between injection cycles, filler agglomeration might occur and therefore change LSR's rheological characteristics. Since material data characterization in the context of processing simulation aims to approximate the computer-estimated and the real polymer flow and subsequent curing, material data methodologies should be able to cover and assess not only the unique processing conditions, but also the microstructural changes experienced by the polymer to be injected.

At this point, it is crucial to point out that the effect of curing in the flow behaviour would also fit into the goals of the present Chapter. However, this topic will be further discussed in Chapter 11, mainly when the rheology approach is employed to determine the curing kinetics characteristics. There, one can derive the effect of curing in the complex viscosity, since oscillatory experiments are conducted. The effect of curing in viscosity under steady shear is rarely studied, since it would demand the preparation of liquid silicone rubber samples with various curing states below the so-called gel or no-flow point.

5.5 CONCLUSIONS OF THE CHAPTER

Various methodologies to determine liquid silicone rubber's viscosity variation with imposed shear and temperature were assessed and critically compared having as background the injection moulding environment. From the state-of-the-art approaches, steady shear-based techniques, such as rotational steady experiments and high pressure capillary rheometer-based ones, are the ones able to consider the changes in microstructure experienced by LSR under shear. These microstructure changes were correlated mostly to the silica filler structure that is present in almost all commercial LSR grades for injection moulding, that is disturbed when a certain level of shear is imposed, and subsequently recovered when shear ceases. The widely employed oscillatory experiments were compared to the steady techniques under linear and non-linear viscoelastic conditions, and the traditional Cox-Merz proposition linking steady and linear viscoelastic oscillatory properties was not evidenced. However, when steady and oscillatory experiments (LAOS) examine an LSR sample with comparable filler structure, the results seem to converge. In this sense, a comparable filler structure is only achieved during oscillatory tests under non-linear viscoelastic conditions, respecting factors regarding the application of linear viscoelastic-related definitions. These definitions under the linear viscoelastic domain were critically analysed employing Fourier-transformation and Chebyshev coefficients analyses, which

allowed the translation of complex viscosity's concept to a non-linear viscoelastic scenario. This finding highlights the importance to acknowledge possible microstructure changes during LSR's viscosity determination. From this perspective, the present investigation adds to the state of the art a processing-oriented analysis of several methods that are rarely discussed in depth in the literature, but merely and widely applied. Furthermore, the broadly employed liquid silicone rubber's rheological properties were scrutinized, bringing additional knowledge not only to future researches dealing with viscosity determination for polymer processing simulation routines, but also to new polymer grades development. In the final Part of this Thesis, two of these methodologies (LAOS and HPCR) will be compared in terms of the processing parameters output from an injection moulding simulation.

Part III

THERMAL PROPERTIES

THEORETICAL BACKGROUND

This Chapter is dedicated to present the main theoretical considerations concerning heat transfer and compressibility of polymers, having the injection moulding process as background for these properties. In this sense, the principal molecular features that explain heat transfer and change in specific volume due to pressure and temperature are stressed, aiming to support the findings presented in Chapter 8.

6.1 HEAT TRANSFER DURING INJECTION MOULDING

From the constitutional equations that explain the polymer flow during injection moulding, the one related to energy conservation dictates the polymer's temperature. From Equation 6.1, one can easily recognize that the total energy (left side of the equation) equals the sum of work and heat added to the system.

$$\rho c_p \left(\frac{\partial T}{\partial t} + \vec{v} \cdot \nabla T \right) = \beta T \left(\frac{\partial p}{\partial t} + \vec{v} \cdot \nabla p \right) + \eta \dot{\gamma}^2 + \lambda \nabla^2 T + \dot{Q} \quad (6.1)$$

In other words, the total energy (left side of the equation) in an infinitesimal control volume within the polymer flow described by such equation is proportional to the polymer's specific enthalpy ($c_p \frac{\partial T}{\partial t}$) and the contribution from convection ($\vec{v} \cdot \nabla T$). The total work then equals the pressure work ($\frac{\partial p}{\partial t}$), the work related to viscous dissipation ($\vec{v} \cdot \nabla p$), the heat due to viscous heating ($\eta \dot{\gamma}^2$), a diffusion term ($\lambda \nabla^2 T$), and a dissipation contribution or heat source (\dot{Q}). This Equation fully describes the energy flow at any given point of the polymer flow during injection moulding, considering the relevant initial and boundary conditions (mainly when applying this equation to mathematically describe the flow in simulations).

As explained in the introductory Chapter of this work, the main difference between thermoplastics injection moulding and rubber injection moulding is the solidification phase. For rubbers, including liquid silicone rubber, the mould is heated to trigger the chemical reaction (curing) that leads to solidification. In this sense, heat transfer in the case of rubber IM is from the mould to the polymer, while for thermoplastics, the molten polymer transfers heat to the cold mould, leading to solidification. During the filling phase, the reactive LSR mixture layer closer to the hot mould wall starts heating up first than the polymer core. Thus, this layer also crosslinks first, imposing at a given point in time during filling, a solid layer of cured LSR between

the hot mould and the non-cured LSR core. A similar phenomenon occurs with thermoplastics, when a frozen layer is created first close the cold mould. Within this scenario, there is a moment during filling that LSR co-exists in two different physico-chemical states before completely curing from the outer to the inner layers inside the mould. This solidified and now elastic layer is crucial as it affects the overall heat transfer, flow dynamics (fountain flow is a consequence of this layer), and final mechanical properties of the moulded part. Even more critical is the effect of this solid layer in performing thin walled IM simulations, in which small deviance in frozen layer estimation strongly affects pressure-drop predictions because the solid-layer fraction in thin-walled parts is much larger. [97]

Understanding the energy conservation equation and the dynamics of heat transfer is crucial for accurately simulating the injection moulding process of liquid silicone rubber. This process highlights the distinct thermal behavior of rubbers compared to thermoplastics, primarily due to the direction of heat flow during curing. To delve deeper into the thermal properties that influence heat transfer, it is essential to examine the molecular mechanisms underpinning thermal conductivity in polymers. Next section will explore phonon conductivity, a key mechanism that governs how heat is conducted at the molecular level in polymers, and its implications for the injection molding of liquid silicone rubber.

6.2 INTERNAL ENERGY AND MECHANISM OF PHONON CONDUCTIVITY IN POLYMERS

Specific heat capacity and thermal conductivity are two distinct but interrelated thermal properties that play crucial roles in the injection molding simulation of polymers, including liquid silicone rubber. Specific (per unit weight) heat capacity under constant pressure (c_p in $J.g^{-1}.K^{-1}$, not to be confused with C_p , the *molar* heat capacity in $J.mol^{-1}.K^{-1}$, or c_v , the same parameter but under constant volume) is defined as the amount of thermal energy absorbed by a material upon heating, or released by it upon cooling. [98] In other others, it is the heat required to raise the temperature of a unit mass of a substance by one degree of temperature, usually in Kelvin. It is an isotropic property and it reflects the material's ability to store thermal energy and is essential for predicting how the polymer temperature will rise during the moulding process. In contrast, thermal conductivity (λ) is a highly anisotropic property and it measures the ability of a material to conduct heat through it. This property, along with considerations concerning the interface between the polymer and the cavity wall, dictates how quickly heat is transferred from the hot mould walls into the polymer and through the material itself, influencing the curing rate and uniformity of the moulded part [99]. In the context of

injection molding, specific heat capacity determines how the polymer's internal energy changes as it heats up, while thermal conductivity affects the rate and distribution of heat flow within the polymer. Given that a certain macromolecule within the material must first absorb heat from the mould to raise its total energy (subsequently leading to curing) before transferring this energy to the neighbouring macromolecules, specific heat capacity is elaborated next, followed by a detailed discussion on thermal conductivity and heat transfer mechanisms.

Specific heat capacity, or its equivalent the molar heat capacity C_p ($c_p \equiv C_p/M$, M is the molar mass), is a fundamental thermodynamic property that is directly correlated to the total thermal energy of a polymer, expressed as internal energy U and reversible work $p.V$ (energy associated to the system at a pressure p as a result of the volume increase V caused by the added thermal energy). In mathematical terms [98]:

$$C_p(T) \equiv \left[\frac{d(U(T) + p.V(T))}{dT} \right]_p \quad (6.2)$$

In practical terms, c_p is crucial to estimate how much heat has to be transferred from the hot mould to heat the polymer to a certain energy level enough to overcome the crosslinking activation energy for liquid silicone rubber, leading to solidification. The referred amount of energy is then connected to the ability of the macromolecules to store energy, thus linked to their molecular structure.

A reasonable point-of-view to understand heat capacity in terms of molecular structure is by analysing how internal energy is expressed as atoms and groups of atoms move with a defined degree of freedom. For polymers, vibrational motion due to temperature encompass all possible modes of motion in the macromolecule, including bond stretching and bending, rocking motion, torsional oscillation, and large-scale cooperative movement. [98] Each atom in a polymer macromolecule has 3 thermodynamic (theoretical) degrees of freedom, which are hindered by physical constraints (van der Waals forces, entanglements, etc.) or by chemical linkages (crosslink points). Thus, the total degree of freedom f for an amorphous polymer can be stated as

$$f = 3 \sum_{i=1}^n N_i \gamma_i - 3 \sum_{i=1}^n N_{c,i} \gamma_{c,i} \quad (6.3)$$

where $\sum_{i=1}^n N_i$ is the total number of macromolecules, N_i is the number of macromolecules with mass M_i , and γ_i is the number of atoms in each macromolecule of mass M_i . The index c (second term in the right side of Equation 6.3) denotes the constraints contribution to the degree

of freedom. [100] Employing f and the Debye function ϕ (θ is the Debye temperature) to define C_p , Debye proposed:

$$C_p = f\phi\left(\frac{\theta}{T}\right)_i \quad (6.4)$$

Equations 6.3 and 6.4 suggest that the heat capacity of a given polymer is determined by the superposition (sum) of motions of atoms and groups of atoms that compose a macromolecule. In this sense, it is expected that long range constraints, such as crystallinity, do not affect atomic vibration, and thus, do not influence on c_p . It is important to consider the case when constraints are composed of crosslink points, i.e., chemical bonding of adjacent macromolecules is responsible to decrease the degree of freedom, and thus the heat capacity. This is demonstrated by the study of McHugh *et al.* [101], which shows that the specific heat capacity of an epoxy-amine system decreases (around 15%) after isothermal crosslinking, as shown in Figure 1 of the cited work. Decrease of c_p is obvious in this case, since there is a stoichiometric reaction between an epoxy group and an amine moiety, hindering vibrational motion in every molecule present in the system. The case of liquid silicone rubber is diametrically different, since the constraint imposed by curing does not occur to every mer unit of the poly(siloxane) macromolecules. The reason why crosslinking does not occur to every mer unit is the fact that not all of these units contain the necessary groups for crosslinking (Si-H and vinyl for hydrosilylation in the case of Pt-catalysed LSR systems). There is so far no study in the available literature (which includes the present work) that establishes or suggests a crosslinking threshold for polymers, and mainly the ones with low glass transition temperature (high macromolecular flexibility) and engineering applications (such as for injection moulding), that is connected to a significant change in the network's degree of freedom necessary to change c_p . It is fair to recognize the contribution of Vera-Graziano and co-workers [100], who studied poly(dimethylsiloxane) networks with various molecular weights and were able to observe such changes for silicones crosslinked via hydrogen abstraction (available in every monomeric unit).

Because specific heat capacity is a measurement of heat within a certain temperature range, calorimeters are employed to determine this property. More specifically, dynamic scanning calorimetry (DSC) devices are used following various methodologies, which differ themselves based on either the use of a standard material with known specific heat capacity, or direct measurements of c_p . For practical reasons, these methods are detailed in the next Chapter.

Heat transport, differently from specific heat capacity, is a phenomenon that occurs between two or more nearby macromolecules in the atomic scale. Low frequency atomic vibrational waves are responsible to carry energy between two entities that have different

energy states and due to their quantized energy are referred as phonons. [102] This mechanism is different from the ones found in metals because in polymers the electrons are localized in inner shells, lone pairs and bonding orbitals, not being available to flow throughout the material to conduct heat. [98] Considering the plane wave nature of phonons, one can expect that they would be strongly scattered by the coiled conformation of polymers chains. Indeed, since phonons in amorphous polymers can only propagate a few nanometers (few monomer lengths) [102], the thermal conductivity of polymers is very low, in the order of $0.1\text{--}0.5 \text{ W}\cdot\text{m}^{-1}\cdot\text{K}^{-1}$ [103]. Heat transfer in the case of amorphous and unfilled polymers occurs mainly along the chain (via the covalent bonds), but Rashidi and co-workers [104] demonstrated the contribution of non-bonding interactions (van der Waals and electrostatic) in the heat transfer of crosslinked polymers.

Phonon transport through a polymeric matrix is changed when fillers are dispersed into the polymer. Fillers with higher thermal conductivity are usually incorporated into polymers to enhance thermal performance when the filler structure (combination of filler content and filler aspect ratio) is able to conduct phonons. [105] However, when either the filler content or the aspect ratio is low, the creation of interfacial thermal resistance can hinder phonon transmission, as observed by Azizi *et al.* [105]. For liquid silicone rubber, Li and co-workers [106] demonstrated the effect of filler thermal conductivity and aspect ratio in the thermal conductivity by incorporating aluminum oxide (spherical, $\lambda = 20\text{--}29 \text{ W}\cdot\text{m}^{-1}\cdot\text{K}^{-1}$), aluminum nitride (irregular particle, $\lambda = 200 \text{ W}\cdot\text{m}^{-1}\cdot\text{K}^{-1}$), and boron nitride (2D sheets, $\lambda > 250 \text{ W}\cdot\text{m}^{-1}\cdot\text{K}^{-1}$). The highest thermal conductivity was achieved by the LSR/boron nitride composites, that presented 316% higher λ ($1.04 \text{ W}\cdot\text{m}^{-1}\cdot\text{K}^{-1}$) when compared to pure LSR (low molecular weight, $\lambda = 0.25 \text{ W}\cdot\text{m}^{-1}\cdot\text{K}^{-1}$). The authors associated the thermal conductivity increase to the continuous pathway for phonon transmission created by the boron nitride 2D sheets in the silicone matrix, as shown in Figure 6.1.

The methods to determine thermal conductivity vary in terms of the physical state of the sample and concerning the measurement mode. As described by Kerschbaumer and co-workers [107], the techniques to measure λ are divided into steady-state and transient. Both methods require sample thermal equilibrium, but the first operates under steady heat flow conditions, while the second deals with a transient heat flow. For liquid silicone rubber in the non-cured state, the transient line source method is advantageous, since it allows the determination of thermal conductivity of liquid samples. For LSR samples in the cured state, the guarded heat flow meter is suitable due to the simple operation and the possibility to determine thermal conductivity in the sample thickness direction. [107] Regardless of the different operation mode, the steady guarded heat flow meter method and the transient

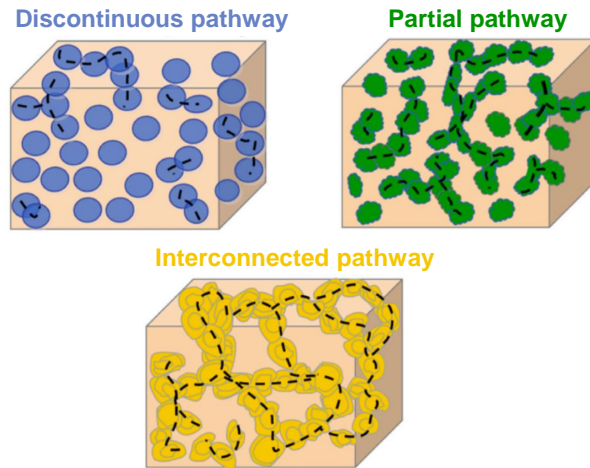


Figure 6.1: Schematic diagram of phonon transport mechanism in LSR composites containing aluminium oxide (blue), aluminium nitride (red), and boron nitride (green). Adapted from [106].

line source technique can be compared in terms of the measured thermal conductivities. [107]

Specific heat capacity and thermal conductivity are properties connected to liquid silicone rubber only and dictate how the polymer will have its thermal state changed when exposed to a heat source. However, these properties are not able to govern the interface behaviour of the LSR/mould pair. Indeed, the interfacial temperature between the polymer and the mould is generally not the same as the mould temperature. [108] The heat transfer between the polymer and the mould is thus characterized by a coefficient that accounts for the three main heat transport mechanisms involved during injection moulding: convected heat from the polymer; heat conducted to the mould; and heat generated inside the polymer, as the heat released by the curing reaction. Since the heat transfer coefficient (HTC) is a system-related property, it is normally [108–110] determined for a polymer/mould material pair by sensing the surface at the interface during the injection moulding cycle and further employing a mathematical model. For the manufacture of liquid silicone rubber-based parts, heat transfer coefficient is more critical for thin-walled parts and for micro-injection moulding. [108] For the present Thesis, a constant value of heat transfer coefficient will be assumed in Chapter 12.

6.3 COMPRESSIBILITY OF POLYMERS

During injection moulding, thermoplastics are injected in the molten state into a cold mould, which triggers solidification. For rubbers, including LSR, the material changes its physical form via a chemical reaction triggered by high temperature. On both cases, thermoplastics and rubbers undergo volume changes due to temperature and pres-

sure. The change in volume for a moulding process is directly connected to the notion of dimensional tolerance, i.e., the ability to mould a part within the designed dimensions. Therefore, volume as a function of pressure and temperature is a property that has to be characterized in order to realistically simulate the injection moulding process.

For polymers, the molar volume (space occupied by 1 mol of polymer chains) is the sum of three contributions [98]:

1. The *van der Waals* volume: space actually occupied by the macromolecules, which is inviolable to other polymer chains.
2. The *packing* volume: "empty" space existing between the macromolecules due to packing constraints, i.e., the macromolecules with their van der Waals volumes are not able to organize themselves in a tightly packed volume, resting space among them.
3. The *expansion* volume: space resulting from thermally induced vibrational motion.

The reason why liquid silicone rubber is injected into the cavity with subvolumetric filling is the increase of the expansion volume, that can lead to over-pressurization and flashing of the cavity if neglected. [48] The change in the expansion volume is normally quantified as coefficient of thermal expansion (unit is *per Kelvin*, or K^{-1}).

For simulation purposes, a mathematical description of $v(p, T)$ is necessary, as it is for all other properties discussed in this work. A suitable way to describe the pressure-volume-temperature (pvT) behaviour of polymers is via equations of state or semi-empirical models that predict the volume response to pressure and temperature conditions. From these semi-empirical models, the two-domain Tait model [111] is the most common and widely employed semi-empirical model. [112] The Tait model describes two temperature domains, the solid and the molten, and each of these domains has a set of equations with proper coefficients to describe $v(p, T)$. Since liquid silicone rubber is far above its glass transition temperature and its melting point, the Tait model can be written only in terms of the equations related to the molten state as:

$$\begin{cases} v(p, T) = v_0[1 - C \cdot \ln(1 + \frac{p}{B})] + v_t \\ v_0 = b_{1m} + b_{2m} \cdot \bar{T} \\ B = b_{3m} \cdot \exp(-b_{4m} \cdot \bar{T}) \\ v_t = 0, \text{ for } T > T_g, T_m \end{cases} \quad (6.5)$$

where $v(p, T)$ is the specific volume in terms of pressure and temperature, v_0 is the specific volume at zero pressure, C is a universal constant taken as 0.0894, and b_{1m} ($m^3 \cdot kg^{-1}$), b_{2m} ($m^3 \cdot kg^{-1}$), b_{3m} (Pa),

and b_{4m} (K^{-1}) are the model parameters for the molten domain. v_t describes the volume change due to crystallization or glass transition. The estimation of these parameters is usually carried out via fitting the pvT data to the Tait model using a least squares method.

In practical terms, the pvT behaviour of polymers can be characterized via two principally different conventional techniques: the confining-fluid and the piston-die techniques. [113] The first technique is based on placing the polymer sample inside a fluid (usually mercury or silicone oil) enclosed by a rigid sample. A hydrostatic pressure is applied by reducing the sample chamber volume, and sensing the cumulative volume change of fluid and polymer. The advantages of this method over the piston-die one is the existence of a pure hydrostatic pressure and the absence of sample leakage or friction. However, the main disadvantages are related to the necessary correction to account for the fluid volumetric change and the possibility of chemical reactions between the sample and the fluid. [113] The piston-die technique, as the one employed in this work, is detailed in the next Chapter.

EXPERIMENTAL DESCRIPTION

This Chapter describes the materials and the methodologies applied to determine the thermal properties of liquid silicone rubber in terms of specific heat capacity under constant pressure c_p , thermal conductivity λ , and specific volume or pvT behaviour. The main aspect of this Chapter is to study how the curing state influences the thermal properties and to compare different methodologies to characterize the properties of liquid silicone rubber to be employed as input for injection moulding simulation routines.

7.1 DETERMINATION OF THE SPECIFIC HEAT CAPACITY UNDER CONSTANT PRESSURE

The specific heat capacity was studied employing two different, but similar, methods. While the standard ASTM E1269 [114] employs sapphire as a reference material for c_p , the temperature-modulated approach is a stand-alone method to determine a polymer's c_p . Since these methodologies differ on how c_p is determined, they are critically compared. Besides, the comparison is made with liquid silicone rubber and a solid synthetic rubber, aiming to broaden the scope of the study.

7.1.1 *Materials*

Liquid silicone rubber (KEG-2003H-70-A, hardness after cured = 70 Shore A), containing approximately 28 wt% of an inorganic filler, was supplied as a 2-component (A and B) system by Shin-Etsu Silicones Limited (USA). EG-2003H-70-A is a standard liquid silicone rubber for injection moulding processes and has a mixing ratio of components A:B = 1:1.

A commercial rubber compound composed of poly(styrene-co-butadiene) filled with carbon black and silica (hardness after cured = 70 Shore A) and containing a sulphur-based crosslinking system was also studied in terms of specific heat capacity for comparison purposes. Due to confidentiality, further details about the compound's formulation cannot be disclosed.

7.1.2 *The sapphire method - ASTM E1296-11*

Determination of c_p according to the ASTM E1269 [114] was accomplished in a dynamic scanning calorimeter (DSC1 STAR System Mettler-Toledo International Inc, Switzerland). Approximately

10-20 mg of A+B 1:1 mixture (triplicate) were placed into aluminium crucibles aiming maximum possible contact with the crucible's bottom. Subsequently and according to the standard ASTM E1269 [114], the following thermal program was applied under $50 \text{ mL}\cdot\text{min}^{-1}$ of nitrogen gas:

- i Isotherm for 4 min at 50°C .
- ii Heating at $20 \text{ K}\cdot\text{min}^{-1}$ until 200°C .
- iii Isotherm for 4 min at 200°C .
- iv Cooling at $20 \text{ K}\cdot\text{min}^{-1}$ until 50°C .
- v Isotherm for 4 min at 50°C .
- vi Heating at $20 \text{ K}\cdot\text{min}^{-1}$ until 200°C .
- vii Isotherm for 4 min at 200°C .

The temperature program was designed to measure the sample's specific heat capacity as non-cured and during curing (step ii), as well as cured (step vi).

The same thermal program was employed for an empty aluminium crucible (reported weight) and for an aluminium crucible containing the specific heat capacity standard (synthetic sapphire disk with reported weight). It is important to highlight that the software connected to the device only automatically calculates the specific heat capacity if the empty pan is tested before all samples/sapphire and is used to subtract the specimen holder's thermal response from the sample's/sapphire's. In this sense, the sample's $c_{p,s}$ ($\text{J}\cdot\text{g}^{-1}\cdot\text{K}^{-1}$) can be calculated in terms of the standard's $c_{p,st}$ as:

$$c_{p,s} = c_{p,st} \cdot \frac{D_s \cdot W_{st}}{D_{st} \cdot W_s} \quad (7.1)$$

D_s is the heat flow difference (mW) at a given temperature between the empty pan and the sample; D_{st} is the heat flow difference (mW) at a given temperature between the sapphire standard and the sample; W_s is the sample's mass (mg); and W_{st} is the sapphire disk's mass (mg). The sample's mass was measured before and after the thermal program and any sample that underwent mass loss higher than 0.3% was repeated, as advised by the ASTM E1269 standard.

From Equation 7.1 one can realize that any disturbance in the sapphire heat flow signal will impact the sample's c_p measurement, since $c_p(s)$ is directly calculated from $c_p(st)$. This feature is not present in the next methodology as it will be described next.

7.1.3 The modulated temperature calorimetry approach

This approach, commonly referred to as MTDSC (modulated temperature DSC), differs from the one described before due to the fact that it applies a sinusoidal thermal perturbation instead of a constant heating rate for non-isothermal experiments. [115, 116] In general terms, during a DSC run, the total heat flow $\frac{dQ}{dt}$ is a contribution of one signal that is dependent on $\frac{dT}{dt}$, and another that is dependent on the value of the temperature T . If there is no significant temperature gradient in the sample, i.e., the sample is able to increase its temperature as a whole, the total heat flow during a DSC run can be mathematically expressed as:

$$\frac{dQ}{dt} = c_{p,t} \cdot \frac{dT}{dt} + f(t, T) \quad (7.2)$$

where $c_{p,t}$ is the specific heat capacity at constant pressure defined here as that due to the energy stored as motion of the sample's molecules; and $f(t, T)$ is a function that governs the kinetic response of temperature-driven transformations, such as crystallization, melting, glass transition, or crosslinking. Following this context, there are two contributions to the DSC response: one thermodynamically governed by $c_{p,t}$ (here with sub-index t to refer as the thermodynamic c_p) and is dependent on $\frac{dT}{dt}$, and another that is kinetically hindered by a mechanism ($f(t, T)$), which is dependent on T . In the case of liquid silicone rubber, the first response is connected to the vibrational, rotational, and translational motions of the poly(siloxane) oligomers; while the second response will be governed by LSR's curing reaction for temperatures above room temperature. One can realize that, as the temperature rises due to a positive $\frac{dT}{dt}$, the sample's response to the bond breaking and forming process of the cure reaction and the response due to increase in oligomers' kinetic energy (molecular motion) are different. This output signal separation between purely thermodynamic and kinetic-governed phenomena is the main difference between conventional (sapphire method) and modulated DSC methods for c_p determination.

To accomplish this distinction, the sample is subjected to a modulated thermal program with an initial temperature T_0 , a heating rate b , and a modulation factor with amplitude B and frequency ω , as follows:

$$T = T_0 + b.t + B.\sin(\omega t) \quad (7.3)$$

For the present research, stochastic temperature modulations, i.e., well-distributed temperature perturbations within the analysed temperature range with random duration, are superimposed on an underlying rate of conventional DSC. This was accomplished employing

a dynamic scanning calorimeter (DSC2 System Mettler-Toledo International Inc, Switzerland) and the TOPEMTM software (Mettler-Toledo International Inc, Switzerland) located in the Faculty of Polymer Technology (FTPO, Slovenia). By applying discrete Laplace transformations, this method is able to determine the quasi-static heat capacity, or the thermodynamic specific heat capacity. This c_p signal will be independent of any thermal event that occurs during the DSC run. The MTDSC-TOPEM experiments were conducted with an underlying heating rate $b = 2 \text{ K}\cdot\text{min}^{-1}$, an amplitude $B = \pm 0.5 \text{ K}$, and a period ($\frac{1}{\omega}$) = 30-60 s under $50 \text{ mL}\cdot\text{min}^{-1}$ of nitrogen gas. The temperature program is as follows:

- i Isotherm for 5 min at 50°C .
- ii Heating at $2 \text{ K}\cdot\text{min}^{-1}$ until 200°C with temperature modulation.
- iii Isotherm for 5 min at 200°C .
- iv Cooling at $2 \text{ K}\cdot\text{min}^{-1}$ until 50°C without temperature modulation.
- v Isotherm for 5 min at 50°C .
- vi Heating at $2 \text{ K}\cdot\text{min}^{-1}$ until 200°C with modulation.

The temperature program was designed to measure the sample's specific heat capacity as non-cured and during curing (step ii), as well as cured (step vi). These experimental parameters were selected according to the literature [101, 117, 118] for thermoset systems.

7.2 MEASUREMENT OF THE THERMAL CONDUCTIVITY

The thermal conductivity of non-cured and cured liquid silicone rubber was determined employing two methods suitable for each state of cure. While the individual components A and B and the mixture (A+B) 1:1 were characterized employing the transient line-source method, crosslinked compression moulded (160°C , 10 min) samples were evaluated employing a steady-state-based guarded heat flow meter. These two methods are distinct in the sense that while transient approaches rely on applying a short energy pulse to the sample and evaluating the transient temperature rise, steady-state techniques determine the thermal conductivity after the sample reaches thermal equilibrium. However, they are comparable, as reported by Kerschbaumer *et al.* [107] when investigating natural and synthetic industrial rubber compounds.

7.2.1 Materials

Liquid silicone rubber (SiloprenTM LSR 2070, $M_w = 86673 \text{ g}\cdot\text{mol}^{-1}$, $M_w/M_n = 1.6$, hardness after cured = 70 Shore A), containing approximately 32 wt% of an inorganic filler, was supplied as a 2-component

(A and B) system by Momentive Performance Materials Inc. (USA). LSR characterization in terms of molecular weight and filler content is described in the Appendix (A.1 and A.3, respectively) of this Thesis. SiloprenTM LSR 2070 is a standard liquid silicone rubber for injection moulding processes and has a mixing ratio of components A:B = 1:1. Mixing of components A and B was accomplished with a dual asymmetric centrifuge (DAC 400.2 VAC-P, Hauschild Speed Mixer, Germany) at room temperature, under vacuum, and according to the following step-wise procedure:

1. 800 rpm, 2 min, 800 mbar vacuum.
2. 1200 rpm, 2 min, 400 mbar vacuum.
3. 1600 rpm, 2 min, 100 mbar vacuum.
4. 1800 rpm, 4 min, 50 mbar vacuum.

7.2.2 Transient line-source technique

Determination of the non-cured samples' thermal conductivity was conducted according to the standard ASTM D5930-09 [119] in a K-System II device (Advanced CAE Technology Inc., USA). This method relies on placing a line source in close contact with the sample and measuring the rate propagation of the heat released by the line source radially through the sample. Since the rate of heat propagation is related to the thermal diffusivity of the sample and the temperature rise of the line source varies with the logarithm of time, the sample's thermal conductivity can be determined.

In practical terms, LSR samples (in triplicate) were placed inside the device's cylinder (9.3 mm diameter) and the line source (1.3 mm diameter) was inserted into the cylinder, through the LSR sample. The whole cylinder was then heated to the desired temperature, thermally-stabilised (15 min), and the measurement proceeded with a predefined amount of energy being dissipated by the immersed line source. Due to the released heat, the temperature increment ΔT as a function of time ($t_1 \rightarrow t_2$) [107] was recorded and the slope C (K^{-1}) was calculated:

$$C = \frac{\ln \frac{t_2}{t_1}}{\Delta T} \quad (7.4)$$

The thermal conductivity λ ($W.m^{-1}.K^{-1}$) was calculated according to the Fourier's heat transfer equation for a radial system:

$$\lambda = \frac{\kappa}{4\pi} \phi C \quad (7.5)$$

where ϕ ($\text{W}\cdot\text{m}^{-1}$) is the line source's heat flow per unit length. The dimensionless calibration factor κ is obtained after calibration conducted against a reference material with known thermal conductivity, as detailed in the standard [119], covering as well the finite probe dimensions, contour effects, and other non-linearities [107]. According to the standard ASTM D5930 [119], this method has an accuracy of $\pm 7\%$.

For each selected temperature, the same procedure was adopted. For the individual components A and B, thermal conductivity was measured at 80°C , 100°C , 120°C , 140°C , and 160°C . However, to avoid the curing reaction, the (A+B) 1:1 mixture was tested at 60°C , 70°C , and 80°C .

7.2.3 Guarded heat flow meter method

This method is based on the heat flux through a sample that is placed between a heat source and a heat sink. 2 mm compression moulded samples (triplicate) were mounted in a thermal conductivity tester DTC-300 (TA Instruments, USA) and tested after reaching thermal equilibrium at 60°C , 70°C , 80°C , 90°C , 120°C , 140°C , and 160°C . By measuring the heat flow \dot{Q} (W) through a specimen with thickness d (m) and area A (m^2) and the temperature difference ΔT across the sample, the thermal conductivity λ ($\text{W}\cdot\text{m}^{-1}\cdot\text{K}^{-1}$) was calculated employing the Fourier's heat transfer equation for linear systems:

$$\lambda = \frac{\dot{Q}\cdot d}{A\cdot\Delta T} \quad (7.6)$$

According to the standard ASTM E1530 [120], this method has an accuracy of $\pm 5\%$.

7.3 DETERMINATION OF THE SPECIFIC VOLUME

For the characterization of the specific volume, one single method was employed, the so called piston-die or piston-based isobaric method. It has been shown [113] that the piston-based method differs from the confining-fluid approach by a maximum of 4%, thus the data reported in this work can be safely compared to specific volumes determined elsewhere.

7.3.1 Materials

For the determination of the pressure-specific volume-temperature behaviour, the same liquid silicone rubber applied to determine the thermal conductivity was employed. Details about the material and the mixing conditions of the 1:1 A:B mixture are described in Section 7.2.1.

7.3.2 *Piston-based isobaric method*

The specific volume dependence on temperature and pressure was characterized in a PVT 100 dilatometer (SWO Polymertechnik GmbH, Germany). This device employs a piston technology and is based on a cylindrical metal cavity where the sample is placed under pressure between two pistons tightly fitting the cylinder. The change in volume $\Delta v(p,T)$ is then calculated under specific pressure and temperature conditions as:

$$\Delta v(p, T) = \frac{\Delta l \cdot \pi \cdot r^2}{m} \quad (7.7)$$

where l is the piston displacement length, r is the cavity's radius, and m is the sample's mass. For these measurements, friction of the sample with the cavity wall was neglected and the temperature was varied from 50°C to 200°C (heating at 2 K.min⁻¹) at increasing constant pressures 5 MPa, 7.5 MPa, 10 MPa, 15 MPa, 20 MPa, 25 MPa, and 30 MPa (isobaric mode). Crosslinking of the mixture occurred during the first heating at the lowest pressure of the cycle. After each isobaric heating, the cavity was cooled to 50°C under 5 MPa pressure, and finally the pressure increased to the next isobaric value. A diagram showing the experiment conditions is shown in Figure 7.1. It is important to highlight that the specific volume at 5 MPa was measured twice: once at the first heating, during which the sample crosslinks; and one second time after the 30 MPa step, with the sample fully crosslinked. The specific volume data (in duplicate) were used to fit the Tait model.

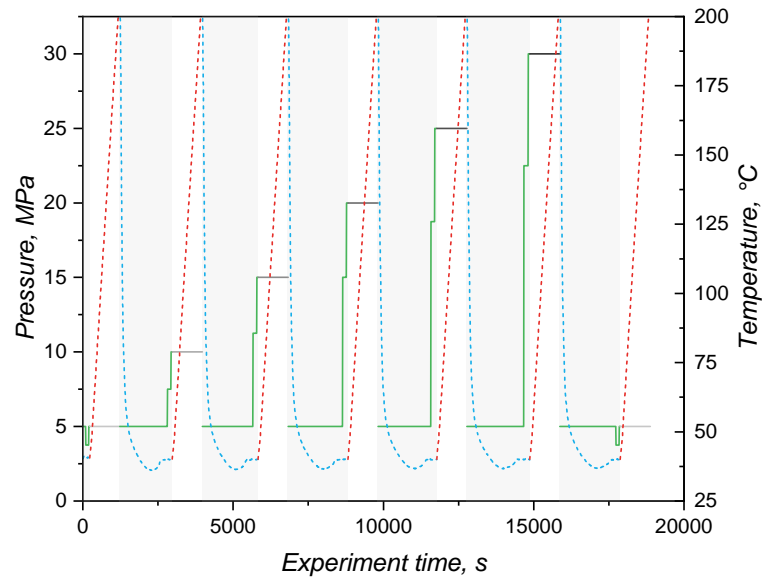


Figure 7.1: Experimental conditions for the determination of the specific volume under different pressures and for a range of temperatures. The full line represents the pressure imposed to the sample and indicates the isobaric conditions of testing (grey segments) and the stabilization period between two consecutive isobars (green segments, shaded areas). The temperature is pictured as dashed lines, showing the heating (red segments) during testing and the cooling (blue segments) during the stabilization period. For the stabilization period prior to the 5 MPa isobaric experiments, the pressure was dropped to 3.5 MPa to allow the sample to fill the whole measurement cavity.

RESULTS AND CONCLUSIONS

This Chapter is dedicated to present and discuss the main thermal properties that are necessary to be implemented in an injection moulding simulation. For the determination of the specific heat capacity, two methodologies are discussed and compared concerning their outputs and their thermodynamic meanings. The thermal conductivity was determined and the physico-chemical state of the samples (uncured and cured) were compared, along with an investigation of the individual component's thermal conductivity. Finally, the specific volume is given and explored in terms of the sample's compressibility.

Note: Part of this work was carried out by the author at the Faculty of Polymer Technology (FTPO, Slovenia).

8.1 SPECIFIC HEAT CAPACITY c_p

The specific heat capacity of an 1:1 A:B mixture of liquid silicone rubber was determined employing the modulated temperature dynamic scanning calorimetry approach and compared to the widely applied sapphire method. The generated heat during the MDSC run is shown in Figure 8.1, where exothermal events are represented by peaks pointing upwards. As explained before, MDSC is able to decompose the total heat (as measured in conventional DSC devices) into reversible and non-reversible components. For liquid silicone rubber, the crosslinking appears as an exothermal signal below 100°C, with 262 mJ released energy, in the total and non-reversible heat curves. Since crosslinking is a kinetic phenomenon, it appears as released non-reversible heat. However, no exothermal signal is present in the reversible heat. This is the first indication that the specific heat capacity, i.e., the amount of energy (J) necessary to increase the temperature of 1 g of material by 1 K, does not change during the crosslinking reaction. Stark, McHugh, and co-workers [101, 118] observed a different behaviour while studying the curing of an epoxy-amine resin without reinforcing fillers. The authors observed a first increase of c_p (consequence of a change in the reversible heat, Fig. 4 in [118]) during the curing reaction and before the onset of vitrification, which for the epoxy-amine resin is due to a specific effect of primary and secondary amine reactions. Subsequently, a sharp decrease of c_p was observed for these epoxy-amine systems, which can be attributed to the abrupt reduction of macromolecular segmental mobility, directly related to the specific heat capacity. [121] For liquid silicone rubber, on the other hand, the hydrosilylation reaction and the resulting crosslinked network do not seem to considerably influence the reversible heat.

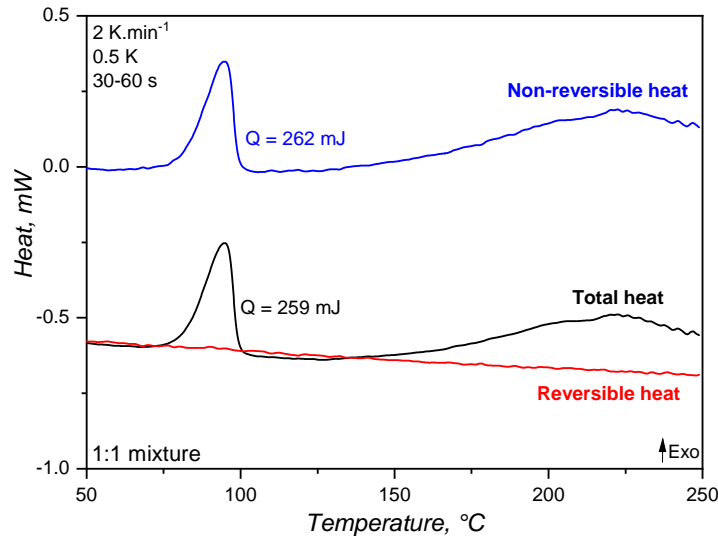


Figure 8.1: Modulated temperature DSC thermogram differentiating the total, the non-reversible, and the reversible (employed to determine c_p) heat quantities for the 1:1 LSR mixture. Sample mass is 15-20 mg.

The specific heat capacity of liquid silicone rubber during crosslinking was then determined based on the reversible heat for the MDSC approach and considering the sapphire reference for the standard ASTM E1269. For this comparison, the 1st heating in the DSC program is related to the uncured sample, during which the crosslinking reaction occurs; whereas the 2nd heating step involves the already crosslinked sample. In Figure 8.2, the standard sapphire method (blue lines) shows a change in the c_p for the first heating, which is related to the way this value is calculated, i.e., based on the total released heat. Since the crosslinking reaction is exothermal, the sample heats up in a faster pace compared to the reference pan of the DSC device, implying in a decrease of the specific heat capacity. As the curing conversion reaches 100%, the rate of heat release decreases and the c_p raises, returning to a stable value after the crosslinking reaction is completed. It is important to notice that the specific heat capacity above 150°C for the first heating returns to the trend established below 100°C (before the reaction onset), suggesting that the c_p change experienced during curing is an artifact of the calculation method, not a consequence of chemical or microstructural change of the liquid silicone rubber. Indeed, it is not reasonable to suggest that the crosslinking reaction leads a decrease and posterior increase of c_p as result of any chemical or microstructural change occurring exclusively due to connection of adjacent poly(siloxane) macromolecules. One must consider, however, that the c_p trend as shown by the full blue line reflects the exothermal nature of crosslinking, which is an important aspect to account for injection moulding simulation. For the completely cured sample, the second heating shows a linear c_p that only increases with temperature.

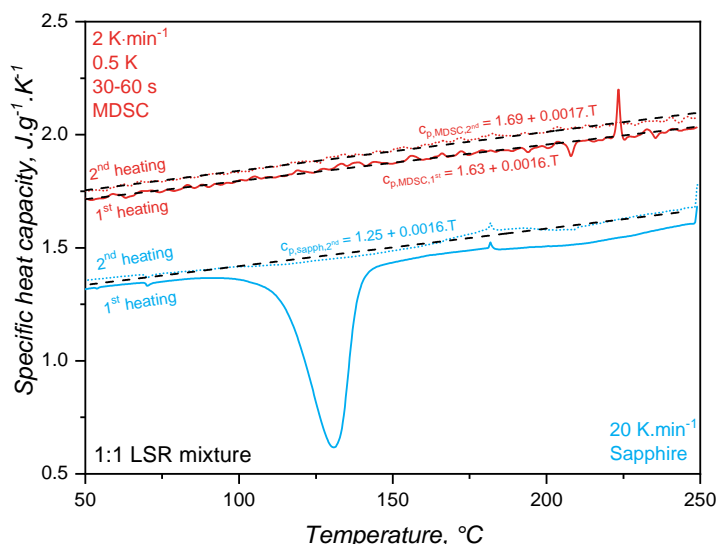


Figure 8.2: Comparison of the LSR's specific heat capacity values determined employing the sapphire (blue lines) and the MDSC (red lines) methods. The full lines represent the first heat run, while the sample is still uncured until the crosslinking reaction starts, whereas the dotted lines show the second heat run for the fully crosslinked samples. The dashed lines are linear fittings (equations are in the plot) with $R_{adj}^2 > 0.99$. The coefficient of variation for the measurement is 7%.

The modulated temperature DSC method results in c_p values as shown in Figure 8.2 by the red lines. As expected, c_p is a linear function of temperature for the first and second heating steps. The linear behaviour of c_p results from the linearity of the reversible heat (red line) over temperature in Figure 8.1. The sample during the first heating does not experience a change in c_p throughout the whole temperature range, showing that the crosslinking reaction *alone* does not change the specific heat capacity, as shown before for the sapphire method. In the case of liquid silicone rubber samples, two are the main reasons why the curing reaction plays an almost insignificant role in changing the c_p . The first and major reason is the presence of a high filler volume (silica), which significantly controls segmental mobility due to interaction with poly(siloxane) macromolecules and energy absorption. Since both uncured and cured samples have the same filler content (they are the same sample, but with distinct physico-chemical states), no change in c_p is observed. The second reason why the curing reaction does not lead to a change in c_p is the macromolecular arrangement prior and after crosslinking. Before curing, poly(siloxane)s are already highly entangled, since the molecular weight surpassed the critical molecular weight for entanglements. After curing, entanglements remain, and crosslinking bridges are building between macromolecules via poly(siloxane) oligomers. Even though these bridges increase substantially the molecular weight, turning the before only crosslinked

network in a 3D network of infinite molecular weight, local segmental mobility is still preserved. In another direction, Vera-Graziano *et al.* [100] observed a decrease of c_p after crosslinking poly(dimethyl siloxane). The authors also studied the specific heat capacity of PDMS with similar molecular weight distribution as the one employed in the current study ($M_n = 66030 \text{ g.mol}^{-1}$, $M_w = 83391 \text{ g.mol}^{-1}$), but crosslinked via hydrogen abstraction with benzoyl peroxide, not via hydrosilylation. Crosslinking via hydrogen abstraction connects adjacent macromolecules via a short covalent bond, hindering segmental motion and, therefore, modifying c_p . In this sense, one can understand that as crosslinking density increases, more heat is required to reach the same segment mobility, leading to a higher c_p , as observed by the authors [100].

Concerning the absolute values of c_p , both methods reached the values reported in the literature [122–124] for poly(siloxane)s. For both methods, c_p for the completely cured sample (2nd heating) appears as higher, but this is actually an artifact from the variable power asymmetry of the sample and the internal DSC reference. Besides, the methods resulted in apparently distinct c_p values (MDSC values are higher than the sapphire one). This baseline shift can be associated to the sample contact with the DSC pan, which is different for every measurement since liquid silicone rubber cannot perfectly sit in the bottom of the pan and the contact is highly dependant on how the operator places the sample inside it. From the linear fittings shown in Figure 8.2, one can interestingly realize that the variation of c_p with temperature (slope) is the same regardless of the method: around $0.0016 \text{ J.g}^{-1}.\text{K}^{-1}/^\circ\text{C}$. This is very close to the slope reported by Bicerano [98] when proposing an equation for $C_p^l(T)$ (*capital C* denotes the molar specific heat capacity) for liquid polymers ($T > T_g$ for rubbery and molten polymers) based on experimental data:

$$C_p^l(T) \approx C_p^l(298\text{K}).(0.613 + 0.0013T) \quad (8.1)$$

For poly(dimethylsiloxane), Bicerano [98] reported $C_p^l(298\text{K}) = 117.8 \text{ J.mol}^{-1}.\text{K}^{-1}$, which considering PDMS mer's molar mass (74.01 g.mol^{-1}) leads to $c_p^l(298\text{K}) = 1.59 \text{ J.g}^{-1}.\text{K}^{-1}$. Since this value was obtained for pure PDMS, the effect of incorporated silica in the LSR under study has to be taken into account when comparisons are made. In this sense, since fumed silica has lower c_p (around $0.9 \text{ J.g}^{-1}.\text{K}^{-1}$) than PDMS and additionally the presence of silica in a poly(siloxane) matrix causes macromolecule immobilization, as explained in Section 1.2.4, one can expect that the silica-filled PDMS has a lower c_p than the pure polymer. Thus, one can conclude that the values reported in Figure 8.2 are comparable to the one found and calculated by Bicerano [98]. For reference, the specific heat capacity of copper is around $0.3 \text{ J.g}^{-1}.\text{K}^{-1}$.

A poly(styrene-co-butadiene) compound was also studied by both methods for determining the specific heat capacity and the results are presented in Figure 8.3. For the standard sapphire approach, the thermal transitions associated to the SBR compound are clearly affecting the c_p values, as in the events related to melting at $T < 100^\circ\text{C}$ and to the curing at $T > 100^\circ\text{C}$. Since melting is an endothermal event, heat absorption leads to an increase of c_p , even though no significant segment mobility change occurs during this thermal event. The same applies for the curing reaction, but in the exothermal sense. Similarly to LSR, the filled SBR compound under study exhibited $c_p(T)$ as predicted by Bicerano [98] and corroborated by Liu and Zhong [125] for solid polymers (for the authors, solid rubbers such as poly(1,4-butadiene) are treated as solid polymers, not as rubbery as for the liquid scenario). The slope of 0.0025 in the linear fittings agrees with the equation proposed by the author [98]:

$$C_p^s(T) \approx C_p^s(298\text{K}) \cdot (0.106 + 0.003T) \quad (8.2)$$

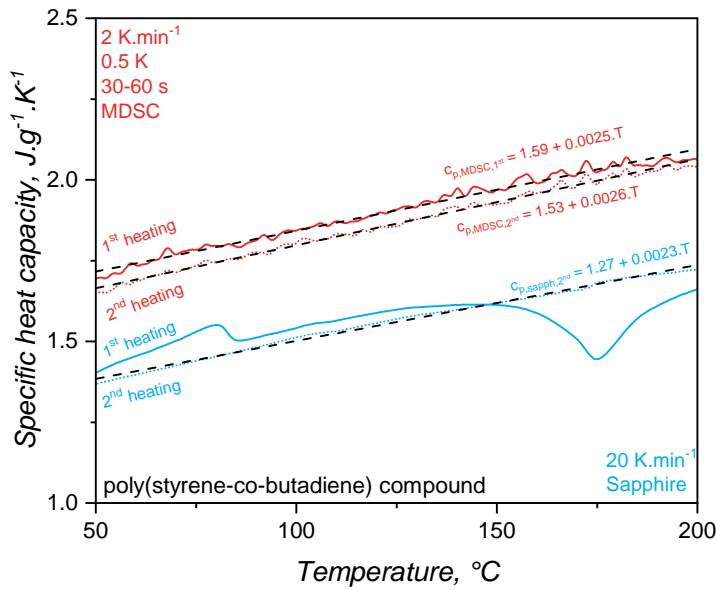


Figure 8.3: Comparison of the SBR compound's specific heat capacity values determined employing the sapphire (blue lines) and the MDSC (red lines) methods. The full lines represent the first heat run, while the sample is still uncured until the crosslinking reaction starts, whereas the dotted lines show the second heat run for the fully crosslinked samples. The dashed lines are linear fittings (equations are in the plot) with $R_{adj}^2 > 0.99$.

It is interesting to note from the equations (8.1 and 8.2) proposed by Bicerano that the slope for $C_p^l(T)$ is lower than the slope for $C_p^s(T)$, indicating the difference in segment mobility between these two phases. Indeed, Bicerano shows in his book [98] the change of c_p around the

glass transition temperature for an amorphous polymer as represented by Figure 8.4. It is possible to see that c_p increases slower at $T > T_g$ than below the glass transition. A parallel can be made between this behaviour, the equations for solid and liquid polymers as presented before, and the uncured/cured states of LSR and SBR as shown in Figures 8.2 and 8.3.

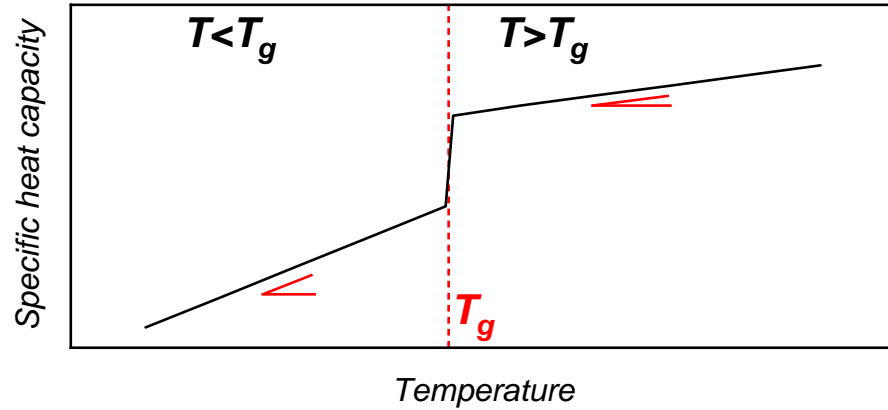


Figure 8.4: Schematic representation of c_p variation with temperature around the glass transition region. Modified from [98].

For LSR and SBR, the slope of $c_p(T)$ before and after the crosslinking event is the same. This indicates that both states probably present similar, if not the same, segment mobility. Indeed, our group studied [25] the variation of T_g and free volume for a poly(dimethylsiloxane) rubber after curing and it was found that curing does not affect neither the free volume and, thus, nor the T_g . The same is very likely occurring here: c_p is only a function of temperature, not of the curing conversion. Another hypothesis to explain such behaviour is the fact that both compounds are highly filled. In this scenario, the filler properties strongly influence the compound's thermal properties, regardless of the curing state.

For both materials (silica-filled LSR and filled SBR), the standard sapphire method and the MDSC approach resulted in comparable values for c_p when the intrinsic differences among the measurements are taken into account. Even though the MDSC method represents what is truly happening in terms of segment motion within a certain temperature range, without kinetic artifacts, the sapphire method incorporates information concerning heat release/absorption as c_p change, which would have to be additionally loaded for the MDSC approach in terms of enthalpy and the rate of heat release, which can be assumed as the relationship presented in Equation 8.3 [126], where α is the curing conversion. To better evaluate the impact of one or the other approach in simulation results, these are studied in Chapter 12.

$$\dot{Q} = Q_{total} \left(\frac{d\alpha}{dt} \right) \quad (8.3)$$

Furthermore, it is important to note that Equations 8.1 and 8.2 can be easily incorporated into simulation software as models for the c_p , requiring only the molar specific heat capacity at 298 K. It was demonstrated here that for a medium molecular weight polymer (LSR) and for a high molecular weight rubber (solid SBR) the equations are able to characterize c_p , becoming interesting for further optimization of injection moulding simulation routines.

8.2 THERMAL CONDUCTIVITY λ

Thermal conductivity was determined for part A, part B, 1:1 A:B mixture in the non-cured state, and 1:1 A:B mixture in the cured state, aiming to check possible differences between these components. Values (average) for λ are shown in Figure 8.5 for all components. It is valuable to remind at this point that the samples 2070 component A, 2070 component B, and the 1:1 mixture A:B uncured were tested employing the transient line source method, since it allows the thermal conductivity determination of liquids. Sample 1:1 mixture A:B cured, on the other hand, had its thermal conductivity measured via guarded heat flow meter device under steady conditions for the temperature. The measurement temperature range for the 1:1 mixture A:B uncured was limited to 80°C to avoid the curing reaction. For all samples, the thermal conductivity did not considerably vary with temperature, being statistically the same for the whole tested temperature range and varying around the value $\lambda = 0.2 \text{ W}\cdot\text{m}^{-1}\cdot\text{K}^{-1}$, which is typical [105, 106, 127, 128] for LSRs.

The variation of polymers' thermal conductivity with temperature depends basically on the polymer morphology and its glass transition and melting/crystallization temperatures. Van Krevelen [129] proposed that the thermal conductivity of amorphous polymers at $T > T_g$ can be estimated based on the thermal conductivity at the glass transition temperature:

$$\lambda(T) = \lambda(T_g) \cdot \left(1.2 - 0.2 \cdot \frac{T}{T_g}\right) \quad (8.4)$$

This equation shows that the variation of thermal conductivity above the glass transition is low, slowly decreasing with the temperature increase. However, van Krevelen proposed this equation considering amorphous polymers in general, being roughly an estimate about the thermal conductivity. Zhong and co-workers [130] compared van Krevelen's assumption with λ data for poly(ethylene) and poly(propylene) and observed a flatter change of thermal conductivity with temperature. For cis-1,4-poly(isoprene) (natural rubber, NR), the relationship proposed in Equation 8.4 is reasonable, as demonstrated by Eiermann and Hellwege [131]. Above 50°C, however, the authors

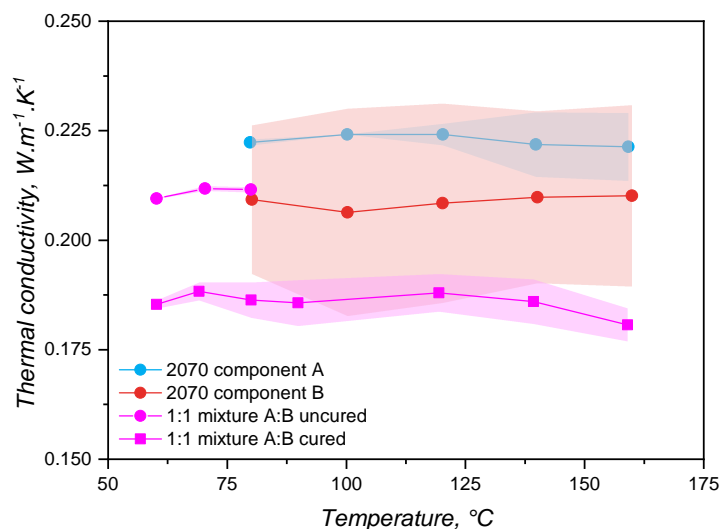


Figure 8.5: Thermal conductivity variation with temperature for the individual A and B components, as well as for the uncured and cured mixtures. The components and the uncured mixed were analysed via a transient method, while the cured mixture was investigated employing a steady-state method. The symbols indicate the average of 3 measurements and the shaded areas represent the standard deviation.

reported a plateau for the thermal conductivity. Kerschbaumer and co-workers [107] also reported a plateau for $\lambda(T)$ when studying rubber compounds based on cis-1,4-poly(isoprene) (NR), poly(styrene-co-butadiene) (SBR), poly(acrylonitrile-co-butadiene) (NBR), hydrogenated NBR, and ethylene propylene diene monomer rubber (EPDM), all of them highly filled with either carbon black, white fillers, or a combination of both. Based on a molecular dynamics simulation, Xu and co-workers [132] determined $\lambda(T)$ for a poly(siloxane) (relative molecular mass = 28000 g.mol⁻¹) and also reported a plateau between -73°C and 226°C. The authors argue that the thermal conductivity is the same because the phonon density of states does not change with temperature (see Figure 8 from [132]), meaning that the temperature does not affect the states available for the phonons to occupy. Based on the reported findings, the results presented in Figure 8.5 for an independence of λ with temperature are reasonable. Poly(siloxane) macromolecules at the studied temperature range are far above their glass transition and melting temperatures and do not experience any thermal transition or chemical change. Thus, it is fair to assume that, as previously reported, neither the phonon density of states (dependent on the backbone atoms, silicon and oxygen) change and, thus, nor the thermal conductivity. Furthermore, since the liquid silicone rubber grades are highly filled with silica, it is also fair to consider that the filler controls phonon transmission in these samples, as described

in Chapter 6 and in accordance with what has been reported in the aforementioned literature.

Between the individual components A and B, no significant difference was detected, indicating that these two parts have similar thermal conductivities. The fact that part B has a higher deviation may be connected to the presence of the crosslinker, which is a poly(siloxane) oligomer with lower molecular weight when compared to the main poly(siloxane) base polymer. The uncured mixture shows a tendency for presenting a similar λ when compared to its single constituents. The cured sample, on the contrary, presented a lower thermal conductivity than the uncured mixture, and an inclination to lower λ than the individual parts. This finding is contrary to that was observed by Cheheb and co-workers [133], that identified a 10% increase in the thermal conductivity for crosslinked rubber compounds when compared to the uncured counterpart. For the present scenario, considering that the samples' thermal conductivity is dominated by the filler thermal properties, and that curing of LSR connects two adjacent macromolecules via a linkage that is oligomeric (the size of the Si-H based crosslinker), a decrease of λ does not seem reasonable. Thus, this apparent decrease in thermal conductivity after crosslinking may be associated to the different measurement method employed between the cured and the uncured samples. In order to clarify this aspect, the averages ($\bar{\lambda}$) for the whole temperature range are shown in Table 8.1, where it is also stated the standard deviation ($\sigma(\lambda)$) and the error associated to each measurement according to Kerschbaumer and co-workers [107]. Furthermore, since the transient line source method requires the filling of a cylinder with liquid sample to perform the analysis of λ , any air bubbles would cause an increase of the sample's thermal conductivity, probably leading to the higher values observed for the uncured samples.

Table 8.1: Thermal conductivity averages $\bar{\lambda}$ for the whole studied temperature range and respective standard deviations $\sigma(\lambda)$, including the associated measurement error.

Sample	$\bar{\lambda}$	$\sigma(\lambda)$	Error
2070 A	0.223	0.001	7%
2070 B	0.209	0.001	7%
A+B uncured	0.211	5.0	7%
A+B cured	0.186	0.002	5%

For simulation, the values reported in Figure 8.5 have practical consequences in terms of how the thermal conductivity data can be input into the routine. The first outcome is that the individual components (either A or B) can be analysed in order to gather thermal conductivity data for the simulation, with the advantage to cover a lar-

ger temperature range without crosslinking. Following this outcome, a completely cured sample could also be employed to measure the thermal conductivity of an LSR grade to be further injection moulded, however demanding a previous sample preparation. Lastly, if required either by the simulation software or to save computational time, the thermal conductivity can be reliably considered as constant within typical liquid silicone rubber injection moulding temperatures.

8.3 SPECIFIC VOLUME OR PVT BEHAVIOUR

The variation of specific volume with temperature and pressure is peculiarly important for liquid silicone rubber, due to the fact that it experiences considerable thermal expansion during processing. [48] For the studied LSR grade, the specific volume under various isobaric conditions as a function of the temperature is presented in Figure 8.6, being consistent with the scarce values reported in the literature [53]. As it was expected, for all pressures, the specific volume increases with temperature. This expansion is driven by the vibrational motion of poly(siloxane) macromolecules, which gain more energy as temperature increases and, therefore, occupy more volume due to increased vibration. Under isothermal conditions, though, the effect of pressure is on decreasing the specific volume and, in this case, it is the packing volume (empty space between the macromolecules) that is reduced. During injection moulding, liquid silicone rubber undergoes slight compression during injection (A-B segment in Figure 8.6) and heating mostly due to shear related dissipation. Injection is over at point B, when the pressure is equalized and the cavity is completely filled. Heat transfer from the hot mould to the uncured LSR occurs, leading to heating and thermal expansion in step B-C. Due to the fact that filling is normally carried out subvolumetrically, LSR is further heated under isochoric pressure to point D. The cavity conditions are held until the part is fully cured, being ejected to point E and further cooled down back to point A.

By combining the effect of pressure and temperature, one can realize that thermal expansion is hindered by the pressure increase, as the slope of the plotted lines in Figure 8.6 get flatter as pressure rises. The slopes were determined via linear fitting and plotted over the applied pressure in Figure 8.7. Volume change decreases almost linearly with the pressure, showing that vibrational mobility triggered by temperature increase is hindered by the reduced empty space between macromolecules.

From the data presented in Figure 8.6, the Tait model (Equation 6.5) coefficients were determined based on a least squares method and shown below. The coefficients b_{1m} and b_{2m} represent the dependence of the specific volume at zero pressure on pressure and temperature;

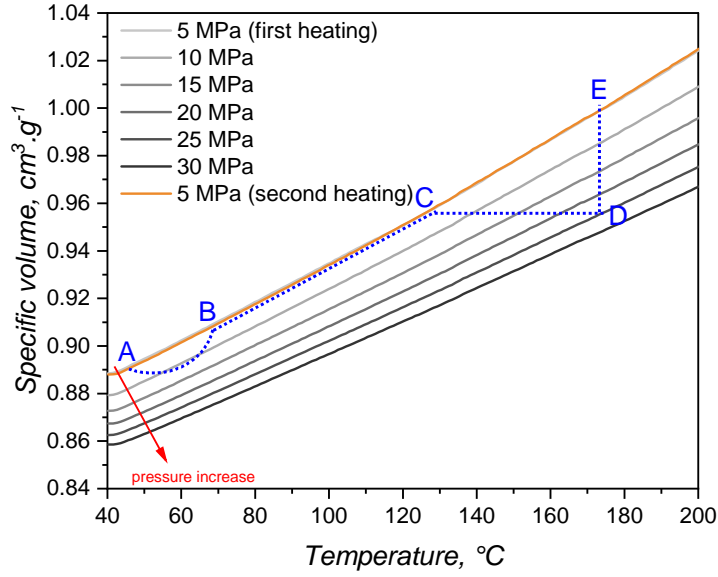


Figure 8.6: Variation of the specific volume (one measurement) as a function of pressure and temperature. The orange line represents the second measurement at 5 MPa at which the sample is fully cross-linked, and is on top of the light gray line representing the 5 MPa isobar. The dotted blue line represents a hypothetical injection moulding cycle, being the phases: A-B injection; B-C expansion; C-D compression; D-E demoulding; and E-A: cooling.

b_{3m} corresponds to the pressure dependency of parameter $B(T)$, and b_{4m} adds the temperature correlation. [112]

$$\begin{cases} b_{1m} = 6.091 \times 10^{-4} \text{ m}^3 \cdot \text{kg}^{-1} \\ b_{2m} = 9.025 \times 10^{-7} \text{ m}^3 \cdot \text{kg}^{-1} \\ b_{3m} = 1.278 \times 10^8 \text{ Pa} \\ b_{4m} = 3.367 \times 10^{-3} \text{ K}^{-1} \end{cases} \quad (8.5)$$

These parameters will be further utilized as input data for the simulation trials carried out in Chapter 12.

8.4 CONCLUSIONS OF THE CHAPTER

In this Chapter, the thermal properties necessary for injection moulding simulation of liquid silicone rubber were comprehensively explored. The study of specific heat capacity, thermal conductivity, and specific volume variation with pressure and temperature was based on not only comparing different methodologies, but also assessing the impact of the LSR curing state in those properties.

The specific heat capacity was successfully measured via the standardized sapphire method and employing the modulated temperature

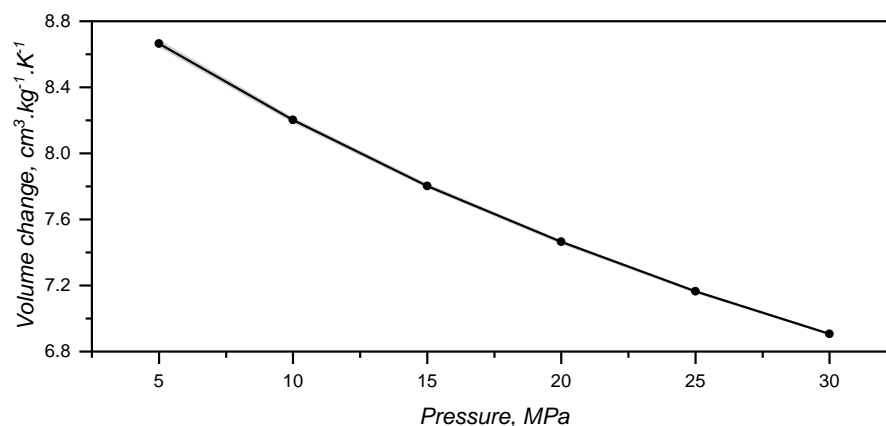


Figure 8.7: Rate of volume change due to temperature ($\text{cm}^3 \cdot \text{kg}^{-1} \cdot \text{K}^{-1}$) for each tested pressure. The shaded area around the plot represents the error connected to the linear fitting of the data in Figure 8.6. The coefficients of determination for such linear fittings are higher than 0.999.

approach. It was demonstrated that the specific heat capacity is dependent only on the temperature, and not on the curing state of the samples. In this sense, for simulation purposes, the modulated temperature approach is able to measure the *true* specific heat capacity, demanding the incorporation of information concerning the curing enthalpy to describe the conservation of energy. On the other hand, the sapphire method allowed to combine enthalpic information into the specific heat capacity data, reflecting the exothermal nature of the curing reaction. It is still necessary to check whether there is a difference in terms of simulation output when one or the other method is applied.

The investigation into thermal conductivity provided essential data for both the uncured and cured states of LSR. It was observed that the thermal conductivity remains relatively stable across the temperature range, aligning with previous findings in the literature. This stability simplifies the integration of thermal conductivity data into simulation routines, allowing for the assumption of a constant value without significant loss of accuracy. Such an assumption is advantageous in reducing computational complexity and time, ensuring efficient and effective simulation processes. Moreover, understanding the minor variations between individual components and their mixtures aids in planning the material data characterization prior to the simulations.

The analysis of specific volume converged to the behaviour reported in the literature and to the expected characteristics based on macromolecular arguments. The coefficients of the Tait model were determined and accurately described the LSR thermal expansion, which is a critical property during injection moulding, since it establishes the most proper filling conditions to avoid processing issues, such as flashing.

Part IV

CROSSLINKING KINETICS

THEORETICAL BACKGROUND

Silicone rubber, and most industrial rubber compounds, despite their medium-to-high molecular weights, must be crosslinked to be employed in engineering applications. The crosslinking reaction turns the soluble and highly viscous silicone rubber into an insoluble and viscoelastic network, following a specific crosslinking mechanism, kinetics, and thermodynamics. Industrially-applied elastomers, such as silicone rubber, are crosslinked by the use of specific chemicals (here denoted as crosslinkers), which are triggered by temperature and in some cases aided by a catalyst, starting the curing reaction. This Chapter is dedicated to assess the crosslinking reaction within the injection moulding context, addressing its possible mechanisms and how it is characterized to be correctly defined in injection moulding simulation routines.

Note: The content of this chapter is partially discussed in the peer-reviewed article 3 (Azevedo et al. 2022, Polymers 14(20) pp.4404).

9.1 CROSSLINKING REACTION IN INJECTION MOULDING

As explained in Chapter 1, the curing reaction is the main feature that distinguishes reactive (rubber, poly(urethane)s, etc.) injection moulding from conventional thermoplastics injection moulding. However, both share one aspect: the solidification phase is the longest step within the injection moulding cycle. For thermoplastics IM, the time taken to solidify the molten polymer until it is mechanically stable to be demoulded is mainly governed by the mould temperature: the colder the mold, the faster the polymer solidifies. For semi-crystalline polymers, the speed of cooling dictates the crystallinity and, therefore, the part's properties. Similarly for LSR, the time necessary to crosslink the A:B mixture is governed by the mould's temperature: the hotter the mould, the faster the curing proceeds. The curing speed, in this sense, is more critical for sulphur-based crosslinking systems (not employed for LSR, but for unsaturated hydrocarbonic rubbers, as the poly(styrene-co-butadiene) studied in Part iii), since these create sulphur bridges with a length distribution that is sensitive to temperature. However, for liquid silicone rubber and poly(siloxane)s in general, the effect of mould temperature is mainly connected to the curing speed, and not to the network's morphology. This is due to the fact that, as it is detailed further in this chapter, the crosslink points are generally either a C–C covalent bond, or composed of a telechelic oligomeric crosslinker.

In this context, to control the injection moulding cycle, one has to precisely understand the kinetics of crosslinking, since these rules

govern the curing reaction and, therefore, most of the cycle time. Therefore, setting the most appropriate curing time not only leads to injected parts with optimum properties, but also saves energy by taking just the necessary amount of time to fully solidify the part to be demoulded, having additionally and economical advantage. For rubber materials, the crosslinking reaction and its duration set the part properties, being a crucial step in the injection moulding cycle.

Similarly to the the flow behaviour described in Chapters 3 and 5 and the thermal properties presented in Chapters 6 and 7, the curing aspects are also implemented in injection moulding simulation routines with the aim to cover the solidification process. Since crosslinking is a chemical process that influences both the flow behaviour and the thermal properties, its peculiarities have to be considered in all aspects of material data determination for simulation. Taking into account the constitutive equations [134] that govern the injection moulding process and are used to simulate it, the curing aspects are highlighted (in bold) as follows.

For the mass conservation equation represented by Equation 9.1, the curing reaction is connected to the density ρ , since crosslinking connects adjacent macromolecules, modifying their occupied volume.

$$\frac{\partial}{\partial t}\rho + \nabla \cdot (\rho \vec{v}) = 0 \quad (9.1)$$

For the momentum conservation equation represented by Equation 9.2, crosslinking not only affects the density ρ , but mainly the viscosity η due to the increase in molecular weight and higher resistance to flow for the same shear profile.

$$\rho \frac{\partial}{\partial t} \vec{v} = \rho \vec{g} - \nabla p + 2\nabla \cdot \eta \vec{D} - \rho \vec{v} \cdot \nabla \vec{v} \quad (9.2)$$

Finally, for the energy conservation equation stated in Equation 9.3, curing can modify the thermal properties c_p and λ , affect the flow behaviour η , and it is responsible for the term \dot{Q} . The energy term \dot{Q} corresponds to a heat source and it is connected to the exothermal curing enthalpy. In these equations, t is time, \vec{v} is velocity vector, \vec{g} is the total body force per unit mass, p is pressure, \vec{D} is the deformation tensor, T is temperature, β is coefficient of volume expansion, and $\dot{\gamma}$ is shear rate.

$$\rho c_p \left(\frac{\partial T}{\partial t} + \vec{v} \cdot \nabla T \right) = \beta T \left(\frac{\partial p}{\partial t} + \vec{v} \cdot \nabla p \right) + \eta \dot{\gamma}^2 + \lambda \nabla^2 T + \dot{Q} \quad (9.3)$$

It becomes then evident that the curing reaction is a key aspect for rubber injection moulding and its virtual analogous, as phase transition for semi-crystalline polymers is crucial in thermoplastics injection

moulding. For these reasons, this Chapter is dedicated to detail the curing behaviour of poly(siloxane)s in terms of its mechanisms and approaches to characterization.

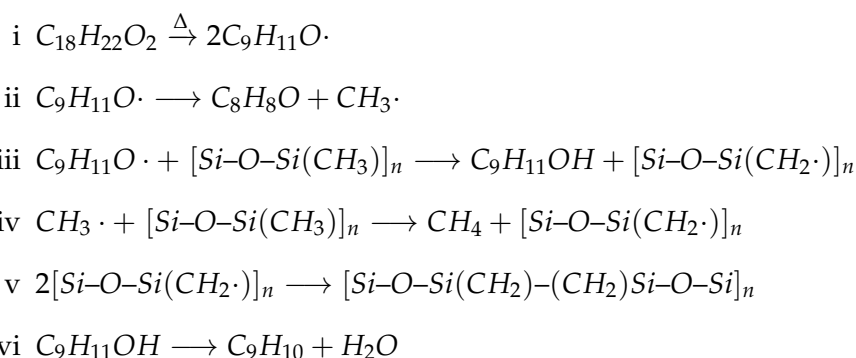
9.2 CURING MECHANISMS OF POLY(SILOXANE)S

Depending on the polymer chemistry, poly(siloxane) macromolecules can be crosslinked via different routes. In this Chapter, two of these routes will be detailed: the radical-based peroxide curing and the catalyst-assisted hydrosilylation crosslinking (addition of Si-H to C=C). The mechanisms and the main features of these routes are given, aiming to support mainly the findings of Chapter 10, but also to serve as basis for whenever the curing of poly(siloxane) is stressed in this work.

9.2.1 Peroxide-based crosslinking

Crosslinks formation between two adjacent silicone macromolecules, as in poly(dimethyl siloxane) (PDMS), when aided by an organic peroxide, is based on the generation of radicals by the peroxide decomposition reaction. The interaction between peroxide radicals and PDMS macromolecules can occur via hydrogen abstraction from a methyl and/or vinyl groups or via addition to the double bond on the vinyl group, if this is present along the chain. If the energies of the resulting radicals are compared and considering that hydrogen abstraction is more favourable if the radical energy is lowered, hydrogen abstraction from the vinyl group is unfavourable, due to the similar energy of alkoxy and vinylic radicals [135].

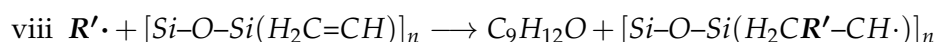
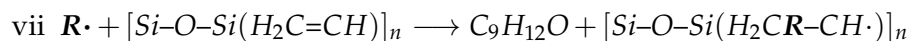
When dicumylperoxide is concerned, the main chemical reactions involved during PDMS crosslinking via hydrogen abstraction from methyl side groups are:



Radical generation is accomplished at reactions i and ii via thermal decomposition of dicumylperoxide and beta scission of the cumyloxy radical, generated in the reaction i, respectively. There are two radicals responsible for silicone crosslinking: the cumyloxy and the methyl

radicals, which are able to abstract a proton from the methyl side group of PDMS (reactions iii and iv), creating two macromolecular radicals. It was shown by Baquey *et al.* [136] that the main responsible for PDMS proton abstraction is the radical directly formed after peroxide decomposition, which in the present case is the cumyloxy. However, the methyl radical is also considered in this study as able to abstract protons from the silicone polymer chain. Finally, the macromolecular radicals, when adjacent to each other, can react with one another, creating a covalent bond between the carbon atoms from the methyl side groups (reaction v).

For the case where double bond addition occurs, the cumyloxy (denoted as R) and the methyl (denoted as R') radicals can add to the less-substituted secondary carbon (due to its higher stability as intermediate radical) of the vinyl group, as shown in reactions vii and viii, leading to the formation of macromolecular radicals. Similar to what occurs in the hydrogen abstraction case, adjacent macromolecular radicals are able to react with each other by recombination, creating a crosslink point (reaction ix), or the macromolecular radical can continue adding to another adjacent vinyl group. It is worth mentioning that additional reactions result in products with fragments from the peroxide initiator, i.e., the fragment R or R' is attached to the polymer chain.



When vinyl moieties are present in the PDMS backbone, hydrogen abstraction and vinyl addition happen simultaneously, even though, considering alkoxy (from dicumylperoxide) and methyl radicals (both $105 \text{ kcal}\cdot\text{mol}^{-1}$), the formation of secondary $R_2CH\cdot$ radicals is more favourable than primary $RCH_2\cdot$ radicals (97 against $100 \text{ kcal}\cdot\text{mol}^{-1}$, respectively) [135], due to the alkyl substitution stability effect. However, vinyl addition extension is limited to the vinyl concentration on the PDMS chain, while hydrogen abstraction has virtually no concentration limitation in terms of methyl presence; it is only limited due to steric hindrance and/or thermodynamical reasons.

Concurrently to dicumylperoxide-mediated crosslink formation in PDMS, by-products are formed due to hydrogen abstraction or decomposition of radicals. In reaction iii, cumyl alcohol $C_9H_{11}OH$ is formed after hydrogen abstraction by the cumyloxy radical, and further dehydrated and converted into α -methylstyrene (reaction vi). In reaction ii, acetophenone C_8H_8O is the by-product of cumyloxy beta scission. All these by-products do not contribute to the network formation, but are treated and understood as low molecular weight and volatile compounds that may migrate, causing mainly the very characteristic

odour of peroxide-crosslinked silicone products. Cumene may also be formed after reduction of α -methylstyrene. [137]

The crosslinking kinetic model employed in this Thesis accounts for the overall crosslink formation. This model is not able to differentiate between abstraction or addition reactions due to its phenomenological approach [138], but clarifies the rate of crosslink formation. A complete description of the complex set of reactions that underline peroxide crosslinking of PDMS can be performed considering mechanistic approaches, like population balance equations, which is not the main focus of the present study, where a phenomenological kinetic model was proven to be sufficient.

9.2.2 Platinum-catalysed curing

Differently from the peroxide-based curing of high consistency silicone rubbers, the curing of liquid silicone rubber is mostly carried out employing an organic metal complex that aids the addition of the crosslinker molecules (Si-H) to the poly(siloxane) oligomers (vinyl end blocked). What these two curing mechanism have in common is the dependence on temperature to occur within reasonable industrial processing conditions, for example, acceptable cycle time for injection moulding. Curing of LSR is based on the hydrosilylation reaction, which is the β -addition of Si-H to olefines and alkynes, for example. [139] This reaction is catalyzed by homogeneous noble metal catalysts, such as the organometallic compounds based on rhodium, iridium, and ruthenium, but the majority of reaction carried out in industrial scale for silicone applications employ a platinum-based organic complex. [140, 141] The mechanism behind this addition is depicted in Figure 9.1 and is referred as the Chalk-Harrod mechanism. [142]

The hydrosilylation according to this mechanism is based on 3 steps according to Lukin *et al.* [143]:

- i Oxidative addition of Si-H (crosslinker) bonds to the platinum atom of the catalyst
- ii Migratory insertion of the coordinated alkene (vinyl terminated poly(siloxane) oligomer) to the Pt-H bond
- iii Reductive elimination with the formation of Si-C bonds

The literature [141, 144] reports an alternative to this mechanism, the *modified* Chalk-Harrod mechanism, which consists of step i, but argues that the alkene is inserted into the Pt-Si bond (instead of the Pt-H one), and that finally the last step is C-H reductive elimination (not Si-C elimination). Regardless of which mechanism is the predominant, this reaction has no elimination of other compounds other than the one containing the Si-C bond. This fact leads to high atomic efficiency and,

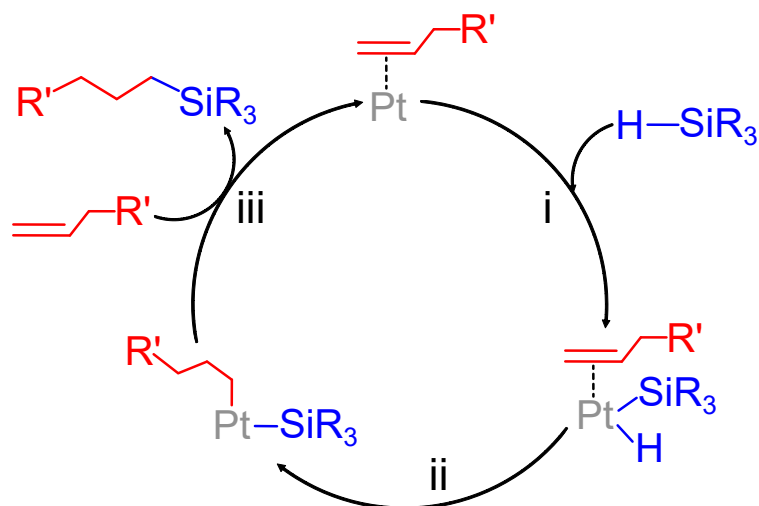


Figure 9.1: Chalk-Harrod mechanism of hydrosilylation reaction. The red elements represent the LSR oligomers (vinyl terminated), while the blue elements illustrate the Si-H-based crosslinker. (adapted from [143].

for processing purposes, it has the advantage of very low shrinkage, since no by-products are synthesized during curing.

For silicone chemistry, the most employed Pt-based catalyst is the Karstedt's catalyst [145], shown in Figure 9.2. This catalyst is based on Pt⁰ and 1,3-divinyl-1,1,3,3-tetramethyldisiloxane (dvtms) ligands, with the general formula [Pt_x(dvtms)_y]. The dominating species however is the [Pt₂(dvtms)₃] complex [143], as depicted in Figure 9.2. During curing, the catalyst is able to coordinate to the poly(siloxane) vinyl moieties, easing the addition of Si-H bond.

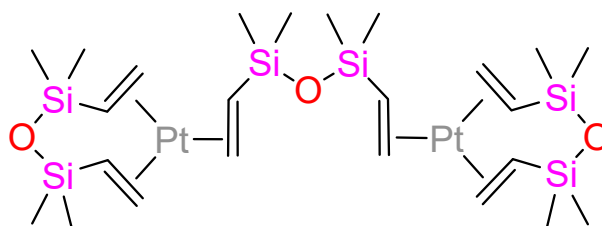


Figure 9.2: Karstedt's catalyst (adapted from [141]).

Aiming to control the catalytic activity and the hydrosilylation reaction to obtain safer processes and longer shelf life, inhibitors are added to the LSR formulation. These compounds interact with and block the Karstedt's catalyst, forming inert complexes of platinum (0) (Pt⁰), until the curing onset temperature is reached, triggering the β -addition following the Chalk-Harrod mechanism. Several chemicals can be used to serve such purpose, e.g., esters, alcohols, ketones, sulfoxides, phosphines, phosphites, nitrogen containing derivatives, hydroperoxides, and acetylenic derivatives. [146] Along with β -alkynols [147],

maleates and fumarates are widely employed as inhibitors for LSR. Their mechanism involves the complexation of Pt to the maleate/fumarate double bond, stabilizing the complex and inhibiting curing. [148]

9.3 CURING KINETICS DETERMINATION

Since the chemical reactions presented in the previous sections occur during injection moulding of solid and liquid silicone rubbers, the associated kinetics has to be accurately determined to be implemented in processing simulation. In order to be able to follow the curing reaction, a measurable property derived from the crosslinking process has to be detected, in a sense that the chemical reaction is detected indirectly. Due to the fact that chemical reactions involve scission and creation of new bonds, spectroscopy techniques are widely employed [149–153] to study the curing kinetics of polymers, including silicones. Zhai and co-workers [151] employed Fourier transform near infrared spectroscopy (FT-NIR) and attenuated total reflectance Fourier spectroscopy (ATR-FTIR) to follow the amount of Si–H content in poly(siloxane) oils. For this study, the authors followed mainly the Si–H stretching vibration ranging from 2302 to 2040 cm^{-1} in ATR-FTIR, with high coefficient of determination for cross-validation and coefficient of determination for external validation. This study would easily allow the determination of curing conversion $\alpha(t)$ as proportional to the consumption of Si–H bonds:

$$\alpha(t) = 1 - \frac{\int I(t)}{\int I(t_i)} \quad (9.4)$$

where $\int I(t)$ is the area of the peak associated to the IR absorption of the monitored chemical bond at time t , and $\int I(t_i)$ is the initial area. For curing kinetics studies employing spectroscopic techniques, it is important to consider the normalization of the studied peak employing a signal that does not change with the curing reaction, i.e., related to a bond that is not broken. Besides, using the area of the peak is the most reliable way to calculate α , however the use of the intensity (height) is also common.

Even though the chemical information is directly detected from the infrared spectra, information concerning the exothermal nature of the hydrosilylation would not be determined, as required for the term \dot{Q} in Equation 9.3. Besides, spectrometers (specially in the near range of infrared or nuclear magnetic resonance ones) are not widely spread in the industry or technological centers, being almost exclusively employed to conduct research and development in terms of, for example, polymer modification.

By far, calorimetric and rheological methods are the most utilized approaches when the curing kinetics of polymers has to be determined.

When compared to spectroscopic methods, these ones detect the curing indirectly, i.e., they measure a signal that is created due to the chemical reaction. Calorimetry-based methods rely on the use of differential scanning calorimetry (DSC) to measure the heat released by the curing reaction. One can easily understand why the measurement of heat is proportional to the curing conversion α when the definition of enthalpy at constant pressure is introduced for a chemical reaction with reactants (vinyl-terminated and Si-H bearing poly(siloxane)s) and a product (crosslinked network):

$$\Delta H = H_{products} - H_{reactants} = \Delta U + P\Delta V = q_p \quad (9.5)$$

Due to the fact that bonds are being created (crosslink points) during curing, ΔH is negative and the reaction releases energy as heat (q_p). The heat that is released is detected during DSC runs when an LSR sample (part A:part B mixture) is heated to at least the hydrosilylation onset temperature. On this bases, the conversion $\alpha(t)$ is calculated based on the area of the exothermal peak that appears in the DSC thermogram:

$$\alpha(t) = \frac{\int_{t_i}^t q dt}{\int_{t_i}^{t_f} q dt} \quad (9.6)$$

where $\int_{t_i}^t q dt$ is the area of the peak at time t and $\int_{t_i}^{t_f} q dt$ is the total peak area. The heat can be measured under either isothermal or dynamic (non-isothermal) conditions. A practical limitation of the isothermal method is the fast curing of LSR, that normally occurs while placing the sample inside the DSC oven. One strategy to overcome this problem is to introduce the sample at room temperature, start data collection, and then heat the oven to the isothermal temperature. However, one must then account for this heating step when conduction kinetic calculations. The main advantage of the calorimetric method is that the curing enthalpy is measured concomitantly to the curing kinetics, however no information about flowability is obtained. Flowability in this sense refers to the ability to move the liquid silicone rubber after it starts to crosslink, normally associated in practical terms to the process safety, i.e., the time required to fill the mould during injection moulding without pre-curing (or *Scorch*). To study the dependence of resistance to flow to the curing conversion, rheology-based techniques have to be employed.

While the calorimetry-based approach detects the heat released due to curing, rheology-based ones rely on measuring the resistance to flow derived from the molecular weight increase that results from crosslinking adjacent poly(siloxane) macromolecules. As the molecules are connected, the ability to slide over each other when shear stress is

imposed is limited, leading to an increase in viscosity. Furthermore, in the perspective of viscoelastic properties, crosslinking leads to an increase of the elastic contribution, normally determined as G' under shear, which is derived from the raw torque measurements from the rheometer. Thus, to determine the curing conversion $\alpha(t)$ under this scenario:

$$\alpha(t) = \frac{G(t) - G(t_i)}{G(t \rightarrow t_f) - G(t_i)} \quad (9.7)$$

where $G(t)$ is the shear modulus at a certain time t during curing, $G(t_i)$ is the initial shear modulus (before curing onset), and $G(t \rightarrow t_f)$ is the final shear modulus (after curing is completed or $\alpha = 1$). The correction to account for the initial shear modulus is employed to effectively account for the shear modulus increase. Similarly to the calorimetric approach, the rheological method can be conducted under isothermal conditions or by employing a defined heating rate. Concerning the shear, the usual procedure is to apply an oscillating shear to the sample to follow G' or the transmitted torque M , which is the measurable signal from the rheometer. The advantage of rheology-based techniques to characterize curing kinetics is the existence of industry-oriented rheometers, as the rubber process analyser (RPA), which is able to impose a defined shear to a sample inside a temperature-controlled chamber. On the other hand, the information concerning \dot{Q} cannot be obtained.

EXPERIMENTAL DESCRIPTION

This Chapter describes the materials and the methods employed to study the crosslinking kinetics of silicones. Curing kinetics studies were conducted first with a high consistency silicone rubber aiming to gather knowledge about the most proper approaches to investigate crosslinking kinetics. Next, liquid silicone rubber was studied applying all know-how built in the preliminary phase with high consistency silicone. The main objective of this part is to study two approaches that are currently employed to characterize the curing kinetics of rubbers aiming injection moulding simulation: calorimetry and rheology.

Note: The content of this chapter is partially discussed in the peer-reviewed article 3 (Azevedo et al. 2022, Polymers 14(20) pp.4404).

10.1 PRELIMINARY INVESTIGATIONS WITH HIGH CONSISTENCY SILICONE

Since most rubber testing standards and methodologies are designed for solid rubber (high molecular weight), these were initially investigated with a high consistency silicone grade. All materials, equipment, methodologies, and mathematical formalism are detailed next.

10.1.1 *Materials*

High consistency poly(dimethyl siloxane), or solid PDMS (Xiameter™ RBB-2100-50, $M_w = 660 \text{ kg}\cdot\text{mol}^{-1}$, $M_w/M_n = 1.8$), containing approximately 26 wt% (moderate to high content) of an inorganic filler and no significant concentration of vinyl side groups (as confirmed by $^1\text{H-NMR}$ studies) was supplied by Dow Inc. (USA). The PDMS characterization in terms of molecular weight, vinyl, and filler contents is described in the Appendix (A.1, A.2, and A.3, respectively). Dicumylperoxide (DCP) 99.9% (Peroxan DC) was supplied by Pergan GmbH (Germany), with active oxygen content of 5.91 wt%. Both components were thoroughly mixed in a 2-roll-mill varying the peroxide concentration: 0, 0.21, 0.35, 0.49, 0.70, 1.00, and 1.50 phr (parts per hundred rubber) of DCP. These concentrations represent fractions of the suggested peroxide concentration (0.70 phr) by the silicone supplier, i.e., 0, 30, 50, 75, 100, 140, and 215%, respectively. The samples up to 0.70 phr were prepared at the same time, employing the same PDMS and DCP batches, while the samples with higher dicumylperoxide concentrations were produced afterwards. Differences between these two groups may arise due to batch variations, such as molecular weight distribution, or M_w . These variations are assigned whenever they are present, but these do not compromise the comparability

between the studied samples. All silicone compounds were stored at low temperatures (5°C) prior to testing, in order to avoid pre-curing.

10.1.2 Isothermal rotational rheometry

Rubber process analyser (D-RPA 3000 Montech Werkstoffprüfmaschinen GmbH, Germany) equipment, or moving die rheometer (MDR), was employed as a rotational oscillatory rheometer to characterize the curing behaviour of the PDMS/DCP compounds at different temperatures: 140°C, 150°C, 160°C, 170°C, and 180°C for 1 h. The rotational deformation was set to 0.5° at a constant frequency of 1.667 Hz, according to the standard the ISO 6502-1 [154]. Processing-related parameters were calculated from the torque vs. time curves: minimum torque (ML), maximum torque (MH , as the torque value at $t = 1$ h, since no reversion or marching modulus was observed), scorch time (t_{s1}), and optimum cure time (t_{90}). The scorch time was defined as the time correspondent to increase ML by 1 dN.m (torque unit), and the optimum cure time as the time correspondent to 90% of MH . All experiments were performed in triplicate for each sample (7 dicumylperoxide concentrations and 5 temperatures).

To describe the effect of temperature and dicumylperoxide concentration on the optimum cure time, fitting of the data was performed using the Levenberg–Marquardt algorithm [155] or damped least squares method. A general equation to define t_{90} was proposed, into which the experimental data was fitted:

$$t_{90} = A_0 \exp\left(\frac{E_a}{RT}\right) (DCP)^\beta \quad (10.1)$$

In Equation 10.1, the optimum cure time is described as a function of two factors. To the temperature was assigned an Arrhenius relation, since time and temperature were under study. The influence of dicumylperoxide concentration, on the other hand, was described by a power law with order β .

For the crosslinking kinetics study, only the data related to the curing temperature of 160°C was used, since this is the common and the manufacturer-advised curing temperature for the silicone rubber under investigation. However, the usual *modus operandi* is to fit the data related to several thermal programs, those being either different temperatures or different heating rates. Three ASTM standards currently describe how to estimate kinetic parameters utilizing thermal analysis: ASTM E2041-13 (Standard test method for estimating kinetic parameters by differential scanning calorimeter using the Borchardt and Daniels method) [156], ASTM E698-18 (Standard test method for kinetic parameters for thermally unstable materials using differential scanning calorimetry and the Flynn/Wall/Ozawa Method) [157], and

ASTM E2781-11 (Standard practice for evaluation of methods for determination of kinetic parameters by thermal analysis) [158]. Along with these standards, the publications by Vyazovkin and co-workers [159–163] give important information related to determining the kinetics of several phenomena, such as crystallization, glass transition, and crosslinking.

For this approach, the crosslink conversion rate $d\alpha/dt$ was calculated considering the difference between the torque before and after the curing reaction and the actual torque at a certain time t . Specifically for RPA, the torque before curing is defined as the minimum torque (ML) and the torque after curing as the maximum torque (MH), being their difference expressed as $\Delta M = MH - ML$. Using Equation 10.2, the conversion rate at a given point in time can be calculated based on the following mathematical relation:

$$\frac{d\alpha}{dt} = \frac{1}{\Delta M} \frac{d(M - ML)}{dt} \quad (10.2)$$

10.1.3 Determination of the activation energy

Considering that crosslink formation is a temperature-induced process, the conversion rate can be represented as a function of temperature $k(T)$, and as a function of the appropriate kinetic model $f(\alpha)$, as reviewed by Vyazovkin [160]:

$$\frac{d\alpha}{dt} = k(T)f(\alpha) \quad (10.3)$$

It is well-known and reported that $k(T)$ is an Arrhenius-like rate constant, i.e., it is a correlation between temperature T (K), a pre-exponential factor A (time^{-1}), an activation energy E ($\text{J}\cdot\text{mol}^{-1}$), and the molar gas constant R ($8.3145 \text{ J}\cdot\text{mol}^{-1}\cdot\text{K}^{-1}$) as follows:

$$k(T) = A \cdot \exp\left(\frac{E}{R \cdot T}\right) \quad (10.4)$$

Substituting Equation 10.4 into Equation 10.3, and taking the logarithm followed by differentiation against $\frac{1}{T}$ gives rise to the equation that defines the isoconversional principle: considering two samples, if the curing rates $d\alpha/dt$ are the same and the conversions α are equal, then the curing rate is only a function of temperature. The isoconversional principal equation is then written as:

$$\left[\frac{\partial \ln\left(\frac{d\alpha}{dt}\right)}{\partial T^{-1}}\right]_{\alpha} = \left[\frac{\partial \ln(A)}{\partial T^{-1}}\right]_{\alpha} + \left[\frac{\partial \ln(f(\alpha))}{\partial T^{-1}}\right]_{\alpha} - \left[\frac{E}{R}\right]_{\alpha} \quad (10.5)$$

Analysing Equation 10.5 enables one to make the following conclusions: the term $\left[\frac{\partial \ln(A)}{\partial T^{-1}}\right]_{\alpha}$ is zero, since differentiating a constant results zero; and $\left[\frac{\partial \ln(f(\alpha))}{\partial T^{-1}}\right]_{\alpha}$ also equals zero, since the kinetic model $f(\alpha)$ is only a function of the conversion. Finally, one can conclude that the activation energy for a certain conversion value α (now referred as E_{α}) does not depend on the chosen kinetic model, i.e., it is model-free:

$$E_{\alpha} = -R \left[\frac{\partial \ln\left(\frac{d\alpha}{dt}\right)}{\partial T^{-1}} \right]_{\alpha} \quad (10.6)$$

The assumption that the kinetic model does not change with temperature is reasonable, since the temperature range related to a given conversion is so narrow that no change would be detected. [160] Obtaining the values for activation energy in terms of conversion without taking the kinetic model into consideration is very convenient and already gives light to important details about the crosslinking mechanism. Thus, this principle was employed to study the crosslinking kinetics here.

There are many different approaches that apply the isoconversional principle to determine the activation energy of thermally-induced processes. Vyazovkin *et al.* [159] and Zhang [164] give a broad overview about these methods, which include the integral isoconversional ones used in this research. The principle for isothermal experiments (as the ones described in Section 10.1.2) is represented by Equation 10.7

$$\ln(t_{\alpha,i}) = \ln[f(\alpha)A_{\alpha}] - \frac{E_{\alpha}}{R \cdot T_{\alpha,i}} \quad (10.7)$$

while the integral isoconversional approach for the case when a constant heating rate β program is employed can be formulated as the Kissinger-Akahira-Sunose [165] equation with Starink [166] improvement:

$$\ln\left(\frac{\beta_i}{T_{\alpha,i}^{1.92}}\right) = Const - 1.0008 \cdot \left(\frac{E_{\alpha}}{RT_{\alpha,i}}\right) \quad (10.8)$$

The subscripts α, i indicate a given conversion α and a given thermal program i (temperature for isothermal experiments or heating rate for dynamic experiments). [161] It is possible to notice after careful analysis that Equations 10.7 and 10.8 can be written in the linear form $y = ax + b$, assuming $1/T_{\alpha}$ as x . Thus, the activation energy E_{α} can be determined for each conversion value (represented by $t_{\alpha,i}$ or $T_{\alpha,i}$) by plotting the left-hand side of the respective Equations over $1/T$. This strategy was used in the present research to determine an initial guess for the activation energy, to be implemented in the subsequent fitting procedure.

10.1.4 Fitting of curing rates $d\alpha/dt$

Regarding the kinetic model function $f(\alpha)$, it is widely accepted [160, 167–169] that the crosslinking reaction of silicone rubbers follows the autocatalytic model, first proposed by Šesták-Berggren [170] in the form of Equation 10.9, and further modified by Kamal [171] to include the temperature dependence, as seen in Equation 10.10:

$$f(\alpha) = \alpha^m(1 - \alpha)^n \quad (10.9)$$

$$\frac{d\alpha}{dt} = (k_1 + k_2 \cdot \alpha^m)(1 - \alpha)^n \quad (10.10)$$

where m and n are the reaction orders and k_1 and k_2 are the Arrhenius rate constants, as previously defined in Equation 10.4. For the present study, a third version of the autocatalytic model was assumed, where k_1 and k_2 are taken as constants with activation energies $E_{\alpha,1}$ and $E_{\alpha,2}$, in a way that the final kinetic model equation can be written, after proper substitution using Equations 10.4 and 10.10, as:

$$\frac{d\alpha}{dt} = \left[A_1 \cdot \exp\left(\frac{-E_{\alpha,1}}{R \cdot T}\right) + A_2 \cdot \exp\left(\frac{-E_{\alpha,2}}{R \cdot T}\right) \alpha^m \right] \cdot (1 - \alpha)^n \quad (10.11)$$

The subscript 1 denotes the n^{th} order contribution to the crosslinking model, while the subscript 2 denotes the auto-catalytic contribution. Similarly, n is the reaction order for the n^{th} model, and m is the reaction order for the auto-catalytic part.

Fitting of the $d\alpha/dt$ data according to the Kamal model was performed for conversion values from 0.05 to 0.95. Initially, it was assumed [167] that $E_{\alpha,1} = E_{\alpha,2} = E_{\alpha}$ as calculated applying the isoconversional approach. This E_{α} value was then implemented as the activation energy at the preliminary fitting routine and the parameters A_1 , A_2 , m , and n were determined employing the Levenberg–Marquardt algorithm [155] or damped least squares method. After the first preliminary fitting, the previously calculated parameters were employed as initial guesses for the final calculations of the kinetic parameters A_1 , A_2 , m , n , $E_{\alpha,1}$, and $E_{\alpha,2}$. All fitting procedures were performed utilizing Python coding language (Python 3.8, PyCharm Community Edition 2021.2.2, Jet Brains, Prague, Czechia) and the code is provided in the Appendix A.9. The code was built with the aid of the chatbot and virtual assistant ChatGPT (OpenAI, USA) version GPT-3.5.

10.2 LIQUID SILICONE RUBBER INVESTIGATION

For the curing kinetics investigation of liquid silicone rubber, methodologies based on the preliminary investigation were employed. Here, the rubber process analyser (RPA, rheology-based) and the dynamic scanning calorimetry (DSC, calorimetry-based) approaches were applied and will be further compared in the next Chapter.

10.2.1 *Materials*

Liquid silicone rubber (SiloprenTM LSR 2070, $M_w = 86673 \text{ g.mol}^{-1}$, $M_w/M_n = 1.603$, hardness after cured = 70 Shore A), containing approximately 32 wt% (high content) of an inorganic filler, was supplied as a 2-component (A and B) system by Momentive Performance Materials Inc. (USA). LSR characterization in terms of molecular weight and filler content is described in the Appendix (A.1 and A.3, respectively) of this thesis. SiloprenTM LSR 2070 is a standard liquid silicone rubber for injection moulding processes and has a mixing ratio of components A:B = 1:1. Mixing of components A and B was accomplished with a dual asymmetric centrifuge (DAC 400.2 VAC-P, Hauschild Speed Mixer, Germany) at room temperature, under vacuum, and according to the following step-wise procedure:

1. 800 rpm, 2 min, 800 mbar vacuum
2. 1200 rpm, 2 min, 400 mbar vacuum
3. 1600 rpm, 2 min, 100 mbar vacuum
4. 1800 rpm, 4 min, 50 mbar vacuum

10.2.2 *Non-isothermal rotational rheometry*

Rubber process analyser (D-RPA 3000 Montech Werkstoffprüfmaschinen GmbH, Germany) equipment, or moving die rheometer (MDR), was employed as a rotational oscillatory rheometer to characterize the curing behaviour of LSR under various curing conditions. For this set of experiments, in triplicate, three heating rates ($\beta = 2, 5, \text{ and } 10 \text{ K.min}^{-1}$), and three shear conditions ($0.4383, 4.383, \text{ and } 13.1476 \text{ s}^{-1}$) were employed. The shear conditions were realized by changing the shear frequencies (1, 10, and 30 Hz) and keeping the shear strain amplitude (0.5°). The shear amplitude (0.5°) is within the non-linear viscoelastic range, i.e., as explained in Chapter 5, it is expected that G'' is higher than G' . Thus, the gel point was defined [167] as the time or temperature at which $G' = G''$. This means that, above this point, the LSR behaves predominantly as an elastic solid ($G' > G''$).

The conversion rate was determined as stated in Equation 10.2. The activation energy was calculated following the integral isoconversional method for non-isothermal experiments depicted in Equation 10.8. Fitting of $d\alpha/dt$ followed the method described in Section 10.1.4.

10.2.3 *Dynamic scanning calorimetry*

The curing kinetics of LSR was studied employing a dynamic scanning calorimeter (DSC1 STAR System Mettler-Toledo International Inc,

Switzerland). Approximately 10-20 mg of A+B 1:1 mixture (triplicate) were placed into aluminium crucibles aiming maximum possible contact with the crucible's bottom. Next, the samples were submitted to the following thermal program, under 50 mL.min⁻¹ of nitrogen as purge gas, in random order to avoid any unmeasured, and uncontrolled, disturbances from the laboratory environment and from the device:

- i Isotherm for 3 min at 50°C
- ii Heating at 2/5/10 K.min⁻¹ until 150°C
- iii Isotherm for 5 min at 150°C
- iv Cooling at 20 K.min⁻¹ until 50°C
- v Isotherm for 3 min at 50°C
- vi Heating at 2/5/10 K.min⁻¹ until 150°C

The crucible's mass was measured before and after the thermal program and any sample that underwent mass loss higher than 0.5% was repeated. As advised by Heinze and Echtermeyer [172], crosslinking enthalpy (H_x) was calculated (mean value) as follows, where $\beta = 2, 5,$ or 10 K.min⁻¹.

$$H_x = \frac{1}{\beta} \int_{T_{onset}}^{T_{endset}} \dot{Q} dT \quad (10.12)$$

The curing conversion α for this calorimetry approach was calculated as the released heat ratio \dot{Q} according to Equation 10.13. The curing speed, or crosslink conversion rate $d\alpha/dt$, was calculated employing the differentiate function from Origin 9.0G software (OriginLab, USA), i.e., the derivative at a given point was computed by taking the average of the slopes between the point and its two closest neighbors.

$$\alpha(t) = \int_{t_{onset}}^t \dot{Q} dt \left(\int_{t_{onset}}^{t_{endset}} \dot{Q} dt \right)^{-1} \quad (10.13)$$

The activation energy for this calorimetry-based approach was also calculated following the integral isoconversional method for non-isothermal experiments depicted in Equation 10.8. Fitting of $d\alpha/dt$ followed the method described in Section 10.1.4.

RESULTS AND CONCLUSIONS

This Chapter is divided into two major sections with correspondent subsections. The first comprehends the preliminary crosslinking study of high consistency silicone (solid poly(siloxane)), including a discussion about curing kinetics and its association with processing conditions, proposing a mathematical relation for the optimum cure time based on the experimental data. Besides, this section covers the crosslinking kinetics considerations and presents the kinetic parameters, along with the reasoning behind their trend as the dicumylperoxide concentration increases. Finally, it presents thermodynamic considerations regarding the dicumylperoxide-based crosslinking of silicone rubber. The second section is dedicated to report the curing kinetics study for liquid silicone rubber, aiming to identify primarily the difference between the calorimetric and the rheological approaches. Furthermore, it studies the influence of shear in the crosslinking kinetics parameters employing the rheological approach.

Note: The content of this chapter is partially discussed in the peer-reviewed article 3 (Azevedo et al. 2022, Polymers 14(20) pp.4404).

11.1 CURING KINETICS OF HIGH CONSISTENCY SILICONE

The crosslinking study of high consistency silicone was analysed only via the rheological approach employing the rubber process analyser. For this section, the influence of dicumylperoxide concentration was investigated, aiming to build a comprehensive analysis of the curing kinetics to be applied further in the liquid silicone rubber study.

11.1.1 Curing characteristics

Figure 11.1 displays the curing curves for the PDMS/DCP systems for different dicumylperoxide concentrations and at different curing temperatures. Curing curves are usually analysed in rubber industry and research to identify the crosslinking profile in terms of minimum detected torque, induction time, velocity, curing time, and maximum detected torque. A torque increase is present for all samples with dicumylperoxide, regardless of the concentration, due to the formation of a denser polymer network, promoted by crosslinking. Connecting adjacent PDMS macromolecules forms a stiffer and more elastic network, which imposes a higher torque to the device, in order to keep the set deformation.

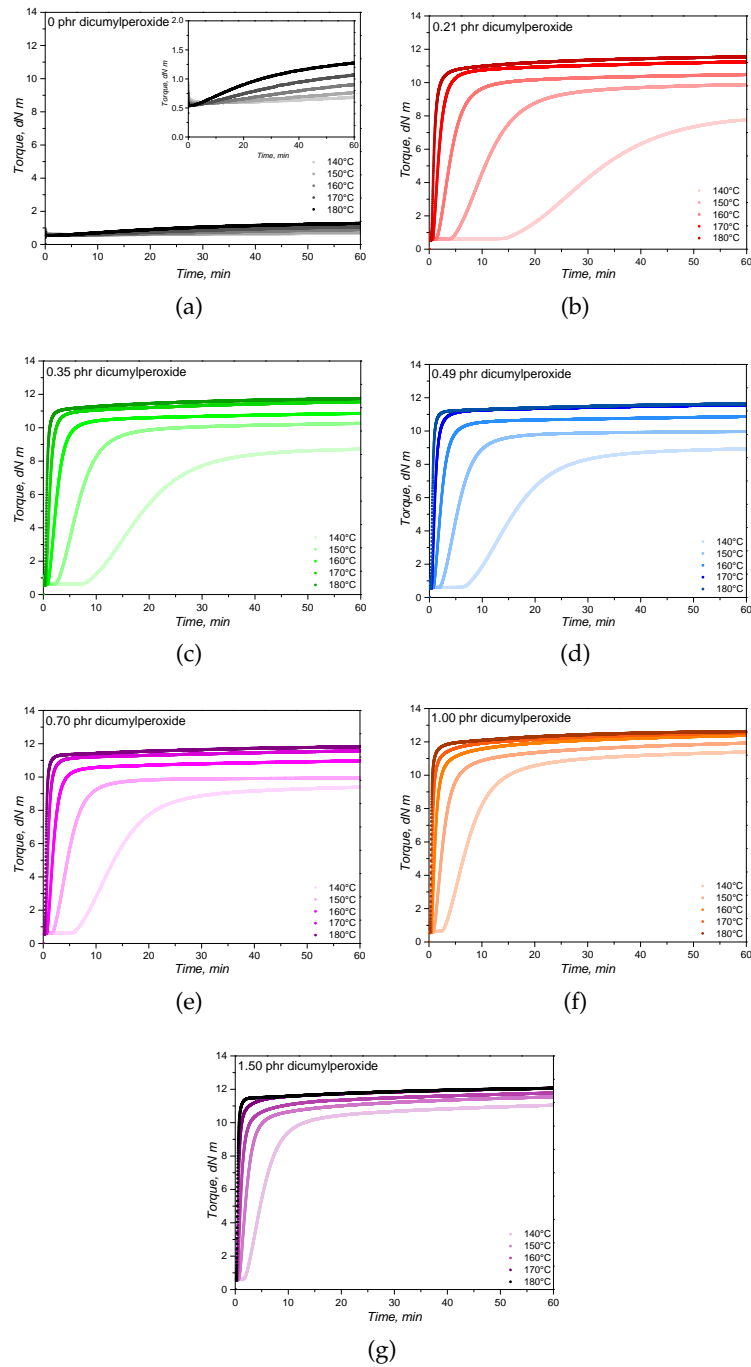


Figure 11.1: Rotational rheometry (RPA, 0.5° deformation at 1.667 Hz) curves for silicone rubber compounds with varied dicumylperoxide concentrations (b-g) at different crosslinking temperatures. The plot (a) (torque vs. time curve) is related to the pure solid silicone rubber without dicumylperoxide.

For all dicumylperoxide concentrations, the temperature increase shortens the induction or scorch time and lowers the minimum detected torque, as also depicted in Table 11.1. Since dicumylperoxide decomposition is initiated and promoted by heat (reaction i in Section 9.2.1), a higher curing temperature delivers more heat to the rubber compound, leading to a shorter crosslinking induction time, represented by the t_{s1} values. For a constant curing temperature, the higher the dicumylperoxide concentration, the lower the induction time. The effect of dicumylperoxide concentration on the induction time is explained by the higher concentration of radicals that are formed after decomposition and by the autocatalytic nature of this process, as also reported by Kruželák *et al.* [173, 174]. Industrially, this value is related to process safety and connected to the mouldability of the rubber compound, which is limited after t_{s1} is reached. As a matter of example, short scorch times are preferred for extrusion of hollow rubber profiles, to avoid extrudate collapse after passing through the matrix. On the other hand, for rubber injection moulding, scorch time must be long enough to guarantee the complete filling of the mould before curing.

The minimum detected torque ML was also slightly lowered by temperature increase, which is mainly an effect of temperature over the rubber compound's viscosity. The effect of temperature over rubber viscosity is well known, and the processability is related to this value when RPA is employed in the rubber industry. Generally, along with the values for Mooney viscosity, the minimum detected torque clarifies aspects about rubber processing, including mixing and moulding. No effects of dicumylperoxide concentration were detected at the minimum torque due to the low concentration, the low molecular weight, and the dispersion of the peroxide into the rubber matrix.

Table 11.1: Curing parameters for silicone rubber compounds concerning minimum torque (ML , dN.m) and induction or scorch time (t_{s1} , min) for different crosslinking temperatures and varied dicumylperoxide concentrations.

Temperature	140°C		150°C		160°C		170°C		180°C	
	ML	t_{s1}	ML	t_{s1}	ML	t_{s1}	ML	t_{s1}	ML	t_{s1}
0 phr	0.58	n/a	0.57	n/a	0.56	n/a	0.54	n/a	0.41	n/a
0.21 phr	0.61	19.98	0.60	6.16	0.58	2.12	0.56	0.96	0.53	0.53
0.35 phr	0.62	11.13	0.62	3.63	0.58	1.29	0.55	0.64	0.55	0.39
0.49 phr	0.60	9.40	0.59	3.02	0.57	1.16	0.55	0.58	0.54	0.36
0.70 phr	0.61	8.06	0.60	2.63	0.58	1.01	0.56	0.53	0.54	0.35
1.00 phr	0.61	3.76	0.58	1.31	0.56	0.63	0.55	0.57	0.56	0.28
1.50 phr	0.58	2.62	0.56	1.05	0.53	0.57	0.57	0.37	0.53	0.28

The curing rate is enhanced by temperature, as the cure plots, for all dicumylperoxide concentrations, become steeper for higher curing temperatures. Dicumylperoxide decomposition kinetics is favoured by temperature [175, 176], leading to a faster crosslinking reaction for the PDMS/DCP systems as well. Crosslinking velocity is also promoted by higher concentrations of dicumylperoxide, due to the higher concentration of radicals and to the autocatalytic nature of this process. Table 11.2 describes the optimal cure time t_{90} , which decreases as temperature and dicumylperoxide concentration increase. This decrease is an effect of temperature over the dicumylperoxide decomposition and rubber crosslinking kinetics, and of the quantity of radicals that are formed. Industrially, the selection of the most appropriate curing time is a compromise between processing time, processing temperature, and part quality in terms of mouldability.

Table 11.2: Curing parameters for silicone rubber compounds concerning maximum torque (MH , dN.m) and optimum cure time (t_{90} , min) for different crosslinking temperatures and varied dicumylperoxide concentrations.

Temperature	140°C		150°C		160°C		170°C		180°C	
	MH	t_{90}	MH	t_{90}	MH	t_{90}	MH	t_{90}	MH	t_{90}
0 phr	0.72	n/a	0.77	n/a	0.91	n/a	1.07	n/a	1.28	n/a
0.21 phr	7.76	45.45	9.89	20.92	10.48	8.91	11.25	4.54	11.54	2.92
0.35 phr	8.72	31.15	10.26	12.94	10.86	5.43	11.57	2.99	11.76	1.64
0.49 phr	8.93	27.07	9.97	10.18	10.87	4.72	11.57	2.44	11.64	1.25
0.70 phr	9.4	24.37	9.95	8.93	10.98	4.21	11.57	2.13	11.82	1.19
1.00 phr	11.40	16.74	11.92	8.75	12.39	4.5	12.56	2.93	12.63	1.22
1.50 phr	11.05	12.58	11.55	6.97	11.78	4.14	12.07	4.53	12.06	1.04

As an indicative of the final crosslink density, the maximum detected torque represents the maximum shear force resistance of the rubber compound at a given time and temperature, for the set deformation. [177] The maximum torque values, as shown in Table 11.2, tend to increase with temperature and with the dicumylperoxide concentration, suggesting that the effective number of crosslink points is also enhanced by temperature and dicumylperoxide amount. Even though the maximum torque values increase with dicumylperoxide, a threshold of approximately 11–12 dN.m is reached for the highest temperatures/dicumylperoxide concentrations.

Regarding the samples without dicumylperoxide, an increase in the detected torque is observed for all samples, with a steeper increase for higher temperatures. Even though a decrease in the torque within the first minutes due to viscosity reduction is detected, torque increases with time, which may indicate some crosslinking phenomenon not

associated to the presence of dicumylperoxide, but also triggered by temperature. This phenomenon may be associated to peroxide or metal contamination, that ultimately would lead to crosslinking when the temperature is increased.

When cycle time for moulding is evaluated for industrial applications, the optimum cure time t_{90} is a factor usually taken into account. An estimation for the optimum cure time within the temperature and dicumylperoxide ranges that were investigated is shown in Figure 11.2, taking Equation 10.1 as the mathematical model for the parameter. The proposed equation can fit almost 99% of the experimental data, as represented by the pseudo adjusted- R^2 factor.

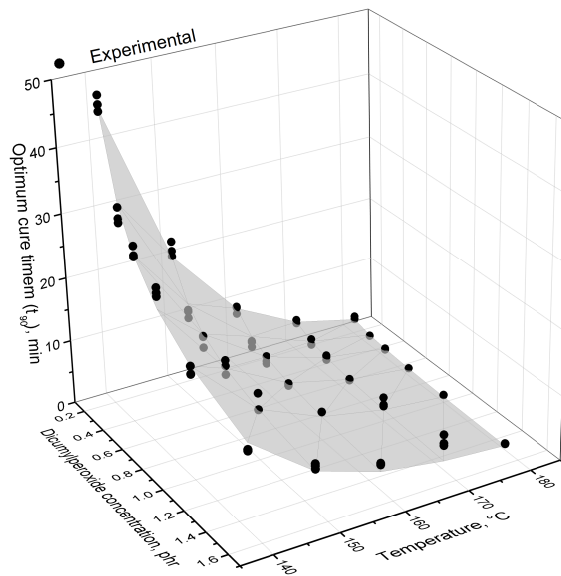


Figure 11.2: Optimum cure time t_{90} as a function of the dicumylperoxide concentration and the temperature. The dots represent the experimental data and the surface indicates the model described at Equation (10.1), with fitting parameters as follows: A_0 (pre-exponential factor) = $2.02 \times 10^{-14} \text{ min}^{-1}$, E_a (activation energy) = $1.18 \times 10^5 \text{ J.mol}^{-1}$, and $\beta = -0.603$. The correlation factor represented by the pseudo adjusted- R^2 was 0.988.

Temperature has a major influence over the optimum cure time for lower peroxide concentrations, while for concentrations above 0.70 phr the effect is not prominent. Similarly, the peroxide concentration has a stronger influence on the optimum cure time for lower temperatures, becoming weaker as the temperature increases. The less distinguished effect on the optimum cure time for higher temperatures and higher DCP concentrations is related to two distinguished reasons. For the temperature, the higher range ($>150^\circ\text{C}$) is well above the dicumylperoxide decomposition temperature, which is around 120°C [175]. This means that the decomposition and the preceding crosslinking reaction will take place almost instantly and rapidly, and the different peroxide concentrations will not impact the optimum cure time in a notable

way. Regarding the DCP concentration, the higher concentration range (>0.70 phr) shows a weaker effect of temperature on the optimum cure time, possibly due to the autocatalytic nature of peroxide-based crosslinking reactions. In these cases, the number of generated radicals is enough to compensate the temperature effect and overlap it. Hou *et al.* [178] recently reported the same effect of temperature on the optimum cure time for dicumylperoxide-crosslinked silicone rubber.

In this work, an equation is proposed to model the optimum cure time for peroxide-cured high consistency silicone elastomers. The parameters for this equation are also described in Figure 11.2. The activation energy is associated to the amount of energy necessary to reach the optimum cure time, which is also associated to the amount of energy necessary to decompose the dicumylperoxide molecules as stated in the chemical equation i in Section 9.2.1. Thus, the value of $115 \text{ kJ}\cdot\text{mol}^{-1}$ is in accordance with the values reported in the literature [175, 176] for DCP decomposition, and with the activation energy values that will be presented further in the crosslinking kinetics discussion. The exponent for the dicumylperoxide concentration has a negative value due to the decrease of the optimum cure time with the peroxide concentration and is less than 1 possibly due to its limitation in crosslinking the polymer, which will also be further explained. The pre-exponential factor, similarly to the activation energy, presents a value that will also be similarly reported when the crosslinking kinetics is discussed further in this work. It is important to state here that these parameters and this specific equation fit to the polymer and to the crosslinking system that were investigated in this Thesis, at the same time. For other polymeric systems, with different crosslinking mechanisms and kinetics, another set of equations and parameters must be proposed and evaluated.

11.1.2 Peroxide-based crosslinking kinetics

Prediction of how a polymer crosslinks when exposed to heat during typical processing conditions, like compression or injection moulding, is a key step to control the overall process and the part quality. The crosslinking kinetics, i.e., the evolution of conversion α over time, was evaluated in terms of the torque increase detected at the rubber process analyser at 160°C , which is a typical temperature for solid silicone processing.

Based on the curves shown in Figure 11.1, the conversion rate $d\alpha/dt$ was calculated employing Equation (10.2) and is plotted versus time in Figure 11.3(a) and versus conversion in Figure 11.3(b). The effect of increasing the dicumylperoxide concentration is seen as an acceleration of the reaction, i.e., higher cure velocity, when analysing the conversion rate evolution on time. Additionally, the maximum cure rate is shifted to lower times. These findings are related to the concentration

of peroxide radicals that are formed at 160°C and its catalytic effect on the formation of further radical species. Regarding the evolution of cure velocity over conversion, or reaction path, the maximum cure rate remains constant at a fixed conversion value between 0.2 and 0.4 for the dicumylperoxide concentrations up to 0.70 phr. This means that the highest rate of crosslink formation occurs at a constant conversion range, regardless of the dicumylperoxide concentration below 0.7 phr. It is possible to speculate that the formation of the characteristic three-dimensional crosslinked network occurs mostly within the 0.2 and 0.4 conversion range for DCP concentration equal or lower than 0.70 phr, as a result of the decomposition of the majority of dicumylperoxide molecules. Within this conversion range, the concentration of radicals likely decreases, either by transfer to the polymer chain or by termination, resulting in the end of the crosslinking reaction. For the samples with higher dicumylperoxide concentrations (1.00 phr and 1.50 phr), the abruptly fast crosslinking reaction, as seen by the conversion rate values, shifts the maximum reaction speed to lower conversion values, probably due to the high amount of radicals that are formed.

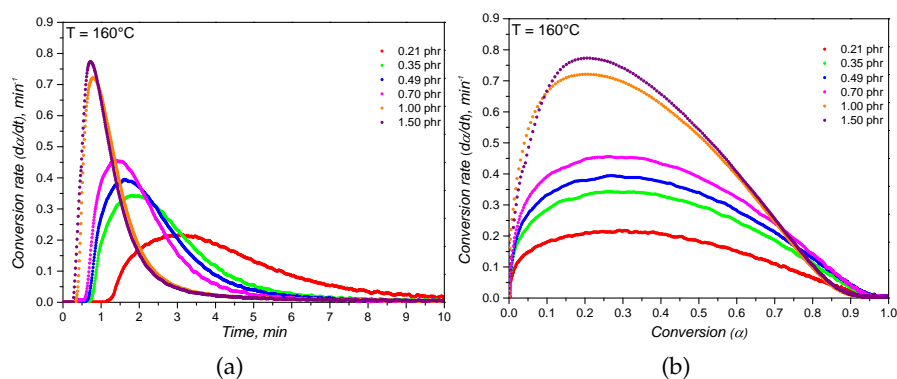


Figure 11.3: Conversion rate $d\alpha/dt$ at 160°C for silicone rubber compounds with different dicumylperoxide concentrations as a function of time (a) and conversion (b).

As extensively described by Vyazovkin *et al.* [159, 160, 163], the determination of the kinetic parameters starts with calculating the activation energy without defining the most appropriate kinetic model, a strategy that is called model-free. The activation energy calculation following a Friedman-like approach as described by Equation (10.7) is exemplified for the 0.21 phr sample in Figure 11.4(a). The slopes of the linear-fitted lines (correlation factors for the linear fittings were higher than 0.960) were used to determine the activation energy variation with conversion, as shown in the diagram of Figure 11.4(b). A decrease of the activation energy is realized as the dicumylperoxide content increases, representing thermodynamically easier crosslinking reactions. This behaviour was already observed before, but in a kinetic way: the higher peroxide concentration accelerated the crosslinking

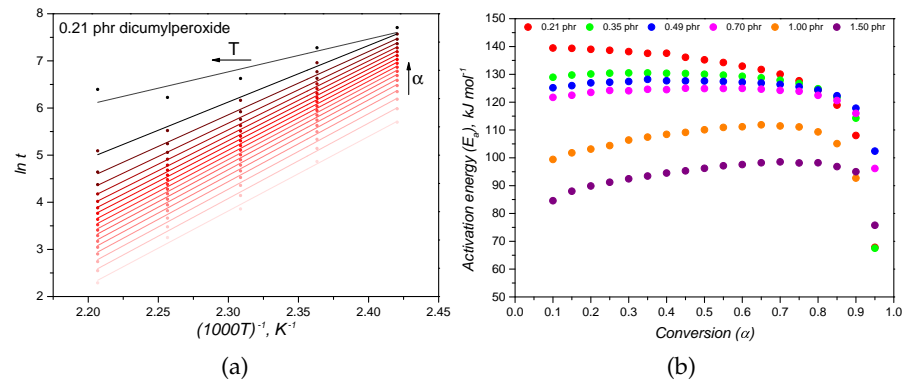


Figure 11.4: Friedman-like isoconversional approach for calculating the activation energy, regarding the sample 0.21 phr (a) and the activation energy for different dicumylperoxide concentration as function of conversion (b).

reaction. Both thermodynamic and kinetic phenomena are behind the autocatalytic nature of dicumylperoxide decomposition, which precedes the polymer crosslinking. Bianchi *et al.* [179] observed the same behaviour when studying the crosslinking of poly(ethylene-vinyl acetate) with dicumylperoxide, similarly reporting activation energy values between 85 and 105 $\text{kJ}\cdot\text{mol}^{-1}$.

Duh *et al.* [176] reported an activation energy for dicumylperoxide thermal decomposition of 110–150 $\text{kJ}\cdot\text{mol}^{-1}$, while Lv *et al.* [175] reported values between 150 $\text{kJ}\cdot\text{mol}^{-1}$ and 200 $\text{kJ}\cdot\text{mol}^{-1}$, which agree with the activation energy determined in the present study, i.e., varying between 85 $\text{kJ}\cdot\text{mol}^{-1}$ and 140 $\text{kJ}\cdot\text{mol}^{-1}$.

The activation energy is fairly constant in the conversion range 0.1–0.9, being reasonable for a system that does not undergo drastic molecular diffusion changes during crosslinking, which would impose mass transfer limitations to the process [160]. Systems that experience a greater change in viscosity, like epoxy thermoset resins, are more sensitive to the diffusion hindrance caused by the crosslinking reaction (due to increase in viscosity), representing an increase of the activation energy. [180] Another consideration that deserves commenting is the heat transfer change due to the formation of a crosslinked layer at the top and bottom of the specimen inside the rubber process analyser during the first instances of curing. As studied by Cheheb *et al.* [133], the thermal conductivity of a crosslinked rubber sample can be 10% higher than a non-crosslinked one, but still much lower than the metallic RPA cavity. This means that, during curing, the heat transfer changes. However, this limitation was not further studied in the present work due to the low thickness of the RPA specimen (which imposes a fast heating of the whole sample) and the lack of scope of this investigation.

Since the activation energy exhibited a relatively constant trend with conversion, the experimental data were fitted to the Kamal model using the mean values to calculate the kinetic parameters. Activation energy deviations that are observed at higher conversion values ($\alpha > 0.9$), which may indicate a decrease of the activation energy, arise from the small variation of torque at the final stages of crosslinking, which leads to high standard deviation of data.

Conversion rate data were fitted applying Equation (10.11), resulting in the kinetic parameters that are shown in Table 11.3. The calculated activation energies are in accordance with the values previously determined via the Friedman approach, and also showing a decrease with the dicumylperoxide concentration. Reaction orders m and n do not follow a specific trend and are considered here as being rather constant. Considerations regarding the reaction orders are associated with the crosslinking reaction mechanism, which is understood as the same regardless of the peroxide's quantity. The pre-exponential values A_1 and A_2 have a tendency of decrease as the dicumylperoxide concentration increases.

Table 11.3: Kinetic parameters determined after fitting of the experimental conversion rate $d\alpha/dt$ to the Kamal model (Equation (10.11)) for silicone rubber compounds crosslinked at 160°C with different dicumylperoxide concentrations.

Sample	A_1 (min^{-1})	A_2 (min^{-1})	$E_{a,1}$ ($\text{kJ}\cdot\text{mol}^{-1}$)	$E_{a,2}$ ($\text{kJ}\cdot\text{mol}^{-1}$)	m (-)	n (-)	k_1 (min^{-1})	k_2 (min^{-1})
0.21 phr	1.1×10^{15}	6.4×10^{15}	131.35	131.35	1.167	1.617	0.159	0.926
0.25 phr	6.4×10^{14}	3.8×10^{15}	127.47	127.47	1.298	1.621	0.272	1.615
0.49 phr	4.4×10^{14}	2.4×10^{15}	125.75	125.75	1.210	1.552	0.302	1.644
0.70 phr	3.4×10^{14}	1.9×10^{15}	123.92	123.92	1.350	1.667	0.387	2.164
1.00 phr	3.2×10^{10}	4.2×10^{11}	87.67	87.60	2.048	2.760	0.872	11.438
1.50 phr	1.0×10^{10}	1.1×10^{11}	83.61	83.61	1.820	2.610	0.827	9.096

However, analysing the pre-exponential factor alone may lead to misunderstandings [163], so the Arrhenius rate constants k_1 and k_2 are also reported in Table 11.3. The constants k_1 and k_2 are indications of the system's reactivity and are enhanced as the dicumylperoxide concentration increases. This is an additional evidence that corroborates the catalytic effect of the dicumylperoxide concentration.

Analysing the pre-exponential factors solely may lead to misinterpretations since it is often related to the activation entropy, meaning that the higher the pre-exponential factor, the more accelerated the chemical reaction is, as stated in Equation (11.1) [181]. This mathematical relation is a different way of expressing the Arrhenius rate constant previously denoted as Equation (10.4).

$$k(T) = \frac{k_B T}{h} \exp\left(\frac{\Delta S}{R}\right) \exp\left(\frac{-\Delta H}{RT}\right) \quad (11.1)$$

The factor that contains the activation entropy ΔS , the Boltzmann constant k_B , and the Planck constant h was previously assigned as the pre-exponential factor A ; while the inverse dependence on temperature is represented by the activation enthalpy ΔH factor. In the case of the present PDMS/DCP systems, it is not correct to assume that due to the decrease of the pre-exponential factor, the crosslinking reaction is decelerated as the dicumylperoxide concentration increases. Actually, the effect on the system's reactivity, or the overall free energy of the activated reaction intermediate ΔG , is dominated by the enthalpy factor ΔH via the decrease of the activation energy, which is a pure effect of the peroxide catalyst's nature, as explained by the usual thermodynamic relationship, derived from the second law of thermodynamics:

$$\Delta G = \Delta H - T\Delta S \quad (11.2)$$

The free energy ΔG is thus lowered strongly by the decrease of the activation enthalpy ΔH in comparison with the not so evident entropic effect. It is beyond the scope of this Thesis to explain why the activation entropy decreases as the dicumylperoxide increases, thus justifying further investigations. However, one rationalization may be that the active sites for radical reaction, which ultimately leads to a crosslink point, become limited as the dicumylperoxide concentration increases, possibly justifying the crosslinking threshold that is observed on the final crosslinked elastomer specimen. A second reasoning is that, as the dicumylperoxide concentration increases, the radical concentration is also enhanced, increasing the probability of radical recombination before the reaction with the polymer chain, likewise limiting the crosslinking process. The last reasoning was already studied by Parks and Lorenz [182] when investigating the efficiency of dicumylperoxide to react with dimethyloctadiene.

After time integration, the conversion values calculated according to the model parameters were compared to the experimental ones, which are plotted in Figure 11.5. Within the conversion range 0.1–0.9, the calculated conversion values accordingly predict the experimental values with correlation factors represented by the pseudo adjusted- R^2 higher than 0.99. From a statistical point-of-view, the pseudo adjusted- R^2 values shown in Figure 11.5 are not intended to compare different mathematical models, since only the one in Equation 10.11 was employed, but instead to compare the variance explained by the model and the total variance. For the specific temperature (160°C) and the dicumylperoxide concentrations that were evaluated, it is possible to

predict how the crosslinking conversion behaves with time, meaning that this model can be possibly integrated into processing simulation routines. Along with the proposed mathematical relationship depicted at Equation 10.1 for the optimum cure time, these suggestions may strongly enhance the quality of processing simulations that deal with reactive systems, such as elastomers.

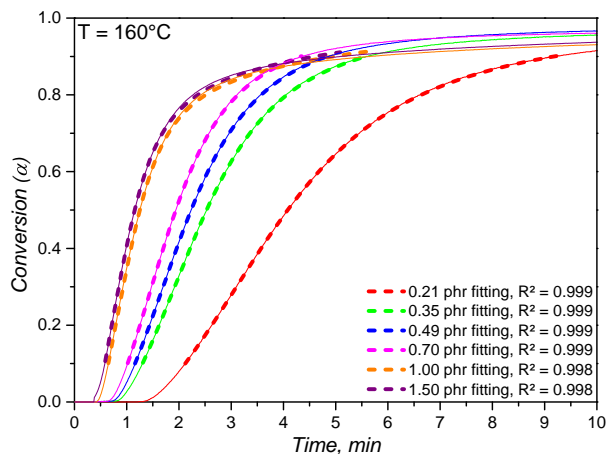


Figure 11.5: Comparison between the experimental and the calculated conversion values for the crosslinking at 160°C of silicone rubber compounds with dicumylperoxide concentrations. The calculated conversion values are plotted from 0.1 to 0.9 of conversion.

Incorporating the variable dicumylperoxide concentration into the crosslinking kinetics model was not included in the scope of this work, since it would demand an effort beyond the selected scientific targets. However, the ideal crosslinking kinetics model should embody not only the temperature of curing, but also a factor that correlates with the elastomer recipe in terms of the crosslinking systems.

The strategy of model fitting developed for the study of high consistency silicone rubber was further optimized to be applied to the study of liquid silicone rubber curing kinetics. For such, a dynamic (non-isothermal) approach was employed, along with a more refined statistical analysis of the obtained model parameters.

11.2 CURING KINETICS OF LIQUID SILICONE RUBBER

As previously described in Chapter 9, even though the curing mechanism of liquid silicone rubber is different from high consistency silicone, the same methodology can be employed to study the curing kinetics for both materials. For LSR, the curing kinetics was studied via a calorimetric approach (DSC), as well as employing a rheology-based approach (rubber process analyser, RPA). In this section, the results obtained from both approaches will be first presented separately, and then compared in terms of the calculated Kamal model (Equation 10.11) parameters.

11.2.1 Curing kinetics via DSC

When studied under a calorimetric perspective, liquid silicone rubber mixture (1:1 A:B) samples show a heat flow behaviour as shown in Figure 11.6. For all heating rates, the exothermic peak related to curing is apparent at temperatures higher than 90°C. As the heating rate increases, the temperature at which the curing speed is maximum (peak apex) shifts to higher values due to the faster heating of the sample (thermal inertia effects), i.e., since the sample is kept under a certain temperature for a longer time, curing occurs at lower temperatures. The crosslinking enthalpy (as defined by Equation 10.12) is the same for all samples and heating rates, being $8.15 \pm 0.27 \text{ J.g}^{-1}$. This quantity is important for injection moulding simulation, since it represents an internal heat source, which is incorporated into the constitutional equations as \dot{Q} , as in Equation 9.3.

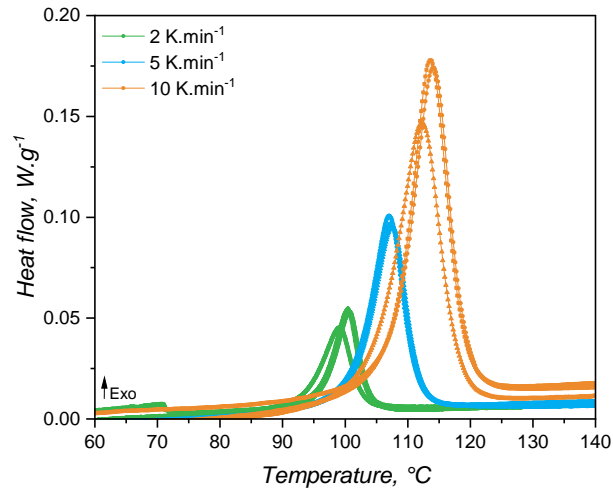


Figure 11.6: Dynamic scanning calorimetry analysis of LSR under 3 heating rates and inert atmosphere, showing the exothermic thermal event related to crosslinking. Each symbol/line represents one repetition.

From the shape of the exothermic peaks, one can realize that the speed of heat release is proportional to the extent of curing or conversion α . Thus, the conversion α was calculated and the conversion speed $d\alpha/dt$ was determined and plotted over temperature and over conversion in Figure 11.7(a) and (b), respectively. From the conversion rate data it is possible to realize that the maximum speed of curing occurs at around $\alpha = 0.6$ for all heating rates. This is a good indication that the curing mechanism is not changing with the heating rate. Besides, it is typical of autocatalytic curing reactions to reach the maximum reaction rate at intermediate conversion values, while n^{th} -order-based reactions have the maximum conversion rate at the beginning of the curing reaction. [183] Thus, it is appropriate to fit the conversion rate data to the autocatalytic, or Kamal, model.

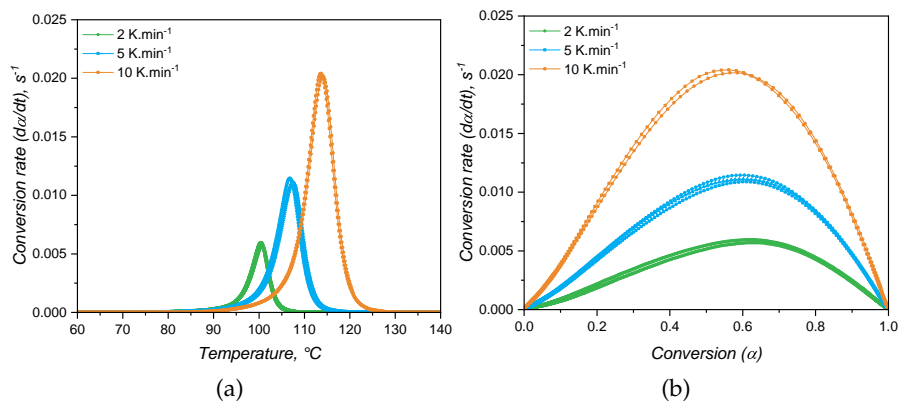


Figure 11.7: Conversion rate da/dt for LSR at several heating rates as a function of temperature (a) and conversion (b).

When the kinetic model of a certain chemical reaction is not known, it is usual to apply isoconversional approaches to determine kinetic parameters, such as the activation energy, that are model independent. This approach was described in Section 10.1.3 (denoted here as the Friedman approach) and employed to determine the activation energy of LSR curing reaction via DSC. The variation of activation energy with the curing extent is shown in Figure 11.8(b), while Figure 11.8(a) shows an example of a plot utilized to calculate E_a for each conversion step. As for the case of high consistency silicone, the activation energy is fairly constant and has an averaged value of $134.5 \text{ kJ} \cdot \text{mol}^{-1}$. This value is consistent with the one found by Hernández-Ortiz and Osswald [13], who studied an injection moulding grade of LSR; and it is slightly greater than the values (between $80 \text{ kJ} \cdot \text{mol}^{-1}$ and $100 \text{ kJ} \cdot \text{mol}^{-1}$) obtained by Ke *et al.* [184], who studied a liquid silicone rubber with lower molecular weight than the one investigated in the present Thesis. The activation energy as determined in the isoconversional approach is the overall energy barrier of the reaction under study. This means that it shows the thermodynamic boundary of curing, regardless of the number of steps involved in the curing mechanism, or the type of mechanism. Next, two values of E_a will be presented, one for the n^{th} -order contribution, and one for the autocatalytic part of the kinetic model, not being related to mechanistic steps of the crosslinking reaction. Thus, for the sake of this study, it is assumed that the curing reaction occurs in one single step with one set of kinetic parameters, neglecting any effects related to diffusion of reactive species that would ultimately lead to more than one activation energy determination. [160]

With the data as presented until here, it is possible to fit the conversion rate as shown in Figure 11.7(b) to the Kamal model to obtain the kinetic parameters A_1 , A_2 , E_1 , E_2 , m , and n . To facilitate the compar-

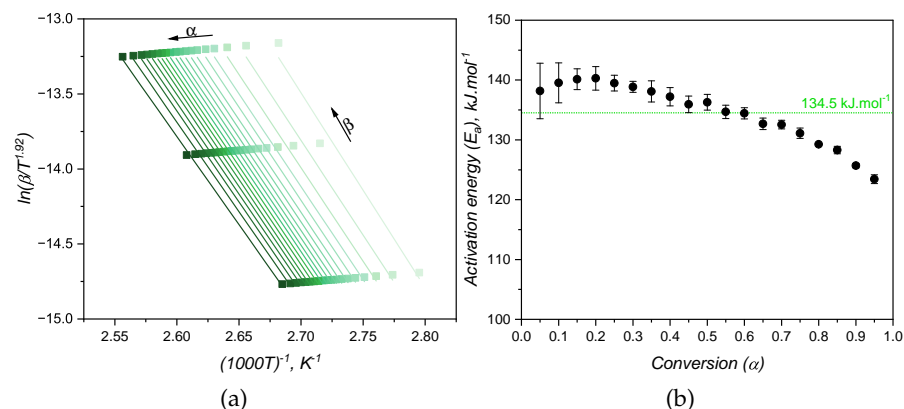


Figure 11.8: Friedman-like isoconversional approach for calculating the activation energy (a) and the activation energy as function of conversion for the calorimetric approach (b).

ison with the rheology-based approach, this will be first introduced next, and the fitting comparison will be made further in this Chapter.

11.2.2 Curing kinetics via RPA

While for the calorimetry-based approach the released heat was employed as measurable quantity to quantify the curing extent, for the rheology-based method, a measurable mechanical response is used to characterize the crosslinking development. Thus, the transmitted torque was recorded for the three heating rates and under three shear rates, and plotted over temperature, leading to the graphics shown in Figure 11.9. For all heating rates and shear rates, the torque increases sharply as the curing reaction starts, due to the increase of molecular weight that imposes high restriction to the set oscillation. As the heating rate increases, the onset temperature of curing is shifted to higher values, as occurred in the calorimetric approach. The effect of shear rate is apparent in the torque values: the higher the imposed shear rate (higher frequency of oscillation), the lower is the transmitted torque. This is due to shear thinning effects, as thoroughly detailed in Chapter 5. There is no significant effect of the shear rate in the onset of curing, i.e., it was not observed neither an activation of the curing reaction, nor an acceleration (higher curing speed, as shown next) by the increasing shear rate, as reported by Ziebell and Bhogesra [59].

One important feature of the torque increase due to curing is the steady and slow increase after the maximum curing rate, which in some cases lasts until the end of the measurement (200°C). This steady increase in the torque during RPA analyses is known as marching modulus, which is a phenomenon related to the filler-filler interactions between silica particles, but still not fully described in the literature. [185] The occurrence of a marching modulus is detrimental to the

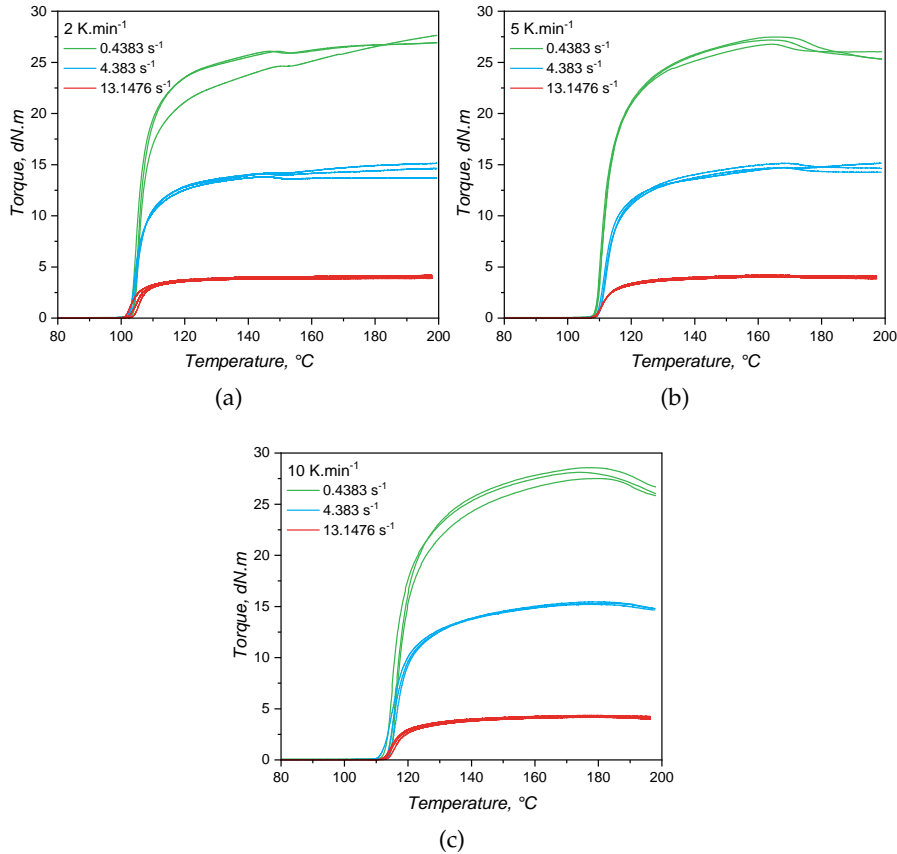


Figure 11.9: Variation of torque over temperature during the experiments at the rubber process analyser (RPA) for various shear rates at 2 K.min^{-1} (a), 5 K.min^{-1} (b), and 10 K.min^{-1} (c).

characterization of curing kinetics, since a definitive end ($\alpha = 1$) of the chemical reaction has to be established. In this sense, the end of curing for these measurements was set at the temperature of maximum transmitted torque.

The speed of reaction, or conversion rate, is shown in Figure 11.10 as a function of temperature (a-c) and of the conversion (d). As stated before, the increase in shear rate does not impose a significant change neither in the onset of curing, nor in the curing speed. Indeed, it is plausible to argue that stronger shear heating is likely to occur when the shear rate is increased, leading to faster curing reaction. However, probably due to the device robustness, this difference could not be monitored. Interesting is to note that the maximum curing speed occurs at low conversion values, which reflects the steep increase of torque right after the onset of curing. This already indicates distinct reaction orders m and n when compared to the calorimetric approach, since there is a close relationship [183] between the conversion at which the curing speed is maximum and the reaction orders:

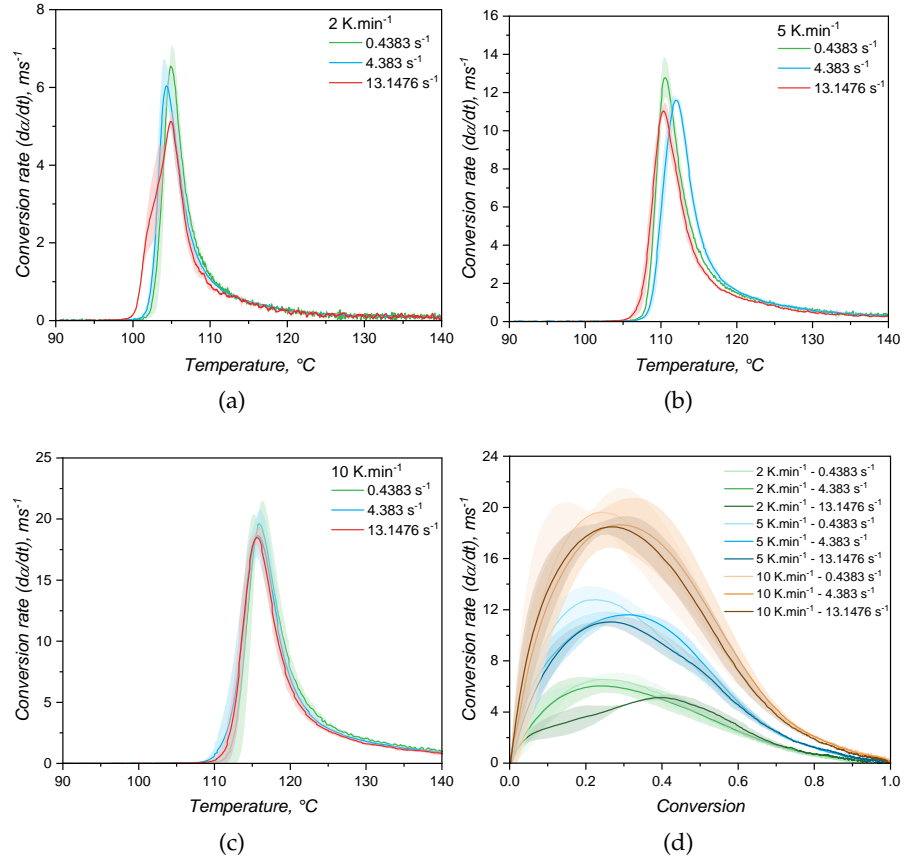


Figure 11.10: Conversion rate $d\alpha/dt$ measured via RPA for LSR as a function of temperature at various shear rates at $2 K.min^{-1}$ (a), $5 K.min^{-1}$ (b), and $10 K.min^{-1}$ (c). The variation of $d\alpha/dt$ over conversion is shown in (d). The shaded areas around the data lines (average) represent the standard deviation around the average.

$$\alpha(\max(\frac{d\alpha}{dt})) = \frac{m}{m+n} \quad (11.3)$$

Another important observation is the variability of $d\alpha/dt$ for the same measurement settings, as represented by the shaded areas around the average (solid lines in Figure 11.10(d)). By comparing with the DSC experiments, the RPA method is more prone to variation within replicates, since the sample mass is higher and the measurable quantity is a mechanical property, whose sensibility is lower than for the modern calorimeters.

Following the isoconversional approach, the activation energy for the curing as measured by the rheology-based approach was calculated and is expressed in Figure 11.11 for all three shear rates. Again, the increase of shear did not impose any change in the activation energy, which showed a slight decrease with the conversion. One can easily realize once more that the reproducibility of DSC measurements

was higher than RPA ones by the variation of the activation energy shown in Figure 11.11. Besides, E_a as determined by DSC is more constant when compared to the one characterized via RPA, suggesting again that the kinetic parameters of the Kamal model will likely be different. Statistically, the activation energies determined from the different approaches are distinct, as also reported by Bardelli *et al.* [167]. However, Bardelli and co-workers reported higher values for the calorimetric analysis when compared to the rheological one. This difference might be related to the different LSR grade studied by the authors, which was the low-viscosity Sylgard184. This LSR is also cured via hydrosilylation reaction, but it is employed as a dielectric gel that is applicable for sealing and protecting various electronic devices.

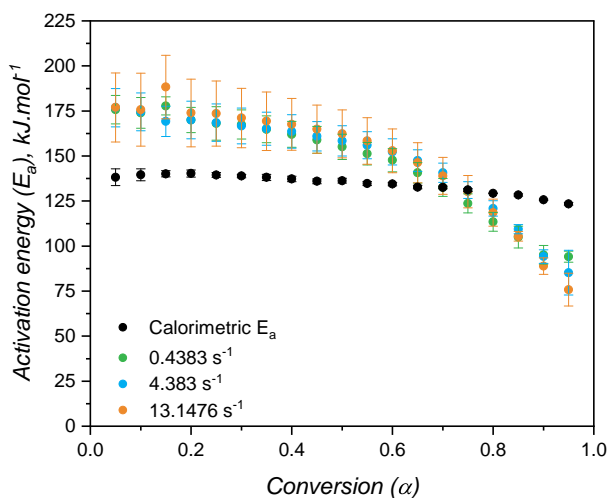
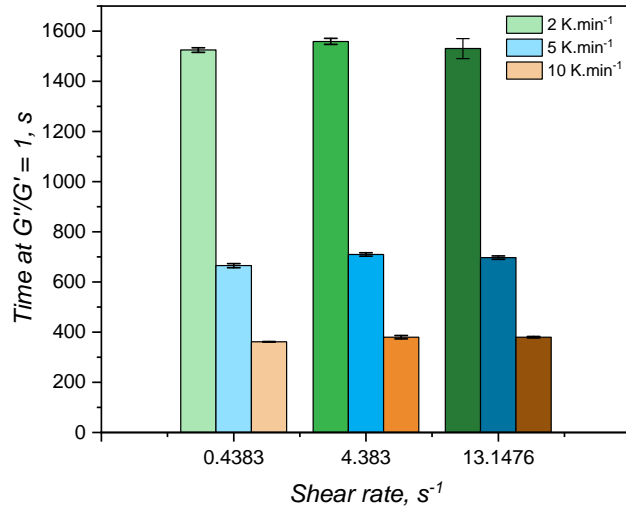
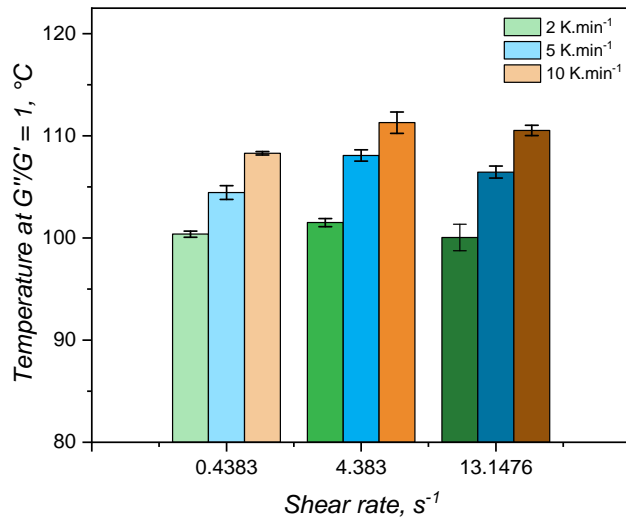


Figure 11.11: Activation energy values for the rheological approach (coloured dots) compared to the calorimetric method (black dots).

The time and temperature at which the viscous (G'') and the elastic (G') contributions are equal are normally employed to determine the gel point for systems that undergo a liquid-gel transition. [186] For the samples under study, these values are reported in Figure 11.12. The shear rate has also no effect on the gel point, as evidenced by the lack of trend in terms of gel time and gel temperature. Besides, more interestingly is to notice that the elastic modulus surpasses the viscous one in the very beginning of the curing detection in the RPA: by comparing with Figure 11.9(a), at 2 K.min⁻¹, the gel temperature is around 100°C, which is the very onset of curing. This behaviour was noticed in the literature by Harkous *et al.* [186] and more recently by Weißer *et al.* [60], who argued the existence of a physical gel (derived from the filler-filler interactions and macromolecular entanglements) before a chemical gel is formed due to curing. This argument is confirmed by the present study, since this physical gel was proven to exist in Chapter 5: the physical gel is disturbed under high shear amplitude and G'' is higher than G' at 10% deformation (see Figure 5.2).



(a)



(b)

Figure 11.12: Gel time (a) and temperature (b) for all heating rates and shear rates as studied by the rheology-based approach.

Thus, one can conclude that the classical definition of gel point very likely cannot be applied to highly elastic and filled systems as injection moulding grades of LSR. Instead, the standard definition of optimum cure time, widely employed in the rubber industry, may seem to be more appropriate here. In this case, the optimum cure time is determined as the time at which 90% of the maximum torque during RPA measurements is reached. [187] It is convenient to point out here that the calorimetry-based method does not offer the possibility to determine the gel point or the optimum cure time. However, as demonstrated before and compared to RPA next, it is able to characterize the curing kinetics of LSR in a sense that the conversion can be determined during simulation to predict the optimum cycle time. [188]

11.2.3 *Fitting and comparison between DSC and RPA*

In order to compare the methods available to characterize the curing kinetics of LSR for injection moulding simulation, qualitative and quantitative analyses are discussed next. Qualitatively, the conversion over temperature is compared in Figure 11.13 for the samples tested at $2 \text{ K}\cdot\text{min}^{-1}$. Only the samples at the lowest shear rate condition are shown, since these are closer to static conditions, as experienced during DSC runs, and because no significant qualitative difference was observed for other shear conditions. From this plot it is possible to clearly see that the DSC samples show higher values of conversion at lower temperatures, i.e., the reaction is detected first. This observation is explained by the fact that, while the calorimetric approach is able to detect the heat released since the very beginning of the curing reaction, the rheology-based method requires that a minimum (according to the device sensitivity) torque increase occurs to be then detected by the device. This means that the reaction response of one mol of Si-H-based crosslinker with one mol of vinyl-modified chain ends of poly(siloxane) oligomers is more strongly detected by its released heat, not by the increase in molecular weight that leads to shear resistance (increase in the transmitted torque). While sensitivity is the key issue here, the fact that enough macromolecules have to be connected to enhance shear resistance also plays a role in the detected differences. In this sense, one can argue that the reaction is happening in the RPA even before a torque increase is detected, but the molecular weight did not increase enough to impose resistance higher than the device's transducer sensitivity. When the torque resistance is enough to reach the device sensitivity, the conversion values are then higher than zero and increase rapidly. Another explanation for such delay is the sample size. DSC measurements require milligrams of sample, while RPA functions with grams of LSR. Thus, the heat is transferred more easily in the DSC when compared to RPA, affecting the measurement.

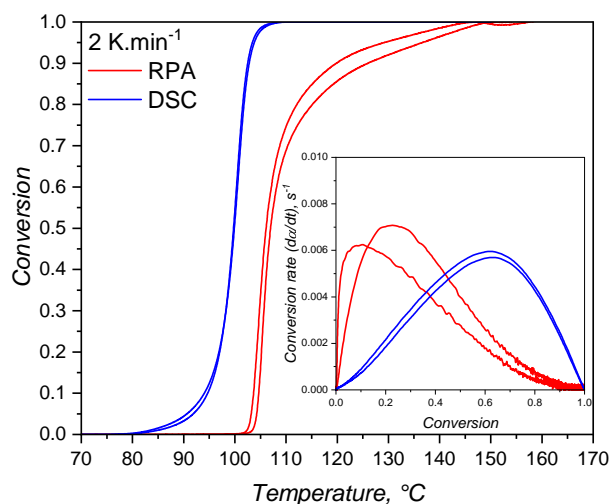


Figure 11.13: Comparison between the calculated conversion for the DSC and the RPA (0.4383 s^{-1}) approaches at $2 \text{ K}\cdot\text{min}^{-1}$ for two replicates. In the detail of the plot, conversion rate as function of the conversion is compared.

Besides, one can notice that the transmitted torque increase is detected at 100°C , when the conversion according to the DSC approach already reached almost 50%. This indicates that the rheology-based method is not able to detect the entire curing behaviour, failing to cover the onset and beginning of crosslinking, as also reported in the literature [186]. Furthermore, this approach is likely to have distinct kinetic parameters when compared to the calorimetric method, due to the fact that it detects only one part (roughly the second half) of the curing process.

Another important difference between the calorimetric and the rheological approaches as shown in Figure 11.13 is the conversion value at which the conversion rate is maximum. For the calorimetric approach, the maximum occurs at $\alpha > 0.5$, while for the rheometry-based method, $d\alpha/dt$ reaches its apex in early conversion values. As mentioned before, it is typical for autocatalytic reactions to present the maximum conversion rate at moderate conversion values, since at low conversion there is less concentration of the product that acts as catalyst, rendering low reaction speeds. As the reaction proceeds and more product is formed, the reaction is boosted by the catalytic effect and it reaches its maximum speed at moderate conversion values. The type of reaction that presents maximum speed in early conversion values is the one that follows n^{th} -order kinetics mechanisms, or diffusion controlled reactions. These reactions present conversion rate apex in the beginning of the reaction due to the reactant species' high mobility. As the reaction proceeds, either due to viscosity increase or formation of a network structure, the reactants are less likely to collide, resulting in a decrease of the curing speed. For the hydrosilylation reaction, the autocatalytic behaviour is explained by the formation

of an active form of the catalyst (Pt complex with alkenyl functional group) in the beginning of curing process that will further catalyse the insertion of the Si-H component. [143] Therefore, first a substantive amount of active catalyst has to be formed before the curing speed increases substantially. This is exactly what can be observed in Figure 11.13 for the blue lines (calorimetric data). On the other hand, the rheology-based approach is only able to detect the curing step after the formation of enough active catalyst, leading to a sudden sharp increase of the conversion, suggesting an n^{th} -order reaction. This is an important differentiation between the two methods that relies only in the detection of a signal that derives from the curing reaction. The hypothesis that the calorimetric method is able to truly characterize an autocatalytic reaction, while the rheological one can only detect the diffusion-controlled portion of the same reaction will be further discussed when the kinetic parameters are presented.

In order to quantitatively compare the approaches, the datasets from Figures 11.7 and 11.10 were fitted to the Kamal model (Equation 10.11) and the experimental and fitted plots are shown in Figure 11.14. The kinetic parameters associated to these plots are detailed in Table 11.4. From the plots, it is possible to see that the calorimetric data is nicely predicted by the Kamal model with the lowest mean residual (see Table A.4 in the Appendix A.11, the closer the mean residual is to zero, the better). The kinetic parameters associated to the DSC experiments are different from the ones obtained by the RPA approach, as it was assumed due to qualitative difference of the conversion rate plots. The difference arises from the fact that the methods are detecting not only different responses of the curing reaction, but they also cover the crosslinking process differently due to method sensitivity. This contrast was even observed when employing more sensitive rheometers, as the strain controlled rheometers employed by Harkous *et al.* [186], Bardelli *et al.* [167], and by Weißer *et al.* [60].

Table 11.4: Kinetic parameters (average) determined after fitting of the experimental conversion rate dx/dt to the Kamal model (Equation 10.11) for LSR employing various experimental procedures (DSC and rheological, from which the employed shear rates are shown).

Parameter	DSC	0.4383 s ⁻¹	4.383 s ⁻¹	13.1476 s ⁻¹
A_1, s^{-1}	1.07×10^{24}	1.00×10^5	1.00×10^5	1.00×10^5
A_2, s^{-1}	4.98×10^{12}	1.35×10^{17}	1.40×10^{17}	7.24×10^{12}
$E_1, \text{kJ.mol}^{-1}$	193.6	171.3	158.9	178.3
$E_2, \text{kJ.mol}^{-1}$	100.9	133.9	134.1	102.2
m	1.52	0.73	0.78	0.84
n	1.24	3.00	3.00	3.00

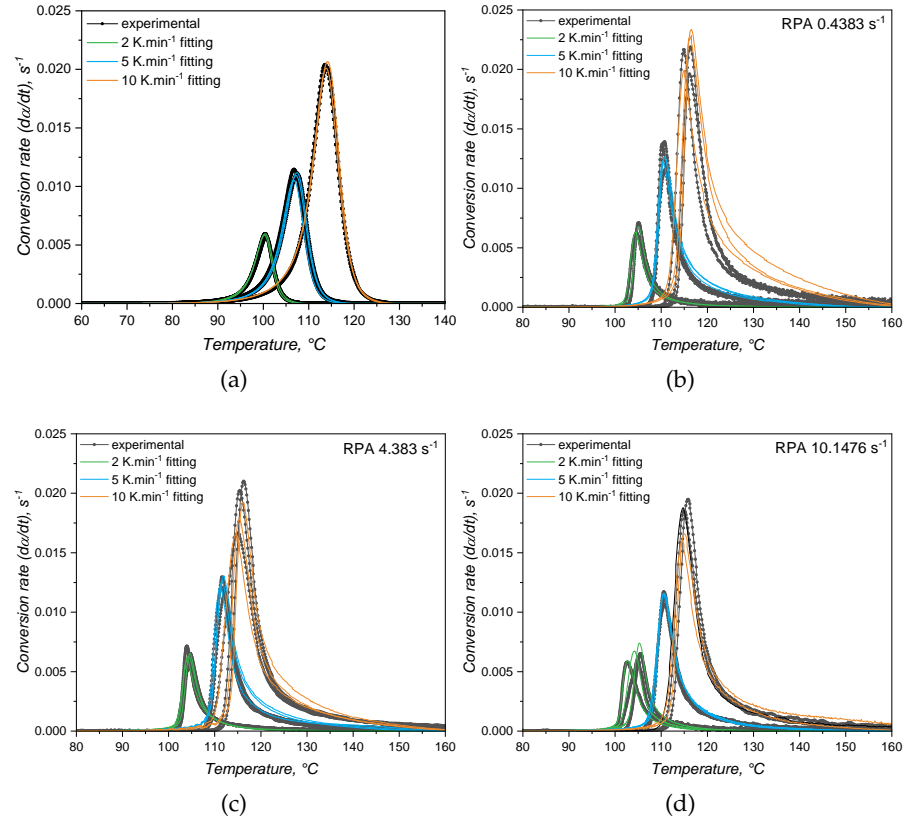


Figure 11.14: Comparison of experimental data (black symbols) and fitting according to the Kamal model (coloured lines) for the conversion rate $d\alpha/dt$ at several heating rates as a function of temperature for the DSC experiments (a) and for the RPA measurements (b-d) at different shear rates.

The kinetic parameters detailed in Table 11.4 show that, for the calorimetry-based approach, the reaction order related to the autocatalytic contribution m is higher than the contribution of the n^{th} -order n portion of the model. This helps to engage in the hypothesis that the DSC is able to detect the whole curing process, from the formation of the active catalyst to the total consumption of the reactants ($\alpha \rightarrow 1$). However, the rheological approach presents a predominance of the n^{th} -order contribution, since $n > m$ for all shear rates. This is a result of the abrupt increase in conversion right after the curing onset, typical of reactions that follow an n^{th} -order kinetic model. Since it is unreasonable to think that the same chemical reaction changes its mechanism depending on the method employed to study it, one can conclude that the way the data is detected plays a roll into the fitting to a certain kinetic model. Although without clear explanations, Hong and Lee [168], Harkous and co-workers [186], and Bardelli and co-workers [167] also reported $n > m$ when employing a rheological analysis, while $m > n$ was determined for the calorimetric one. All fittings performed with the data obtained via RPA presented $n = 3$

due to the fact that this parameter was allowed to vary during fitting from 0 to 3. Thus, this is an artifact from the fitting process.

11.3 CONCLUSION OF THE CHAPTER

From what was discussed in this Chapter, one can confirm that both calorimetry- and rheology-based approaches are suitable to determine the curing kinetics of silicone rubber. Besides, the Kamal model (autocatalytic) was enough to describe the curing speed (conversion rate $d\alpha/dt$) of high consistency and liquid silicone rubbers. Concerning the high consistency silicone, rheological experimental data showed that dicumylperoxide concentration enhancement accelerates the cross-linking reaction by shortening the induction time and increasing the reaction velocity. Besides, it results in higher but limited detected maximum torque, with distinguished extents for lower and higher temperatures. A correlation between the optimum cure time, the curing temperature, and the dicumylperoxide concentration was given, aiming to predict the cycle time during compression or injection moulding, for example. Determination of the kinetics parameters showed that even though there was a decrease of the pre-exponential factor, the overall reactivity (represented by the Arrhenius rate constant) increased as the dicumylperoxide concentration rose. The overall reactivity was boosted due to the activation energy decrease caused by the increase on the dicumylperoxide concentration. This effect was associated to the catalytic effect of the radicals responsible for crosslinking. In this sense, curing was understood to be dependant not only on the crosslinker (peroxide) concentration, but also on the thermodynamic and kinetic characteristics of the curing mechanism, i.e., limitation in terms of active sites for radical reaction and radical recombination.

In terms of liquid silicone rubber, the classical definition of gel time was proven to not be reliable to determine the point at which LSR stops flowing, since a physical gel derived mainly from filler-filler interactions and entanglements exists from the early stages of curing. Moreover, it is important to highlight that characterizing the curing kinetics via dynamic scanning calorimetry (based on released heat) or via rheology (based on increase of resistance to shear) leads to different kinetic parameters. While the calorimetric approach is able to follow the whole curing process, the rheology-based method cannot detect the real onset of curing due to the device limitation on sensitivity. It was possible to show that these methods, when connected to the Kamal model, lead to different inferences concerning the most appropriate kinetic models to describe the curing reaction. The calorimetric method delivers data to the Kamal model that are consistent with the autocatalytic kinetic model, while the rheological analysis provided information that are rational to the n^{th} -order model.

It is important to state though that both methods were able to produce conversion rate data that could be fitted to the Kamal model with low residuals, being the calorimetric method less prone to variation when compared to the rheological one. Within this context, it is advised that when determining the kinetic parameters for simulation, one has to pay attention to such differences, mainly because the RPA device is widely spread in the rubber industry, while DSC devices are not. The way these differences affect simulation results will be discussed in the next and final Part of this Thesis.

Part V

INJECTION MOULDING SIMULATION

This final Chapter deals with the theoretical and practical aspects of injection moulding simulation. The first part introduces common concepts and definitions that condition the simulation routines. Next, the simulation experiments are presented, as well as the analysis strategy is introduced. Finally, the material datasets obtained in the previous Chapters are compared in terms of the simulation output parameters.

12.1 THE GOVERNING CONSTITUTIVE EQUATIONS

Liquid silicone rubber (LSR) injection moulding simulation is an essential tool for predicting the behavior and quality of molded parts, relying heavily on the constitutive equations of mass conservation, momentum conservation, and energy conservation. The mass conservation equation (Equation 12.1), also known as the continuity equation, ensures that the mass of LSR is preserved throughout the moulding process. During LSR injection moulding, this equation is critical for accurately predicting the filling phase, where the silicone rubber is injected into the heated mould cavity. The simulation software solves the mass conservation equation using a discretized mesh, which divides the mould cavity into small elements. By ensuring that the mass flow rate into each element equals the mass flow rate out of the element, the software maintains a balance, thereby predicting how the material fills the mould and identifying potential defects like voids or incomplete filling. The continuity equation is a function of the density ρ and of the flow velocity \vec{v} .

$$\frac{\partial}{\partial t}\rho + \nabla \cdot (\rho \vec{v}) = 0 \quad (12.1)$$

The momentum conservation equation (Equation 12.2), derived from Newton's second law, is fundamental in capturing the flow dynamics of the LSR during injection moulding. This equation accounts for the forces acting on the silicone rubber, including pressure gradients, viscous forces, and inertial effects. In the context of LSR injection moulding, the momentum conservation equation helps to simulate the velocity field of the silicone rubber as it moves through the running channels and the heated mould. The software solves this equation on the mesh by iteratively updating the velocity and pressure fields within each element, ensuring that the momentum is conserved. This

aspect of the simulation is important for predicting flow front advancement, identifying potential flow-related issues such as weld lines, and ensuring the overall stability of the flow. In this equation, \vec{g} is the total body force per unit mass, p is pressure, η is shear viscosity, and \vec{D} is deformation tensor.

$$\rho \frac{\partial}{\partial t} \vec{v} = \rho \vec{g} - \nabla p + 2\nabla \cdot \eta \vec{D} - \rho \vec{v} \cdot \nabla \vec{v} \quad (12.2)$$

Finally, the energy conservation plays an important role in LSR injection moulding simulations by accounting for the thermodynamics and crosslinking reactions of the silicone rubber. The energy conservation equation ensures that the energy balance is maintained, considering factors like heat conduction, convection, and the viscous dissipation of heat due to shear forces within the material. During the injection and subsequent crosslinking process, this equation helps to predict the temperature distribution throughout the mould, which is crucial for understanding the curing phase and the resulting material properties. The simulation software solves the energy conservation equation on the mesh by calculating the temperature changes and crosslinking reactions within each element, allowing for accurate predictions of curing rates and cycle times. For such, c_p is specific heat capacity at constant pressure, T is temperature, β is coefficient of volume expansion, $\dot{\gamma}$ is shear rate, λ is thermal conductivity, and \dot{Q} represents a heat source, which for LSR injection moulding is the exothermal nature of the crosslinking reaction

$$\rho c_p \left(\frac{\partial T}{\partial t} + \vec{v} \cdot \nabla T \right) = \beta T \left(\frac{\partial p}{\partial t} + \vec{v} \cdot \nabla p \right) + \eta \dot{\gamma}^2 + \lambda \nabla^2 T + \dot{Q} \quad (12.3)$$

These constitutive equations of mass conservation, momentum conservation, and energy conservation form the backbone of LSR injection moulding simulations. The simulation software employs these equations within the framework of a discretized mesh, solving them iteratively to predict the behavior of the silicone rubber during the moulding process. By accurately modeling the filling, packing, and curing phases, the software can provide valuable insights into the performance and quality of the moulded parts. The following section will delve into the simulation boundary conditions and meshing, highlighting how these elements influence the accuracy and reliability of the simulation outcomes, and how different datasets for material properties can impact the simulation results.

12.2 BOUNDARY CONDITIONS AND MESHING

In order to correctly solve the equations presented before, specific boundary conditions have to be set, aiming to define the circumstances

at which the injection moulding process is occurring. These boundary conditions are responsible for capturing the physics of the process and ensuring that simulations provide reliable predictions of the moulding behavior. These conditions are mainly concerning the flow entrance into the mould, the mould itself, and the interaction between the mould and the polymer flow. Thus, in general, these conditions include the surfaces through which the melt enters the cavity, the edges of the mould, the top and bottom surfaces of the mould, and the wall slip condition. [134] Mitsoulis [49] differentiates the boundary conditions related to the flow from the ones related to the temperature and heat exchange, which will be detailed next.

The flow boundary conditions associated to a non-axisymmetric polymer flow are usually the following:

- At the mould inlet, the polymer flow presents a fully developed velocity profile, which is related to the volumetric flow rate.
- Along the cold runner and mould walls, which will be considered here as stationary, the flow velocity is zero, i.e., the no-slip velocity boundary condition is imposed. In case strong slippage is known to occur, Tran [134] suggests two ways to account for it in simulation routines: one can either specify a wall shear stress threshold at which the friction coefficient is higher than zero (slippage); or implement the commonly mathematical slip model developed by Mooney.

The thermal boundary conditions, on the other hand, are implemented as follows:

- At the mould inlet, the polymer presents a constant temperature, which for LSR is set to room temperature [48].
- The cold runner and mould walls are assumed to either present constant temperature, or to involve a heat balance with the LSR flow.

Equations 12.1, 12.2, and 12.3 are then solved using the aforementioned boundary condition to describe the polymer flow during injection moulding. However, since analytical solutions for these equations are not known, a system of differential equations is solved numerically and partial derivatives are converted into finite differences via discretization of the runner and cavity volumes. [189] Discretization is carried out by dividing the volume under study into smaller and simpler cells (mesh elements), which are characterized by their nodes. Solving the differential equations can then be either executed for each node in a fashion that the differential at one node can be replaced by the difference in the values at the neighboring nodes [189], or by using the differential equations in their integral and transforming the volume integral into a surface integral via the Gauss theorem.

In current simulation software employed to solve flow problems in engineering applications, three-dimensional meshes are employed for discretizing the geometry, while beam elements are used for the feed system and cooling channels, for example. [190]

It is well-established that increasing the number of mesh elements, resulting in finer meshes, enhances the accuracy of simulation results in finite element analysis (FEA). [191, 192] However, this improvement in precision comes at the cost of significantly higher computational resources and time. Conversely, simulations utilizing coarser meshes with fewer elements are computationally less demanding and more cost-effective, although at the expense of accuracy. Therefore, in practical applications, the number of mesh elements can be adjusted to balance the trade-off between simulation accuracy and computational efficiency.

12.3 AVAILABLE COMMERCIAL SOFTWARE

The software marketing for injection moulding simulation is quite diverse. Specifically for reactive injection moulding, as the case for liquid silicone rubber, there are four available software to be employed to predict flow and curing, all of them being able to cover all injection moulding phases (filling, packing, curing). Autodesk Moldflow Insight (provided by Autodesk Inc., USA) [193] has the option to analyse reactive moulding. This software employs 2.5D and 3D models for the finite element analysis, and has the advantage to allow user-defined functions for some material properties, such as viscosity and specific volume.

Cadmould 3D-F, from SIMCON kunststofftechnische Software GmbH (Germany) [194] also enables to simulate elastomer injection moulding. It employs a patented 2.5D-based 3D-lattice model (3D-F) for finite element analysis. The software developed by CoreTech System Co. Ltd. (Taiwan) called Moldex3D [195] also employs 2.5D models, but has the advantage to enable 3D models with finite volume method approach, being well-suited for continuous flow problems, where the balance of fluxes for each control volume is considered. [196]

At last, SIGMASOFT is the injection moulding simulation software from SIGMA Engineering GmbH (Germany), which has a dedicated module for liquid silicone rubber injection moulding [197]. Similarly to Moldex3D, SIGMASOFT operates exclusively with 3D models under the finite volume method approach, being able to simulate polymer flow through complex geometries. SIGMASOFT is the software employed in this work (version 6.1.0.2) not only due to the license availability, but also because it allows tailoring the material data properties according to the user's discretion, which is essential for the purposes of the present investigation.

12.4 COMPARISON ROUTINES - SIMULATION SETUP

In order to compare the several characterization methods presented in the previous Chapters, simulations were carried out employing different sub-datasets for viscosity, specific heat capacity, and curing kinetics. In this sense, five different LSR material data arrays were considered, which are detailed in Table 12.1.

Table 12.1: Material data employed to run the comparison simulation routines according to each sub-dataset and the employed characterization technique. DSC* denotes calorimetry data without input for the curing enthalpy.

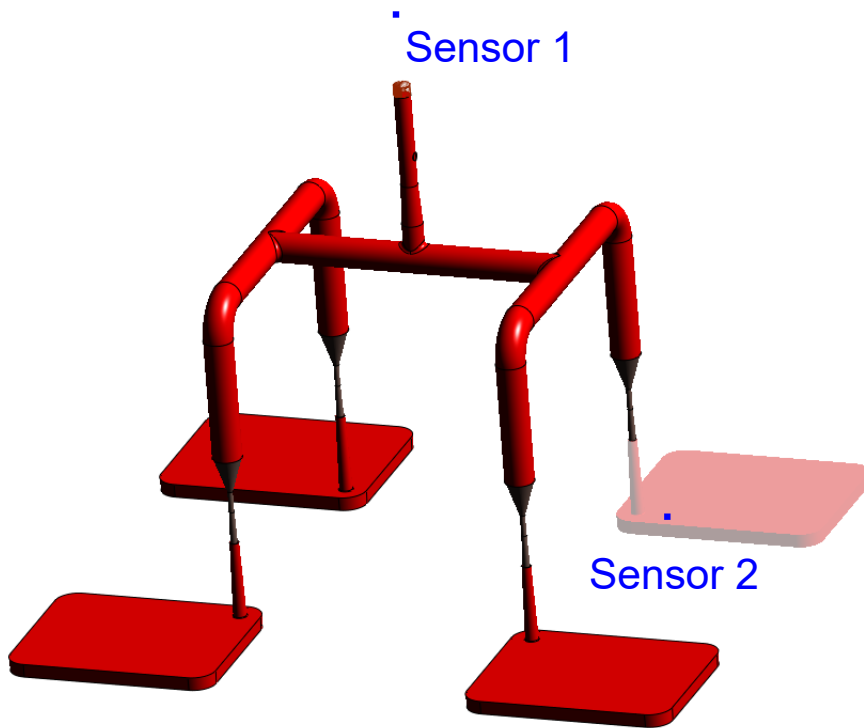
Dataset	A	B	C	D	E
Viscosity	LAOS	HPCR	HPCR	HPCR	HPCR
c_p	MDSC 1 st	MDSC 1 st	sapphire 1 st	sapphire 2 nd	MDSC 1 st
λ			cured sample		
pvT			See Section 8.3		
Curing	DSC	DSC	DSC*	DSC	RPA

For the viscosity sub-dataset, the viscosity variation with temperature and shear rate was compared between the data obtained via LAOS (see Section 5.2) or HPCR (see Section 5.4); therefore, datasets A and B were compared. The comparison between measuring c_p via the sapphire method or the modulated DSC approach (see Section 8.1) is made between datasets B and C for the first heating (considering the curing step) and B and D (linear relationship of c_p with temperature, without crosslinking), taking into account the c_p trend shown in Figure 8.2. Finally, to compare the two studied approaches to determine the curing kinetics, datasets B and E were compared: the first employed the sub-dataset obtained from calorimetry-based experiments (see Section 11.2.1), and the second obtained from rheology-based tests (see Section 11.2.2). For all datasets (A-E), the thermal conductivity was assumed to be a function of temperature as reported in Section 8.2 for the 1:1 mixture A:B cured sample (the trend of λ with temperature is shown in Figure 8.5). Since viscosity, c_p , and the curing parameters can vary, when these are set as constants for comparing datasets, the HPCR data were employed for the viscosity information; the 1st heating of the MDSC technique was chosen to represent the specific heat capacity; and the curing kinetics as determined via DSC was used to set the crosslinking characteristics.

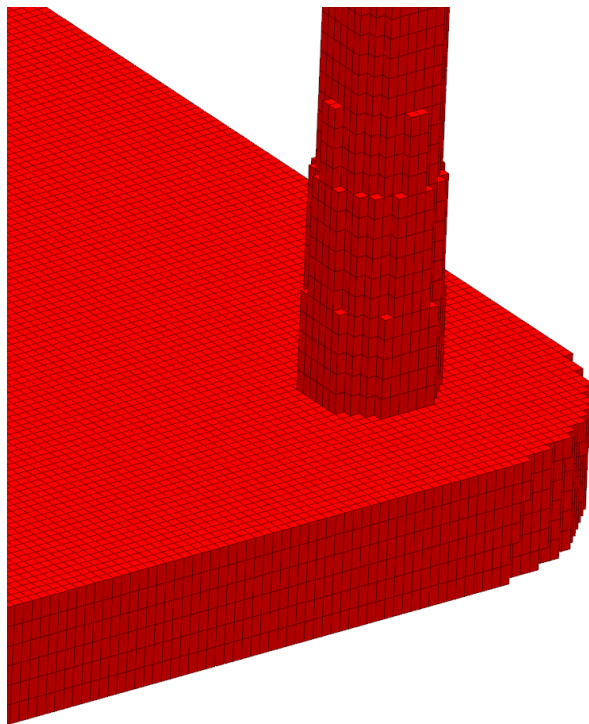
12.4.1 Part geometry and simulation settings

The simulation was carried out employing a rubber injection moulding multi-cavity mould configuration as described by Traintinger [198] in his Ph.D. thesis, coupled with a cold running system. The 4 cavities are all equal, being $161.3 \times 110.6 \times 6.3 \text{ mm}^3$, as shown in Figure 12.1(a). The mould temperature was set to 180°C by heating cartridges positioned above and below the cavities; filling time was set to 10 s, and the curing time to 210 s. Steel was defined as the mould material, with thermal conductivity at 100°C equal to $46.6 \text{ W}\cdot\text{m}^{-1}\cdot\text{K}^{-1}$. Heat transfer coefficients were set as the software-suggested default values: $10 \text{ kW}\cdot\text{m}^{-2}\cdot\text{K}^{-1}$ for steel-steel contact surfaces, and $0.8 \text{ kW}\cdot\text{m}^{-2}\cdot\text{K}^{-1}$ for liquid silicone rubber-steel surfaces. A generic injection moulding machine was chosen from SIGMASOFT database (*SIGMA/generics160-50*), with 1600 kN maximum clamping force, 1300 bar maximum injection pressure, and $3000 \text{ bar}\cdot\text{s}^{-1}$ maximum pressure increase rate. This virtual injection moulding machine is characterized by 60 cm^3 nozzle volume and 50 mm piston diameter, leading to a maximum dosage volume of 510.51 cm^3 . Three heating cycles were defined and the data were gathered at the fourth cycle.

To compare the various dataset, pressure, temperature, and curing degree information at the sensors (blue squares at the sprue and in the cavity in Figure 12.1(a)) were obtained and analysed for each pair. sensor 1 in the sprue (mould inlet) was placed to check the flow characteristics at the very beginning of injection, being important to derive the necessary parameters for the injection moulding machine. In Figure 12.1(a), sensor 1 is shown above the running system, in the position where the polymer flows from outside the mould into the sprue. sensor 2 in the part was placed close to the cavity entrance to monitor the flow properties. This sensor is positioned in close to the wall opposing the flow entrance into the cavity. This spot in the cavity will face LSR flow during most of the filling stage, being an adequate place to locate the sensor. Only one sensor was employed, since the mould is considered balanced concerning the flow into the four cavities, i.e., the analysis of one cavity is expected to derive the same conclusions as for the other three. Besides, qualitative information concerning the filling pattern was also employed to compare the effect of using different material data to run the simulations. Meshing was accomplished via setting equidistant mesh parameters, with $0.5 \times 0.5 \times 1.0 \text{ mm}^3$ elements, resulting in 937246 cells composing the cavity. A detail of the mesh is shown in Figure 12.1(b). For the gate and the runners, $1.6 \times 1.6 \times 1.6 \text{ mm}^3$ elements were set.



(a)



(b)

Figure 12.1: Runner system and cavity geometry applied in the simulation, showing the position of the pressure and temperature sensors (a), where sensor 1 is located in the mould inlet and sensor 2 is placed inside the cavity facing the flow entrance into the cavity; and detail of the mesh (b) employed in the volume discretization. The geometry is inspired by the work of Traintinger [198].

12.4.2 Viscosity data: oscillatory LAOS and HPCR

The viscosity sub-datasets obtained in Chapter 5 are employed here as input for an injection moulding simulation. For this comparison, datasets A and B from Table 12.1 were utilized and fitted to the Carreau-Yasuda model (Equation 12.4) [199, 200] with the William-Landel-Ferry (WLF) equation (Equation 12.5) [201] to describe the temperature dependency, as follows:

$$\eta(T, \dot{\gamma}) = \eta_{\infty} \alpha_T + \alpha_T (\eta_0 - \eta_{\infty}) [1 + (\lambda \alpha_T \dot{\gamma})^a]^{\frac{n-1}{a}} \quad (12.4)$$

$$\log \alpha_T = \frac{8.86(T_0 - T_S)}{101.6 + (T_0 - T_S)} - \frac{8.86(T - T_S)}{101.6 + (T - T_S)} \quad (12.5)$$

where η_{∞} is the infinite shear viscosity, α_T is the temperature dependence given by Equation 12.5, η_0 is the zero shear viscosity, λ is a time constant, a is a transition parameter, n is the model order, T_0 is the reference temperature, and T_S is the standard temperature. The fitting was conducted by the simulation software and the parameters were obtained for dataset A (viscosity data from oscillatory experiments LAOS) and B (high pressure capillary rheometer) as shown in Table 12.2.

Table 12.2: Carreau-Yasuda model parameters as obtained by fitting the viscosity data from datasets A and B.

Parameter	A	B
η_{∞} , Pa.s	0.0248	0.00917
η_0 , Pa.s	22.75	8.0
a , -	5.0	5.0
n , -	0.103	0.368
λ , s	12.64	12.0
T_0 , °C	72.0	72.0
T_S , °C	-273.0	-103.22

The values reported in Table 12.2 are the parameters that minimize the sum of the squares of the residuals concerning Equations 12.4 and 12.5. The fittings are shown in the Appendix A.12, which contains the plots obtained directly from the simulation software. In this sense, no physical meaning will be derived from these values.

12.4.3 Specific heat capacity: standard and modulated DSC

The specific heat capacity sub-datasets obtained in Chapter 8 are employed here as input for the injection moulding simulations. For

this comparison, two pairs of datasets were used: first datasets B and C from Table 12.1 to compare the effect of the curing signal in c_p data; and second the datasets B and D to compare the magnitude of c_p as varying linearly with temperature.

12.4.4 Curing kinetics: calorimetry and rheology approaches

To compare the approaches employed to characterize LSR curing kinetics, the Kamal model parameters from Table 11.4 were employed for the calorimetry and for the rheological approaches. In this sense, the parameters obtained from the lowest shear rate (0.4383 s^{-1}) were employed. For clarity, the Kamal model parameters obtained in Chapter 11 are repeated in Table 12.3 for the calorimetry-based (dataset D) and the rheological approaches (dataset E).

Table 12.3: Kinetic parameters (average) determined after fitting of the experimental conversion rate $\frac{da}{dt}$ to the Kamal model (Equation (10.11)) for LSR employing the calorimetry approach (dataset B) and the rheological method (dataset E).

Parameter	B	E
$\log(A_1), \text{ s}^{-1}$	24.03	5.00
$\log(A_2), \text{ s}^{-1}$	12.69	17.13
$E_1, \text{ kJ.mol}^{-1}$	193.6	171.3
$E_2, \text{ kJ.mol}^{-1}$	100.9	133.9
$m, -$	1.52	0.73
$n, -$	1.24	3.00
Enthalpy, kJ.kg^{-1}	8.15	8.15

12.5 COMPARISON RESULTS

Following the strategy outlined before, processing parameters related to the simulation output are compared next in pairs, aiming to contrast two datasets obtained via distinct experimental methods. For each pair, the most significant injection moulding phase will be assessed, for example, the effect of different curing kinetics parameters is studied only during the solidification (curing) phase, not during filling.

12.5.1 Viscosity datasets A and B

The effect of distinct viscosity sub-datasets in filling and curing simulations are analysed next mostly in terms of the filling phase. Figure 12.2 shows the flow behaviour of LSR at 20% cavity filling for datasets

A and B. It is possible to see that the flow profile is very similar for both simulations, which is the typical parabolic flow characteristic of the velocity profile described by fluid mechanics. The flow behaviour similarity continues during the whole filling stage. From Figure 5.10, one can realize that at the highest studied temperature (90°C), the viscosity values for both methods (LAOS and HPCR) are comparable for the whole shear rate range. Thus, it is expected that the flow front behaves similarly.

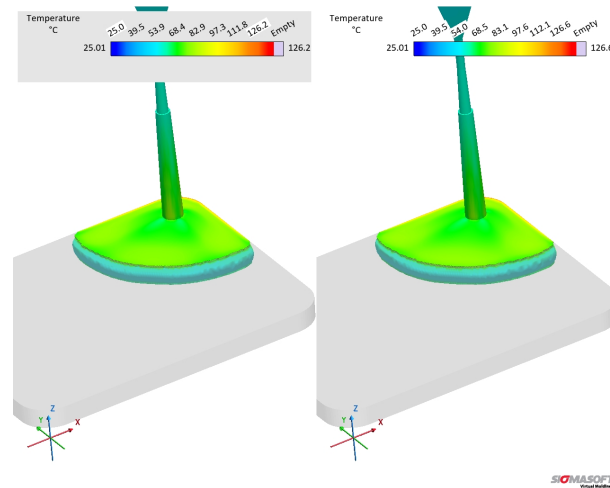
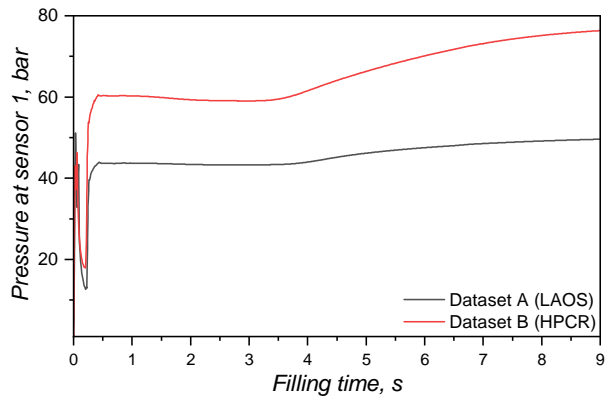


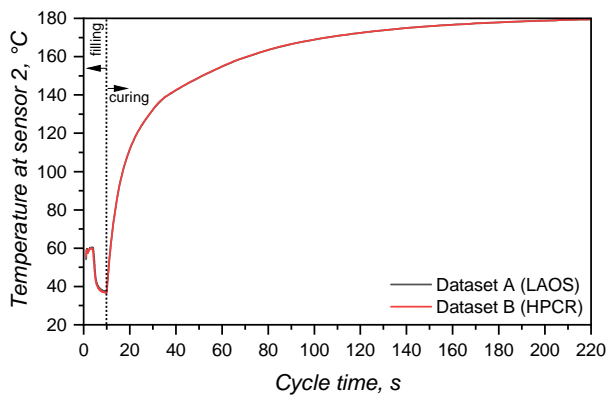
Figure 12.2: Simulated LSR flow behaviour for datasets A (left, LAOS) and B (right, HPCR) at 20% filling for one cavity.

At the sprue, the pressure was monitored via a virtual sensor and plotted over the filling time in Figure 12.3(a). Since LSR flows into the mould at 25°C , higher viscosity for the LAOS dataset is expected, due to the fact that at 50°C (Figure 5.10) $\eta_{LAOS} > \eta_{HPCR}$. This difference in viscosity, i.e., resistance to flow, leads to a difference in pressure as presented in Figure 12.3(a): it is expected a higher pressure for the more viscous sample (dataset B HPCR). The significant increase of pressure at the sprue indicates that, when designing the injection moulding process, distinct injection force/pressure and speed would have to be defined.

In order to check which pressure curve predicts better the actual pressure at the sprue during a real LSR injection moulding process, further experiments would be necessary. This limitation in terms of the scope of the present work is discussed in the conclusion of this Chapter. Nevertheless, this evidence is the most important one concerning the effect of distinct viscosity sub-datasets, since it shows that processing conditions would also be differently set for each dataset. The pressure profile at the surface of the sprue, running system, and cavities is also shown qualitatively in Figure 12.4, where it becomes evident the higher pressure for the simulation ran employing dataset B. Inside the cavity, there is no significant pressure difference at the end of filling for the simulations.



(a)



(b)

Figure 12.3: Simulated pressure at the sprue (sensor 1) during the filling stage (a) and simulated temperature at one cavity (sensor 2) during the injection moulding cycle (b) for two different datasets with distinct viscosity input as described in Table 12.2.

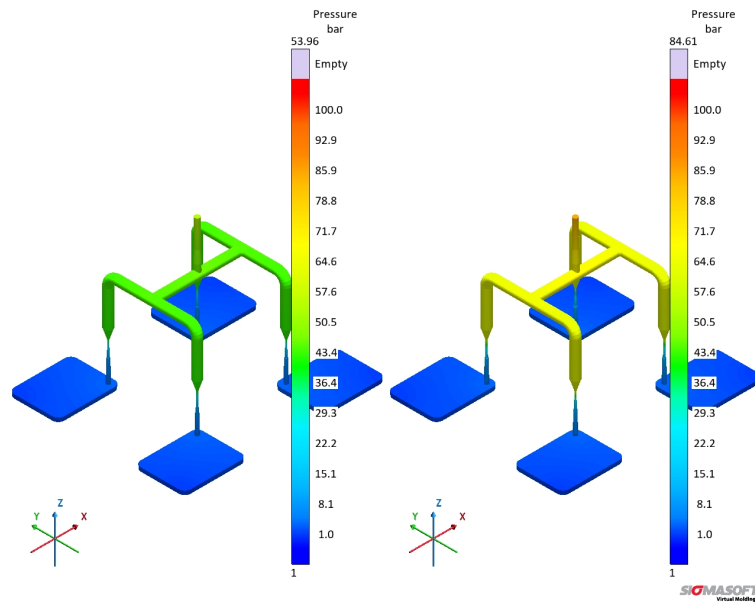
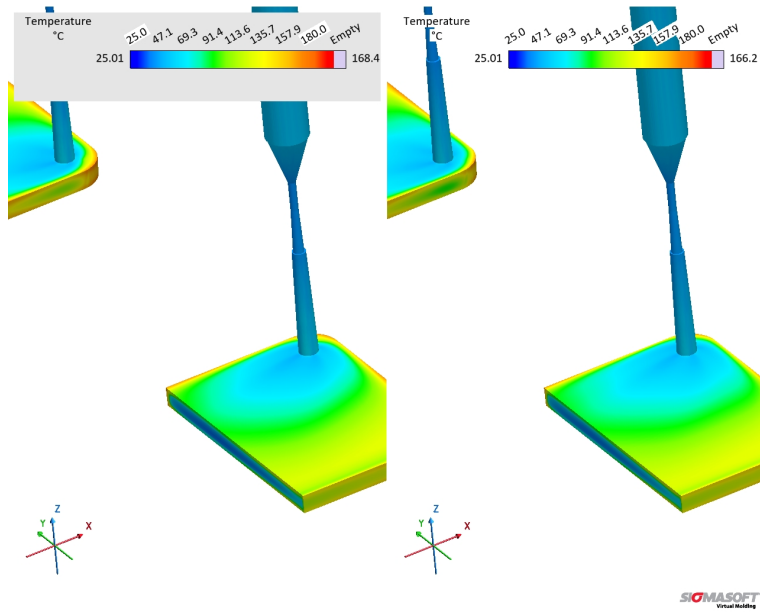


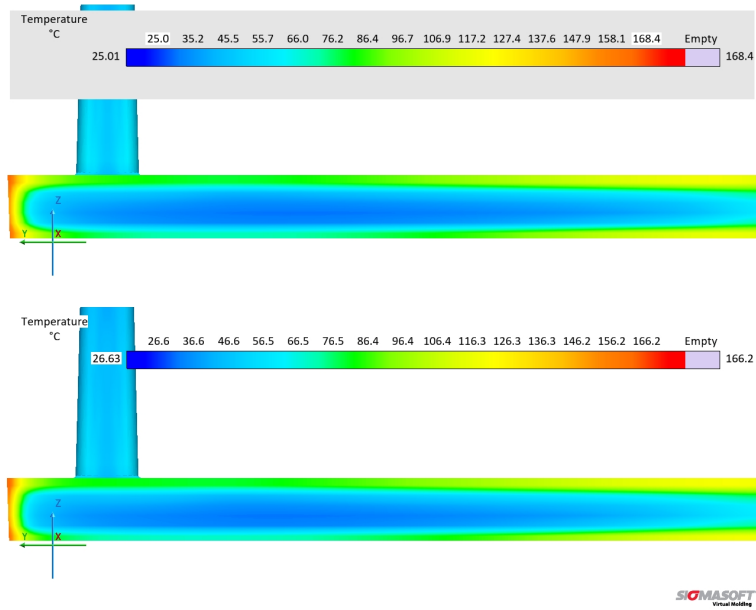
Figure 12.4: Simulated pressure for the whole studied volume, including the sprue and the running system, for datasets A (left, LAOS) and B (right, HPCR), where the pressure difference is evident at the sprue at the end of filling.

The comparison between datasets A and B kept constant the specific heat capacity and thermal conductivity sub-datasets, leading to the simulated temperature curve at Figure 12.3(b). During the whole cycle, the temperature measured at the sensor was the same for both datasets, indicating that the viscosity data did not effect how LSR heats up inside the cavity. Indeed, this difference will be observed in the next comparison concerning c_p . Qualitatively, the cavity temperature at the end of filling is also shown in Figure 12.5. It is valuable to analyse the thermal state of the cavity at the end of filling because no significant crosslinking should occur before the cavity is completely filled. From the figure, besides the fact that both datasets lead to similar simulated temperature profiles, one can realized that the temperature at the surface is in the vicinity of curing onset. On the other hand, at the center of the cavity (visible in the cross-section region shown in Figure 12.5), the temperature is below the curing temperature.

In order to demonstrate the curing state at the end of filling, Figure 12.6 shows the curing degree for the cavity. This confirms the indications that no significant curing occurs during filling, avoiding pre-curing (scorch). There are regions close to the walls near the cavity entrance that indicate curing. This happens because the flow reached those areas first, leading to higher residence time in contact with the walls at 180°C. These areas, however, do not hinder or disturb the flow, since it flows away and parallel (see Figure 12.2) to these walls.



(a)



(b)

Figure 12.5: Simulated cavity temperature at the end of the filling stage for datasets A (left, LAOS) and B (right, HPCR) (a), with snapshot of the part cross-section for datasets A (top, LAOS) and B (bottom, HPCR) (b).

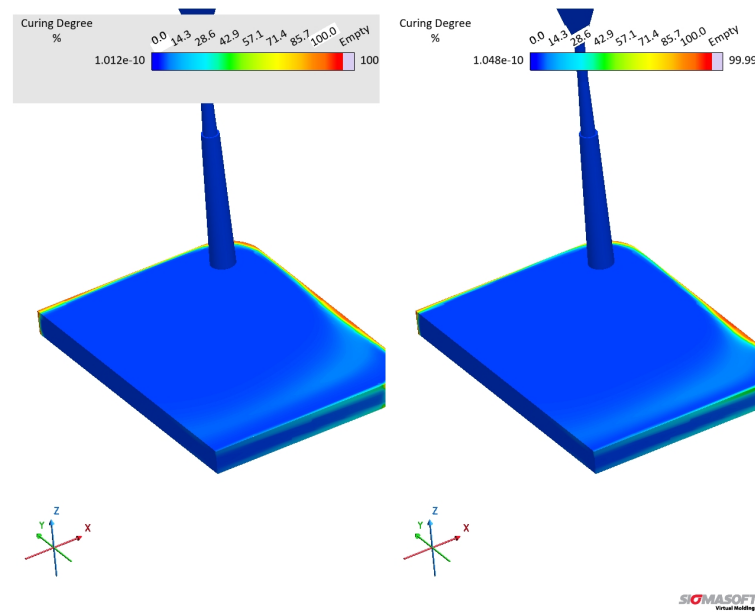


Figure 12.6: Simulated curing degree at the cavity for datasets A (left, LAOS) and B (right, HPCR) at the end of the filling step.

12.5.2 Specific heat capacity datasets B and C

Differently from the comparison concerning viscosity sub-datasets, the specific heat capacity affects mostly the temperature profile and, therefore, the solidification (curing) phase of the injection moulding cycle. At Figure 12.7, it is possible to check that the pressure at sensor 1, located at the sprue, is very similar for both datasets. The pressure is slightly higher for dataset B (MDSC 1st heating) because the higher c_p values for this sub-dataset (for reference, see Figure 8.2) cause lower flow temperature for the same mould temperature, leading to a higher viscosity. Overall, however, the different specific heat capacity values did not significantly affect the pressure at the sprue. This means that, for a real process, no critical difference would rise if the processing set was based on simulation B or C.

The effect of different c_p values on the cavity temperature is quantitatively shown in Figure 12.7(b) and qualitative shown in Figure 12.8(a). Dataset C causes higher temperatures throughout the whole cycle than dataset B, which is a direct consequence of the lower c_p determined by the sapphire method during the first heating. Besides, it is possible to realize that the input concerning enthalpy (8.15 kJ.kg^{-1}) in dataset B was not enough to equalize the temperature to dataset C. This probably occurs due to the fact that the software apparently does not connect the released heat with the curing rate, as stated in Equation 8.3, in order to account for the internal heat source. If this is the case, then it is more reliable to input specific heat capacity data set determined by the sapphire 1st heating method, since it accounts for the heat release that ultimately raises the polymer temperature.

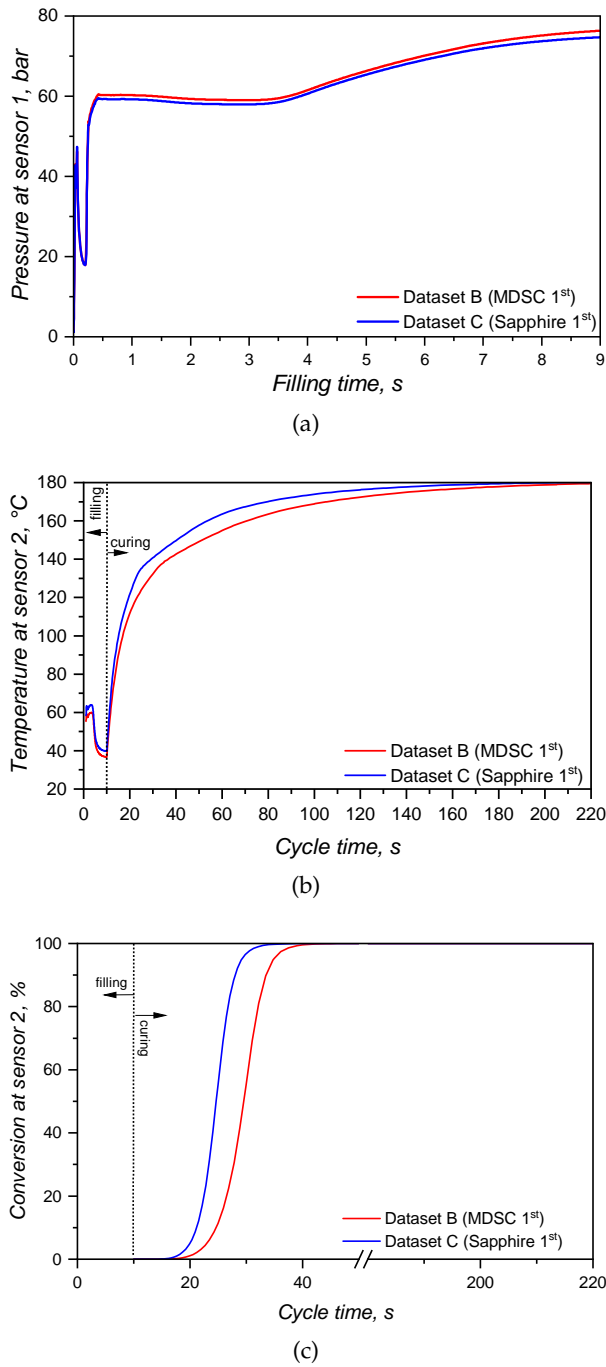


Figure 12.7: Simulated pressure at the sprue (sensor 1) during the filling stage (a), simulated temperature at one cavity (sensor 2) during the injection moulding cycle (b), and curing degree (c) for the two different datasets B and C with distinct specific heat capacity input as shown in Table 12.1. The c_p data concerning MDSC 1st and sapphire 1st can be consulted at Figure 8.1.

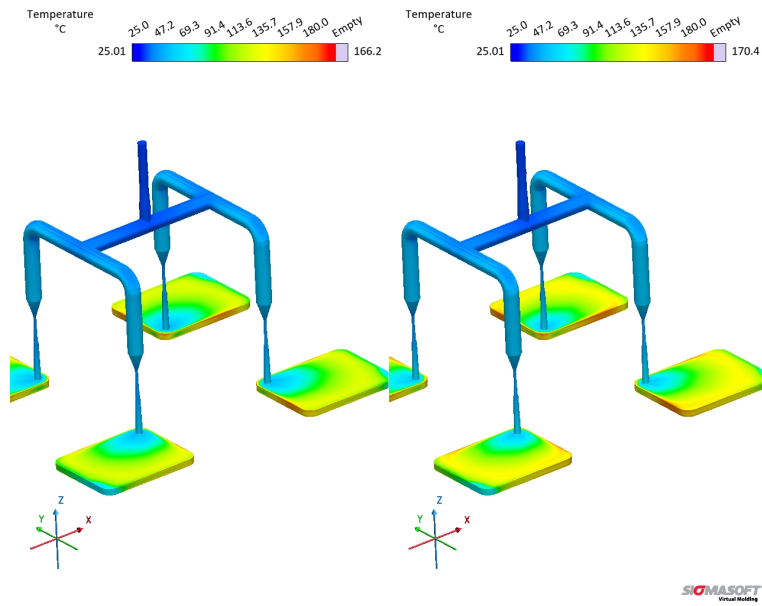
The curing degree or conversion calculated at the sensor 2 position is shown for the whole cycle duration in Figure 12.7(c), while it is qualitatively shown for the cavity surface at Figure 12.8(b). The curing degree behaviour is directly connected to the temperature profile analysed before, i.e., the higher the temperature at a given cycle time t , the higher the conversion, as it can be seen in the Figure 12.8(c). Both datasets contain the same curing kinetics information, but heat up at different paces, leading to distinct curing times. At the end of the filling stage, it is possible to realize from Figure 12.8 that the simulation carried out with dataset C indicates a curing degree at the cavity surface around 30% in some regions, while the whole cavity upper surface shows negligible curing degree. In this sense, there is no possibility of scorch for any of the scenarios.

The curing degree development during the curing phase is shown in Figure 12.9 for $t = 25$ s and $t = 55$ s (cycle time). At 25 s (Figure 12.9(a)), the crosslinking degree difference can be observed, being low close to the cavity entrance for both datasets (lower residence time when compared to the other cavity areas), but still higher for dataset C. At 55 s, the simulation showed for dataset C complete curing for the part, while dataset B's simulation presented an uncured core. Even though dataset B is not completely cured after 55 s, it is possible to state that the part could still be ejected at this condition, since ejection typically occurs between 75% and 95% completion of cure [48].

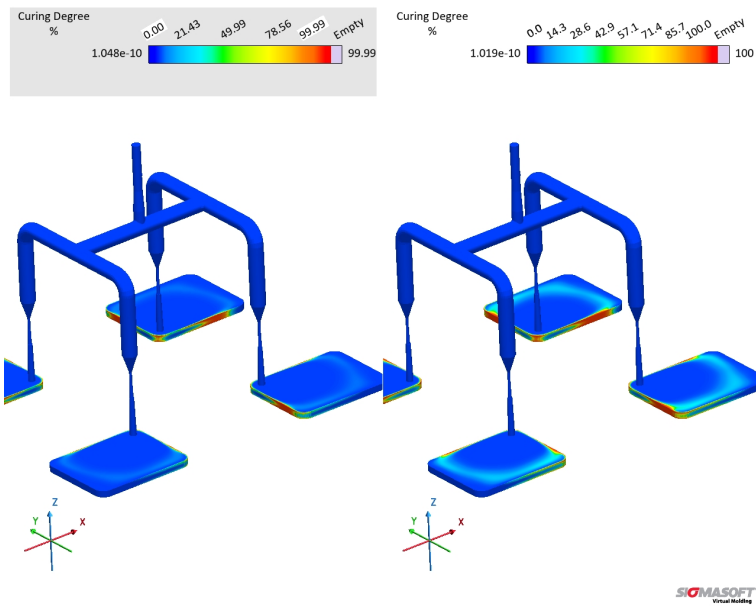
12.5.3 Specific heat capacity datasets B and D

In order to compare the specific heat capacity datasets that have a linear relationship of c_p with temperature (MDSC 1st and sapphire 2nd), i.e., without the crosslinking contribution, datasets B and D were compared in terms of their simulation outputs. From the pressure and temperature signals presented in Figure 12.10, one can realize that both datasets present similar results, having dataset D slightly higher temperature development than dataset B. The higher temperature related to dataset D reflects in an earlier curing onset, as presented in Figure 12.10(c). The curing degree behaviour for dataset C is shown for comparison, where it is possible to observe not only the effect of the lower average c_p , but also the heat release contribution (realized as a downward peak at c_p).

When comparing the temperature at the end of the filling stage, datasets B and D present similar behaviour, as shown in Figure 12.11. The temperature difference at the center of the part is 1.7 K, which is also the average for the temperature close to the cavity upper surface. These dataset will eventually lead to higher temperature differences as the cycle proceeds (Figure 12.10). In this sense, there is no significant impact of the specific heat capacity in the filling phase, resulting in no scorch or problems to fill the whole cavity within the set filling time.

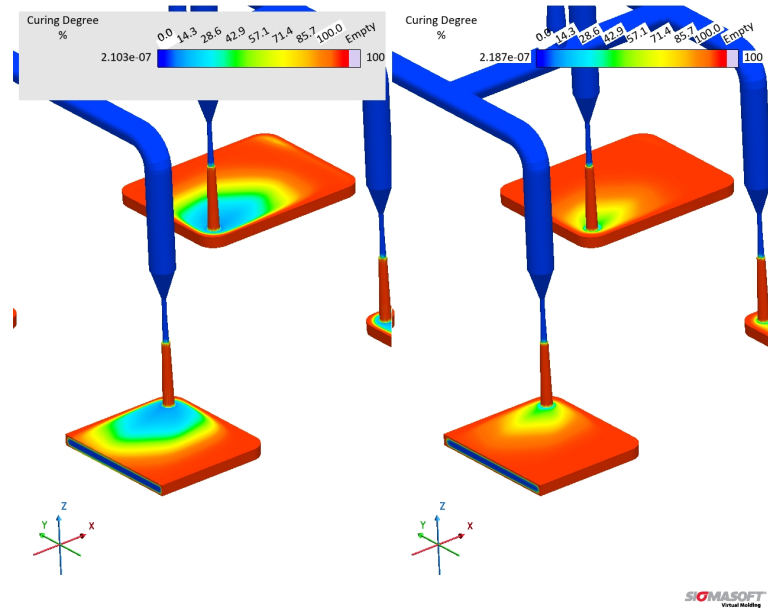


(a)

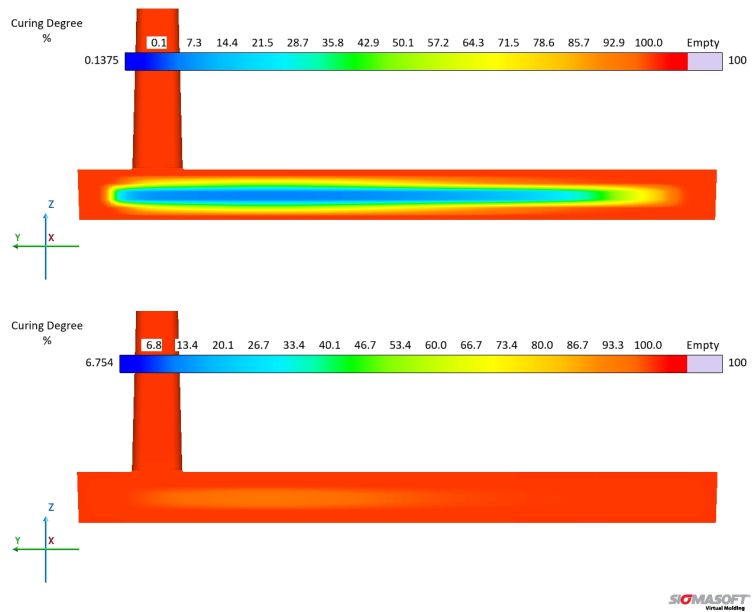


(b)

Figure 12.8: Simulated cavity temperature at the end of the filling stage for datasets B (left, MDSC 1st) and C (right, sapphire 1st) (a), with the correspondent curing degree (conversion 0-100%) (b).

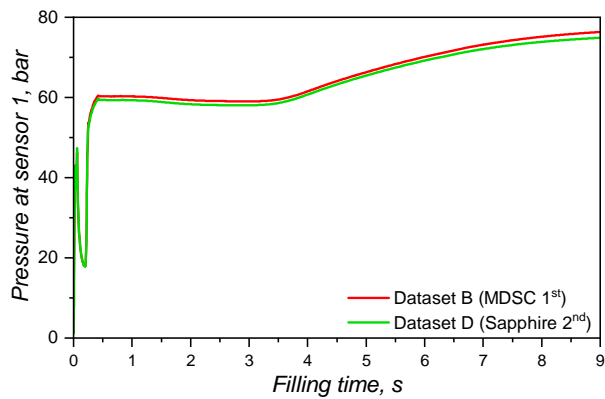


(a)

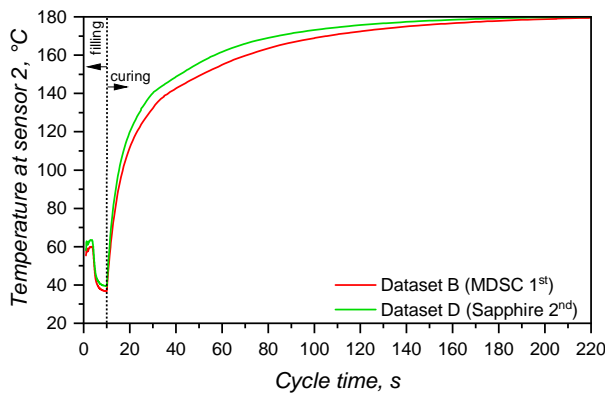


(b)

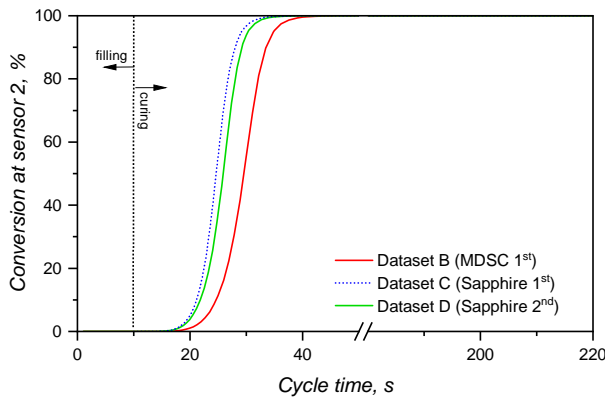
Figure 12.9: Curing degree at $t = 25$ s (a) and at $t = 55$ s (a) for datasets B (left and top, MDSC 1^{st}) and C (right and bottom, sapphire 1^{st}).



(a)



(b)



(c)

Figure 12.10: Simulated pressure at the sprue (sensor 1) during the filling stage (a), simulated temperature at one cavity (sensor 2) during the injection moulding cycle (b), and curing degree (c) for the different datasets B and D with distinct specific heat capacity input as shown in Table 12.1. The c_p data concerning MDSC 1st and sapphire 1st can be consulted at Figure 8.1. The conversion values for dataset C are shown in (c) for comparison purposes.

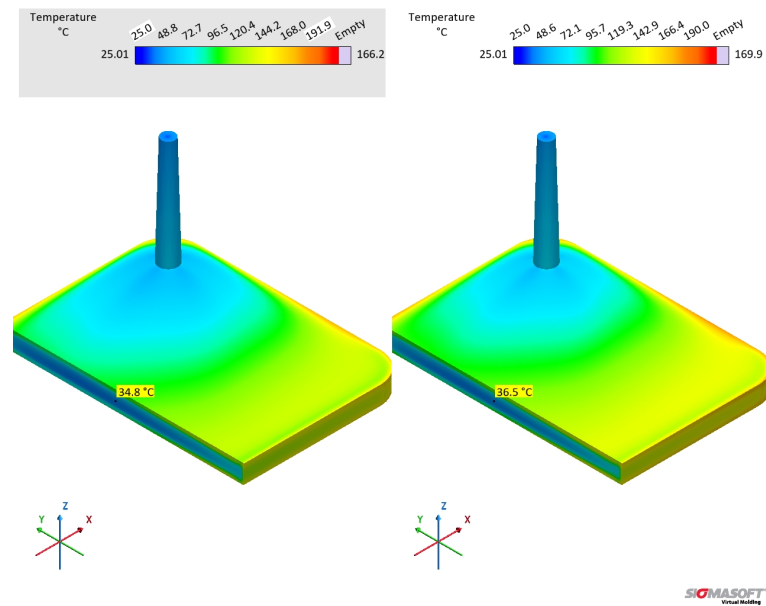


Figure 12.11: Simulated temperature at the cavity for datasets B (left, MDSC 1st) and D (right, sapphire 2nd) at the end of the filling step, with the assigned local temperature at the center of the cavity cross-section: 34.8°C (left) and 36.5°C (right).

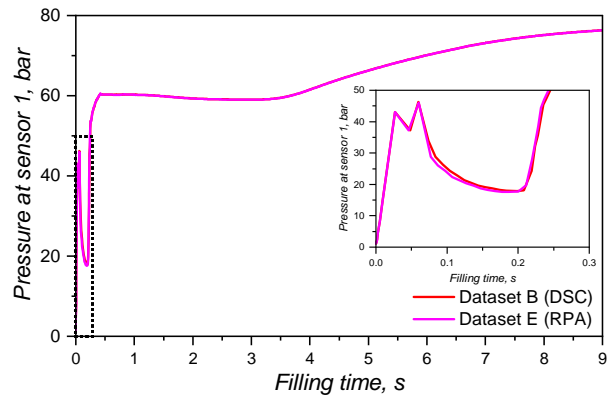
12.5.4 Curing kinetics datasets B and E

Finally, the impact of distinct curing kinetics parameters (Table 12.3) in the filling and curing simulation of LSR injection moulding was studied, and the pressure, temperature, and curing degree development within the injection moulding cycle is shown in Figure 12.12. As it was already demonstrated for the c_p study, the pressure measured by sensor 1 did not present significant difference when comparing datasets B (curing parameters based on DSC experiments) and E (curing kinetics characterized via rubber process analyser). This is due to the fact that the position where sensor 1 is located does not reach the curing onset temperature, thus not being affected by the cross-linking kinetics. Therefore, both datasets present the same pressure profile (Figure 12.12(a)) at the sprue, leading to possibly the same setups when concerning the injection moulding machine capacity (force, injection speed, etc.).

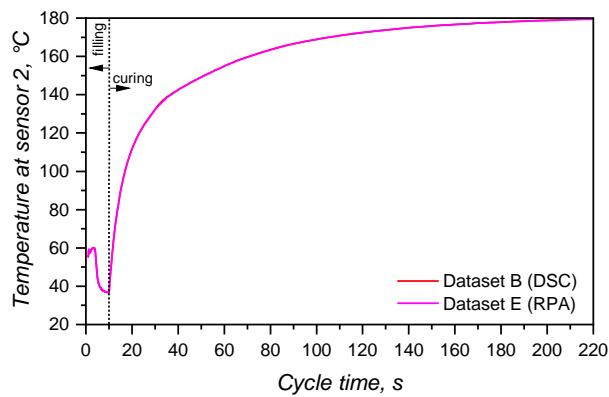
At sensor 2, which is located close to the cavity entrance, the temperature development (Figure 12.12(b)) is also the same for both datasets, reflecting the equal specific heat capacities that were set for these samples. However, since the Kamal model parameters are different, distinct curing degree were measured at sensor 2, which are shown in Figure 12.12(c). As it was explained before, no scorch occurs during filling, since the curing degree is negligible before $t = 10$ s at the location of sensor 2. This is shown in qualitative terms by Figure 12.13: even though the curing onset is already reached at the end of filling (Figure 12.13(a)), no significant curing occurs (Figure 12.13(b)).

The curing degree inside the cavity follows the conversion trend presented in Chapter 11, where the calorimetric data displayed an earlier onset compared to the rheological one. Besides, the curing degree calculated for dataset B reached 90% 19 s before dataset E, demonstrating once again the problem related to the rheological data concerning marching modulus (conversion values were calculated based on the torque data, that were sensitive to the marching modulus). However, when one considers that ejection typically occurs between 75% and 95% completion of cure for LSR [48] due to the fact that the remaining internal heat after ejection is capable to complete the part curing, datasets B and E experience 5 s difference in the curing time, reaching 75% curing degree at around 32 s and 37 s, respectively.

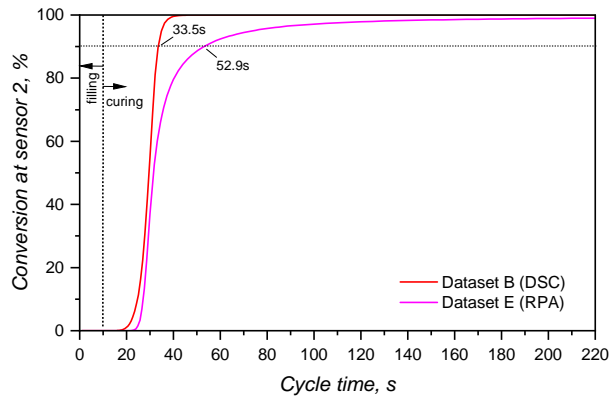
Qualitatively, Figure 12.14 shows the curing degree development for various cycle times, highlighting the differences in terms of cross-linking onset and speed for the distinct datasets. Between 30 s (Figure 12.14(b)) and 40 s (Figure 12.14(c)), the part upper surface already reaches at least 70% of curing, while the part core (blue area evidenced by the cross-section) is still mostly uncured for both datasets.



(a)



(b)



(c)

Figure 12.12: Simulated pressure at the sprue (sensor 1) during the filling stage (a), simulated temperature at one cavity (sensor 2) during the injection moulding cycle (b), and curing degree (c) for the different datasets B and E with distinct curing kinetics inputs as shown in Table 12.3. The dashed area shown in (a) between 0 and 0.3 s is enlarged in the same plot to aid differentiation of the curves. The time at which curing degree = 90% is marked in (c) as 33.5 s for dataset B and 52.9 s for dataset E.

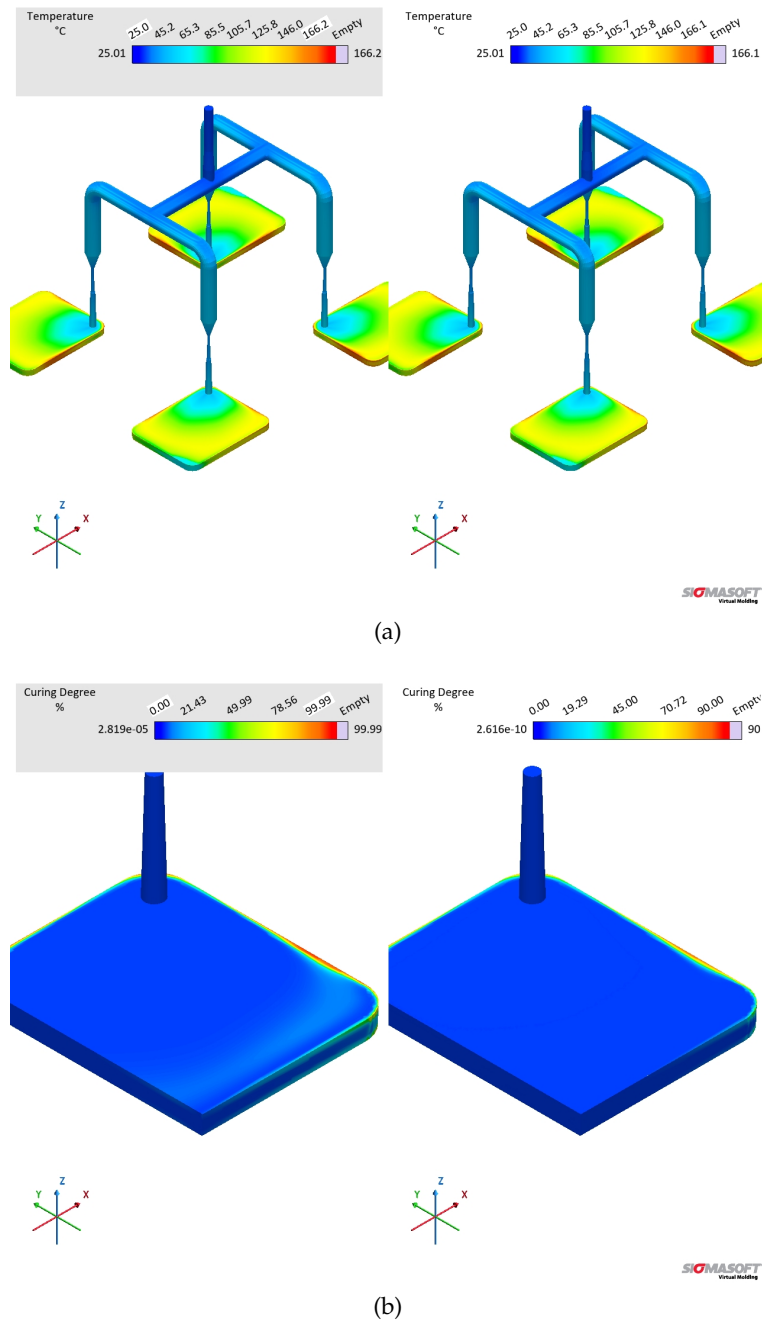
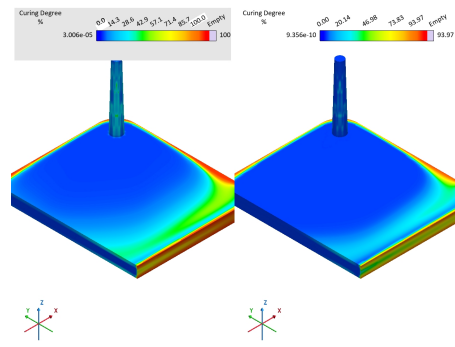
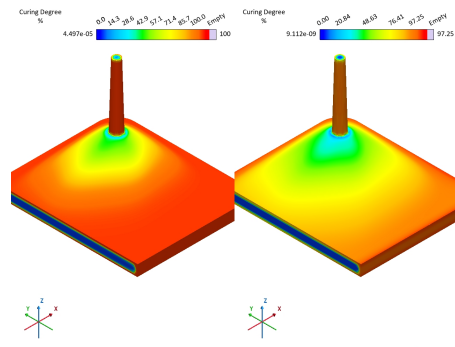


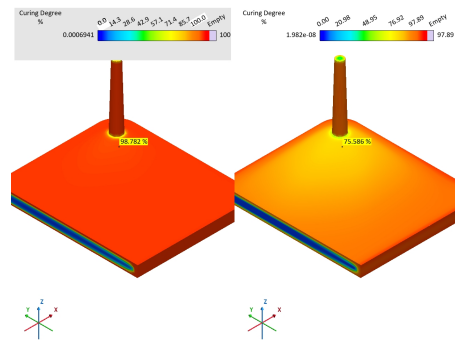
Figure 12.13: Simulated cavity temperature at the end of the filling stage for datasets B (left, DSC) and E (right, RPA) (a), with the corresponding curing degree (conversion 0-100%) (b).



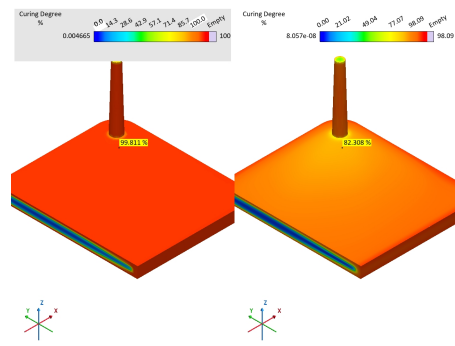
(a)



(b)



(c)



(d)

Figure 12.14: Simulated cavity curing degree (conversion 0-100%) for datasets B (left, DSC) and E (right, RPA) at the cycle times $t = 15$ s (a), 30 s (b), 40 s (c), and 45 s (d). The local surface indications for the curing degree assign 98.78% (left) and 85.59% (right) at (c); and 98.81% (left) and 82.31% (right) at (d).

12.6 CONCLUSIONS OF THE CHAPTER

It was demonstrated in the previous Chapters of this work that the main properties necessary to perform injection moulding simulation of liquid silicone rubber can be assessed via different experimental methods. Thus, it becomes reasonable to compare these distinct material datasets in actual injection moulding simulations. Thus, pairs of datasets related to viscosity (fully described in Chapter 5), specific heat capacity (presented in Chapter 8), and curing kinetics (studied in Chapter 11) were investigated. The main results of this Chapter were the processing-related signals: pressure at the sprue (measured by sensor 1), temperature at the cavity (measured by sensor 2), and curing degree (also referred as conversion, measured by sensor 2). Besides, the spacial qualitative variation in the mould of these parameters were also taken into consideration.

The investigation of the viscosity datasets revealed significant insights into the influence of different viscosity inputs on the simulation outcomes. Utilizing two distinct datasets, obtained from oscillatory experiments at large amplitude under non-linear viscoelastic conditions (LAOS) and high-pressure capillary rheometry (HPCR), it was found that both datasets produced similar flow profiles during the filling phase, indicative of a typical parabolic velocity profile. However, at lower temperatures, the LAOS dataset exhibited higher viscosity compared to the HPCR dataset, resulting in a higher pressure at the sprue for the LAOS dataset. This difference in pressure highlights the need for adjusting injection force and speed based on the specific viscosity dataset used to perform the simulation, as higher viscosity increases resistance to flow and, consequently, the required injection pressure. Despite the differences in pressure, the temperature profiles within the cavity remained consistent across both datasets, suggesting that viscosity variations did not significantly impact the thermal behaviour of LSR during the injection moulding process. Furthermore, the curing degree analysis indicated that minimal curing occurred during the filling phase, with only slight curing observed near the cavity walls due to higher residence time in contact with the heated mould surfaces.

The analysis of specific heat capacity datasets elucidated the impact of this thermal property on the simulation results. The study compared two pairs of datasets: one obtained via MDSC at 1st heating and another via the standardized sapphire method at 1st heating, which differ in the effect of curing on specific heat capacity; and via MDSC at 1st heating and by the sapphire method at 2nd heating, which vary linearly with temperature. For MDSC 1st heating and sapphire 1st heating, the pressure at the sprue remained similar, although slightly higher for MDSC 1st heating due to its higher specific heat capacity, resulting in a lower flow temperature and higher viscosity. This indic-

ates that in a real process, choosing between these datasets would not significantly affect the pressure profile. However, the cavity temperature showed noticeable differences, with sapphire 1st heating causing higher temperatures throughout the cycle due to its lower specific heat capacity. This discrepancy suggests that sapphire 1st heating may provide a more accurate thermal prediction, as it better accounts for heat release during curing, which the simulation software did not fully capture with MDSC 1st heating. Consequently, the curing degree was higher for sapphire 1st heating, indicating faster curing and a reduced risk of scorch. In contrast, MDSC 1st heating showed an uncured core at the end of the cycle, although still within acceptable limits for part ejection. When comparing MDSC 1st heating and sapphire 2nd heating, both exhibited similar temperature and pressure profiles, but sapphire 2nd heating led to slightly higher temperatures and earlier curing onset, reflecting the influence of its lower specific heat capacity. This comparison underscores that while specific heat capacity variations do not critically impact the filling phase, they significantly influence the curing behavior and thermal management during the injection moulding process.

The analysis of curing kinetics datasets compared two distinct approaches: calorimetric (DSC-based) and rheological (rubber process analyser-based) methods. Both datasets showed no significant difference in pressure at the sprue due to the location of the sensor, which does not reach curing onset temperatures, indicating that injection moulding machine setups (such as force and injection speed) would remain unaffected by the choice of curing kinetics dataset. Besides, the temperature development near the cavity entrance was identical for both datasets, owing to the same specific heat capacities used in the simulation. Despite this, the curing degrees differed significantly due to the distinct Kamal model parameters. The calorimetric dataset exhibited an earlier onset and faster curing rate compared to the rheological dataset, with the curing degree reaching 90% approximately 19 seconds earlier. This disparity highlights the challenges associated with using rheological data, particularly the issue of marching modulus affecting the torque-based conversion calculations. Nonetheless, both datasets reached 75% curing degree within a close timeframe (32 seconds for the calorimetric data and 37 seconds for the rheological data), aligning with the typical ejection criterion for LSR parts, which relies on the remaining internal heat to complete curing post-ejection. Qualitative analysis of the curing degree development further illustrated these differences, with both datasets showing at least 70% curing at the part's upper surface between 30 s and 40 s, while the part's core remained mostly uncured.

Part VI

CONCLUSIONS AND FINAL REMARKS

FINAL REMARKS

This final Chapter concludes the present work assessing the proposed objectives and resuming the main outcomes. Besides, it is discussed the limitations of this Thesis and future investigations are prospected, aiming to continue advancing in this topic.

13.1 PHILOSOPHICAL OBJECTIVES

As proposed in the introductory part, the following philosophical objectives can now be assessed:

1. How has this research contributed to the *generation of knowledge*?
2. How has this investigation contributed to the *development of individuals*?
3. How has this thesis contributed to the *wider research community*?
4. How has this work contributed to *broader society*?

Considering the current gap in the scientific literature concerning the investigation of injection moulding grades of liquid silicone rubber, the present Thesis adds to the state of the art in terms of novel findings and methodological insights to characterize LSR for simulation purposes. In this sense, the knowledge generated in this regards is useful not only for the research community, but also, and very importantly, to the industry. Simulation software developers can employ the disclosed knowledge described in this work to develop their routines. Additionally, companies that employ the injection moulding process to manufacture liquid silicone rubber-based products benefit from this Thesis by having a deep study of many phenomena related to LSR characterization. Since the development of This thesis involved different institutions and, consequently, numerous people (bachelor, master, and Ph.D. students, among other researchers and professores), it is understood that the present work added to their overall knowledge about liquid silicone rubber, mainly the peculiarities of this material. Finally, by adding scientific and industrial knowledge to the current technological state of the society, this Thesis impacts the broader society by aiding the manufacture of high-quality products, with longer lifetime, and improving the life quality of their users.

13.2 SCIENTIFIC GOALS

Furthermore, the general scientific goals can now be assessed for each of the Parts of this work, linking the material data characterization (Parts II, III, and IV) to the simulation comparisons presented in Part V.

The specific objective of Part II was to reliably define LSR's viscosity as a function of temperature and shear rate, considering the material's complex interactions among polymer chains and fillers. This objective was met through a comprehensive investigation of various methodologies for determining the viscosity of liquid silicone rubber (LSR) under different conditions that mimic the injection moulding environment. The study critically and systematically compared state-of-the-art approaches, suggesting that steady shear-based techniques like rotational steady experiments and high-pressure capillary rheometer (HPCR) methods are most effective in capturing the microstructural changes of LSR under shear. These changes are primarily attributed to the structure of silica fillers present in commercial LSR grades, which undergo disruption under shear and recovery when shear ceases.

Oscillatory experiments, commonly used in rheological studies, were also examined. The traditional Cox-Merz rule, which links steady and oscillatory shear properties, was not upheld in this study. However, under non-linear viscoelastic conditions, the results from steady and oscillatory (LAOS) experiments converged, indicating a comparable filler structure only achievable in non-linear regimes. This was further analyzed using Fourier-transformation and Chebyshev coefficients, translating the concept of complex viscosity to a non-linear viscoelastic scenario. These findings underscore the importance of considering microstructural changes during viscosity determination.

The rheological properties of LSR were scrutinized in detail, providing insights for future research on viscosity determination for polymer processing simulations. The methodologies employed were critically analyzed, contributing to a deeper understanding of the rheological behavior of LSR. In Part V of this Thesis, the LAOS and HPCR methodologies were compared in terms of their impact on injection moulding simulation parameters, achieving the objective of correlating rheological data with processing conditions. The results demonstrated that different viscosity datasets can significantly affect the simulation outcomes. Specifically, the LAOS dataset exhibited higher viscosity at lower temperatures, resulting in higher pressure requirements during mould filling compared to the HPCR dataset. This indicates that the choice of viscosity dataset is crucial for accurately predicting processing parameters and ensuring the quality of the final product. Therefore, this study successfully achieved its objective by providing a detailed analysis of viscosity determination methods and their implications for LSR injection moulding.

The objective of Part III was to accurately determine LSR's specific heat capacity (c_p) and thermal conductivity (λ) concerning temperature and the chemical state (non-crosslinked or cured), and to assess the pressure-volume-temperature (pvT) behavior of LSR. This objective was achieved through a detailed analysis of the thermal properties necessary for the injection moulding simulation of LSR. The study employed both the standardized sapphire method and the modulated temperature approach to measure the specific heat capacity, demonstrating that while c_p is temperature-dependent, it is not influenced by the curing state of the samples. The modulated temperature approach captured the true specific heat capacity, necessitating the inclusion of curing enthalpy information to accurately describe energy conservation. Conversely, the sapphire method integrated enthalpic data into the specific heat capacity, reflecting the exothermic nature of the curing reaction, which is crucial for energy balance in simulations.

The investigation into thermal conductivity revealed that it remains relatively stable across LSR processing temperatures for both uncured and cured states of LSR. This stability supports the assumption of a constant thermal conductivity in simulation routines, thereby simplifying the computational process without significant accuracy loss. This finding is beneficial for reducing computational complexity and time, ensuring efficient simulations. Additionally, understanding the minor variations between individual components and their mixtures aids in planning material data characterization before simulations.

The analysis of specific volume, described accurately by the Tait model, confirmed the expected behavior based on macromolecular arguments and literature reports. This aspect of the study is critical for determining the most suitable filling conditions in injection moulding to prevent processing issues such as flashing. Thus, the thermal properties investigated in the dedicated study provide essential data for improving the accuracy and efficiency of LSR injection moulding simulations.

Connecting these findings with the simulation comparisons carried out at the final Part of this Thesis, it was observed that the choice of specific heat capacity datasets significantly impacted the temperature profile and curing behaviour during the injection moulding cycle. The sapphire method, which accounts for the heat release during curing, provided a more reliable temperature profile in simulations compared to the modulated temperature approach. This difference in temperature profiles influenced the curing kinetics, where higher temperatures led to faster curing rates and earlier completion of the curing process.

Ultimately, a crosslinking study aimed to precisely identify LSR's crosslinking kinetics and compare different approaches to determining the curing behavior. This goal was met by confirming that both calorimetry- and rheology-based methods are effective in determining

the curing kinetics of silicone rubber. The Kamal model (autocatalytic) was found sufficient for describing the curing speed (conversion rate $d\alpha/dt$) of both high consistency and liquid silicone rubbers.

For high consistency silicone, rheological data demonstrated that increasing dicumylperoxide concentration accelerates the crosslinking reaction, reducing the induction time and increasing reaction velocity. This acceleration results in a higher but limited maximum detected torque, which varies significantly at different temperatures. A correlation was established between optimum cure time, curing temperature, and dicumylperoxide concentration, providing a predictive tool for cycle times in compression or injection moulding. The kinetic parameters indicated that while the pre-exponential factor decreased, the overall reactivity (represented by the Arrhenius rate constant) increased with higher dicumylperoxide concentration, attributed to the catalytic effect of radicals involved in crosslinking. This illustrates that curing depends not only on crosslinker concentration but also on the thermodynamic and kinetic characteristics of the curing mechanism, including limitations due to active sites for radical reaction and radical recombination.

For liquid silicone rubber, the classical definition of gel time was found unreliable for determining when LSR ceases to flow, as physical gels from filler-filler interactions and entanglements occur from the early stages of curing. Notably, characterizing curing kinetics via dynamic scanning calorimetry (based on released heat) or rheology (based on increasing resistance to shear) yields different kinetic parameters. While the calorimetric approach effectively follows the entire curing process, the rheology-based method struggles with detecting the real onset of curing due to device sensitivity limitations. These methods, when linked to the Kamal model, suggest different kinetic models best describe the curing reaction: the calorimetric method aligns with the autocatalytic model, while rheological analysis fits the n^{th} order model. Despite these differences, both methods produced conversion rate data that fit well to the Kamal model with low residuals, though the calorimetric method showed less variation compared to the rheological approach.

Linking these findings with the simulation comparisons, it became clear that the choice of kinetic parameters and the method used to obtain them significantly impact the simulation outcomes. Specifically, simulations using calorimetric data, which align with the autocatalytic model, showed a more predictable and consistent curing process compared to those using rheological data. This difference highlights the need for careful selection of curing kinetic data in simulation routines, given the different behaviors observed between the two approaches.

13.3 LIMITATIONS OF THE STUDY

This Thesis has brought forward important insights into the simulation of liquid silicone rubber (LSR) injection moulding, yet there are several limitations that merit discussion. The principal limitation is the inability to conduct actual injection moulding experiments to directly validate the simulation findings. Access to LSR-specific injection moulding machines is limited, as these machines are specialized and were not available in either university labs or through industrial partners. This restriction made it impossible in the scope of this work to empirically verify which material dataset could more precisely predict processing signals during actual manufacturing conditions.

Additionally, the study was limited to only two grades of liquid silicone rubber designed for injection moulding. While these grades are representative of typical industry materials, LSR formulations are diverse, especially in terms of filler content, which can significantly impact the material's rheological and thermal properties. Most commercial LSR grades contain fillers, and although the outcomes of this Thesis are likely relevant to other filled grades, the specific effects of different fillers and their concentrations were not examined.

These limitations point towards potential areas for future research, particularly the need for collaborations that could provide access to specialized LSR moulding equipment and the extension of the research to include a broader array of LSR grades. Such future studies would deepen the understanding of LSR processing dynamics and improve the precision of simulation models, effectively closing the gap between theoretical simulations and practical manufacturing realities.

13.4 FUTURE RESEARCH DIRECTIONS

To address the limitations identified in this Thesis and to further enhance the predictive accuracy of LSR injection moulding simulations, several directions for future research are proposed:

1. Empirical validation of simulation models: collaborations with industry partners or research institutions that have access to specialized LSR injection moulding machines would be invaluable. Conducting real-world moulding experiments would allow for direct validation of simulation results, assessing the precision of different material datasets in predicting processing signals.
2. Expansion of material grades: broadening the scope of investigated LSR grades can provide a more comprehensive understanding of how variations in formulations affect processing dynamics. Including a wider range of filler contents would help in generalizing the simulation models to be applicable to a broader spectrum of commercial LSR grades.

3. Development of real-time measurement devices: advancing and implementing devices that can measure key properties during the injection moulding process could significantly enhance the real-time monitoring and control of the moulding process. On-line viscosimeters and infrared sensors for measuring curing degree are examples of technologies that could be further developed and validated for this purpose.
4. Innovation in modelling approaches: the development of new models that more accurately predict the flow and curing behaviours of LSR during injection moulding would help in bringing simulation closer to reality. These models could incorporate more complex aspects of material behaviour under the dynamic conditions of moulding, such as phase changes and chemical reactions.
5. Comparison with alternative simulation software and independent methods: exploring the efficacy of different simulation software or employing independent finite element methods could provide deeper insights into the strengths and weaknesses of current approaches. Tailoring simulations in more advanced ways, possibly by integrating custom modifications or enhancements to existing models, could lead to more accurate and reliable predictive models.
6. Integration of advanced sensing technologies: integrating sensors that can provide real-time data during the moulding process, such as pressure sensors, thermal cameras, or acoustic emission sensors, could improve the understanding of the material behavior under process conditions. This integration would also facilitate the development of more adaptive and responsive control systems for the injection moulding process.

By pursuing these research directions, the field can move closer to developing highly accurate, reliable, and comprehensive simulation tools that faithfully replicate the complexities of LSR injection moulding. This would not only improve the efficiency and quality of manufactured products but also enhance the scientific understanding of polymer processing.

Part VII
APPENDIX

APPENDIX

This Appendix provides additional information, mostly concerning the experimental sections of the previous Parts. It covers not only material characterization aspects, but also practical and statistical considerations. The sequence in which the topics are covered follow the original order in which these information were introduced in the preceding Parts.

A.1 MOLECULAR WEIGHT DISTRIBUTION

A.1.1 *High consistency silicone*

The molecular weight distribution of high consistency poly(dimethyl siloxane), or solid PDMS Xiameter™ RBB-2100-50 was determined via gel permeation chromatography (GPC) by employing a GPC analyser (Shimadzu Corp., Japan) coupled with a refractive index detector RID-20 and a MZ-Gel SDplus Linear 5 μm column. Sample preparation was accomplished by producing three 10 $\text{mg}\cdot\text{mL}^{-1}$ silicone rubber solution samples in triplicate (samples 1, 2, and 3) in tetrahydrofuran by solubilization. Only the sample containing 0 phr dicumylperoxide was analysed. These solutions were subsequently filtered through a 0.45 μm PTFE membrane filter, aiming to get rid of the filler incorporated to the silicone rubber gum. Calibration was made using poly(styrene) references and a calibration curve was built. Several averaged molecular weights are reported in Table A.1, along with the polydispersity indexes M_w/M_n and M_z/M_w .

Table A.1: Averaged molecular weights and polydispersity indexes for three high consistency silicone samples (sample A, 0 phr dicumylperoxide) as determined by GPC.

Sample	M_n ($\text{g}\cdot\text{mol}^{-1}$)	M_w ($\text{g}\cdot\text{mol}^{-1}$)	M_z ($\text{g}\cdot\text{mol}^{-1}$)	M_{z+1} ($\text{g}\cdot\text{mol}^{-1}$)	M_w/M_n (-)	M_z/M_w (-)
1	373,887	677,037	1,043,506	1,397,882	1.811	1.541
2	365,736	650,012	1,007,852	1,356,495	1.778	1.550
3	358,198	647,947	1,015,985	1,377,667	1.809	1.568
Mean	365,940	658,330	1,022,450	1,377,350	1.799	1.553
\pm std. dev	± 6406	$\pm 13,253$	$\pm 15,256$	$\pm 16,896$	± 0.015	± 0.011

Values for averaged molecular weights and polydispersity indexes are in accordance with typical values for solid poly(siloxane) elastomers. [202] The polydispersity $\frac{M_w}{M_n}$ of around 2 is also typical for polycondensation polymerization reactions, one of the normally employed synthesis route for poly(siloxane)s. [11]

A.1.2 Liquid silicone rubber

The molecular weight distribution of liquid silicone rubber SiloprenTM LSR 2070 was characterized via gel permeation chromatography (GPC) by employing a GPC analyser (Shimadzu Corp., Japan) coupled with a refractive index detector RID-20 and a MZ-Gel SDplus Linear 5 μm column. Sample preparation was accomplished by producing three 10 $\text{mg}\cdot\text{mL}^{-1}$ LSR solution samples in triplicate (samples 1, 2, and 3) in tetrahydrofuran by solubilization. Only part B was analysed. These solutions were subsequently filtered through a 0.45 μm PTFE membrane filter, aiming to get rid of the filler incorporated to the liquid silicone rubber matrix. Calibration was made using poly(styrene) references and a calibration curve was built. The molecular weight distribution information is shown in Table A.2.

Table A.2: Averaged molecular weights and polydispersity indexes for three LSR samples (part B, only the base polymer) as determined by GPC.

Sample	M_n ($\text{g}\cdot\text{mol}^{-1}$)	M_w ($\text{g}\cdot\text{mol}^{-1}$)	M_z ($\text{g}\cdot\text{mol}^{-1}$)	M_{z+1} ($\text{g}\cdot\text{mol}^{-1}$)	M_w/M_n (-)	M_z/M_w (-)
1	55265	88108	131661	182966	1.594	1.494
2	51798	86688	133102	188745	1.673	1.535
3	55274	85223	129952	187987	1.542	1.525
Mean	54112	86673	131571	186566	1.603	1.518
\pm std. dev	± 1636.5	± 1177.8	± 1287.5	± 2564.3	± 0.05	± 0.02

A.2 CHEMICAL CHARACTERIZATION

A.2.1 High consistency silicone

The investigated high consistency silicone was chemically characterized via infrared spectroscopy aiming to identify the type of siloxane monomer (specifically, R_1 and R_2 from Figure 1.1). The presence or absence of vinyl moieties, which are important to define the curing mechanism, was determined via proton nuclear magnetic resonance spectroscopy.

Fourier-transform infrared spectroscopy (FTIR) was conducted in a PerkinElmer Spectrum Two spectrometer (USA) in the transmittance mode over a wavenumber range of 4000 cm^{-1} to 400 cm^{-1} , with accumulated 16 scans at a resolution of 4 cm^{-1} in the attenuated total reflectance (ATR) mode. Characteristic absorption peaks are present in Figure A.1, where the following wavenumbers can be assigned [152, 203–205]: 2961 cm^{-1} (and shoulder at around 2910 cm^{-1}) to CH_3 asymmetric stretch; 1410 cm^{-1} to CH_3 asymmetric bending; 1258 cm^{-1} to CH_3 symmetric bending; 1004 cm^{-1} to Si-O-Si asymmetric stretch; and 789 cm^{-1} to Si- CH_3 asymmetric stretch and Si- CH_3 asymmetric rocking (shoulder at around 860 cm^{-1}). Based on these characteristic absorption peaks, one can conclude that the sample is likely to be a poly(dimethylsiloxane). Since the sensibility of infrared spectroscopy to double bonds is low, nuclear magnetic resonance spectroscopy was applied and will be described next.

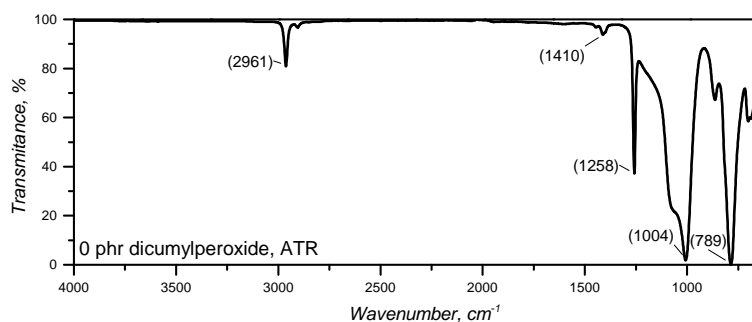


Figure A.1: Infrared (IR) spectrum of the high consistency silicone sample without dicumylperoxide (0 phr) indicating the characteristic IR absorptions of poly(dimethylsiloxane).

Determination of the vinyl presence or absence in the silicone rubber under study was vital to correctly describe the crosslinking mechanism taking the thermodynamic and kinetic parameters that were calculated into consideration. The vinyl content was then determined via high-field solution proton nuclear magnetic resonance spectroscopy (^1H NMR), by analysing the vinyl signals at about 6 ppm. The silicone rubber gum without dicumylperoxide (0 phr sample) was solubilized in deuterated chloroform (CDCl_3) and analysed in a 300 MHz Bruker Advance III spectrometer (Bruker, USA) with 64 scans and reference as the residual solvent peak at 7.26 ppm.

Figure A.2 shows the ^1H NMR full spectrum, as well as a detailed ^1H NMR spectrum with focus on the 5.5–6.5 ppm chemical shift (δ) region (usually where vinyl peaks show up [206]), for the 0 phr dicumylperoxide solid silicone sample. The full spectrum shows characteristic poly(dimethylsiloxane) signals, mainly between -0.20 ppm and 0.20 ppm. Peaks at the 1.5 ppm region can be associated to water. No significant vinyl signals were present at the 5.5–6.5 ppm region. Normally, even at low concentrations (down to 2%, for example), vinyl

groups appear as a set of multiple peaks at about 6 ppm. Thus, it is possible to state that this silicone grade has no significant amount of vinyl moieties, being mainly composed of poly(dimethylsiloxane).

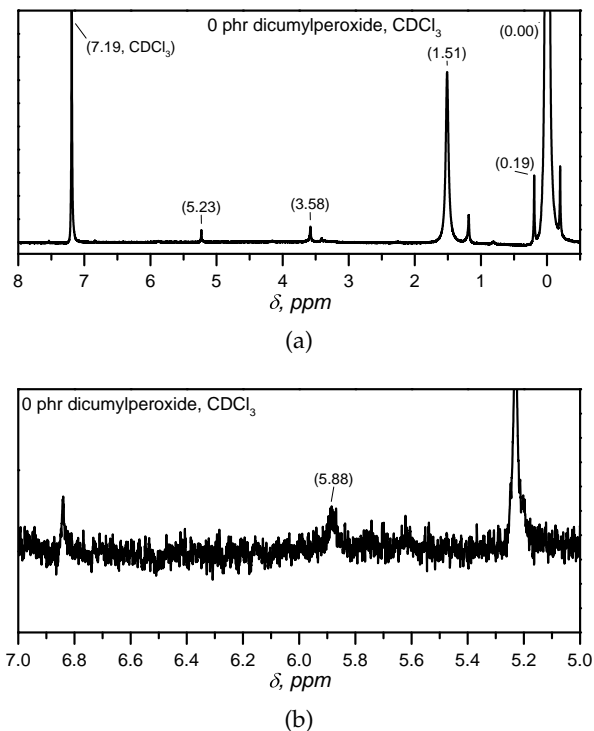


Figure A.2: (a) ^1H NMR spectrum in CDCl_3 for the 0 dicumylperoxide solid silicone, and detailed spectrum (b) for the vinyl region.

A.2.2 Liquid silicone rubber

The chemical characterization of liquid silicone rubber (KEG-2003H-70-A, hardness after cured = 70 Shore A) was conducted via infrared spectroscopy employing a PerkinElmer Spectrum Two spectrometer (USA) in the transmittance mode over a wavenumber range of 4000 cm^{-1} to 400 cm^{-1} , with accumulated 16 scans at a resolution of 4 cm^{-1} in the attenuated total reflectance (ATR) mode. Figure A.3 shows the spectra for part A and part B, where absorption peaks are assigned to characteristic molecular features as described before for high consistency silicone rubber. Part B shows two additional absorptions at 2159 cm^{-1} and 911 cm^{-1} that are absent in part A. These peaks can be attributed to the Si-H group [207] present in the crosslinker, which is added to part B.

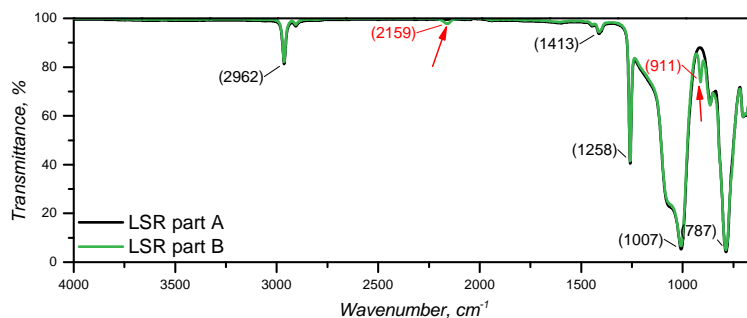


Figure A.3: Infrared (IR) spectrum of LSR's part A and B indicating the characteristic IR absorption wavenumbers of poly(dimethylsiloxane).

A.3 FILLER CONTENT DETERMINATION

A.3.1 High consistency silicone

The filler content of high consistency poly(dimethylsiloxane), or solid PDMS Xiameter™ RBB-2100-50 was determined by thermogravimetric analysis (TGA). TGA was performed in a TGA/DSC 1 device (Mettler Toledo, Switzerland) under $20 \text{ mL}\cdot\text{min}^{-1}$ of N_2 at $10 \text{ K}\cdot\text{min}^{-1}$ from 25°C to 900°C . Filler content was determined as the mass residue at 900°C , since pure silicone rubber gum experiences no residue at this temperature according to the literature [32]. The thermogram for the sample without dicumylperoxide is shown in Figure A.4, where it is possible to observe the high thermal stability of silicone rubbers [208], and the residue at 900°C .

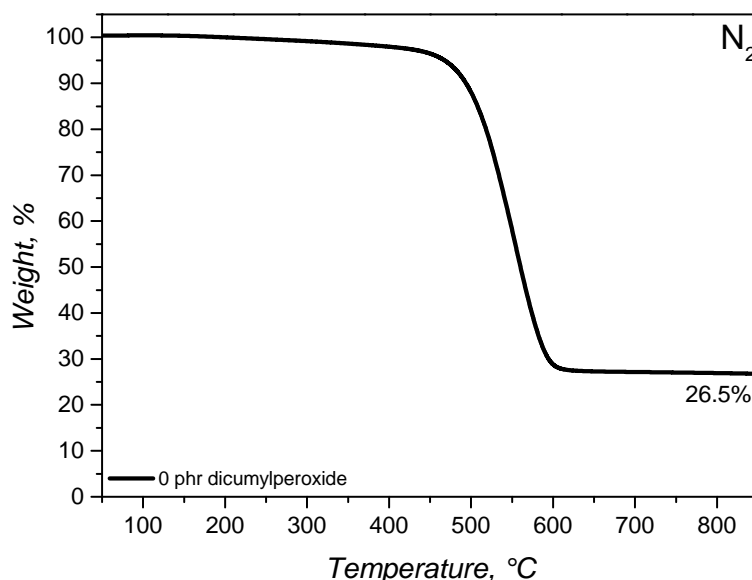


Figure A.4: Thermogram for the 0 phr dicumylperoxide silicone rubber under inert atmosphere (N_2). The residue values were taken as the % weight at 800°C .

A.3.2 Liquid silicone rubber

The filler content of liquid silicone rubber SiloprenTM LSR 2070 was determined via thermogravimetric analysis (TGA). TGA was performed in a TGA 2 device (Mettler Toledo, Switzerland) from 25°C to 900°C. The atmosphere was changed from N₂ (20 mL.min⁻¹) to synthetic air (20 mL.min⁻¹) at 700°C. The thermograms for samples 2070 part A and 2070 part B are shown in Figure A.5.

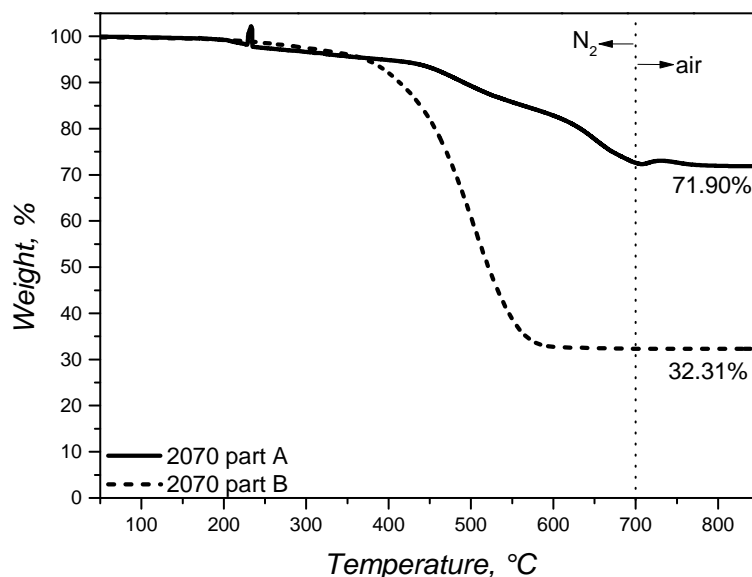


Figure A.5: 2070 A (full line) and 2070 B (dashed line) thermograms under inert (N₂) (until 700°C) and air atmospheres. The residue values were taken as the % weight at 800°C.

Manufacturing of LSR is usually conducted via synthesizing the base polymer (poly(siloxane) oligomers), incorporating the filler (silica), and finally adding to each respective part the platinum catalyst (to part A), and the crosslinker (low molecular weight poly(siloxane) to part B). In this sense, both part A and part B contain the exact same amount of filler. However, they showed different thermal degradation profiles, mainly regarding the amount of residue (% weight) at 800°C, as depicted in Figure A.5. The reason behind the difference on the residue content is related to the presence of platinum catalyst at part A and the silica surface's chemical nature. As explained by Delebecq *et al.* [36], the chemical modification of silica particle's surface (mainly via addition of vinyl moieties) and the presence of platinum catalyst lead to the coupling reaction between the filler particles and the LSR oligomers, ultimately leading to ceramization and thus increasing the sample's thermal stability. This thermal degradation pathway increases the residue at 800°C (71.9 wt% in the present case) when compared to an only silica-filled LSR polymer. Thus, the filler content based on the residue amount was determined by 2070 part B's residue value,

since no platinum catalyst is incorporated to this component. For the samples under study, a filler content of 32.3 wt% was established.

A.4 RHEOLOGY - REPRODUCIBILITY STUDY

To establish the highest variation concerning the oscillatory experiments described in Section 4.2.1, three repetitions were conducted for the strain amplitude sweep measurements under 0.1 Hz, 1.0 Hz, and 10 Hz. All triplicates are shown in Figure A.6(a), and the respective coefficients of variation are shown in Figure A.6(b). For all frequencies, the maximum determined coefficient of variation was lower than 5%. Thus, this variation was assumed for all other oscillatory experiments conducted at the strain-controlled rheometer (ARES-G2, TA Instruments, USA).

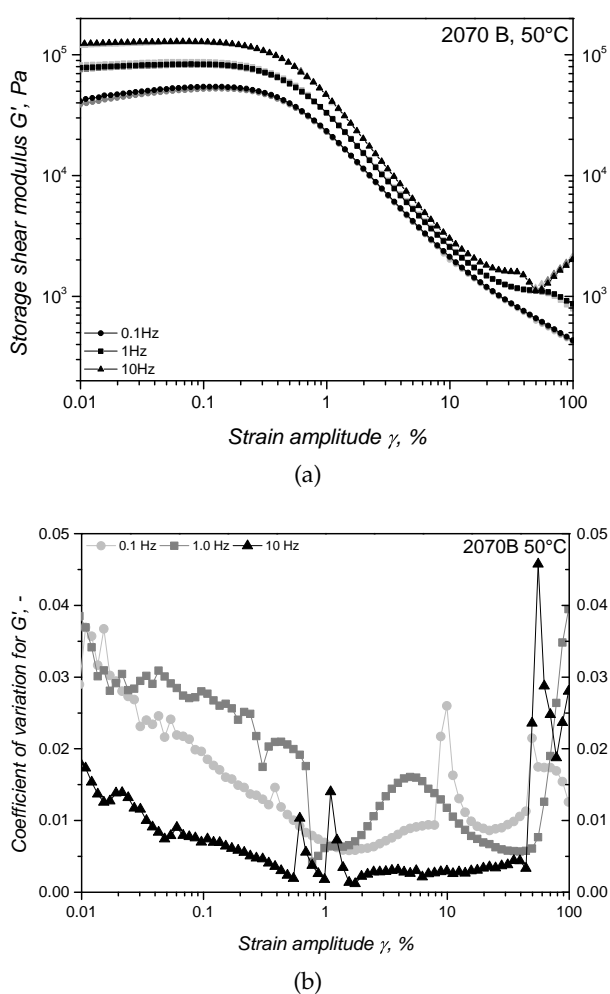
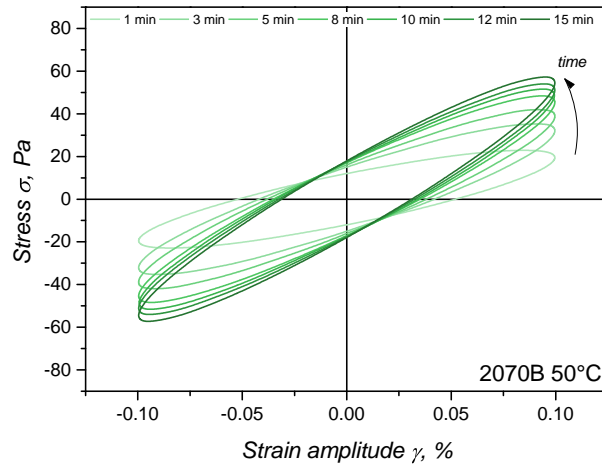


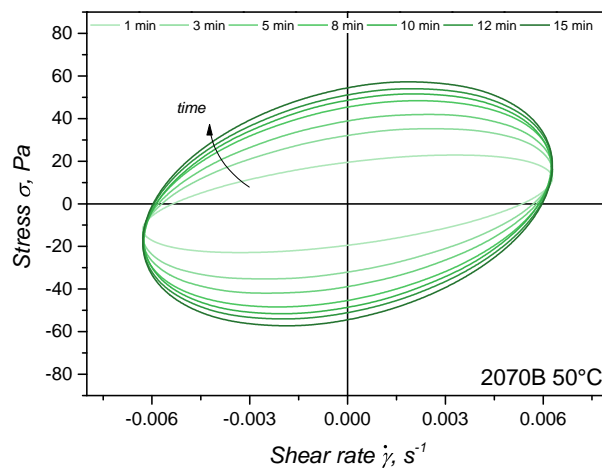
Figure A.6: Variability study for oscillatory experiments: (a) three strain amplitude sweep repetitions at 50°C for sample 2070 B under different strain amplitudes and (b) coefficient of variation for the amplitude sweeps shown in (a).

A.5 HYSTERESIS CURVES FOR 2070 B

$\sigma(\gamma)$ (elastic) and $\sigma(\dot{\gamma})$ (viscous) hysteresis curves for sample 2070 B during the recovery phase after intense shear are shown in Figure A.7(a) and (b), respectively. From these hysteresis curves and comparing with 2070 A's curves (presented in Figure 5.13(a) and (d)), one can derive the similarity regarding filler structure of both LSR parts.



(a)



(b)

Figure A.7: Elastic $\sigma(\gamma)$ (a) and viscous $\sigma(\dot{\gamma})$ (b) LB curves for sample 2070 B at 50°C recorded during recovery period after intense shear.

A.6 STRAIN AND STRESS SINUSOIDAL SIGNALS

By imposing a sinusoidal shear strain $\gamma(t) = \gamma_0 \sin(\omega t)$ and a consequent orthogonal strain rate $\dot{\gamma}(t) = \gamma_0 \omega \cos(\omega t)$, a stress response arises. These signals are presented in Figure A.8 for sample 2070 A under linear ($\gamma = 0.1\%$) and non-linear ($\gamma = 10\%$) viscoelastic conditions for three angular frequencies and three temperatures. Non-linearity can be detected by the distorted stress signals at $\gamma = 10\%$, which are not smooth, but are still periodic sinusoidal signals. Note that the curves show a time window within the stationary regime, i.e., when successive strain cycles show equal stress responses. Figure A.8 does not show the initial part of the experiment, where transient conditions occur (strain is applied for the first time and stress is measured).

A.7 INTENSITY OF CHEBYSHEV COEFFICIENTS AT 90°C

The variation of the Chebyshev coefficients $e_{3/1}$ and $v_{3/1}$ as a function of amplitude at 90°C is shown in Figure A.9. As demonstrated for 50°C, the coefficients are close to zero under linear viscoelastic conditions, while they reach values close to ± 0.1 at 10% amplitude.

A.8 EDGE INSTABILITY DURING STEADY SHEAR EXPERIMENTS

In order to better visualize the edge instabilities that occur during steady shear experiments, Figure A.10 shows the details of the snapshots provided in Figure 5.8 for each sequential shear rate. It is possible to clearly see shear bands occurring at $\gamma = 0.3 \text{ s}^{-1}$ and the formation of a concave gap edge (red arrow). At $\gamma = 0.7 \text{ s}^{-1}$, edge instability occurs more strongly, deforming completely the gap edge geometry.

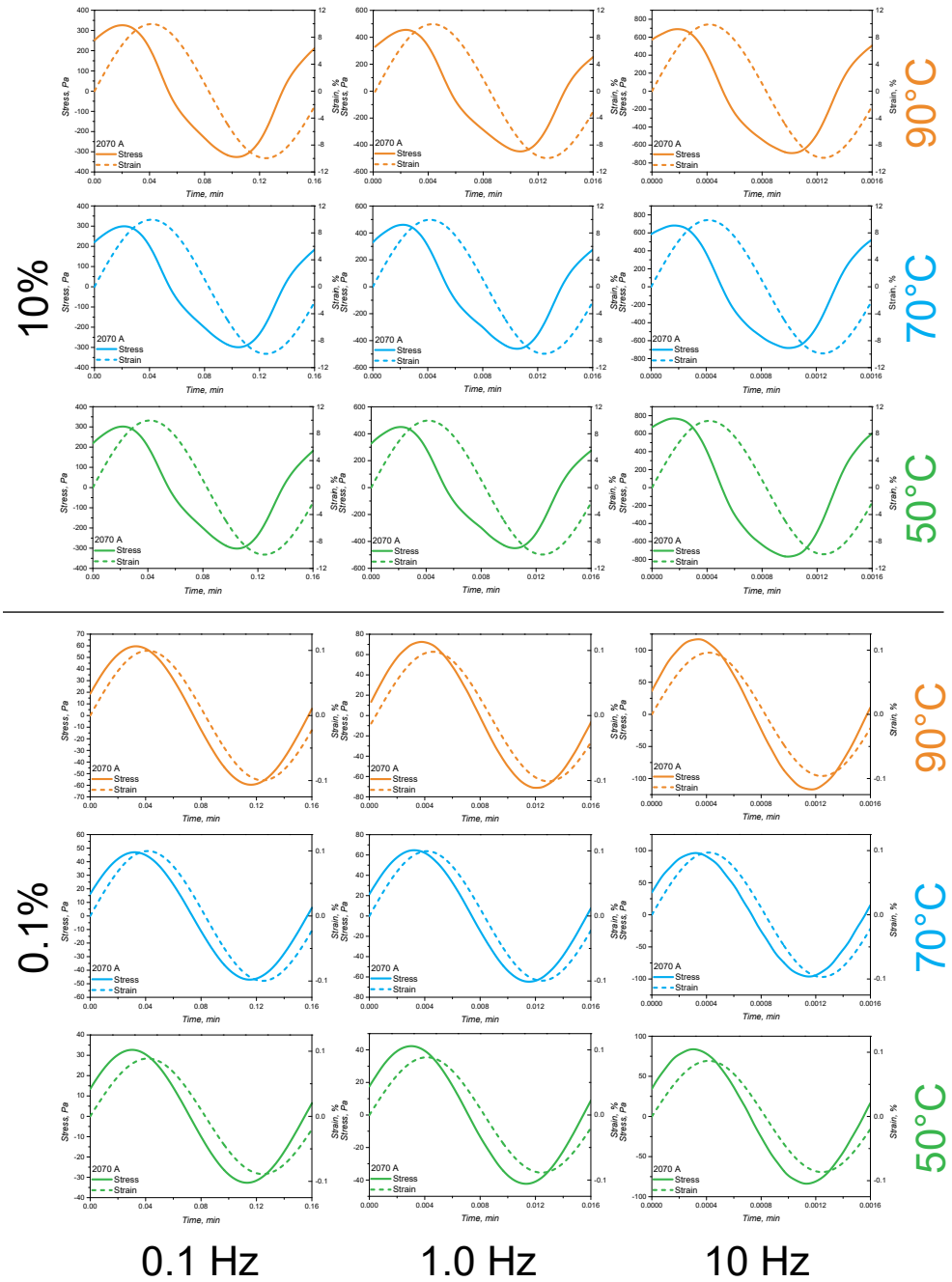
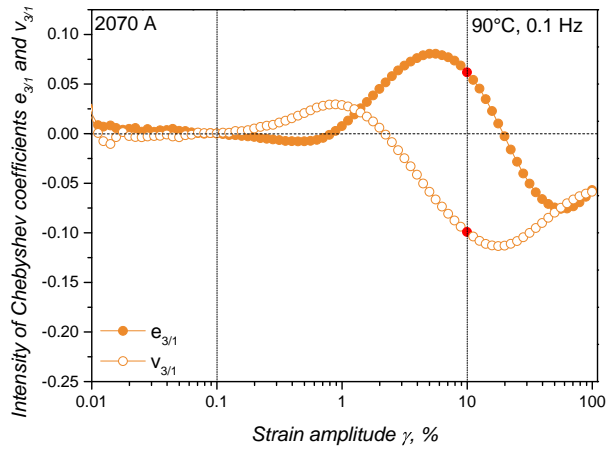
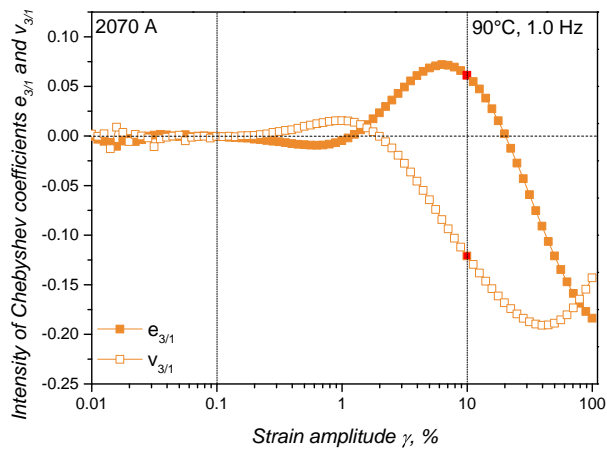


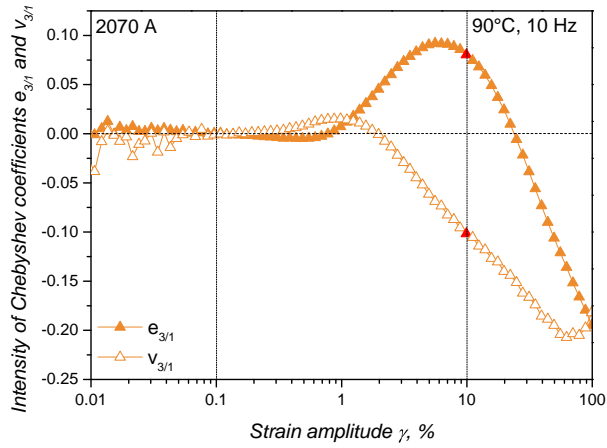
Figure A.8: Imposed strain (dashed lines) and measured stress (full line) for sample 2070 A under SAOS (bottom, $\gamma = 0.1\%$) and LAOS (top, $\gamma = 10\%$) conditions for 3 different temperatures under stationary regime.



(a)



(b)



(c)

Figure A.9: Intensity of the Chebyshev coefficients $e_{3/1}$ and $v_{3/1}$ as a variation of the strain amplitude for 3 imposed angular frequencies (a) 0.1 Hz; (b) 1.0 Hz; and (c) 10 Hz and at 90°C. For the ease of interpretation, the vertical lines indicate the studied amplitudes $\gamma = 0.1\%$ (SAOS) and $\gamma = 10\%$ (LAOS), and the horizontal line shows where the coefficients are zero.

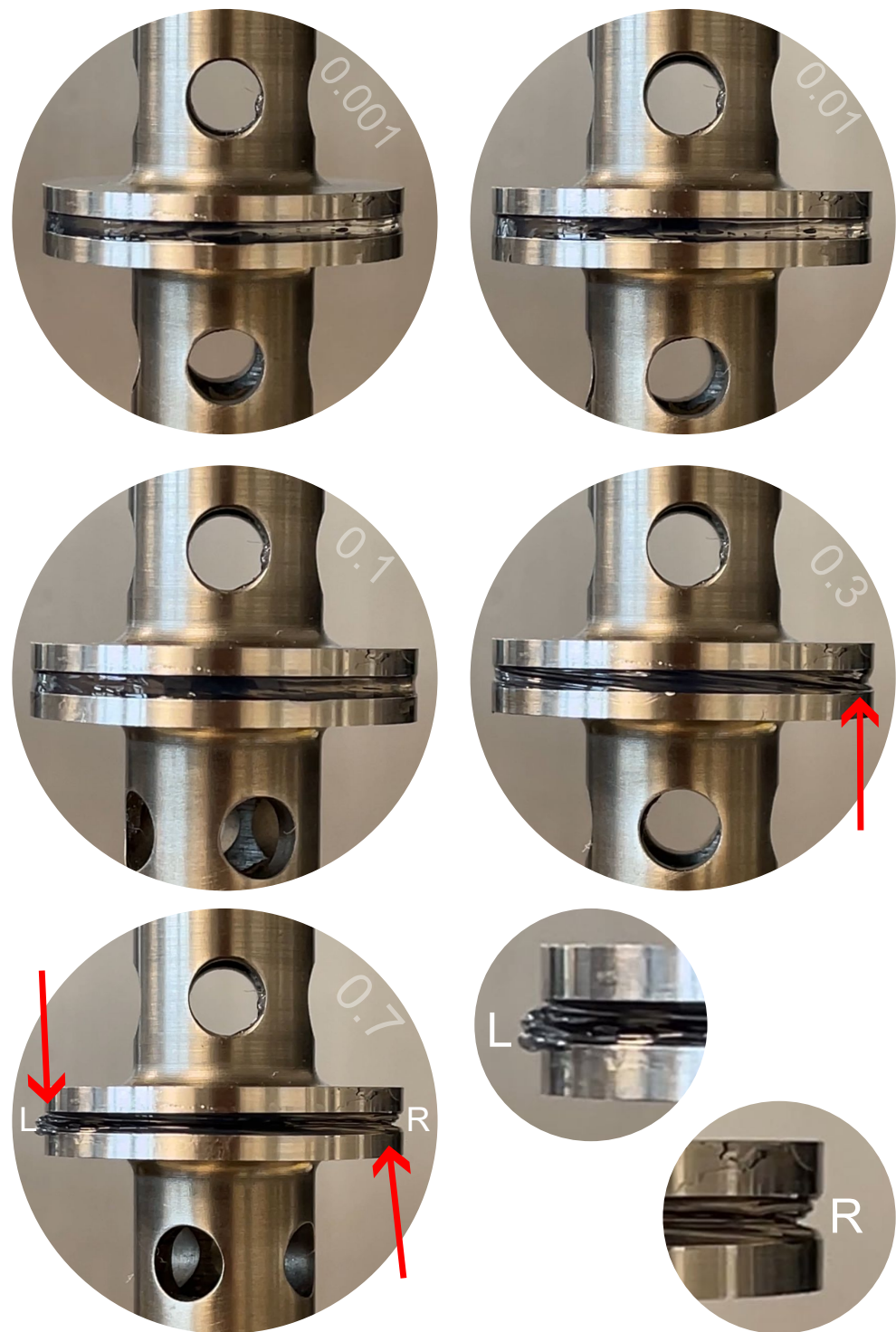


Figure A.10: Gap snapshots for sequential shear rates during the steady shear experiments as showed in the plot of Figure 5.8. These snapshots show details of edge instabilities as indicated by the red arrows.

A.9 PYTHON SCRIPTS

The following script was used to fit the conversion rate data to the Kamal model, as described in Chapter 10. This code was generated with the aid of ChatGPT version GPT-3.5 (OpenAI) and the details concerning the script are available in Section A.10 of this Appendix.

```
import numpy as np
import pandas as pd
import matplotlib.pyplot as plt
from scipy.optimize import curve_fit
from scipy.stats import norm

# Define the Kamal model equation with fixed E1 and E2
def kamal_model_fixed_E(T, A1, A2, m, n, alpha, E1=134500, E2=134500,
R=8.314):
    return (A1 * np.exp(-E1 / (R * T)) + (A2 * np.exp(-E2 / (R * T))) *
alpha**m) * (1 - alpha)**n

# Validation checks
if np.any(T <= 0):
    raise ValueError("Temperature values must be greater than zero")
if np.any(alpha < 0) or np.any(alpha > 1):
    raise ValueError("Alpha values must be between 0 and 1")

# Model calculation
term1 = A1 * np.exp(-E1 / (R * T))
term2 = A2 * np.exp(-E2 / (R * T)) * alpha ** m
term3 = (1 - alpha) ** n

# Check for invalid values in intermediate terms
if np.any(np.isnan(term1)) or np.any(np.isinf(term1)):
    print("Invalid values found in term1")
if np.any(np.isnan(term2)) or np.any(np.isinf(term2)):
    print("Invalid values found in term2")
if np.any(np.isnan(term3)) or np.any(np.isinf(term3)):
    print("Invalid values found in term3")

return (term1 + term2) * term3

# Define the Kamal model equation with E1 and E2 as variables
def kamal_model(T, A1, A2, E1, E2, m, n, alpha, R=8.314):
    return (A1 * np.exp(-E1 / (R * T)) + (A2 * np.exp(-E2 / (R * T))) *
alpha**m) * (1 - alpha)**n

# Validation checks
if np.any(T <= 0):
```

```

        raise ValueError("Temperature values must be greater than zero")
    if np.any(alpha < 0) or np.any(alpha > 1):
        raise ValueError("Alpha values must be between 0 and 1")

    # Model calculation
    term1 = A1 * np.exp(-E1 / (R * T))
    term2 = A2 * np.exp(-E2 / (R * T)) * alpha ** m
    term3 = (1 - alpha) ** n

    # Check for invalid values in intermediate terms
    if np.any(np.isnan(term1)) or np.any(np.isinf(term1)):
        print("Invalid values found in term1")
    if np.any(np.isnan(term2)) or np.any(np.isinf(term2)):
        print("Invalid values found in term2")
    if np.any(np.isnan(term3)) or np.any(np.isinf(term3)):
        print("Invalid values found in term3")

    return (term1 + term2) * term3

# Specify the file path to your Excel file
file_path = 'Momentive_data fitting.xlsx' # Replace with the actual path
to your file

# Read the data from the Excel file into a DataFrame
df = pd.read_excel(file_path)

# Extract data from DataFrame
alpha = df['alpha'].values
d_alpha_dt = df['d_alpha_dt'].values
T = df['T'].values

# Check for invalid data and remove it
valid_indices = ~np.isnan(alpha) & ~np.isnan(d_alpha_dt) & ~np.isnan(T) & \
    ~np.isinf(alpha) & ~np.isinf(d_alpha_dt) & ~np.isinf(T) & \
    (alpha >= 0) & (alpha <= 1) & (T > 0)

alpha = alpha[valid_indices]
d_alpha_dt = d_alpha_dt[valid_indices]
T = T[valid_indices]

# Initial parameters and bounds for A1, A2, m, n for the first fit
initial_params_first_fit = [1e8, 1e8, 1, 1] # Initial guesses for
A1, A2, m, n
bounds_first_fit = ([1e5, 1e5, 0, 0], [1e30, 1e30, 3, 3]) # Bounds for
A1, A2, m, n

```

```

# Perform the first curve fitting on the concatenated data with fixed
E1 and E2
params_first_fit, covariance_first_fit = curve_fit(
    lambda T, A1, A2, m, n: kamal_model_fixed_E(T, A1, A2, m, n, alpha),
    T, d_alpha_dt, p0=initial_params_first_fit,
    bounds=bounds_first_fit, maxfev=10000
)

# Calculate standard deviations from the covariance matrix
param_std_devs_first_fit = np.sqrt(np.diag(covariance_first_fit))

# Display optimized parameters with standard deviations
print("First fitting with fixed E1 and E2 - Optimized parameters with
standard deviations:")
print(f"A1: {params_first_fit[0]} ± {param_std_devs_first_fit[0]}")
print(f"A2: {params_first_fit[1]} ± {param_std_devs_first_fit[1]}")
print(f"m: {params_first_fit[2]} ± {param_std_devs_first_fit[2]}")
print(f"n: {params_first_fit[3]} ± {param_std_devs_first_fit[3]}")

# Store the initial guesses for the second fit
initial_params_second_fit = [params_first_fit[0], params_first_fit[1],
100000, 100000, params_first_fit[2], params_first_fit[3]]

# Bounds for the second fitting (you can adjust these as needed)
bounds_second_fit = (
    [1e5, 1e5, 5e4, 5e4, 0, 0], # Lower bounds for A1, A2, E1, E2, m, n
    [1e30, 1e30, 5e5, 5e5, 3, 3] # Upper bounds for A1, A2, E1, E2, m, n
)

# Perform the second curve fitting
params_second_fit, covariance_second_fit = curve_fit(
    lambda T, A1, A2, E1, E2, m, n: kamal_model(T, A1, A2, E1, E2, m, n, alpha),
    T, d_alpha_dt, p0=initial_params_second_fit, bounds=bounds_second_fit, maxfev=10000
)

# Calculate standard deviations from the covariance matrix
param_std_devs_second_fit = np.sqrt(np.diag(covariance_second_fit))

# Display optimized parameters with standard deviations
print("\nSecond fitting to estimate E1 and E2 - Optimized parameters with
standard deviations:")
print(f"A1: {params_second_fit[0]} ± {param_std_devs_second_fit[0]}")
print(f"A2: {params_second_fit[1]} ± {param_std_devs_second_fit[1]}")
print(f"E1: {params_second_fit[2]} ± {param_std_devs_second_fit[2]}")
print(f"E2: {params_second_fit[3]} ± {param_std_devs_second_fit[3]}")

```

```

print(f"m: {params_second_fit[4]} ± {param_std_devs_second_fit[4]}")
print(f"n: {params_second_fit[5]} ± {param_std_devs_second_fit[5]}")

# Calculate residuals for the second fit
d_alpha_dt_fit_second = kamal_model(T, *params_second_fit, alpha)
residuals_second = d_alpha_dt - d_alpha_dt_fit_second

# Create a DataFrame for residuals
residuals_df = pd.DataFrame({'Temperature': T,
                             'Residuals': residuals_second})

# Specify the file path to save the residuals
residuals_file_path = 'residuals_data_Momentive RPA 0.4.xlsx'
# Replace with your desired file path

# Save residuals to Excel
residuals_df.to_excel(residuals_file_path, index=False)
print(f"Residuals data saved to {residuals_file_path}")

# Plot the data and the fitted curve for the second fit
plt.figure(figsize=(10, 10))
plt.scatter(T, d_alpha_dt, label='Data', color='red')
T_fit = np.linspace(min(T), max(T), 100)
d_alpha_dt_fit_second = kamal_model(T_fit, *params_second_fit, T.mean())
# Use average T for fit
plt.plot(T_fit, d_alpha_dt_fit_second, label='Fitted Curve', color='blue')
plt.xlabel('Temperature (T)')
plt.ylabel('dAlpha/dt')
plt.title('Kamal Model Fitting (Estimating E1 and E2)')
plt.legend()
plt.show()

# Plot the residuals for the second fit
plt.figure(figsize=(10, 10))
plt.scatter(T, residuals_second, label='Residuals', color='green')
plt.hlines(0, min(T), max(T), colors='black', linestyle='dashed')
plt.xlabel('Temperature (T)')
plt.ylabel('Residuals')
plt.title('Residuals (Second Fit)')
plt.legend()
plt.show()

plt.figure(figsize=(10, 6))
plt.hist(residuals_second, bins=20, color='green', alpha=0.7)
plt.xlabel('Residuals')
plt.ylabel('Frequency')

```

```

plt.title('Histogram of Residuals')
plt.grid(True)
plt.show()

# Calculate histogram of residuals
residuals = residuals_second
counts, bins = np.histogram(residuals, bins='auto') # 'auto' determines the
number of bins automatically

# Create a DataFrame with counts and bin edges
histogram_data = pd.DataFrame({
    'Bin Edges': bins[:-1], # Exclude last bin edge because counts correspond to edges
    'Counts': counts
})

# Export to Excel
histogram_data.to_excel('residuals_histogram_data_Momentive DSC with different
conditions.xlsx', index=False)

# Plot histogram
plt.figure(figsize=(8, 8))
plt.hist(residuals_second, bins=20, color='green', alpha=0.7, density=True)
# density=True for normalized histogram
plt.xlabel('Residuals', fontsize=14)
plt.ylabel('Frequency', fontsize=14)
plt.title('Histogram of Residuals')
plt.grid(False) # Turn off grid

# Fit a normal distribution to the data
mu, std = norm.fit(residuals_second)
xmin, xmax = plt.xlim()
x = np.linspace(xmin, xmax, 100)
p = norm.pdf(x, mu, std)
plt.plot(x, p, 'k', linewidth=2) # 'k' is black color

# Add text annotation
plt.text(0.95, 0.95, 'LSR calorimetry', verticalalignment='top',
horizontalalignment='right',
        transform=plt.gca().transAxes, fontsize=12,
        backgroundcolor='white', alpha=0.5)

plt.show()

residuals_mean = np.mean(residuals_second)
residuals_std = np.std(residuals_second)
residuals_min = np.min(residuals_second)

```

```

residuals_max = np.max(residuals_second)

print(f"Mean of residuals: {residuals_mean}")
print(f"Standard deviation of residuals: {residuals_std}")
print(f"Minimum residual: {residuals_min}")
print(f"Maximum residual: {residuals_max}")

```

A.10 USE OF AI-BASED TOOLS

As described in Section 10.1.4, the code employed to fit the conversion rate data to the Kamal model was generated with the aid of ChatGPT. The details concerning this tool and the artificial intelligence input share into the generated code are described in Table A.3. Besides, the use of an online translator to convert the English abstract to a German version is detailed.

Table A.3: Declaration of artificial intelligence-based tools and their characteristics.

Output	AI share (%)	Tool/version	Remarks	Reference to prompting
Code for model fitting	85	ChatGPT-3.5	The code was modified by the author	https://shorturl.at/k4AAL
Translation of abstract	85	DeepL-24.7.3.12895	The text was modified by the author	Direct translation
Writing assistance	5%	ChatGPT-4.0	Grammar and consistency check	-

A.11 RESIDUAL ANALYSIS OF THE KAMAL MODEL FITTING

In order to analyse the goodness of fit, residual characteristics are presented in Table A.4. The mean value represents the average residual, i.e., the mean of ϵ distribution in a non-linear regression model (as the Kamal model), generally represented by:

$$Y_i = f(X_i, \theta) + \epsilon_i \quad (\text{A.1})$$

where, for the Kamal model (Equation 10.11), Y is the conversion rate $d\alpha/dt$, X is the conversion α and the temperature, and θ is the set of parameters A_1 , A_2 , E_1 , E_2 , m , and n . It is assumed [209] that the residuals are random, independent, and normally distributed variables with mean 0 and variance σ^2 . From Table A.4 it is possible to see that indeed the residuals have mean values around 0, with the lowest value attributed to the DSC measurements. Besides, the requirement of normality for the residuals distribution is met, as represented qualitatively by the histograms in Figure A.11. Quantitative inspection for the residuals normality was not carried out, since the qualitative analysis of the residuals distribution already presented a normal behaviour.

Table A.4: Residual characteristics for the fittings described by the parameters in Table 11.4.

Residual	DSC	0.4383 s ⁻¹	4.383 s ⁻¹	13.1476 s ⁻¹
Mean	2.50×10^{-06}	4.43×10^{-05}	-4.43×10^{-05}	-1.32×10^{-05}
Standard deviation	1.14×10^{-04}	3.43×10^{-04}	2.74×10^{-04}	2.76×10^{-04}
Minimum	-7.26×10^{-04}	-3.06×10^{-03}	-2.21×10^{-03}	-2.60×10^{-03}
Maximum	9.58×10^{-04}	3.75×10^{-03}	2.62×10^{-03}	3.47×10^{-03}

A.12 VISCOSITY DATA FITTING

The fitting of viscosity data obtained via large amplitude oscillatory shear (LAOS) experiments and via high pressure capillary rheometer (HPCR) are shown in Figure A.12(a) and (b), respectively. The full lines show the fitting employing the parameters presented in Table 12.2. The fittings were carried out by the Sigmasoft software.

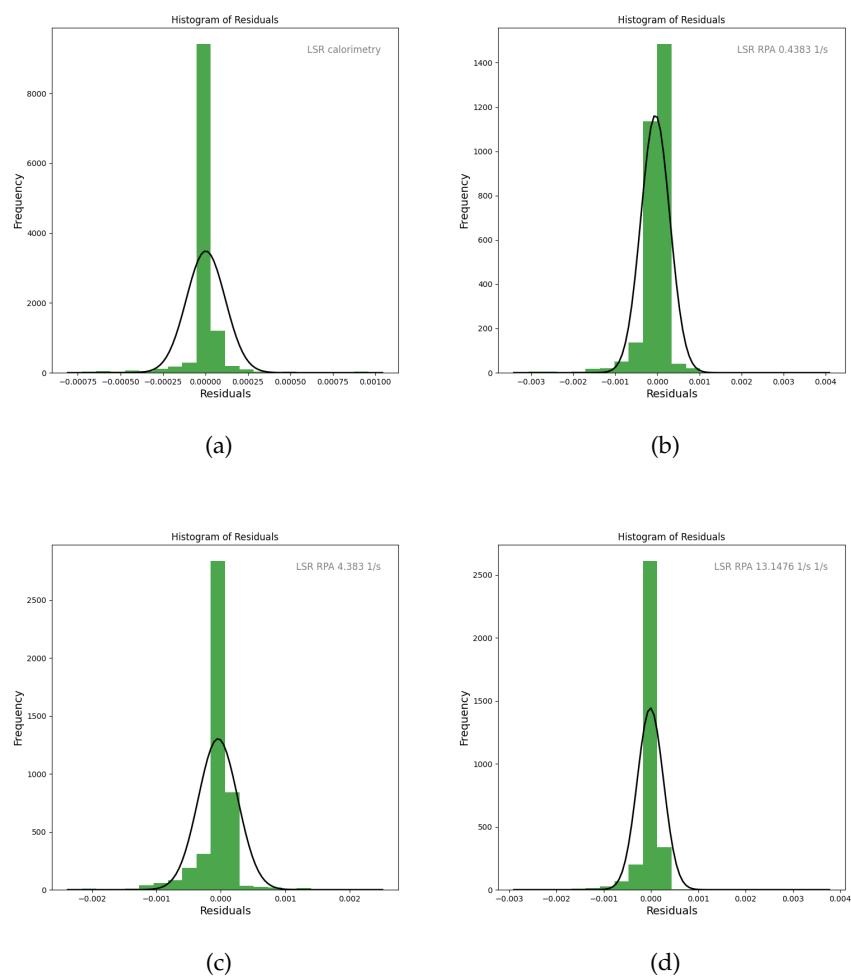
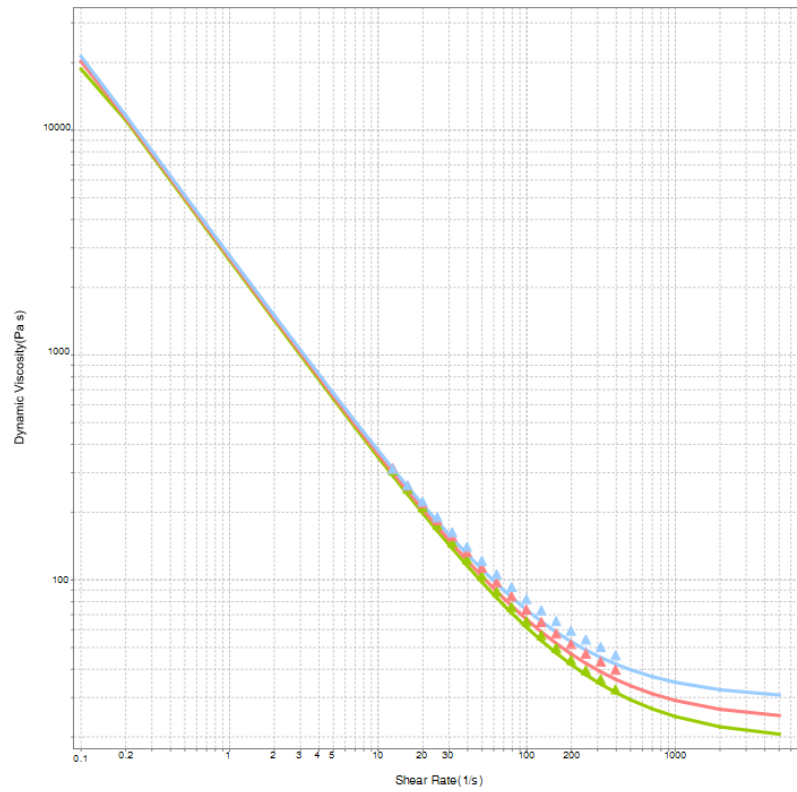
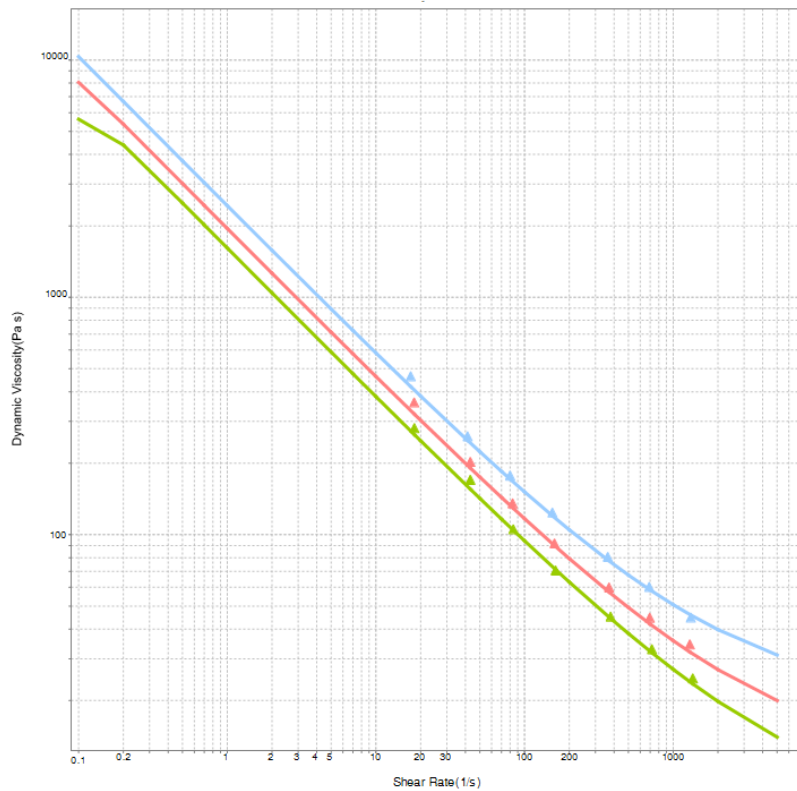


Figure A.11: Distribution of residuals from the conversion rate data fitting that generated the model parameters described in Table 11.4. The black line shows the normal distribution associated to the residual distribution.



(a)



(b)

Figure A.12: Viscosity plots showing the measured data (triangles) at three temperatures: 50°C (blue), 70°C (red), and 90°C (green) and the respective fittings (full lines) for (a) LAOS (dataset A) and (b) HPCR (dataset B). The plots were obtained directly from the Sigmasoft simulation software.

LIST OF FIGURES

Figure 1.1	Molecular structure of a general poly(siloxane) and a hypothetical hydrocarbon polymer, where, for instance, for poly(siloxane)s, $R_1 = R_2 = CH_3$ for poly(dimethylsiloxane) (PDMS). For the hydrocarbon polymer, $R_1 = R_2 = H$ for poly(ethylene), and $R_1 = H$ and $R_2 = CH_3$ for poly(propylene), for example. 4
Figure 1.2	Main thermal degradation mechanism of poly(dimethyl siloxane) based on intramolecular back-biting and formation of a cyclic oligomer ([35], adapted from [29]). 8
Figure 1.3	Schematics illustration of the hierarchical structure of distinct silicas in silicone rubber: SR_{PA} : precipitated silica; SR_{FB} and SR_{FC} : fumed silica modified by hexamethyldisilazane (from [40]) 9
Figure 1.4	SEM and TEM images of (a) fumed and (b) precipitated silica. The schematics in the bottom right portion of the figures represent the tightly bound rubber layer in orange, while the silica particle is depicted in gray (adapted from [45]) 11
Figure 1.5	For shaping and solidification, the phenomena involved in (a) conventional thermoplastics injection moulding and (b) liquid silicone rubber (reactive) injection moulding (adapted from [47]) 12
Figure 2.1	Thesis' structure diagram. 18
Figure 3.1	Schematic formation of edge fracture during steady-shear viscosity determination via rotational rheology (adapted from [76]). 27
Figure 4.1	Graphic representation of the methods applied to study filler recovery on (a) sample 2070 B after amplitude sweep and on (b) sample 2070 A after pre-shear. 31

- Figure 5.1 Viscoelastic properties G' (full symbol) and G'' (open symbols) of sample 2070 A for a range of strain amplitudes and temperatures under **(a)** 0.1 Hz, **(b)** 1.0 Hz, and **(c)** 10 Hz frequency. For the ease of interpretation, the vertical lines indicate the studied amplitudes $\gamma = 0.1\%$ (SAOS) and $\gamma = 10\%$ (LAOS). 34
- Figure 5.2 Viscoelastic properties G' (full symbol) and G'' (open symbols) of sample 2070 A for a range of strain amplitudes and frequencies at **(a)** 50°C, **(b)** 70°C, and **(c)** 90°C. For the ease of interpretation, the vertical lines indicate the studied amplitudes $\gamma = 0.1\%$ (SAOS) and $\gamma = 10\%$ (LAOS). 36
- Figure 5.3 Lissajous-Bowditch curves (elastic, filled symbols; and viscous, open symbols) associated to the strain amplitudes $\gamma = 0.1\%$ (bottom, SAOS) and $\gamma = 10\%$ (top, LAOS) at various temperatures and frequencies for sample 2070 A. 37
- Figure 5.4 Variation of the third harmonic intensity $I_{3/1}$ for the three studied temperatures **(a)-(c)** with the strain amplitude under various frequencies for sample 2070 A. A comparison with G' and G'' is shown in **(d)** for 90°C and 10 Hz. For the ease of interpretation, the vertical lines indicate the studied amplitudes $\gamma = 0.1\%$ (SAOS) and $\gamma = 10\%$ (LAOS), and the horizontal line represents the level where the 3rd is 10% of the fundamental harmonic. 39
- Figure 5.5 Intensity of the Chebyshev coefficients $e_{3/1}$ and $v_{3/1}$ as a variation of the strain amplitude for 3 imposed angular frequencies **(a)** 0.1 Hz; **(b)** 1.0 Hz; and **(c)** 10 Hz and at 50°C. For the ease of interpretation, the vertical lines indicate the studied amplitudes $\gamma = 0.1\%$ (SAOS) and $\gamma = 10\%$ (LAOS), and the horizontal line shows where the coefficients are zero. 40

- Figure 5.6 Viscoelastic properties G' (full symbol) and G'' (open symbols) of sample 2070 A for a range of angular frequencies and under 0.1% **(a)**, SAOS, circles) or 10% **(b)**, LAOS, squares) amplitudes, for three temperatures (50°C, 70°C, and 90°C). $G'(\omega, \gamma)$ and $G''(\omega, \gamma)$ at 90°C are also plotted in **(c)** for comparison purposes. The arrow indicates that frequency sweeps were conducted with decreasing frequency. 41
- Figure 5.7 2070 A's complex viscosity variation with angular frequency for all temperatures and strain amplitudes. The arrow indicates that frequency sweeps were conducted with decreasing frequency. 43
- Figure 5.8 Steady shear viscosity variation for sample 2070 A under steady shear for various temperatures. The snapshots taken at 50°C at certain shear rates highlight the sample's conditions inside the gap until edge instabilities occur at high shear rates. The arrow indicates that shear rate sweeps were conducted with increasing shear rate. 44
- Figure 5.9 Viscosity as determined (average out of 3 replicates, coefficient of variation is less than 5%) by the high pressure capillary rheometer as a function of the imposed shear rate for sample 2070 A under various temperatures. The arrow indicates that the measurement was conducted with decreasing shear rates. 45
- Figure 5.10 Comparison among the several experimental approaches covered in this work for the three studied temperatures: **(a)** 50°C, **(b)** 70°C, and **(c)** 90°C. LVR is the linear viscoelastic range, where small amplitude oscillatory shear (SAOS) experiments are held. On the other hand, large amplitude oscillatory shear (LAOS) experiments are conducted in non-linear viscoelastic conditions. $\eta^*(\omega)$ is the complex viscosity determined either via SAOS or LAOS, while $\eta_s(\dot{\gamma})$ is the steady shear viscosity. 48
- Figure 5.11 **(a)** Complex viscosity (measured under SAOS conditions) increase with time after amplitude sweep (0.01 - 100%, at either low (0.1 and 1.0 Hz) or high frequency (10 Hz)) for various temperatures and **(b)** viscosity ratio as the amount of viscosity recovery after shear. 50

- Figure 5.12 Viscoelastic parameters G' and G'' during the intense pre-shear under LAOS conditions **(a)** and during recovery under SAOS conditions **(b)**. 51
- Figure 5.13 Elastic $\sigma(\gamma)$ **(a)**, **(c)**, and **(e)** and viscous $\sigma(\dot{\gamma})$ **(b)**, **(d)**, and **(f)** LB curves for sample 2070 A at various temperatures recorded during recovery period after intense shear. 52
- Figure 6.1 Schematic diagram of phonon transport mechanism in LSR composites containing aluminium oxide (blue), aluminium nitride (red), and boron nitride (green). Adapted from [106]. 62
- Figure 7.1 Experimental conditions for the determination of the specific volume under different pressures and for a range of temperatures. The full line represents the pressure imposed to the sample and indicates the isobaric conditions of testing (grey segments) and the stabilization period between two consecutive isobars (green segments, shaded areas). The temperature is pictured as dashed lines, showing the heating (red segments) during testing and the cooling (blue segments) during the stabilization period. For the stabilization period prior to the 5 MPa isobaric experiments, the pressure was dropped to 3.5 MPa to allow the sample to fill the whole measurement cavity. 72
- Figure 8.1 Modulated temperature DSC thermogram differentiating the total, the non-reversible, and the reversible (employed to determine c_p) heat quantities for the 1:1 LSR mixture. Sample mass is 15-20 mg. 74
- Figure 8.2 Comparison of the LSR's specific heat capacity values determined employing the sapphire (blue lines) and the MDSC (red lines) methods. The full lines represent the first heat run, while the sample is still uncured until the crosslinking reaction starts, whereas the dotted lines show the second heat run for the fully crosslinked samples. The dashed lines are linear fittings (equations are in the plot) with $R_{adj}^2 > 0.99$. The coefficient of variation for the measurement is 7%. 75

- Figure 8.3 Comparison of the SBR compound's specific heat capacity values determined employing the sapphire (blue lines) and the MDSC (red lines) methods. The full lines represent the first heat run, while the sample is still uncured until the crosslinking reaction starts, whereas the dotted lines show the second heat run for the fully crosslinked samples. The dashed lines are linear fittings (equations are in the plot) with $R_{adj}^2 > 0.99$. 77
- Figure 8.4 Schematic representation of c_p variation with temperature around the glass transition region. Modified from [98]. 78
- Figure 8.5 Thermal conductivity variation with temperature for the individual A and B components, as well as for the uncured and cured mixtures. The components and the uncured mixed were analysed via a transient method, while the cured mixture was investigated employing a steady-state method. The symbols indicate the average of 3 measurements and the shaded areas represent the standard deviation. 80
- Figure 8.6 Variation of the specific volume (one measurement) as a function of pressure and temperature. The orange line represents the second measurement at 5 MPa at which the sample is fully crosslinked, and is on top of the light gray line representing the 5 MPa isobar. The dotted blue line represents a hypothetical injection moulding cycle, being the phases: A-B injection; B-C expansion; C-D compression; D-E demoulding; and E-A: cooling. 83
- Figure 8.7 Rate of volume change due to temperature ($\text{cm}^3 \cdot \text{kg}^{-1} \text{K}^{-1}$) for each tested pressure. The shaded area around the plot represents the error connected to the linear fitting of the data in Figure 8.6. The coefficients of determination for such linear fittings are higher than 0.999. 84
- Figure 9.1 Chalk-Harrod mechanism of hydrosilylation reaction. The red elements represent the LSR oligomers (vinyl terminated), while the blue elements illustrate the Si-H-based crosslinker. (adapted from [143]). 92
- Figure 9.2 Karstedt's catalyst (adapted from [141]). 92

- Figure 11.1 Rotational rheometry (RPA, 0.5° deformation at 1.667 Hz) curves for silicone rubber compounds with varied dicumylperoxide concentrations (**b-g**) at different crosslinking temperatures. The plot (**a**) (torque vs. time curve) is related to the pure solid silicone rubber without dicumylperoxide. 106
- Figure 11.2 Optimum cure time t_{90} as a function of the dicumylperoxide concentration and the temperature. The dots represent the experimental data and the surface indicates the model described at Equation (10.1), with fitting parameters as follows: A_0 (pre-exponential factor) = $2.02 \times 10^{-14} \text{ min}^{-1}$, E_a (activation energy) = $1.18 \times 10^5 \text{ J.mol}^{-1}$, and $\beta = -0.603$. The correlation factor represented by the pseudo adjusted- R^2 was 0.988. 109
- Figure 11.3 Conversion rate $d\alpha/dt$ at 160°C for silicone rubber compounds with different dicumylperoxide concentrations as a function of time (**a**) and conversion (**b**). 111
- Figure 11.4 Friedman-like isoconversional approach for calculating the activation energy, regarding the sample 0.21 phr (**a**) and the activation energy for different dicumylperoxide concentration as function of conversion (**b**). 112
- Figure 11.5 Comparison between the experimental and the calculated conversion values for the crosslinking at 160°C of silicone rubber compounds with dicumylperoxide concentrations. The calculated conversion values are plotted from 0.1 to 0.9 of conversion. 115
- Figure 11.6 Dynamic scanning calorimetry analysis of LSR under 3 heating rates and inert atmosphere, showing the exothermic thermal event related to crosslinking. Each symbol/line represents one repetition. 116
- Figure 11.7 Conversion rate $d\alpha/dt$ for LSR at several heating rates as a function of temperature (**a**) and conversion (**b**). 117
- Figure 11.8 Friedman-like isoconversional approach for calculating the activation energy (**a**) and the activation energy as function of conversion for the calorimetric approach (**b**). 118

- Figure 11.9 Variation of torque over temperature during the experiments at the rubber process analyser (RPA) for various shear rates at 2 K.min⁻¹ (a), 5 K.min⁻¹ (b), and 10 K.min⁻¹ (c). 119
- Figure 11.10 Conversion rate $d\alpha/dt$ measured via RPA for LSR as a function of temperature at various shear rates at 2 K.min⁻¹ (a), 5 K.min⁻¹ (b), and 10 K.min⁻¹ (c). The variation of $d\alpha/dt$ over conversion is shown in (d). The shaded areas around the data lines (average) represent the standard deviation around the average. 120
- Figure 11.11 Activation energy values for the rheological approach (coloured dots) compared to the calorimetric method (black dots). 121
- Figure 11.12 Gel time (a) and temperature (b) for all heating rates and shear rates as studied by the rheology-based approach. 122
- Figure 11.13 Comparison between the calculated conversion for the DSC and the RPA (0.4383 s⁻¹) approaches at 2 K.min⁻¹ for two replicates. In the detail of the plot, conversion rate as function of the conversion is compared. 124
- Figure 11.14 Comparison of experimental data (black symbols) and fitting according to the Kamal model (coloured lines) for the conversion rate $d\alpha/dt$ at several heating rates as a function of temperature for the DSC experiments (a) and for the RPA measurements (b-d) at different shear rates. 126
- Figure 12.1 Runner system and cavity geometry applied in the simulation, showing the position of the pressure and temperature sensors (a), where sensor 1 is located in the mould inlet and sensor 2 is placed inside the cavity facing the flow entrance into the cavity; and detail of the mesh (b) employed in the volume discretization. The geometry is inspired by the work of Traintinger [198]. 137
- Figure 12.2 Simulated LSR flow behaviour for datasets A (left, LAOS) and B (right, HPCR) at 20% filling for one cavity. 140

- Figure 12.3 Simulated pressure at the sprue (sensor 1) during the filling stage (a) and simulated temperature at one cavity (sensor 2) during the injection moulding cycle (b) for two different datasets with distinct viscosity input as described in Table 12.2. 141
- Figure 12.4 Simulated pressure for the whole studied volume, including the sprue and the running system, for datasets A (left, LAOS) and B (right, HPCR), where the pressure difference is evident at the sprue at the end of filling. 142
- Figure 12.5 Simulated cavity temperature at the end of the filling stage for datasets A (left, LAOS) and B (right, HPCR) (a), with snapshot of the part cross-section for datasets A (top, LAOS) and B (bottom, HPCR) (b). 143
- Figure 12.6 Simulated curing degree at the cavity for datasets A (left, LAOS) and B (right, HPCR) at the end of the filling step. 144
- Figure 12.7 Simulated pressure at the sprue (sensor 1) during the filling stage (a), simulated temperature at one cavity (sensor 2) during the injection moulding cycle (b), and curing degree (c) for the two different datasets B and C with distinct specific heat capacity input as shown in Table 12.1. The c_p data concerning MDSC 1st and sapphire 1st can be consulted at Figure 8.1. 145
- Figure 12.8 Simulated cavity temperature at the end of the filling stage for datasets B (left, MDSC 1st) and C (right, sapphire 1st) (a), with the correspondent curing degree (conversion 0-100%) (b). 147
- Figure 12.9 Curing degree at $t = 25$ s (a) and at $t = 55$ s (a) for datasets B (left and top, MDSC 1st) and C (right and bottom, sapphire 1st). 148
- Figure 12.10 Simulated pressure at the sprue (sensor 1) during the filling stage (a), simulated temperature at one cavity (sensor 2) during the injection moulding cycle (b), and curing degree (c) for the different datasets B and D with distinct specific heat capacity input as shown in Table 12.1. The c_p data concerning MDSC 1st and sapphire 1st can be consulted at Figure 8.1. The conversion values for dataset C are shown in (c) for comparison purposes. 149

- Figure 12.11 Simulated temperature at the cavity for datasets B (left, MDSC 1st) and D (right, sapphire 2nd) at the end of the filling step, with the assigned local temperature at the center of the cavity cross-section: 34.8°C (left) and 36.5°C (right). 150
- Figure 12.12 Simulated pressure at the sprue (sensor 1) during the filling stage (a), simulated temperature at one cavity (sensor 2) during the injection moulding cycle (b), and curing degree (c) for the different datasets B and E with distinct curing kinetics inputs as shown in Table 12.3. The dashed area shown in (a) between 0 and 0.3 s is enlarged in the same plot to aid differentiation of the curves. The time at which curing degree = 90% is marked in (c) as 33.5 s for dataset B and 52.9 s for dataset E. 152
- Figure 12.13 Simulated cavity temperature at the end of the filling stage for datasets B (left, DSC) and E (right, RPA) (a), with the correspondent curing degree (conversion 0-100%) (b). 153
- Figure 12.14 Simulated cavity curing degree (conversion 0-100%) for datasets B (left, DSC) and E (right, RPA) at the cycle times $t = 15$ s (a), 30 s (b), 40 s (c), and 45 s (d). The local surface indications for the curing degree assign 98.78% (left) and 85.59% (right) at (c); and 98.81% (left) and 82.31% (right) at (d). 154
- Figure A.1 Infrared (IR) spectrum of the high consistency silicone sample without dicumylperoxide (0 phr) indicating the characteristic IR absorptions of poly(dimethylsiloxane). 169
- Figure A.2 (a) ¹H NMR spectrum in CDCl₃ for the 0 dicumylperoxide solid silicone, and detailed spectrum (b) for the vinyl region. 170
- Figure A.3 Infrared (IR) spectrum of LSR's part A and B indicating the characteristic IR absorption wavenumbers of poly(dimethylsiloxane). 171
- Figure A.4 Thermogram for the 0 phr dicumylperoxide silicone rubber under inert atmosphere (N₂). The residue values were taken as the % weight at 800°C. 171
- Figure A.5 2070 A (full line) and 2070 B (dashed line) thermograms under inert (N₂) (until 700°C) and air atmospheres. The residue values were taken as the % weight at 800°C. 172

- Figure A.6 Variability study for oscillatory experiments: (a) three strain amplitude sweep repetitions at 50°C for sample 2070 B under different strain amplitudes and (b) coefficient of variation for the amplitude sweeps shown in (a). 173
- Figure A.7 Elastic $\sigma(\gamma)$ (a) and viscous $\sigma(\dot{\gamma})$ (b) LB curves for sample 2070 B at 50°C recorded during recovery period after intense shear. 174
- Figure A.8 Imposed strain (dashed lines) and measured stress (full line) for sample 2070 A under SAOS (bottom, $\gamma = 0.1\%$) and LAOS (top, $\gamma = 10\%$) conditions for 3 different temperatures under stationary regime. 176
- Figure A.9 Intensity of the Chebyshev coefficients $e_{3/1}$ and $v_{3/1}$ as a variation of the strain amplitude for 3 imposed angular frequencies (a) 0.1 Hz; (b) 1.0 Hz; and (c) 10 Hz and at 90°C. For the ease of interpretation, the vertical lines indicate the studied amplitudes $\gamma = 0.1\%$ (SAOS) and $\gamma = 10\%$ (LAOS), and the horizontal line shows where the coefficients are zero. 177
- Figure A.10 Gap snapshots for sequential shear rates during the steady shear experiments as showed in the plot of Figure 5.8. These snapshots show details of edge instabilities as indicated by the red arrows. 178
- Figure A.11 Distribution of residuals from the conversion rate data fitting that generated the model parameters described in Table 11.4. The black line shows the normal distribution associated to the residual distribution. 186
- Figure A.12 Viscosity plots showing the measured data (triangles) at three temperatures: 50°C (blue), 70°C (red), and 90°C (green) and the respective fittings (full lines) for (a) LAOS (dataset A) and (b) HPCR (dataset B). The plots were obtained directly from the Sigmasoft simulation software. 187

LIST OF TABLES

Table 8.1	Thermal conductivity averages $\bar{\lambda}$ for the whole studied temperature range and respective standard deviations $\sigma(\lambda)$, including the associated measurement error. 81
Table 11.1	Curing parameters for silicone rubber compounds concerning minimum torque (ML , dN.m) and induction or scorch time (t_{s1} , min) for different crosslinking temperatures and varied dicumylperoxide concentrations. 107
Table 11.2	Curing parameters for silicone rubber compounds concerning maximum torque (MH , dN.m) and optimum cure time (t_{90} , min) for different crosslinking temperatures and varied dicumylperoxide concentrations. 108
Table 11.3	Kinetic parameters determined after fitting of the experimental conversion rate $d\alpha/dt$ to the Kamal model (Equation (10.11)) for silicone rubber compounds crosslinked at 160°C with different dicumylperoxide concentrations. 113
Table 11.4	Kinetic parameters (average) determined after fitting of the experimental conversion rate $d\alpha/dt$ to the Kamal model (Equation 10.11) for LSR employing various experimental procedures (DSC and rheological, from which the employed shear rates are shown). 125
Table 12.1	Material data employed to run the comparison simulation routines according to each subdataset and the employed characterization technique. DSC* denotes calorimetry data without input for the curing enthalpy. 135
Table 12.2	Carreau-Yasuda model parameters as obtained by fitting the viscosity data from datasets A and B. 138
Table 12.3	Kinetic parameters (average) determined after fitting of the experimental conversion rate $\frac{d\alpha}{dt}$ to the Kamal model (Equation (10.11)) for LSR employing the calorimetry approach (dataset B) and the rheological method (dataset E). 139
Table A.1	Averaged molecular weights and polydispersity indexes for three high consistency silicone samples (sample A, 0 phr dicumylperoxide) as determined by GPC. 167
Table A.2	Averaged molecular weights and polydispersity indexes for three LSR samples (part B, only the base polymer) as determined by GPC. 168

Table A.3	Declaration of artificial intelligence-based tools and their characteristics.	184
Table A.4	Residual characteristics for the fittings described by the parameters in Table 11.4.	185

BIBLIOGRAPHY

- [1] Johannes Karl Fink. *Liquid Silicone Rubber - Chemistry, Materials, and Processing*. 1st ed. United States of America: John Wiley, Sons Inc. and Scrivener Publishing LLC, 2019.
- [2] F. Barca, T. Caporossi and S. Rizzo. "Silicone Oil: Different Physical Properties and Clinical Applications". In: *Biomed. Res. Int.* 2014 (2014), pp. 1–7. DOI: [10.1155/2014/502143](https://doi.org/10.1155/2014/502143).
- [3] F. Dankert and C. von Hänisch. "Siloxane Coordination Revisited: Si–O Bond Character, Reactivity and Magnificent Molecular Shapes". In: *Eur. J. Inorg. Chem.* 2021 (2021), pp. 2907–2927. DOI: [10.1002/ejic.202100275](https://doi.org/10.1002/ejic.202100275).
- [4] A.L. Allred and E.G. Rochow. "A scale of electronegativity based on electrostatic force". In: *J. Inorg. Nucl. Chem.* 5 (1958), pp. 264–268. DOI: [10.1016/0022-1902\(58\)80003-2](https://doi.org/10.1016/0022-1902(58)80003-2).
- [5] J.-X. Yang, H.-J. Qian, Z. Gong, Z.-Y. Lu and S.-X. Cui. "Stretching Elasticity and Flexibility of Single Polyformaldehyde Chain". In: *Chin. J. Polym. Sci* 40 (2022), pp. 333–337. DOI: [10.1007/s10118-022-2679-3](https://doi.org/10.1007/s10118-022-2679-3).
- [6] S.C. Shit and P. Shah. "A Review on Silicone Rubber". In: *Nat. Acad. Sci. Let.* 36 (2013), pp. 355–365. DOI: <https://doi.org/10.1007/s40009-013-0150-2>.
- [7] Q. Zaman, K.M. Zia, M. Zuber, Y.N. Mabkhot, F. Almalki and T.B. Hadda. "A comprehensive review on synthesis, characterization, and applications of polydimethylsiloxane and copolymers". In: *Int. J. Plast. Technol.* 2 (2019), pp. 261–282. DOI: <https://doi.org/10.1007/s12588-019-09259-y>.
- [8] T. Köhler, A. Gutacker and E. Mejía. "Industrial synthesis of reactive silicones: reaction mechanisms and processes". In: *Org. Chem. Front.* 7 (2020), pp. 4108–4120. DOI: <https://doi.org/10.1039/d0qo01075h>.
- [9] R. Müller. *Verfahren zur Herstellung von Kohlenstoff-Silicium-Halogenverbindungen*, VEB Silikonchemie. DD Patent D.R.P. C 57411, 1953.
- [10] E.G. Rochow. *Preparation of organosilicon halides*. U.S. Patent 2380995, 1945.
- [11] T. Yokozawa and A. Yokoyama. "Chain-Growth Polycondensation: Living Polymerization Nature in Polycondensation and Approach to Condensation Polymer Architecture". In: *Polym. J. (Tokyo, Jpn.)* 36 (2004), pp. 65–83. DOI: <https://doi.org/10.1002/chin.200430250>.

- [12] E. Delebecq and F. Ganachaud. "Looking over Liquid Silicone Rubbers: (1) Network Topology vs Chemical Formulations". In: *ACS Appl. Mater. Interfaces* 4 (2012), pp. 3340–3352. DOI: <https://dx.doi.org/10.1021/am300502r>.
- [13] J.P. Hernández-Ortiz and T.A. Osswald. "Modeling Processing of Silicone Rubber: Liquid Versus Hard Silicone Rubbers". In: *J. Appl. Polym. Sci.* 119 (2010), pp. 1864–1871. DOI: <https://dx.doi.org/10.1002/app.31995>.
- [14] M. Doi and S.F. Edwards. *The Theory of Polymers Dynamics*. 1st ed. Oxford Science Publications, 1988.
- [15] D. Osmanović and Y. Rabin. "Dynamics of active Rouse chains". In: *Soft Matter* 13 (2017), pp. 963–968. DOI: <https://doi.org/10.1039/C6SM02722A>.
- [16] P.R. Dvornic, J.D. Jovanovic and M.N. Govedarica. "On the Critical Molecular Chain Length of Polydimethylsiloxane". In: *J. Appl. Polym. Sci.* 49 (1993), pp. 1497–1507. DOI: <https://doi.org/10.1002/app.1993.070490901>.
- [17] J. Hintermeyer, A. Herrmann, R. Kahlau, C. Goiceanu and E.A. Rässler. "Molecular Weight Dependence of Glassy Dynamics in Linear Polymers Revised". In: *Macromolecules* 41 (2008), pp. 9335–9344. DOI: <https://doi/10.1021/ma8016794>.
- [18] P. Klonos, K. Kulyk, M.V. Borysenko, V.M. Gunko, A. Kyritsis and P. Pissis. "Effects of Molecular Weight below the Entanglement Threshold on Interfacial Nanoparticles/Polymer Dynamics". In: *Macromolecules* 49 (2016), pp. 9457–9473. DOI: <https://doi/10.1021/acs.macromol.6b01931>.
- [19] L. Chu, K. Xu, R. Graf, Z.-C. Yan, J. Li and Y.-F. Yao. "Dynamic heterogeneity in homogeneous polymer melts". In: *Soft Matter* 17 (2021), pp. 6081–6087. DOI: <https://doi.org/10.1039/D1SM00017A>.
- [20] Z. Dobkowski. "Determination of critical molecular weight for entangled macromolecules using the tensile strength data". In: *Rheol. Acta* 34 (1995), pp. 578–585. DOI: <https://doi.org/10.1007/BF00712317>.
- [21] R. Lund, A. Alegría, L. Goitandía, J. Colmenero, González. M.A. and P. Lindner. "Dynamical and Structural Aspects of the Cold Crystallization of Poly(dimethylsiloxane) (PDMS)". In: *Macromolecules* 41 (2008), pp. 1364–1376. DOI: <https://doi.org/10.1021/ma702055b>.
- [22] N. Bosq, N. Guigo, J. Persello and N. Sbirrazzuoli. "Melt and glass crystallization of PDMS and PDMS silica nanocomposites". In: *Phys. Chem. Chem. Phys.* 16 (2014), pp. 7830–7840. DOI: <https://doi.org/10.1039/c4cp00164h>.

- [23] I. Chiulan, D.M. Panaitescu, E.-R. Radu, A.N. Frone, R.A. Gabor, C.A. Nicolae, G. Jinescu, V. Tofan and G. Chinga-Carrasco. "Comprehensive characterization of silica-modified silicon rubbers". In: *J. Mech. Behav. Biomed. Mater.* 101 (2020), p. 103427. DOI: <https://doi.org/10.1016/j.jmbbm.2019.103427>.
- [24] K. Zalewski, Z. Chyłek and W.A. Trzeciński. "A Review of Polysiloxanes in Terms of Their Application in Explosives". In: *Polymers* 13 (2021), p. 1080. DOI: <https://doi.org/10.3390/polym13071080>.
- [25] M. Azevedo, A.-M. Monks, R.C. Kerschbaumer, S. Schlögl, K. Saalwächter, M. Walluch, G. Consolati and C. Holzer. "Peroxide-based crosslinking of solid silicone rubber, part II: The counter-intuitive influence of dicumylperoxide concentration on cross-link effectiveness and related network structure". In: *J. Appl. Polym. Sci.* 140 (2023), e54111. DOI: <https://doi.org/10.1002/app.54111>.
- [26] R. Winkler, W. Tu, L. Laskowski and K. Adrjanowicz. "Effect of Surface Chemistry on the Glass-Transition Dynamics of Poly(phenyl methyl siloxane) Confined in Alumina Nanopores". In: *Langmuir* 36 (2020), pp. 7553–7565. DOI: <https://doi.org/10.1021/acs.langmuir.0c01194>.
- [27] E.A. Gruschevenco, I.L. Borisov and A.V. Volkov. "High-Selectivity Polysiloxane Membranes for Gases and Liquids Separation (A Review)". In: *Pet. Chem.* 61 (2021), pp. 956–976. DOI: <https://doi.org/10.1134/S0965544121090103>.
- [28] C.M. Roland and C.A. Aronson. "Crystallization of polydimethylsiloxane end-linked networks". In: *Polym. Bull.* 45 (2000), pp. 439–445. DOI: <https://doi.org/10.1007/s002890070019>.
- [29] G. Camino, S.M. Lomakin and M. Lazzari. "Polydimethylsiloxane thermal degradation Part 1. Kinetic aspects". In: *Polymer* 42 (2001), pp. 2395–2402. DOI: [https://doi.org/10.1016/S0032-3861\(00\)00652-2](https://doi.org/10.1016/S0032-3861(00)00652-2).
- [30] G. Camino, S.M. Lomakin and M. Lagueard. "Thermal polydimethylsiloxane degradation. Part 2. The degradation mechanisms". In: *Polymer* 43 (2002), pp. 2011–2015. DOI: [https://doi.org/10.1016/S0032-3861\(01\)00785-6](https://doi.org/10.1016/S0032-3861(01)00785-6).
- [31] J.P. Levicki, J.L. Liggat and M. Patel. "The thermal degradation behaviour of polydimethylsiloxane/montmorillonite nanocomposites". In: *Polym. Degrad. Stab.* 94 (2009), pp. 1548–1557. DOI: <https://doi.org/10.1016/j.polymdegradstab.2009.04.030>.

- [32] X. Gao, H. Liu, H. Wei, J. Zheng and G. Huang. "Effect of incompletely condensed tri-silanol-phenyl-POSS on the thermal stability of silicone rubber". In: *Polym. Bull.* 76 (2019), pp. 2835–2850. DOI: <https://doi.org/10.1007/s00289-018-2499-3>.
- [33] S. Venkatachalam and F. Hourlier. "Heat treatment of commercial Polydimethylsiloxane PDMS precursors: Part I. Towards conversion of patternable soft gels into hard ceramics". In: *Ceram. Int.* 45 (2019), pp. 6255–6262. DOI: <https://doi.org/10.1016/j.ceramint.2018.12.106>.
- [34] G. Deshpande and M.E. Rezac. "Kinetic aspects of the thermal degradation of poly(dimethyl siloxane) and poly(dimethyl diphenyl siloxane)". In: *Polym. Degrad. Stab.* 76 (2002), pp. 17–24. DOI: [https://doi.org/10.1016/S0141-3910\(01\)00261-0](https://doi.org/10.1016/S0141-3910(01)00261-0).
- [35] I.V. Elmanovich, V.E. Sizov, V.V. Zefirov, A.A. Kalinina, M.O. Gallyamov, V.S. Papkov and A.M. Muzafarov. "Chemical Recycling of High-Molecular-Weight Organosilicon Compounds in Supercritical Fluids". In: *Polymers* 14 (2022), p. 5170. DOI: <https://doi.org/10.3390/polym14235170>.
- [36] E. Delebecq, S. Hamdani-Devarenes, J. Raeke, J.M.L. Cuesta and F. Ganachaud. "High Residue Contents Indebted by Platinum and Silica Synergistic Action during the Pyrolysis of Silicone Formulations". In: *ACS Appl. Mater. Interfaces* 3 (2011), pp. 869–880. DOI: <https://doi.org/10.1021/am101216y>.
- [37] J. Chen, J. Liu, Z. Peng, Y. Yao and S. Chen. "The microscopic mechanism of size effect in silica-particle reinforced silicone rubber composites". In: *Eng. Fract. Mech.* 255 (2021), p. 107945. DOI: <https://doi.org/10.1016/j.engfracmech.2021.107945>.
- [38] L. Huang et al. "Structural analysis of the bound rubber in silica-filler silicone rubber nanocomposites reveal mechanisms of filler-rubber interaction". In: *Compos. Sci. Technol.* 233 (2023), p. 109905. DOI: <https://doi.org/10.1016/j.compscitech.2022.109905>.
- [39] Y. Tong, H. Liu, A. Chen, H. Guan, J. Kong, S. Liu and C. He. "Effect of surface chemistry and morphology of silica on the thermal and mechanical properties of silicone elastomers". In: *J. App. Polym. Sci.* 135 (2018), p. 46646. DOI: <https://doi.org/10.1002/app.46646>.
- [40] Y. Shui, L. Huang, C. Wei, G. Sun, J. Chen, A. Lu, L. Sun and D. Liu. "How the silica determined properties of filled silicone rubber by the formation of filler networking and bound rubber". In: *Compos. Sci. Technol.* 215 (2021), p. 109024. DOI: <https://doi.org/10.1016/j.compscitech.2021.109024>.

- [41] A.M. Stricher, R.G. Rinaldi, C. Barrès, F. Ganachaud and L. Chazeau. "How I met your elastomers: from network topology to mechanical behaviours of conventional silicone materials". In: *RSC Advances* 5 (2015), pp. 53713–53725. DOI: <https://doi.org/10.1039/c5ra06965c>.
- [42] F. Yan, X. Zhang, F. Liu, X. Li and Z. Zhang. "Adjusting the properties of silicone rubber filled with nanosilica by changing the surface organic groups of nanosilica". In: *Composites Part B* 75 (2015), pp. 47–52. DOI: <http://dx.doi.org/10.1016/j.compositesb.2015.01.030>.
- [43] Y. Zhang, W. Liu, Q. Zhou, Y. Meng, Y. Zhong, J. Xu, C. Xiao, G. Zhang and Y. Zhang. "Effects of Vinyl Functionalized Silica Particles on Thermal and Mechanical Properties of Liquid Silicone Rubber Nanocomposites". In: *Polymers* 15 (2023), p. 1224. DOI: <https://doi.org/10.3390/polym15051224>.
- [44] T. Goudarzi, D.W. Spring, G.H. Paulino and O. Lopez-Pamies. "Filled elastomers: A theory of filler reinforcement based on hydrodynamic and interphasial effects". In: *J. Mech. Phys. Solids* 80 (2015), pp. 37–67. DOI: <http://dx.doi.org/10.1016/j.jmps.2015.04.012>.
- [45] L. Huang et al. "Understanding the Reinforcement Effect of Fumed Silica on Silicone Rubber: Bound Rubber and Its Entanglement Network". In: *Macromol.* 56 (2023), pp. 323–334. DOI: <https://doi.org/10.1021/acs.macromol.2c01969>.
- [46] M.-J. Wang, M.D. Morris and Y. Kutsovsky. "Effect of Fumed Silica Surface Area on Silicone Rubber Reinforcement". In: *KGK Kautschuk Gummi Kunststoffe* 61 (2008), pp. 107–117.
- [47] J.M. Castro, M.C. Ríos and C.A. Mount-Campbell. "Modelling and simulation in reactive polymer processing". In: *Modelling Simul. Mater. Sci. Eng.* 12 (2004), S121–S149. DOI: <https://doi.org/10.1088/0965-0393/12/3/S06>.
- [48] M. Bont, C. Barry and S. Johnston. "A review of liquid silicone rubber injection molding: Process variables and process modeling". In: *Polym. Eng. Sci.* 61 (2021), pp. 331–347. DOI: <https://doi.org/10.1002/pen.25618>.
- [49] E. Mitsoulis. "Computational Polymer Processing". In: *Modeling and Simulation in Polymers*. Ed. by P.D. Gujrati and A.I. Leonov. Weinheim, Germany: Wiley-VCH Verlag GmbH and Co. KGaA, 2010, pp. 127–193. ISBN: 9783527324156. URL: <https://onlinelibrary.wiley.com/doi/book/10.1002/9783527630257>.
- [50] L. Matysiak, X. Kornmann, P. Saj and R. Sekula. "Analysis and Optimization of the Silicone Molding Process Based on Numerical Simulations and Experiments". In: *Adv. Polym. Tech.*

- 32 (2012), E258–E273. DOI: <https://doi.org/10.1002/adv.21272>.
- [51] M. García-Camprubí, C. Alfaro-Isac, B. Hernández-Gascón, J.R. Valdés and S. Izquierdo. “Numerical Approach for the Assessment of Micro-Textured Walls Effects on Rubber Injection Moulding”. In: *Polymers* 13 (2021), p. 1739. DOI: <https://doi.org/10.3390/polym13111739>.
- [52] R.G. Speight, F. Costa, P.K. Kennedy and C. Friedl. “Best practice for benchmarking injection moulding simulation”. In: *Plast. Rubber. Compos.* 37 (2013), pp. 124–130. DOI: <https://doi.org/10.1179/174328908X283203>.
- [53] E. Haberstroh, W. Michaeli and E. Heize. “Simulation of the Filling and Curing Phase in Injection Molding of Liquid Silicone Rubber (LSR)”. In: *Plast. Rubber. Compos.* 21 (2002), pp. 461–471. DOI: <https://doi.org/10.1106/073168402026476>.
- [54] R. Capellmann, E. Haberstroh, T. Häuser and H. Wehr. “Development of simulation software for the injection moulding of liquid silicone rubber”. In: *Int. Polym. Sci. Tech.* 30 (2003), pp. 1–8. DOI: <https://doi.org/10.1177/0307174X0303001101>.
- [55] H. Ou, M. Sahli, T. Barnière and J.C. Gelin. “Mutiphysics modelling and experimental investigations of the filling and curing phases of bi-injection moulding of thermoplastic polymer/liquid silicone rubbers”. In: *Int. J. Adv. Manuf. Technol.* 92 (2017), pp. 3871–3882. DOI: <https://doi.org/10.1007/s00170-017-0425-8>.
- [56] United Nations. *The 17 UN Sustainable Goals*. 2015. URL: <https://sdgs.un.org/goals> (visited on 18/04/2024).
- [57] P. Brincat, K. Talwar and C. Friedl. “Extensional Viscosity Modelling for Injection Molding Simulation.” In: *J. Reinf. Plast. Compos.* 18 (1999), pp. 499–507. DOI: <http://dx.doi.org/10.1177/073168449901800602>.
- [58] P. Taheri, M. Torrilhon and H. Struchtrup. “Couette and Poiseuille microflows: Analytical solutions for regularized 13-moment equations”. In: *Phys. Fluids* 21 (2009), p. 017102. DOI: <https://doi.org/10.1063/1.3064123>.
- [59] R. Ziebell and H. Bhogesra. “LIM Simulation Modeling Using Newly Developed Chemorheological Methods”. In: *Proceedings of the International Silicone Conference*. 2016.
- [60] D.F. Weißer, A. Shakeel, D. Mayer, J. Schmid, S.J. Heienbrock, M. Deckert and B.E. Rapp. “Gel point investigation of liquid silicone rubber using rheological approaches”. In: *Polymer* 283 (2023), p. 126286. DOI: <https://doi.org/10.1016/j.polymer.2023.126286>.

- [61] L. Yu and A.L. Skov. "Silicone rubbers for dielectric elastomers with improved dielectric and mechanical properties as a result of substituting silica with titanium dioxide". In: *Int. J. Smart Nano Mater.* 6 (2015), pp. 268–289. DOI: <http://dx.doi.org/10.1080/19475411.2015.1119216>.
- [62] T. Ma, R. Yang, Z. Zheng and Y. Song. "Rheology of fumed silica/polydimethylsiloxane suspensions". In: *J. Rheol.* 61 (2017), pp. 205–2015. DOI: <http://dx.doi.org/10.1122/1.4973974>.
- [63] C. Geng, Q. Zhang, W. Lei, F. Yu and A. Lu. "Simultaneously reduced viscosity and enhanced strength of liquid silicone rubber/silica composites by silica surface modification". In: *J. App. Polym. Sci.* 134 (2017), p. 45544. DOI: <https://doi.org/10.1002/app.45544>.
- [64] J. Stieghorst and T. Doll. "Rheological behavior of PDMS silicone rubber for 3D printing of medical implants". In: *Addit. Manuf.* 24 (2018), pp. 217–223. DOI: <https://doi.org/10.1016/j.addma.2018.10.004>.
- [65] K. Hyun, M. Wilhelm, C.O. Klein, K.S. Cho, J.G. Nam, K.H. Ahn, S.J. Lee, R.H. Ewoldt and G.H. McKinley. "A review of nonlinear oscillatory shear tests: Analysis and application of large amplitude oscillatory shear (LAOS)". In: *Prog. Polym. Sci.* 36 (2011), pp. 1697–1753. DOI: <https://doi.org/10.1016/j.progpolymsci.2011.02.002>.
- [66] M. Wilhelm, D. Maring and H.-W. Spiess. "Fourier-transform rheology". In: *Rheol. Acta* 37 (1998), pp. 399–405. DOI: <https://doi.org/10.1007/s003970050126>.
- [67] John M. Dealy and Kurt F. Wissbrun. *Melt Rheology and Its Role in Plastics Processing: Theory and Application*. 1st ed. Dordrecht, Netherlands: Springer Dordrecht, 1999.
- [68] R. Byron Bird, Robert C. Armstrong and Ole Hassager. *Dynamics of Polymeric Liquids, Volume 1: Fluid Mechanics*. 2nd ed. Hoboken, USA: Wiley, 1987.
- [69] K. Atalik and R. Keunings. "On the occurrence of even harmonics in the shear stress response of viscoelastic fluids in large amplitude oscillatory shear". In: *J. Non-Newtonian Fluid Mech.* 122 (2004), pp. 107–116. DOI: <https://doi.org/10.1016/j.jnnfm.2003.11.012>.
- [70] M.D. Graham. "Wall slip and the nonlinear dynamics of large-amplitude oscillatory shear flows". In: *J. Rheol.* 39 (1995), pp. 697–712. DOI: <https://doi.org/10.1122/1.550652>.
- [71] M. Kamkar et al. "Large amplitude oscillatory shear flow: Microstructural assessment of polymeric systems". In: *Prog. Polym. Sci.* 132 (2022), p. 101580. DOI: <https://doi.org/10.1016/j.progpolymsci.2022.101580>.

- [72] R.H. Ewoldt, A.E. Hosoi and G.H. McKinley. "New measures for characterizing nonlinear viscoelasticity in large amplitude oscillatory shear". In: *J. Rheol.* 52 (2008), pp. 1427–1458. DOI: <https://doi.org/10.1122/1.2970095>.
- [73] M. Laun, D. Auhl, R. Brummer, D.J. Dijkstra, C. Gabriel, M.A. Mangnus, M. Rüllmann, W. Zoetelief and U.A. Handge. "Guidelines for checking performance and verifying accuracy of rotational rheometers: viscosity measurements in steady and oscillatory shear (IUPAC Technical Report)". In: *Pure Appl. Chem.* 86 (2014), pp. 1945–1968. DOI: <https://doi.org/10.1515/pac-2013-0601>.
- [74] S.S. Datta et al. "Perspectives on viscoelastic flow instabilities and elastic turbulence". In: *Phys. Rev. Fluids* 7 (2022), p. 080701. DOI: <https://doi.org/10.1103/PhysRevFluids.7.080701>.
- [75] E.J. Hemingway and S.M. Fielding. "Edge fracture instability in sheared complex fluids: Onset criterion and possible mitigation strategy". In: *J. Rheol.* 63 (2019), pp. 735–750. DOI: <https://doi.org/10.1122/1.5095717>.
- [76] E.J. Hemingway, H. Kusumaatmaja and S.M. Fielding. "Edge fracture in complex fluids". In: *Phys. Rev. Lett.* 119 (2017), p. 028006. DOI: <https://doi.org/10.1103/PhysRevLett.119.028006>.
- [77] K.M. Mattes, R. Vogt and C. Friedrich. "Analysis of the edge fracture process in oscillation for polystyrene melts". In: *Rheol. Acta* 47 (2008), pp. 929–942. DOI: <https://doi.org/10.1007/s00397-008-0286-z>.
- [78] W. Cox and E. Merz. "Correlation of dynamic and steady flow viscosities". In: *J. Polym. Sci.* 28 (1958), pp. 619–622. DOI: <https://doi.org/10.1002/pol.1958.1202811812>.
- [79] F. Snijkers and D. Vlassopoulos. "Appraisal of the Cox-Merz rule for well-characterized entangled linear and branched polymers". In: *Rheol. Acta* 53 (2014), pp. 935–946. DOI: <https://doi.org/10.1007/s00397-014-0799-6>.
- [80] J.D.J. Rathinaraj, B. Keshavarz and G.H. McKinley. "Why the Cox-Merz rule and Gleissle mirror relation work: A quantitative analysis using the Wagner integral framework with a fractional Maxwell kernel". In: *Phys. Fluids* 34 (2022), p. 033106. DOI: <https://doi.org/10.1063/5.0084478>.
- [81] Y.H. Shim, J.J. Griebler and S.A. Rogers. "A reexamination of the Cox-Merz rule through the lens of recovery rheology". In: *J. Rheol.* 68 (2024), pp. 381–396. DOI: <https://doi.org/10.1122/8.0000811>.

- [82] E.M. Burgeson and S.A. Rogers. "The mathematics of oscillatory recovery rheology with applications to experiments, the Cox-Merz rules, and the nonlinear modeling of common amplitude sweep behaviors." In: *Rheol. Acta* – (2024), pp. –. DOI: <https://doi.org/10.1007/s00397-024-01448-w>.
- [83] C. Kukla, I. Duretek, J. Gonzalez-Gutierrez and C. Holzer. "Polymer Rheology". In: Online: InTech, 2018. Chap. 8, pp. 153–.
- [84] B. Rabinowitsch. "Über die Viskosität und Elastizität von Solen". In: *Z. Für Phys. Chem.* 145A (1929), pp. 1–26. DOI: [10.1515/zpch-1929-14502](https://doi.org/10.1515/zpch-1929-14502).
- [85] E.B. Bagley. "End Corrections in the Capillary Flow of Polyethylene". In: *J. Appl. Phys.* 28 (1957), pp. 624–627. DOI: [10.1063/1.1722814](https://doi.org/10.1063/1.1722814).
- [86] H.T. Lim, K.H. Ahn, J.S. Hong and K. Hyun. "Nonlinear viscoelasticity of polymer nanocomposites under large amplitude oscillatory shear flow". In: *J. Rheol.* 57 (2013), pp. 767–789. DOI: <https://doi.org/10.1122/1.4795748>.
- [87] L. Heymann, S. Peukert and N. Aksel. "Investigation of the solid-liquid transition of highly concentrated suspensions in oscillatory amplitude sweeps". In: *J. Rheol.* 46 (2002), pp. 93–112. DOI: <https://doi.org/10.1122/1.1423314>.
- [88] G. Filippone and M.S. de Luna. "A Unifying Approach for the Linear Viscoelasticity of Polymer Nanocomposites". In: *Macromol.* 45 (2012), pp. 8853–8860. DOI: <https://doi.org/10.1021/ma301594g>.
- [89] J. Wang, Y. Guo, W. Yu, C. Zhou and P. Steeman. "Linear and nonlinear viscoelasticity of polymer/silica nanocomposites: an understanding from modulus decomposition". In: *Rheol. Acta* 55 (2016), pp. 37–50. DOI: <https://doi.org/10.1007/s00397-015-0895-2>.
- [90] B. Li, Y. Guo, P. Steeman, M. Bulters and W. Yu. "Shear-induced breakdown and agglomeration in nanoparticles filled polymers: The shift of phase boundary and kinetics". In: *J. Rheol.* 65 (2021), pp. 291–309. DOI: <https://doi.org/10.1122/8.0000032>.
- [91] J. Launay, N. Allanic, P. Mousseau, R. Deterre and C. Plot. "Effect of viscous dissipation in the prediction of thermal behavior of an elastomer cylindrical flow". In: *J. Mater. Process. Technol.* 252 (2018), pp. 680–687. DOI: <https://doi.org/10.1016/j.jmatprotec.2017.10.035>.
- [92] D. Kleinschmidt, F. Brüning and J. Petzke. "Wall Slip-Free Viscosity Determination of Filled Rubber Compounds Using Steady-State Shear Measurements". In: *Polymers* 15 (2023), p. 4406. DOI: <https://doi.org/10.3390/polym15224406>.

- [93] M. Ramini and S. Agnelli. "Monitoring of shear heating effects during injection molding of rubber to improve the process control". In: *Polym. Bull.* 80 (2023), pp. 6707–3723. DOI: <https://doi.org/10.1007/s00289-022-04376-y>.
- [94] I.S. Sohn and R. Rajagopalan. "Microrheology of model quasi-hard-sphere dispersions". In: *J. Rheol.* 48 (2004), pp. 117–142. DOI: <https://doi.org/10.1122/1.1626678>.
- [95] C. Carotenuto, G. Rexha, R. Martone and M. Minale. "The microstructural change causing the failure of the Cox-Merz rule in Newtonian suspensions: experiments and simulations". In: *Rheol. Acta* 60 (2021), pp. 309–325. DOI: <https://doi.org/10.1007/s00397-021-01270-8>.
- [96] P. Beyer and H.P. Wolf. "Effizienz und Qualität durch eine neue Generation rheologieoptimierter Flüssigsiliconelastomere". In: *GAK* 10 (2015), pp. 676–83.
- [97] G.A. Mannella, V. La Carrubba, V. Brucato, W. Zoetelief and G. Haagh. "No-flow temperature in injection molding simulation." In: *J. App. Polym. Sci.* 119 (2010), pp. 3382–3392. DOI: <https://doi.org/10.1002/app.32987>.
- [98] Jozef Bicerano. *Prediction of Polymer Properties*. 3rd ed. United States of America: Marcel Dekker, Inc., 2002.
- [99] Theodore L. Bergman and Adrienne S. Lavine. *Fundamentals of Heat and Mass Transfer*. 8th ed. United States of America: John Wiley and Sons, 2018.
- [100] R. Vera-Graziano, F. Hernandez-Sanchez and J.V. Cauich-Rodriguez. "Study of Crosslinking Density in Polydimethylsiloxane Networks by DSC." In: *J. App. Polym. Sci.* 55 (1995), pp. 1317–1327. DOI: <https://doi.org/10.1002/app.1995.070550905>.
- [101] J. McHugh, P. Fideu, A. Herrmann and W. Stark. "Determination and review of specific heat capacity measurements during isothermal cure of an epoxy using TM-DSC and standard DSC techniques". In: *Polym. Test.* 29 (2010), pp. 759–765. DOI: <https://doi.org/10.1016/j.polymertesting.2010.04.004>.
- [102] Vish Prasad, Yogesh Jaluria and Zhuomin M. Zhang. *Annual Review of Heat Transfer*. 16th ed. United States of America: Begell House, 2013.
- [103] C. Huang, X. Qian and R. Yang. "Thermal conductivity of polymers and polymer nanocomposites." In: *Mat. Sci. Eng. R* 132 (2018), pp. 1–22. DOI: <https://doi.org/10.1016/j.mser.2018.06.002>.
- [104] V. Rashidi, E.J. Coyle, K. Sebeck, J. Kiefer and K.P. Pipe. "Thermal Conductance in Cross-linked Polymers: Effects of Non-Bonding Interactions." In: *J. Phys. Chem. B.* 121 (2017), pp. 4600–4609. DOI: <http://dx.doi.org/10.1021/acs.jpcc.7b01377>.

- [105] S. Azizi, G. Momen, C. Ouellet-Plamondon and E. David. "Enhancement in electrical and thermal performance of high-temperature vulcanized silicone rubber composites for outdoor insulating applications." In: *J. App. Polym. Sci.* 137 (2020), e49514. DOI: <https://doi.org/10.1002/app.49514>.
- [106] Y.-T. Li, W.-J. Liu, F.-X. Shen, G.-D. Zhang, L.-X. Gong, L. Zhao, P. Song, J.-F. Gao and L.-C. Tang. "Processing, thermal conductivity and flame retardant properties of silicone rubber filled with different geometries of thermally conductive fillers: A comparative study." In: *Compos. B Eng.* 232 (2022), p. 109907. DOI: <https://doi.org/10.1016/j.compositesb.2022.109907>.
- [107] R.C. Kerschbaumer et al. "Comparison of steady-state and transient thermal conductivity testing methods using different industrial rubber compounds". In: *Polym. Test.* 80 (2019), p. 106121. DOI: <https://doi.org/10.1016/j.polymertesting.2019.106121>.
- [108] Q. Su, N. Zhang and M.D. Gilchrist. "Precision injection moulding of micro components: Determination of heat transfer coefficient and precision process simulation." In: *Int. J. Mech. Sci.* 269 (2024), p. 109065. DOI: <https://doi.org/10.1016/j.ijmecsci.2024.109065>.
- [109] M. Stricker and G. Steinbichler. "Determination of heat transfer coefficients at the polymer-mold-interface for injection molding simulation by means of calorimetry." In: *AIP Conf. Proc* 1593 (2014), pp. 137–141. DOI: <https://doi.org/10.1063/1.4873750>.
- [110] M. Babenko, J. Sweeney, P. Petkov, F. Lacan, S. Bigot and B. Whiteside. "Evaluation of heat transfer at the cavity-polymer interface in microinjection moulding based on experimental and simulation study." In: *Appl. Therm. Eng.* 130 (2018), pp. 865–876. DOI: <https://doi.org/10.1016/j.applthermaleng.2017.11.022>.
- [111] J.H. Dymong and R. Malhotra. "The Tait equation: 100 years on." In: *Int. J. Thermophys.* 9 (1988), pp. 941–951. DOI: <https://doi.org/10.1007/BF01133262>.
- [112] J. Wang, C. Hopmann, M. Schmitz, T. Hohlweck and J. Wipperfurth. "Modeling of pvT behavior of semi-crystalline polymer based on the two-domain Tait equation of state for injection molding." In: *Mater. Des.* 183 (2019), p. 108149. DOI: <https://doi.org/10.1016/j.matdes.2019.108149>.
- [113] J. Wang. "Some Critical Issues for Injection Moulding". In: <https://www.intechopen.com/chapters/33643>: InTech, 2012. Chap. PVT Properties of Polymers for Injections Molding, pp. 3–30.

- [114] ASTM. *Standard test method for determining specific heat capacity by differential scanning calorimetry*. Standard ASTM E1269-(2011). American Society for Testing and Materials, 2011.
- [115] M. Reading, A. Luget and R. Wilson. "Modulated differential scanning calorimetry". In: *Thermochim. Acta* 238 (1994), pp. 295–307. DOI: [https://doi.org/10.1016/S0040-6031\(94\)85215-4](https://doi.org/10.1016/S0040-6031(94)85215-4).
- [116] K.J. Jones, I. Kinshott, M. Reading, A.A. Lacey, C. Nikolopoulos and H.M. Pollock. "The origin and interpretation of the signals of MTDSC". In: *Thermochim. Acta* 304/305 (1997), pp. 187–199. DOI: [https://doi.org/10.1016/S0040-6031\(97\)00096-8](https://doi.org/10.1016/S0040-6031(97)00096-8).
- [117] I. Fraga, S. Montserrat and J.M. Hutchinson. "TOPEM, a new temperature modulated DSC technique - Application to the glass transition of polymers". In: *J. Therm. Anal. Calorim.* 87 (2007), pp. 119–124. DOI: <https://doi.org/10.1007/s10973-006-7969-4>.
- [118] W. Stark, M. Jaunich and J. McHugh. "Cure state detection for pre-cured carbon-fibre epoxy prepreg (CFC) using Temperature-Modulated Differential Scanning Calorimetry (TMDSC)". In: *Polym. Test.* 32 (2013), pp. 1261–1272. DOI: <http://dx.doi.org/10.1016/j.polymertesting.2013.07.007>.
- [119] ASTM. *Standard test method for thermal conductivity of plastics by means of a transient line-source technique*. Standard ASTM D5930-(2019). American Society for Testing and Materials, 2019.
- [120] ASTM. *Standard test method for evaluating the resistance to thermal transmission of materials by guarded heat flow meter technique*. Standard ASTM E1530-(2006). American Society for Testing and Materials, 2006.
- [121] G. Van Assche, A. Van Hemelrijck, H. Rahier and B. Van Mele. "Modulated differential scanning calorimetry: isothermal cure and vitrification of thermosetting systems." In: *Thermo. Acta* 268 (1995), pp. 121–142. DOI: [https://doi.org/10.1016/0040-6031\(95\)02693-2](https://doi.org/10.1016/0040-6031(95)02693-2).
- [122] G. Zhang, Y. Sun, B. Qian, H. Gao and D. Zuo. "Experimental study on mechanical performance of polydimethylsiloxane (PDMS) at various temperatures." In: *Polym. Test.* 90 (2020), p. 106670. DOI: <https://doi.org/10.1016/j.polymertesting.2020.106670>.
- [123] M. Meléndez-Zamudío, A. Villegas, J.A. González-Calderón, R. Meléndrez, M. Meléndez-Lira and J. Cervantes. "Study of Polydimethylsiloxane (PDMS) Elastomer Generated by Gamma Irradiation: Correlation Between Properties (Thermal and Mechanical) and Structure (Crosslink Density Value)." In: *J. Inorg. Organomet. Polym.* 27 (2017), pp. 622–632. DOI: <https://doi.org/10.1007/s10904-017-0503-2>.

- [124] S. Gong, C. Shi and M. Li. "Flow Performance and Its Effect on Shape Formation in PDMS Assisted Thermal Reflow Process." In: *Appl. Sci.* 12 (2022), p. 8282. DOI: <https://doi.org/10.3390/app12168282>.
- [125] D. Liu and C. Zhong. "Modeling of the Heat Capacity of Polymers with the Variable Connectivity Index." In: *Polym. J.* 35 (2002), pp. 954–961. DOI: <https://doi.org/10.1295/polymj.34.954>.
- [126] M. Rafei, M.H.R. Ghoreishy and G. Naderi. "Development of an advanced computer simulation technique for the modeling of rubber curing process." In: *Comput. Mater. Sci.* 47 (2009), pp. 539–547. DOI: <http://dx.doi.org/10.1016/j.commatsci.2009.09.022>.
- [127] Z. Zou, W. Wu, Y. Wang and L. Wang. "Enhancement of thermal conductivity and tensile strength of liquid silicone rubber by threedimensional alumina network." In: *Soft Mater.* 17 (2019), pp. 297–307. DOI: <https://doi.org/10.1080/1539445X.2019.1601110>.
- [128] W.-C. Cheng, Y.-T. Hsieh and W.-R. Liu. "Enhanced Thermal Conductivity of Silicone Composites Filled with Few-Layered Hexagonal Boron Nitride." In: *Polymers* 12 (2020), p. 2072. DOI: <http://dx.doi.org/10.3390/polym12092072>.
- [129] D.W. van Krevelen. *Properties of Polymers. Their Correlation with Chemical Structure, Their Numerical Estimation and Prediction from Additive Group Contributions*. 3rd ed. Netherlands: Elsevier, 1990.
- [130] C. Zhong, Q. Yang and W. Wang. "Correlation and prediction of the thermal conductivity of amorphous polymers." In: *Fluid Ph. Equilib.* 181 (2001), pp. 195–202. DOI: [https://doi.org/10.1016/S0378-3812\(01\)00492-7](https://doi.org/10.1016/S0378-3812(01)00492-7).
- [131] K. Eiermann and K.-H. Hellwege. "Thermal Conductivity of High Polymers from -180°C to 90°C." In: *J. Polym. Sci.* 57 (1962), pp. 99–106. DOI: <http://dx.doi.org/10.1002/pol.1962.1205716508>.
- [132] W. Xu, Y. Wu, Y. Zhu and X.-G. Liang. "Molecular dynamics simulation of thermal conductivity of silicone rubber." In: *Chin. Phys. B* 29 (2020), p. 046601. DOI: <http://dx.doi.org/10.1088/1674-1056/ab7743>.
- [133] Z. Cheheb, P. Mousseau, A. Sarda and R. Deterre. "Thermal Conductivity of Rubber Compounds Versus the State of Cure". In: *Macromol. Mater. Eng.* 297 (2012), pp. 228–236. DOI: <https://doi.org/10.1002/mame.201100127>.

- [134] N.T. Tran. "Creating material properties for thermoset injection molding simulation process". PhD thesis. Chemnitz, Germany, 2020.
- [135] P. Dluzneski. "Peroxide vulcanization of elastomers". In: *Rubber Chem. Technol.* 74 (2001), pp. 451–492. DOI: <https://doi.org/10.1016/j.polymer.2005.05.07810.5254/1.3547647>.
- [136] G. Baquey, L. Moine, O. Babot, M. Degueil and B. Maillard. "Model study of the crosslinking of polydimethylsiloxanes by peroxides". In: *Polymer* 46 (2005), pp. 6283–6292. DOI: <https://doi.org/10.1016/j.polymer.2005.05.078>.
- [137] P. Wiśniewska, Ł. Zedler and K. Formela. "Processing, Performance Properties, and Storage Stability of Ground Tire Rubber Modified by Dicumyl Peroxide and Ethylene-Vinyl Acetate Copolymers". In: *Polymer* 13 (2021), p. 4041. DOI: <https://doi.org/10.3390/polym13224014>.
- [138] B. Likozar and M. Krajnc. "Simulation of chemical kinetics of elastomer crosslinking by organic peroxides". In: *Polym. Eng. Sci.* 49 (2009), pp. 60–72. DOI: <http://dx.doi.org/10.1002/pen.21218>.
- [139] L.D. de Almeida, H. Wang, K. Junge, X. Cui and M. Beller. "Recent Advances in Catalytic Hydrosilylations: Developments beyond Traditional Platinum Catalysts." In: *Angew. Chem. Int. Ed.* 60 (2021), pp. 550–565. DOI: <http://dx.doi.org/10.1002/anie.202008729>.
- [140] Y. Nakajima and S. Shimada. "Hydrosilylation reaction of olefins: recent advances and perspectives." In: *RSC Adv.* 5 (2015), p. 20603. DOI: <http://dx.doi.org/10.1039/c4ra17281g>.
- [141] R.J. Hofmann, M. Vlatkovic and F. Wiesbrock. "Fifty Years of Hydrosilylation in Polymer Science: A Review of Current Trends of Low-Cost Transition-Metal and Metal-Free Catalysts, Non-Thermally Triggered Hydrosilylation Reactions, and Industrial Applications." In: *Polymers* 9 (2017), p. 534. DOI: <http://dx.doi.org/10.3390/polym9100534>.
- [142] A.J. Chalk and J.F. Harrod. "Homogeneous Catalysis. II. The Mechanism of the Hydrosilation of Olefins Catalyzed by Group VIII Metal Complexes." In: *J. Am. Chem. Soc.* 87 (1964), pp. 16–21. DOI: <https://doi.org/10.1021/ja01079a004>.
- [143] R.Y. Lukin, A.M. Kuchkaev, A.V. Sukhov, G.E. Bekmukhamedov and D.G. Yakhvarov. "Platinum-Catalyzed Hydrosilylation in Polymer Chemistry." In: *Polymers* 12 (2020), p. 2174. DOI: <https://dx.doi.org/10.3390/polym12102174>.

- [144] G. Giorgi, F. De Angelis, N. Re and A. Sgamellotti. "A theoretical investigation of the Chalk-Harrod and modified Chalk-Harrod mechanisms involved in hybrid integrated circuit building." In: *Future Gener. Comput. Syst.* 20 (2004), pp. 781–791. DOI: <https://doi.org/10.1016/j.future.2003.11.018>.
- [145] B. Karstedt. *Platinum complexes of unsaturated siloxanes and platinum containing organopolysiloxanes*. U.S. Patent 3775452A, 1973.
- [146] I. Kownacki, B. Marciniak, H. Steinberger, M. Kubicki, M. Hoffmann, A. Ziarko, K. Szubert, M. Majchrzak and S. Rubinsztajn. "Effect of triorganophosphites on platinum catalyzed curing of silicon rubber." In: *Appl. Catal. A Gen.* 362 (2009), pp. 106–114. DOI: <https://doi.org/10.1016/j.apcata.2009.04.027>.
- [147] Z. Li, P.M. Chevalier and Z. Niu. "Investigation of -alkynol inhibition mechanism and Ru/Pt dual catalysis in Karstedt catalyzed hydrosilylation cure systems." In: *J. Organomet. Chem.* 928 (2020), p. 121541. DOI: <https://doi.org/10.1016/j.jorganchem.2020.121541>.
- [148] L.N. Lewis, J. Stein, R.E. Colborn, Y. Gao and J. Dong. "The chemistry of fumarate and maleate inhibitors with platinum hydrosilylation catalysts." In: *J. Organomet. Chem.* 521 (1996), pp. 221–227. DOI: [https://doi.org/10.1016/0022-328X\(96\)06247-X](https://doi.org/10.1016/0022-328X(96)06247-X).
- [149] A.C.C. Esteves, J. Brokken-Zijp, J. Laven, H.P. Huinink, N.J.W. Reuvers, M.P. Van and G. de With. "Influence of cross-linker concentration on the cross-linking of PDMS and the network structures formed." In: *Polymer* 50 (2009), pp. 3955–3966. DOI: <https://doi.org/10.1016/j.polymer.2009.06.022>.
- [150] G. Rajesh, P.K. Maji, M. Bhattacharya, A. Choudhury, N. Roy, A. Saxena and A.K. Bhowmick. "Liquid Silicone Rubber Vulcanizates: Network Structure - Property Relationship and Cure Kinetics." In: *Polym. Polym. Compos.* 18 (2010), pp. 477–488. DOI: <https://doi.org/10.1177/096739111001800902>.
- [151] Q. Zhai, S. Zhao, C. Zhou, W. Li and C. Peng. "Determination of the SiAH Content of Hydrogen Silicone Oil by a Combination of the Fourier Transform Near Infrared, Attenuated Total Reflectance–Fourier Transform Infrared, and Partial Least Squares Regression Models." In: *J. App. Polym. Sci.* 131 (2014), p. 40694. DOI: <https://doi.org/10.1002/app.40694>.
- [152] Q. Zhai, X. Wu, S. Zhao and C. Zhou. "Curing Kinetics Study by FTIR Spectroscopy and Properties Analysis of Methyl Silicone Resin Membrane". In: *Silicon* 12 (2020), pp. 2761–2768. DOI: <https://doi.org/10.1007/s12633-019-00369-1>.

- [153] S. Muroga, Y. Takahashi, Y. Hikima, S. Ata, M. Ohshima, T. Okazaki and K. Hata. "New evaluation method for the curing degree of rubber and its nanocomposites using ATR-FTIR spectroscopy." In: *Polym. Test.* 93 (2021), p. 106993. DOI: <https://doi.org/10.1016/j.polymertesting.2020.106993>.
- [154] ISO. *Rubber — Measurement of vulcanization characteristics using curemeters*. Standard ISO 6502-1:2018. International Organization for Standardization, 2018.
- [155] D. Marquardt. "An Algorithm for Least-Squares Estimation of Nonlinear Parameters". In: *J. Soc. Indust. App. Math.* 11 (1963), pp. 431–441. DOI: <https://doi.org/10.1137/0111030>.
- [156] ASTM. *Standard test method for estimating kinetic parameters by differential scanning calorimeter using the Borchardt and Daniels method*. Standard ASTM E2041-13(2018). American Society for Testing and Materials, 2018.
- [157] ASTM. *Standard Test Method for Kinetic Parameters for Thermally Unstable Materials Using Differential Scanning Calorimetry and the Flynn/Wall/Ozawa Method*. Standard ASTM E698-18. American Society for Testing and Materials, 2018.
- [158] ASTM. *Standard Practice for Evaluation of Methods for Determination of Kinetic Parameters by Thermal Analysis*. Standard ASTM E2781-11. American Society for Testing and Materials, 2016.
- [159] S. Vyazovkin, A.K. Burnham, J.M Criado, L.A. Pérez-Maqueda, C. Popescu and N. Sbirrazzuoli. "ICTAC Kinetics Committee recommendations for performing kinetic computations on thermal analysis data". In: *Thermochim. Acta* 520 (2011), pp. 1–19. DOI: <https://doi.org/10.1016/j.tca.2011.03.034>.
- [160] S. Vyazovkin. "A time to search: finding the meaning of variable activation energy". In: *Phys. Chem. Chem. Phys.* 18 (2016), pp. 18643–18656. DOI: <https://doi.org/10.1039/C6CP02491B>.
- [161] S. Vyazovkin. "Kissinger Method in Kinetics of Materials: Things to Beware and Be Aware of". In: *Molecules* 25 (2020), p. 2813. DOI: <https://doi.org/10.3390/molecules25122813>.
- [162] S. Vyazovkin, A.K. Burnham, L. Favergeon, N. Koga, E. Moukhina, L.A. Pérez-Maqueda and N. Sbirrazzuoli. "ICTAC Kinetics Committee recommendations for analysis of multi-step kinetics". In: *Thermochim. Acta* 689 (2020), p. 178597. DOI: <https://doi.org/10.1016/j.tca.2020.178597>.
- [163] S. Vyazovkin. "Determining Preexponential Factor in Model-Free Kinetic Methods: How and Why?" In: *Molecules* 26 (2021), p. 3077. DOI: <https://doi.org/10.3390/molecules26113077>.
- [164] X. Zhang. "Application of Kinetic Methods in Thermal Analysis: A Review". In: *Eng. Sci.* 14 (2021), pp. 1–13. DOI: <http://dx.doi.org/10.30919/es8d1132>.

- [165] T. Akahira and T. Sunose. "Method of determining activation deterioration constant of electrical insulating materials". In: *Res. Rep. Chiba Inst. Technol.* 16 (1971), pp. 22–31. DOI: - .
- [166] M.J. Starink. "The determination of activation energy from linear heating rate experiments: a comparison of the accuracy of isoconversion methods". In: *Thermochim. Acta* 404 (2003), pp. 163–176. DOI: [https://doi.org/10.1016/S0040-6031\(03\)00144-8](https://doi.org/10.1016/S0040-6031(03)00144-8).
- [167] T. Bardelli, C. Marano and F.B. Vangosa. "Polydimethylsiloxane crosslinking kinetics: A systematic study on Sylgard184 comparing rheological and thermal approaches". In: *J. Appl. Polym. Sci.* 138 (2021), p. 51013. DOI: <https://doi.org/10.1002/app.51013>.
- [168] I-K. Hong and S. Lee. "Cure kinetics and modeling the reaction of silicone rubber". In: *J. Ind. Eng. Chem.* 19 (2013), pp. 42–47. DOI: <https://doi.org/10.1016/j.jiec.2012.05.006>.
- [169] Z. Karami, O.M. Jazani, A.H. Navarchian and M.R. Saeb. "Cure Kinetics of Silicone/Halloysite Nanotube Composites". In: *J. Vinyl Addit. Technol.* 26 (2020), pp. 548–565. DOI: <https://doi.org/10.1002/vnl.21769>.
- [170] J. Šesták. "Šesták–Berggren equation: now questioned but formerly celebrated—what is right". In: *J. Therm. Anal. Calorim.* 127 (2017), pp. 1117–1121. DOI: <https://doi.org/10.1007/s10973-015-4998-x>.
- [171] M.R. Kamal. "Thermoset characterization for moldability analysis". In: *Polym. Eng. Sci.* 14 (1974), 231–239. DOI: <https://doi.org/10.1002/pen.760140312>.
- [172] S. Heinze and A. Echtermeyer. "A Practical Approach for Data Gathering for Polymer Cure Simulations". In: *Appl. Sci.* 8 (2018), p. 2227. DOI: <https://doi.org/10.3390/app8112227>.
- [173] J. Kruželák, S. Hakošová, A. Kvasničáková and I. Hudec. "Dicumyl Peroxide used as curing Agent for different Typer of Rubber Matrices Part I: Effect of Temperature". In: *KGK Kautschuk Gummi Kunststoffe* 10 (2020), pp. 36–42.
- [174] J. Kruželák, S. Hakošová, A. Kvasničáková and I. Hudec. "Dicumyl Peroxide used as curing Agent for different Typer of Rubber Matrices Part I: Effect of peroxide Content". In: *KGK Kautschuk Gummi Kunststoffe* 11-12 (2020), pp. 36–40.
- [175] J. Lv, L. Chen, W. Chen, H. Gao and M. Peng. "Kinetic analysis and self-accelerating decomposition temperature (SADT) of dicumyl peroxide". In: *Thermochim. Acta* 571 (2013), pp. 60–63. DOI: <http://dx.doi.org/10.1016/j.tca.2013.08.029>.

- [176] Y.-S. Duh, C.-S. Kao and W.-L.-W. Lee. "Chemical kinetics on thermal decompositions of dicumyl peroxide studies by calorimetry". In: *J. Therm. Anal. Calorim.* 127 (2017), pp. 1089–1098. DOI: <http://dx.doi.org/10.1007/s10973-016-5797-8>.
- [177] D.Y. Kim, J.W. Park, D.Y. Lee and K.H. Seo. "Correlation between the Crosslink Characteristics and Mechanical Properties of Natural Rubber Compound via Accelerators and Reinforcement". In: *Polymers* 12 (2020), pp. 1–14. DOI: <https://doi.org/10.3390/polym12092020>.
- [178] Q. Hou, L. Yin, L. Xu and J. Tan. "Effects of composite reinforcing filler, vulcanizing temperature, and pressure on mechanical properties of gasket material for proton exchange membrane fuel cells". In: *J. Appl. Polym. Sci.* 139 (2022), p. 52298. DOI: <https://doi.org/10.1002/app.52298>.
- [179] O. Bianchi, J. Martins, R. Fiorio, R.V.B. Oliveira and L.B. Canto. "Changes in activation energy and kinetic mechanism during EVA crosslinking". In: *Polym. Test.* 30 (2011), pp. 616–624. DOI: <https://doi.org/10.1016/j.polymertesting.2011.05.001>.
- [180] L. Granado, R. Tavernier, G. Foyer, G. David and S. Caillo. "Comparative curing kinetics study of high char yield formaldehyde- and terephthalaldehyde-phenolic thermosets". In: *Thermochim. Acta* 667 (2018), pp. 42–49. DOI: <https://doi.org/10.1016/j.tca.2018.06.013>.
- [181] S. Glasstone, K. Laidler and H. Eyring. *The Theory of the Rate Processes*. 1st ed. United States of America: McGraw-Hill Book Co., 1941.
- [182] C.R. Parks and O. Lorenz. "Crosslinking efficiency in the reaction of dicumyl peroxide with dimmethyl octadiene". In: *J. Polym. Sci.* 50 (1961), pp. 287–298.
- [183] L. Zhao and X. Hu. "Autocatalytic curing kinetics of thermosetting polymers: A new model based on temperature dependent reaction orders." In: *Polymer* 51 (2010), pp. 3841–3820. DOI: <https://doi.org/10.1016/j.polymer.2010.05.056>.
- [184] Q. Ke, W. Chonggang and X. Chen. "Model-free cure kinetics of additional liquid silicone rubber." In: *Thermochim. Acta* 688 (2020), p. 178584. DOI: <https://doi.org/10.1016/j.tca.2020.178584>.
- [185] J. Jin, J.W.M. Noordermeer, A. Blume and W.K. Dierkes. "Effect of SBR/BR elastomer blend ratio on filler and vulcanization characteristics of silica filled tire tread compounds." In: *Polym. Test.* 99 (2021), p. 107212. DOI: <https://doi.org/10.1016/j.polymertesting.2021.107212>.

- [186] A. Harkous, G. Colomines, E. Leroy, P. Mousseau and R. Deterre. "The kinetic behavior of Liquid Silicone Rubber: A comparison between thermal and rheological approaches based on gel point determination." In: *React. Funct. Polym.* 101 (2016), pp. 20–27. DOI: <https://doi.org/10.1016/j.reactfunctpolym.2016.01.020>.
- [187] M. Azevedo, A.-M. Monks, R.C. Kerschbaumer, S. Schlögl and C. Holzer. "Peroxide-Based Crosslinking of Solid Silicone Rubber, Part I: Insights into the Influence of Dicumylperoxide Concentration on the Curing Kinetics and Thermodynamics Determined by a Rheological Approach." In: *Polymers* 14 (2022), p. 4404. DOI: <https://doi.org/10.3390/polym14204404>.
- [188] D.F. Weißer, D. Walz, J. Schmid, D. Mayer and M.H. Deckert. "Calculating the temperature and degree of cross-linking for liquid silicone rubber processing in injection molding." In: *Adv. Manuf. Process.* 3 (2020), e10072. DOI: <https://doi.org/10.1002/amp2.10072>.
- [189] J Knoll and H.-P. Heim. "Analysis of the Similarity between Injection Molding Simulation and Experiment." In: *Polymers* 16 (2024), p. 1265. DOI: <https://doi.org/10.3390/polym16091265>.
- [190] Jay Shoemaker. *Moldflow Design Guide*. 1st ed. Framingham, USA: Moldflow Corporation, 2006.
- [191] F. Marin, A.F. de Souza, R.G. Pabst and C.H. Ahrens. "Influences of the mesh in the CAE simulation for plastic injection molding.." In: *Polímeros* 29 (2019), e2019043. DOI: <https://doi.org/10.1590/0104-1428.05019>.
- [192] H.S. Yuchi, V.R. Joseph and C.F.J. Wu. "Design and Analysis of Multifidelity Finite Element Simulations." In: *J. Mech. Des.* 145 (2023), p. 061703. DOI: <https://doi.org/10.1115/1.4056874>.
- [193] Autodesk Inc. *Reactive Molding analysis*. <https://help.autodesk.com/view/MFIA/2023/ENU/?guid=GUID-4BFB7160-A39C-4063-A839-8B2431B25AAC>. Accessed: 16-07-2024.
- [194] SIMCON kunststofftechnische Software GmbH. *Elastomer injection molding simulation*. <https://www.simcon.com/cadmould/rubber-injection-molding>. Accessed: 16-07-2024.
- [195] CoreTech System Co. Ltd. *Why Reactive Injection Molding?* <https://www.moldex3d.com/solutions/solutions-by-application/reactive-injection-molding/>. Accessed: 16-07-2024.
- [196] B. Kistner. "Modellierung und numerische Simulation der Nachlaufstruktur von Turbomaschinen am Beispiel einer Axialturbinenstufe." PhD thesis. Darmstadt, Germany, 1999.
- [197] SIGMA Engineering GmbH. *The Best Tool for LSR Simulation*. <https://www.sigmasoft.de/en/applications/sigmasoft-lsr/index.html>. Accessed: 16-07-2024.

- [198] M. Traintinger. "Produkt-adaptive Regelung des Kautschukpritzgießens." PhD thesis. Leoben, Austria, 2022.
- [199] P.J. Carreau. "Rheological Equations from Molecular Network Theories." In: *J. Rheol.* 16 (1972), pp. 99–127. DOI: <https://doi.org/10.1122/1.549276>.
- [200] K. Yasuda, R.C. Armstrong and R.E. Cohen. "Shear flow properties of concentrated solutions of linear and star branched polystyrenes." In: *Rheol. Acta* 20 (1981), pp. 163–178. DOI: <https://doi.org/10.1007/BF01513059>.
- [201] M.L. Williams, R.F. Landel and J.D. Ferry. "The Temperature Dependence of Relaxation Mechanisms in Amorphous Polymers and Other Glass-forming Liquids." In: *J. Am. Chem. Soc.* 77 (1955), pp. 3701–3707. DOI: <https://doi.org/10.1021/ja01619a008>.
- [202] A. Soroceanu and G. Stiubianu. "Siloxane Matrix Molecular Weight Influences the Properties of Nanocomposites Based on Metal Complexes and Dielectric Elastomer". In: *Materials* 14 (2021), p. 3352. DOI: <https://doi.org/10.3390/ma14123352>.
- [203] J. González-Rivera, R. Iglío, G. Barillaro, C. Duce and M.R. Tinè. "Structural and Thermoanalytical Characterization of 3D Porous PDMS Foam Materials: The Effect of Impurities Derived from a Sugar Templating Process". In: *Polymers* 10 (2018), p. 616. DOI: <https://doi.org/10.3390/polym10060616>.
- [204] V. Jankauskaitė, P. Narmontas and A. Lazauskas. "Control of Polydimethylsiloxane Surface Hydrophobicity by Plasma Polymerized Hexamethyldisilazane Deposition". In: *Coatings* 9 (2019), p. 36. DOI: <https://doi.org/10.3390/coatings9010036>.
- [205] J. Ji, X. Ge, X. Pang, R. Liu, S. Wen, J. Sun, W. Liang, Ge. J. and X. Chen. "Synthesis and Characterization of Room Temperature Vulcanized Silicone Rubber Using Methoxyl-Capped MQ Silicone Resin as Self-Reinforced Cross-Linker". In: *Polymers* 11 (2019), p. 1142. DOI: <https://doi.org/10.3390/polym11071142>.
- [206] K. Saalwächter and D. Reichert. *Polymer Applications of NMR in Encyclopedia of Spectroscopy and Spectrometry* 3ed. 1st ed. Amsterdam, Netherlands: Elsevier Ltd., 2017.
- [207] D. Cai, A. Neyer, R. Kuckuk and H.M. Heise. "Raman, mid-infrared, near-infrared and ultraviolet-visible spectroscopy of PDMS silicone rubber for characterization of polymer optical waveguide materials". In: *J. Mol. Struct.* 976 (2010), pp. 274–281. DOI: <https://doi.org/10.1016/j.molstruc.2010.03.054>.

- [208] S. Shi, B. Lei, M. Li, X. Cui, X. Wang, X. Fan, S. Tang and J. Shen. "Thermal decomposition behaviour of a thermal protection coating composite with silicone rubber: Experiment and modelling". In: *Prog. Org. Coat.* 143 (2020), p. 105609. DOI: <https://doi.org/10.1016/j.porgcoat.2020.105609>.
- [209] R.D. Cook and C.-L. Tsai. "Residuals in nonlinear regression." In: *Biometrika* 72 (1985), pp. 23–29. DOI: <https://doi.org/10.1093/biomet/72.1.23>.

COLOPHON

This document was typeset using the typographical look-and-feel `classicthesis` developed by André Miede and Ivo Pletikosić. The style was inspired by Robert Bringhurst's seminal book on typography "*The Elements of Typographic Style*". `classicthesis` is available for both \LaTeX and \LyX :

<https://bitbucket.org/amiede/classicthesis/>

Happy users of `classicthesis` usually send a real postcard to the author, a collection of postcards received so far is featured here:

<http://postcards.miede.de/>

Thank you very much for your feedback and contribution.

Final Version as of 1st October 2024 (`classicthesis v4.6`).